ON VORTICAL DISTURBANCES IN SINGLE AND TWO-FLUID BOUNDARY LAYERS

Sandeep Saha

Thermo-Fluids group
Department of Mechanical Engineering
Imperial College London, UK

Submitted in partial fulfilment of the requirements for the degree of Doctor of Philosophy
Department of Mechanical Engineering, Imperial College London
February 2011

Abstract

The vortical disturbance environment surrounding a laminar boundary layer affects the proceedings of transition to turbulence. The exponentially growing Tollmien–Schlichting wave is observed under low free-stream turbulence levels, and is replaced by the algebraically growing streaks upon further increase in the turbulence intensity. This scenario is significantly affected by the presence of wall films which introduce additional instabilities and alter the amplification of the streaks. In this work, the effect of wall films on the linear stability of boundary layers is investigated using the Orr-Sommerfeld, Squire and the interface displacement equations.

A modal analysis is conducted first, in order to identify all the unstable modes and their respective regimes of dominance. Furthermore, the physical mechanisms contributing to disturbance growth are studied using the kinetic energy equation. No unstable eigenvalues are found for wall films less viscous than the outer stream. Under such conditions, the streaks are likely to dominate; their amplification being dependent on the penetration of the free-stream vortical disturbances into the boundary layer.

The ingestion of the free-stream vorticity in the mean shear is explained using the continuous spectrum of the Orr-Sommerfeld equation. A unique parameter is identified to distinguish three asymptotic regimes representing complete, partial and negligible penetration into the boundary layer, respectively. The physical mechanism is a competition between viscous diffusion and convection by the mean flow. The wall film affects the penetration into the boundary layer by modifying the wall-normal wavenumber across the interface.

The penetrating free-stream disturbances efficiently generate streaks by tilting the mean vorticity. Their amplification is investigated using an initial value problem that describes the evolution of a linear perturbation. Lower viscosity wall films reduce the amplification of the streaks. However, another growth mechanism arising from the interfacial displacement dominates at long time and is enhanced for lower viscosity films.

Acknowledgements

I would like to sincerely acknowledge the support that I have received from my principal supervisor, Dr. Tamer Zaki, during the course of my doctoral study. He has provided me with much needed encouragement to overcome the technical challenges. I am grateful to him for devoting much of his time towards numerous discussions on the physical aspects of my research. I am also indebted to him for bestowing upon me the true values of a researcher which are to question and understand, without which my doctoral training would have been incomplete. My gratitude is also reserved for the Department of Mechanical Engineering, Imperial College London, which has been extremely generous in providing me financial assistance over the period of my doctoral study.

I am indebted to my colleague Nick from the bottom of my heart for the numerous technical and personal discussions we had over our late afternoon strolls. He has cherished every success of mine as one of his own and comforted me in every loss of mine. I would also like to thank him for correcting me on every occasion when my usage of the English language was incorrect. Also, I would like to mention his frequent jokes flavoured with the British sense of humour kept the atmosphere in Room 503 lively. My dear flatmate Srikrishna deserves a special mention in this section. I have always found in him the person whom I could approach for any help at any hour and he has never disappointed me. From preparing dinners to looking after me every time I have been taken ill, he has stood by as a true friend. My gratitude is also reserved for Saverio, one of my closest friends. He has been a great moral support and has kept me company every time I was lonely. His uncanny knack of cheering me up by cooking a dinner will forever be memorable to me.

Laura requires special mention in the list of people to whom I am grateful. She has been a very caring friend and consoled me on numerous occasions. She always took an extra step to comfort me each time I was upset. I will always remember that she bought me the most appropriate birthday present in my second year. I would like to thank Lars, with whom I have had numerous technical discussions. His witty jokes would often cheer me up in an otherwise mundane lunch at the senior common room. Luca, Tom and Ed have been extraordinarily helpful during my stay at room 503.

I am indebted to my good old neighbour Pankaj. I have always had the privilege to look

up to Pankaj as a role model and he has been a source of inspiration for me. I would like to acknowledge useful insights obtained from technical discussions with Lawrence and Seo Yoon. I have inevitably benefited much from these discussions.

I owe my gratitude to Olli, Jeremy, Phillip and Michele who have made every effort to make my stay at room 503 pleasant by involving me in various social activities. Friends from room 600, Regina, Iro, Nakul and Francesco also deserve a special mention in this section. They have always invited me to various events, to keep my social life in London active.

Finally, I would like to acknowledge the love and affection of my parents. They have always encouraged me to pursue the noblest of dreams and advised me appropriately in all my endeavours. I would not have reached this milestone, had it not been for their support.

Disclaimer

This thesis includes part of the research I have published with my supervisor Dr. Tamer Zaki, in the following articles:

a) Zaki, T. A. & Saha, S. 2009 On shear sheltering and the structure of vortical modes in single and two-fluid boundary layers. Journal of Fluid Mechanics 626, 113 148.

b) Saha S., Jung S. Y. & Zaki T. A., Stabilization of wall shear beneath vortical disturbances using a thin film, 7th International Conference on Multiphase Flow - ICMF 2010.

The research reported in this document is original and the work of any other researcher has been appropriately referenced.

"It is an old maxim of mine that when you have excluded the impossible, whatever remains, however improbable, must be the truth"

- Sherlock Holmes, *The Adventure of the Beryl Coronet*
Sir Aurthur Conan Doyle

To my parents,

MANJUSHA & NATARAJ

Contents

Abstract **2**

Acknowledgements **3**

Disclaimer **5**

1 Introduction **17**

1.1 Motivation 19

1.2 Modal stability 20

1.2.1 The long wavelength instability 21

1.2.2 The short wavelength instability 21

1.2.3 The high Reynolds number instability 22

1.2.4 Mode competition 22

1.3 Role of continuous modes in transition 23

1.3.1 Modal penetration 24

1.4 Transient growth 25

1.4.1 The algebraic instability 26

1.4.2 Optimal disturbances 28

1.5 Problem definition 29

1.6 Overview 31

2 Modal stability **33**

2.1 Introduction 33

2.2 The base flow 34

2.2.1 Viscosity stratification effects on base flow 36

2.3 The linear perturbation equations 36

2.3.1 Governing equations and boundary conditions 38
2.3.2 The numerical scheme 41
2.3.3 The discrete and continuous spectrum 42
2.4 The modal instabilities 47
2.5 The kinetic energy equation 51
2.5.1 Discussion 57
2.6 Viscosity stratification effects 59
2.7 Conclusion 61

3 The continuous spectrum 63
3.1 Introduction 63
3.1.1 A historical perspective 63
3.1.2 The shear-sheltering phenomenon 65
3.2 The single-fluid theoretical formulation 67
3.2.1 The continuous spectrum 67
3.2.2 Analytical solution for piece-wise linear profile 69
3.3 Asymptotic solutions in the single-fluid boundary layer 72
3.3.1 The convective shear-sheltered regime 72
3.3.2 The diffusive regime 78
3.3.3 The convective-diffusive regime 80
3.3.4 Discussion 83
3.3.5 Penetration depth 85
3.4 The two-fluid theoretical formulation 86
3.4.1 The piecewise linear mean flow 87
3.4.2 Analytical solution for piece-wise linear profile 88
3.5 Asymptotic solutions in the two-fluid boundary layer 91
3.5.1 The convective shear-sheltered regime 91
3.5.2 The diffusive regime 94
3.5.3 The convective-diffusive regime 98
3.6 Discussion 102
3.6.1 Viscosity stratification effects 103
3.6.2 Density stratification 104
3.6.3 Surface tension 106

3.7 Conclusion . . . 107

4 Transient growth of linear perturbations 109

4.1 Introduction . . . 109

4.1.1 The initial value problem . . . 110

4.2 The initial value problem . . . 113

4.2.1 The evolution of normal velocity and interface disturbance . . . 115

4.2.2 The evolution of normal vorticity perturbation . . . 118

4.2.3 Summary of the solution to the initial value problem . . . 121

4.3 The amplification of linear disturbances . . . 122

4.3.1 The single-fluid boundary layer . . . 122

4.3.2 The two-fluid boundary layer . . . 125

4.3.3 Long wavelength limit of the interface mode . . . 131

4.3.4 Viscosity stratification effects . . . 135

4.4 Optimal disturbances . . . 141

4.4.1 The single-fluid boundary layer . . . 143

4.4.2 The two-fluid boundary layer . . . 146

4.4.3 Viscosity stratification effects . . . 150

4.5 Conclusion . . . 155

5 Conclusions 157

5.1 Summary and key results . . . 157

5.1.1 Modal stability . . . 157

5.1.2 Modal penetration . . . 158

5.1.3 Non-modal stability . . . 160

5.2 Discussion . . . 161

A Continuous modes for the piecewise linear boundary layer profile 163

A.1 Coefficients of the single-fluid eigenfunctions . . . 163

A.1.1 Analytical solution . . . 163

A.1.2 The convective shear sheltered regime . . . 164

A.1.3 The diffusive regime . . . 165

A.1.4 The convective-diffusive regime . . . 166

A.2 Coefficient of the two-fluid eigenfunctions . . . 167

A.2.1 Analytical solution 167
A.2.2 The convective shear-sheltered regime 171
A.2.3 The diffusive regime 173
A.2.4 The convective-diffusive regime 174
A.2.5 Thin film solution 175

B The long wavelength limit of the interface mode **177**

C Kinetic energy density **180**

D Adjoint Orr-Sommerfeld operator **182**
D.1 Bi-orthogonality condition 185

E Adjoint Squire operator **188**
E.1 Bi-orthogonality condition 190

F M-norm and its convergence **192**

List of Tables

2.1 Comparison of 10 least stable eigenvalues with Malik & Hooper (2007). . 43
2.2 Modal instability regime map. 51
2.3 Energy terms for different modes of two-fluid boundary layer 57

4.1 Comparison of asymptotically and numerically obtained eigenvalues of the interface mode. 134

List of Figures

1.1 Various routes of transition to turbulence. 18

2.1 Schematic of the base flow of a two-fluid boundary layer. 36
2.2 The mean velocity profile at different viscosity ratios and the variation in boundary layer thickness with viscosity ratio. 37
2.3 Comparison of eigenvalues of Orr-Sommerfeld equation obtained from spectral code to those from literature for the Blasius boundary layer and plane Poiseuille flow. 42
2.4 Comparison of eigenvalues of Orr-Sommerfeld and Squire equation for two-layered Poiseuille flow obtained from two-phase spectral code to results in literature. 44
2.5 The eigenvalue spectrum for the Blasius boundary layer at a subcritical Reynolds number. 44
2.6 Eigenfunctions of the Tollmien–Schlichting mode and a continuous Orr-Sommerfeld mode. 45
2.7 Eigenfunctions of a discrete and a continuous Squire mode. 46
2.8 Eigenvalue spectrum of a two-fluid boundary layer. 47
2.9 Eigenfunctions of the Tollmien–Schlichting mode and the soft mode. . . . 48
2.10 Eigenfunctions of the short wavelength and the high Reynolds number instabilities. 49
2.11 Variation in growth rate of various modal instabilities with streamwise wavenumber. 50
2.12 Distribution of kinetic energy, Reynolds stress and dissipation for various modal instabilities. 58
2.13 Variation in growth rate of modal instabilities with viscosity ratio. 60

3.1 Example of continuous mode shapes for the Blasius boundary layer in three different regimes. 68
3.2 Schematic of the single-fluid piecewise linear mean velocity profile. 70
3.3 Example of continuous mode shapes for piecewise linear profile in the convective shear-sheltering, convective-diffusive and the diffusive regimes. 71
3.4 Continuous mode shape in convective shear-sheltered regime. 75
3.5 Spanwise vorticity in the convective shear-sheltered regime. 76
3.6 Streamlines of a continuous mode in the convective shear-sheltered regime. 77
3.7 Effect of Reynolds number on the thickness of the edge and wall-layer. . . 77
3.8 Continuous mode shape in the diffusive regime. 80
3.9 Spanwise vorticity in convective-diffusive regime. 82
3.10 Schematic of modal penetration for low- and high-frequency free-stream vortical perturbations. 84
3.11 Variation in penetration depth with k_xRe and k_xRe/k_y^2. 86
3.12 Schematic of the two-fluid mean velocity profile. 87
3.13 Examples of continuous mode shape for two-fluid boundary layer and piecewise linear profile in three asymptotic regimes. 90
3.14 Continuous mode shape in convective shear-sheltering regime of a two-fluid boundary layer. 92
3.15 Spanwise vorticity in convective shear-sheltering regime of a two-fluid boundary layer. 93
3.16 Change in nature of spanwise vorticity from oscillatory to exponential in the wall film at different ratios. 95
3.17 Effect of ν_{BT} on penetration of continuous modes. 96
3.18 Normal velocity eigenfunction for a thin film. 97
3.19 Spanwise vorticity for a thin film. 99
3.20 Spanwise vorticity in convective-diffusive regime of a two-fluid boundary layer. 102
3.21 Variation of penetration depth with viscosity ratio. 103
3.22 Variation of penetration depth with density ratio. 104
3.23 High frequency oscillations in mode shape for an extremely dense film. . 105
3.24 Variation of penetration depth with surface tension. 107

4.1 Schematic of a two-fluid boundary layer under the influence of a continuous mode and an interface mode. 113
4.2 Evolution of normal velocity and normal vorticity in the Blasius boundary layer. 124
4.3 Tilting term, $|d_y U\phi|$ for a single-fluid boundary layer. 125
4.4 Coupling coefficient, θ for a single-fluid boundary layer. 125
4.5 Evolution of normal velocity and interface displacement in a two-fluid boundary layer. 127
4.6 Normal vorticity response to forcing arising from normal velocity and interface displacement. 129
4.7 Projection of forcing function $\mathscr{F}$ on the homogeneous Squire eigenfunctions. 129
4.8 Variation in energy with time. 130
4.9 Comparison of numerically and asymptotically obtained eigenfunctions of the interface mode. 136
4.10 Energy, E_η of the interface mode as a function of the viscosity ratio. . . . 136
4.11 Normal vorticity response at various viscosity ratios and the variation in its maximum as a function of viscosity ratio. 138
4.12 The tilting term, $|d_y U\phi|$, for a two-fluid boundary layer. 138
4.13 Energy amplification at various viscosity ratios for different film thicknesses. 139
4.14 Contours of coupling coefficient at different viscosity ratios. 139
4.15 Variation in optimum coupling coefficient with viscosity ratio. 140
4.16 Transient energy amplification for the Blasius boundary layer. 143
4.17 Optimal perturbation in the Blasius boundary layer which gives rise to maximum amplification. 144
4.18 Eigenvalue and projection spectrum for the Blasius boundary layer. 145
4.19 Contours of G_{max} for a single fluid boundary layer. 146
4.20 Transient energy amplification in a two-fluid boundary layer. 146
4.21 Eigenvalue spectrum of a two-fluid boundary layer. 147
4.22 Projection spectrum for the first peak. 148
4.23 Optimal perturbation for the first peak. 149
4.24 Projection spectrum for the second peak. 150
4.25 Optimal perturbation for the second peak. 151

4.26 Variation in interfacial displacement of the optimal disturbance with time. 151
4.27 Variation in $G(t)$ at different viscosity ratios. 152
4.28 Contours of G_{max} at various viscosity ratios. 152
4.29 Locus of k_x^o and k_z^o as a function of μ_{BT}. 153
4.30 Variation in G_{opt} with μ_{BT}. 154

F.1 Convergence of the kinetic energy norm for a single fluid boundary layer 193
F.2 Convergence of the kinetic energy and the M-norm 193
F.3 Comparison of the M-norm and the kinetic energy norm 194

Chapter 1

Introduction

Boundary layer flows are commonly observed in our daily life: from small-scale shear flows on aerodynamically designed cars to large-scale atmospheric flows. Numerous industrial applications also involve boundary layer flows, for instance flows on aircraft wings, gas turbine blades and submarines (Reed *et al.*, 1996). Transition to turbulence of a laminar boundary layer is frequently observed in most of the aforementioned applications. The flow is laminar near the leading edge and transitions to turbulence downstream due to the presence of disturbances in the surrounding environment.

Transition is not a random event, rather a series of events precede the onset of transition. These involve inception of disturbances into the boundary layer. Thereafter instability mechanisms cause these disturbances to amplify, leading to turbulent spots that spread and contaminate the laminar flow, marking the onset of transition. Such transitional flow is observed over the majority of a blade surface in a turbine (Hodson & Howell, 2005). A significant portion of the loss in efficiency in a low pressure turbine is due to the flow characteristics on the suction-side boundary layer of the blade (Hodson & Howell, 2005). Performance of the turbine can be improved by controlling the transitional flow on the blades by introducing surface trips and air jets (Zhang *et al.*, 2006).

In the aircraft industry a delay in transition is desirable as it reduces the drag force leading to an increase in the fuel efficiency, longer range and increased speed (Reed *et al.*, 1996; Gad-el Hak, 2000; Kim & Bewley, 2007).

Wall-films sheared by boundary layers are also relevant to transitional flows. For instance, the performance of an aircraft wing is affected by the presence of de-icing agents during take-off (Yih, 1990; Ozgen *et al.*, 1998, 2002). Similar transition processes occur in pipeline lubrication and surface oil flow visualization techniques (Timoshin,

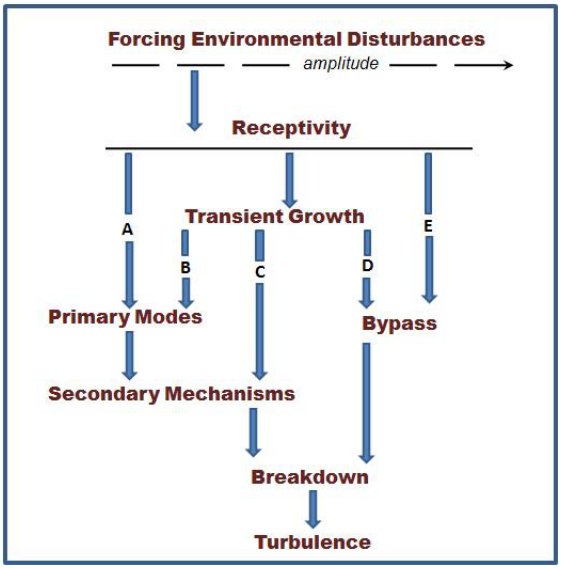


Figure 1.1: Various routes of transition to turbulence (Morkovin *et al.*, 1994; Saric *et al.*, 2002).

1997; Miesen & Boersma, 1995; Ludwieg & Hornung, 1989).

Since transition is commonly observed in boundary layers and its control yields many advantages, an improved understanding of the various mechanisms underlying the process is important.

There are numerous sources of the disturbances such as surface roughness, sound or vorticity perturbations (Saric *et al.*, 2002) which affect the transition process. Albeit transition is an overly complex process, a general overview of the various routes of transition to turbulence has developed over the past decades.

Figure 1.1 shows the various stages of transition proposed by Morkovin *et al.* (1994). The first stage is known as receptivity, which concerns the manner in which any external disturbance excites a boundary layer instability (Morkovin, 1969; Reshotko, 1976). This stage governs the nature of the instability observed in the boundary layer. Upon the inception of the disturbance into the boundary layer, the receptivity stage is over and various linear and non-linear instability mechanisms cause the disturbance to amplify. Depending on the initial amplitude of the disturbance different transition scenarios emerge.

Transition route A is observed under extremely low levels of free-stream turbulence. A linear stability analysis of the flow using the Orr-Sommerfeld equation reveals that an exponentially growing two-dimensional instability, the Tollmien–Schlichting wave

(Tollmien, 1929; Schlichting, 1933), can exist under such conditions. It is observed that the Tollmien–Schlichting wave amplifies over a slow viscous time-scale and undergoes a secondary instability. The secondary instability grows on a fast convective time-scale and is followed by the breakdown of laminar flow into rapidly spreading turbulent spots (Saric *et al.*, 2002). This path to transition has been traditionally referred to as the *natural route*. The process of natural transition begins at a Reynolds number (based on momentum thickness) of $1,165$ and ends approximately at $3,100$ (Abu-Ghannam & Shaw, 1980).

However, an increase in the level of free-stream turbulence, causes the transition route to change. Another instability mechanism, transient growth, supersedes the growth of the Tollmien–Schlichting wave. Klebanoff (1971) reported the presence of a three dimensional instability characterized by large fluctuations in streamwise velocity. This instability unlike the Tollmien–Schlichting wave, is not an eigenmode of the system but rather a superposition of eigenmodes which amplifies over a short time-scale and decays at long time. The associated streamwise lengthscale is large compared to the boundary layer thickness, resembling alternating forward and backward jets and are usually referred to as Klebanoff modes (Kendall, 1991) or streaks. Transient growth is however not the only mechanism to generate streaks, for example see Chernyshenko & Baig (2005) who describe another streak generation mechanism for near-wall turbulent flows. Saric *et al.* (2002) and Reshotko (2001) suggest that the extent of streak amplification can lead to transition either by:
i) route B, wherein the growth of the Tollmien–Schlichting wave is altered by the streaks,
ii) route C, where the base flow is non-linearly distorted by the streaks giving rise to secondary instabilities,
iii) route D where transient growth leads to a turbulence like disturbance spectrum inside the boundary layer.
Under high levels of free-stream turbulence, the traditionally known transition paths are circumvented as shown in route E.

1.1 Motivation

The initial growth of disturbances in paths A to D can be explained within the purview of linear stability theory (Reshotko, 2001). Linear stability analysis of a flow is performed

by perturbing the basic state, which is a solution to the Navier-Stokes equations, with an infinitesimal disturbance and evaluating the temporal or spatial response of the flow. In this work the linear stability of boundary layers is investigated using the Orr-Sommerfeld and Squire equations, which represent the velocity-vorticity form of linearized Navier-Stokes equations under the parallel flow assumption.

Exponential instabilities and transient growth play a key role in driving the initial instability observed in boundary layers. In this study the exponential instabilities and transient growth of perturbations are examined in a viscous, incompressible flow over a flat plate. The study is motivated by the fact that *all transition routes except for path E* are affected by the linear stability of the boundary layer. In particular the effects of introducing an immiscible wall-film on the linear stability of the boundary layer are investigated. Introduction of a wall film of different viscosity can significantly alter the stability characteristics of the boundary layer. For instance, the theoretical investigations of Hooper & Boyd (1987), Yih (1990), Boomkamp *et al.* (1997), Ozgen *et al.* (1998) and Miesen & Boersma (1995) reveal the presence of additional instabilities due to the film and the interface. Instability waves distinct from Tollmien–Schlichting waves have been also reported in the experiments of Craik (1966) and Ozgen *et al.* (2002).

Linear stability theory has been successful in explaining phenomena which occur in the laminar to turbulent transition. The theoretically predicted Tollmien–Schlichting wave (Tollmien, 1929; Schlichting, 1933) was observed in the experiments of Schubauer & Skramstad (1947). In two-fluid boundary layers, the experimental results of Ozgen *et al.* (2002) show good agreement with the linear stability predictions of Miesen & Boersma (1995). The success of linear stability theory is attributed to the fact that the physical mechanisms at work are already determined at the onset of the instability. The subsequent non-linear evolution depends on the nature of primary instability (Yecko *et al.*, 2002; Lasheras & Hopfinger, 2000). In order to understand the different physical phenomena at play, linear stability theory is reviewed in the following sections.

1.2 Modal stability

Classical linear stability analysis of boundary layers concerns the unstable modes in the eigenvalue spectrum of the Orr-Sommerfeld equation. The minimum Reynolds number

at which an exponentially unstable mode is found is defined as the critical Reynolds number. Beyond the critical Reynolds number the flow is deemed unstable to infinitesimal perturbations. For example, the Tollmien–Schlichting wave, which is an eigen-solution of the Orr-Sommerfeld equation, grows exponentially for $Re_{\delta^*} > 520$, where Re_{δ^*} is the Reynolds number based on displacement thickness, δ^*. Apart from the Tollmien–Schlichting wave there exist three more unstable modes in two-fluid flows.

1.2.1 The long wavelength instability

The pioneering work of Yih (1967) established the existence of a long-wavelength interfacial instability or the 'soft mode'. The instability arises from the viscosity mismatch across the interface in two-fluid flows. The author derived closed-form asymptotic solution to the Orr-Sommerfeld equation in the long wavelength limit for two-layered Couette and Poiseuille flows. Yih also demonstrated the instability can exist at *any Reynolds number*, unlike the Tollmien–Schlichting wave which is unstable only at supercritical Reynolds numbers. The growth rate of the soft mode depends on the viscosity ratio, the density ratio and the depth ratio of the two layers.

The work of Renardy (1987) demonstrated that the soft mode is stable if the lower layer is thinner and less viscous compared to the upper layer. Yih (1967) having considered this possible configuration of two-fluid flows, had not highlighted the stabilization of the soft mode in his article. In the absence of density stratification and surface tension the soft mode is stabilized at low and moderate wavenumbers. Charru & Hinch (2000) presented the physical mechanism associated with the thin layer effect. The authors argued that the long wavelength limit does not introduce a vertical velocity perturbation instantaneously but only a streamwise velocity perturbation. In order to conserve mass the interface decays to compensate for the fluid accumulated by displacing the low viscosity fluid in the bottom. The contrary is true if the lower layer is more viscous.

1.2.2 The short wavelength instability

Two-layered flows are susceptible not only to long wavelength instability but also to a short wavelength instability. By considering the stability of unbounded Couette flow for two fluids Hooper & Boyd (1983) concluded that such flows are *always* unstable with respect to short wavelength perturbations. They found that surface tension always

has a stabilizing effect on this instability. Energy considerations revealed that, apart from Reynolds stress mechanism, work done by tangential stresses at the interface can transfer energy from the mean flow to the perturbation. This instability is referred to as HB(1983) in this work.

The physical mechanism driving the short wavelength instability was proposed by Hinch (1984). The author argued that continuity of streamwise velocity at the disturbed interface gave rise to vorticity fluctuations. To leading order these vorticity fluctuations are in phase in the two fluids. However, inclusion of the higher order *inertial* effects leads to a phase difference between the vorticity fluctuations thereby causing the disturbance to grow at the interface. Upon considering realistic values of surface tension and shear rate for two-fluid flows Hinch concluded that the short wavelength instability is unlikely to be observed under experimental conditions.

1.2.3 The high Reynolds number instability

Another kind of instability exists at high Reynolds number, when the kinematic viscosity of the lower bounded fluid is less than that of the upper fluid (Hooper & Boyd, 1987) (referred to as HB(1987) hereafter). The wavelength of the instability is of the order of the film thickness and is unaffected by surface tension. The instability derives energy largely from the Reynolds stress in the lower fluid and has its origin in the viscous layer near the wall. This instability is distinct from the Tollmien–Schlichting wave and has not been reported in experiments.

1.2.4 Mode competition

Due to the presence of a multiplicity of instability mechanisms in two-fluid flows, the growth rate of the various exponential instabilities is often comparable. For instance, the most unstable mode switches character with variation in streamwise wavenumber, an effect referred to as mode competition (Yecko *et al.*, 2002). Ozgen *et al.* (1998) report mode competition for two-fluid boundary layers wherein the soft mode and HB(1983) modes dominate at low and high wavenumbers respectively, and the intermediate wavenumber range is dominated by the Tollmien–Schlichting wave.

1.3 Role of continuous modes in transition

In boundary layer flows, the eigenvalue spectrum of the Orr-Sommerfeld equation possesses a continuous spectrum of modes and a discrete spectrum (Jordinson, 1971; Grosch & Salwen, 1978; Gustavsson, 1979). All the exponential instabilities belong to the discrete spectrum of the Orr-Sommerfeld eigenvalue problem. In this subsection, the continuous modes are described which, despite being asymptotically stable, play a crucial role in the transition process. Since the continuous modes have been explored extensively for single-phase boundary layers only, the review in this section is limited to the single-fluid system.

An increase in the free-stream turbulence intensity causes the growth of Klebanoff modes instead of the discrete modes (Klebanoff, 1971; Kendall, 1991; Westin *et al.*, 1994; Matsubara & Alfredsson, 2001). Further, the experiments of Kendall (1991) report that the leading edge bluntness and lift do not affect the streaks (Saric *et al.*, 2002). The generation of Klebanoff modes as a response to increased free-stream turbulence intensity therefore suggests the existence of a localized receptivity mechanism for free-stream vortical disturbances.

Jacobs & Durbin (2001) accurately simulated the transition scenario under moderate levels of free-stream turbulence without a leading edge. They used a superposition of continuous Orr-Sommerfeld modes only to generate a turbulent inflow and achieved good agreement with the experimental results of Roach & Brierley (1992). The Fourier-like behavior of the eigenfunctions in the free stream provided an ideal basis to construct an isotropic free-stream disturbance field with a prescribed energy spectrum. Inside the boundary layer the perturbations satisfy the linear stability equations. Unlike the eigenfunctions of exponential instabilities which decay away from the mean shear, the continuous mode eigenfunctions remain oscillatory in the free stream and resemble Fourier modes. Inside the boundary layer, they decay with increasing depth. These modes, therefore, establish a link between free-stream vortical disturbances and the boundary layer – a matter of debate in earlier literature where only a remarkably weak link could be established (Berger & Aroesty, 1977; Mack, 1976).

In place of the spectrum of inlet perturbations, Zaki & Durbin (2005, 2006) simulated the interaction of pairs of continuous modes. The direct numerical simulations demonstrated the role that different frequency components of the continuous spectrum

can play in bypass transition: low-frequency modes penetrate the shear and force boundary layer streaks while the high-frequency modes trigger the secondary instability and breakdown. Numerical experiments of Liu *et al.* (2008) highlighted that transition can also be triggered by the non-linear interaction of the Tollmien–Schlichting wave with a continuous mode.

The idea that decaying eigenmodes of the Orr-Sommerfeld equation would play such a significant role in our understanding of flow instability, for instance bypass transition, would have left many researchers incredulous in the era of Tollmien (1929) and Schlichting (1933) where the focus of linear stability research was on exponentially unstable solutions.

1.3.1 Modal penetration

Numerical simulations of transition under the influence of free-stream turbulence by Jacobs & Durbin (2001), Brandt *et al.* (2004) and Zaki & Durbin (2005, 2006), have demonstrated two receptivity mechanisms for continuous modes: a linear and a non-linear mechanism. The non-linear mechanism was proposed by Berlin & Henningson (1999) and is effective in generating streaks when the free-stream turbulence spectrum contains high-frequency fluctuations. For a free-stream turbulence spectrum with energy content in the low frequency range, the linear mechanism is more effective (Brandt *et al.*, 2004). This observation suggests that there is a selectivity mechanism in the boundary layer which lets only low frequency free-stream perturbations penetrate and generate streaks. Conversely, the high frequency disturbances must interact non-linearly to generate a low frequency disturbance which then enters the boundary layer and generates streaks.

Indeed, Zaki & Durbin (2005) have shown that there exists a coupling coefficient which is a measure of the propensity of *a continuous Orr-Sommerfeld mode* to generate streaks. The coupling coefficient in turn, depends on the extent of penetration of the normal velocity of the continuous mode into the mean shear. Large eddy simulations of transition under free-stream turbulence by Voke & Yang (1995) have also reported that the coupling between wall-normal velocity and mean shear leads to streamwise velocity fluctuations. Penetration of continuous modes is also important in Falkner-Skan-Cooke boundary layers. The work of Schrader *et al.* (2009) shows continuous modes which

penetrate deep into the boundary layer are more effective in triggering the cross-flow instability. The influence of a particular component of the continuous spectrum on boundary layer stability is therefore largely affected by the structure of the eigenfunction and its extent of penetration into the boundary layer.

The study of continuous mode penetration into the boundary layer sheds light on why low-frequency disturbances are more effective in triggering Klebanoff modes compared to high frequency disturbances. However, the modal penetration study does not explain the process of streak generation and its subsequent amplification. Continuous Orr-Sommerfeld and Squire modes belong to the stable half of the eigenvalue spectrum but their interaction can lead to streak amplification levels where non-linear effects are no longer negligible (Trefethen *et al.*, 1993). The long time modal stability analysis fails to predict any such behavior and therefore a short time stability analysis is essential (Schmid, 2007). In the following subsection the investigations carried out by researchers is reviewed to explain the transient growth of linear perturbations.

1.4 Transient growth

The origin of transient growth theory is intricately linked to the ubiquity of streaks in shear flows. The amplification of a three dimensional streaks at subcritical Reynolds numbers could not be attributed to the two dimensional Tollmien–Schlichting waves (Gaster, 1975). Since the Tollmien–Schlichting wave is an eigenmode of the boundary layer, it represents a long time solution to the stability problem where the initial transients have died out. However, the streaks which appear at subcritical Reynolds number could only be explained if the transients were considered. Therefore there arose the need to obtain the temporal or spatial evolution of disturbances from the initial condition. To this end, transient growth theory has been developed over the last three decades. The initial investigations were aimed at demonstrating amplification of disturbances, distinct from the Tollmien–Schlichting wave, evolving from particular initial conditions. For instance, a number of papers explicitly showed three-dimensional perturbations could amplify linearly with time in various shear flows (Ellingsen & Palm, 1975; Landahl, 1980; Gustavsson & Hultgren, 1980; Benney & Gustavsson, 1981; Gustavsson, 1981; Hultgren & Gustavsson, 1981). However, later the focus shifted to identifying the initial conditions which lead to maximum transient growth. Gustavsson (1991) investigated the

amplification of a perturbation comprising of the least damped Orr-Sommerfeld mode with zero normal vorticity in plane Poiseuille flow. He computed the spanwise wavenumber of the perturbations which amplified the most. However, his conclusions could not be generalized as the analysis was restricted by the specificity of the initial condition considered. This drawback was overcome by the work of Butler & Farrell (1992) who found optimal initial conditions for maximizing the growth of the kinetic energy of the perturbation. This approach was subsequently adopted in numerous papers (Reddy & Henningson, 1993; South & Hooper, 1999; Andersson *et al.*, 1999; Luchini, 2000).

Recent transient growth computations have been largely successful in explaining experimentally observed phenomena. For instance, the calculations of Luchini (2000) and Andersson *et al.* (1999) show good agreement with the experimental measurements of streamwise velocity fluctuations by Westin *et al.* (1994). The theoretical analysis of Luchini (2000) also predicts the spanwise scale of the streaks observed in experiments. Moreover, Andersson *et al.* (1999) came up with a transition prediction scheme for moderate free-stream turbulence intensities based on their transient growth computations. The scheme could accurately predict transition location in the numerical experiments of Voke & Yang (1995).

Transient growth theory predicts that streamwise oriented vortices cause strong streamwise velocity fluctuations which are elongated in the streamwise direction (Butler & Farrell, 1992). This prediction is concordant with experimental observations of Klebanoff (1971), Kendall (1991), Westin *et al.* (1994) and Matsubara & Alfredsson (2001) who all observed streamwise elongated structures or Klebanoff modes.

In the context of two-phase flows streamwise oriented structures (ligaments) superimposed on spanwise roll-ups (Kelvin-Helmholtz instability) have been also reported in experiments on plane free shear layers (Lasheras *et al.*, 1986; Lasheras & Choi, 1988). Transient growth computations of the most amplified spanwise vortical wave by Yecko & Zaleski (2005) predicted the number of ligaments formed in the coaxial liquid jet breakup experiments of Marmottant & Villermaux (2004).

1.4.1 The algebraic instability

Transient growth has its origin in the work of Ellingsen & Palm (1975), who first reported the existence of an inviscid algebraic instability. This instability could arise despite the

lack of an inflectional mean velocity profile. The disturbances which lead to algebraic growth were three-dimensional and had not received attention from researchers until then owing to the Squire's theorem. The theorem states: "To obtain the minimum critical Reynolds number it is sufficient to consider only two-dimensional disturbances" (Drazin & Reid, 1981, pp 155). The instability was termed algebraic as the streamwise velocity grew linearly with time, unlike the previously known exponential instabilities. Landahl (1980) examined general localized perturbations and concluded that the disturbance kinetic energy increases indefinitely with time due to the inviscid lift-up mechanism. He further demonstrated that the streamwise extent of the localized disturbance grows with time. However, these analyses were inviscid and restricted to streamwise independent perturbations.

A viscous analysis of nearly streamwise independent disturbances by Hultgren & Gustavsson (1981) demonstrated growth in streamwise velocity on short time-scale. Nevertheless, viscous dissipation dominated at long time and the perturbation decayed. This result was particularly interesting, as the discrete modes are absent from the eigenvalue spectrum of the Orr-Sommerfeld and Squire equations in the limit of streamwise independent perturbations. Therefore, perturbations comprising of *continuous modes only* cause growth on a short time-scale and hence the importance of modal penetration. A similar attempt to obtain the temporal evolution of linear perturbations by Salwen & Grosch (1981) had failed to demonstrate amplification. They considered only two-dimensional Orr-Sommerfeld modes instead of the three dimensional modes. The temporal evolution of a general three dimensional linear perturbation was obtained by Zaki & Durbin (2005). The authors showed that streamwise independent perturbations are the most likely to generate Klebanoff modes as they have the highest coupling coefficient. Perturbations with high streamwise wavenumbers have a low coupling coefficient and, therefore, do not generate streaks.

The physical explanation of the algebraic instability is provided in the original work of Phillips (1969) and is similar to the Orr mechanism (Orr, 1907) for disturbance amplification. For a more elaborate description of the Orr mechanism see Lindzen (1988) . With the help of rapid distortion theory, Phillips explained why streamwise independent perturbations cause the algebraic instability. Perturbation velocity fields which are dependent on the streamwise axis generate smaller wall normal scales as time increases

due to presence of mean shear. The amplitude of the wall-normal perturbation velocity being inversely proportional to the magnitude of the wavenumber, tends to zero at long time. However, streamwise independent perturbations are unaffected by the mean shear. Hence they do not generate smaller wall-normal scales thereby leading to a constant amplitude normal velocity perturbation. As a result, low velocity fluid is lifted from the near wall region to the outer edge of the boundary layer causing backward perturbation jets. Similarly, high velocity fluid from the outer edge is pushed deeper into the boundary layer generating forward perturbation jets. Thus, the streamwise independent disturbances lead to the algebraic instability.

1.4.2 Optimal disturbances

An alternative to obtaining the evolution of perturbations from a specific initial condition is to compute the optimal initial condition. This approach has been the focus of many recent investigations on transient growth of shear flows (Butler & Farrell, 1992; Reddy & Henningson, 1993; South & Hooper, 1999; Schmid & Henningson, 2001; Malik & Hooper, 2005, 2007; Schmid, 2007). The perturbation energy is optimized over all initial conditions and a transient growth curve is computed which represents the maximum possible amplification in energy of a general disturbance at any instant of time compared to the initial state. Hence, the computation of optimal perturbations can predict the disturbances which are most likely to occur in flows exposed to random perturbations(Butler & Farrell, 1992).

In this alternative approach, the energy growth is viewed as a result of the non-normality of the coupled system of the Orr-Sommerfeld and Squire equations (Schmid & Henningson, 2001). The dynamics of a non-normal system over a finite time-scale is not governed by the leading eigenmode but rather by the entire spectrum of eigenmodes. Though the non-orthogonal eigenmodes may individually be decaying, their superposition can lead to algebraic growth over a short time-scale (Schmid, 2007). Initial conditions corresponding to streamwise oriented vortices have been reported to give rise to maximum amplification of energy in two dimensional shear flows (Butler & Farrell, 1992; Reddy & Henningson, 1993; Luchini, 2000). These streamwise oriented vortices have a spanwise and wall-normal scale of the order of the shear layer thickness.

Optimal disturbances that give rise to maximal transient amplification have also

been computed by researchers for two-phase mixing layers (Yecko & Zaleski, 2005), two-layer Poiseuille flow (South & Hooper, 1999; Malik & Hooper, 2005, 2007) and two-fluid channel flow (Yecko, 2008). Olsson & Henningson (1995), Yecko & Zaleski (2005) and Yecko (2008) reported the presence of multiple peaks in the transient amplification curves for two-fluid flows. Presence of multiple peaks in transient amplification curves is a characteristic of two-fluid flows which is usually not observed in single-fluid shear flows. Transient amplification curves for single fluid system have one peak due to the presence of the algebraic instability at subcritical Reynolds numbers. The present analysis reveals that there is an additional instability mechanism associated with the interface which affects the transient amplification curves and leads to multiple peaks.

1.5 Problem definition

The various instability mechanisms present in shear flows were reviewed in the last three sections. There exist long-wavelength, short-wavelength and high-Reynolds-number instabilities for two-fluid flows in addition to the Tollmien–Schlichting waves. However, the long-wavelength instability is stable when the lower layer is thin and less viscous. The role of the continuous modes in triggering the transition process was also discussed. The penetration of continuous modes into the boundary layer has a pronounced effect on its stability with respect to excitation of the algebraic instability. The algebraic instability is most effective in generating Klebanoff modes for streamwise independent perturbations. Finally the concept of optimal disturbances, which can be used to evaluate the stability of boundary layers at any given instant of time, was discussed.

Boundary layer stability depends on many parameters. For instance, the free-stream turbulence intensity, the disturbance spectrum, the associated length scales and the Reynolds number. The situation is complicated further when a film of different viscosity is introduced next to the wall. The introduction of the film has a three fold effect: (a) the mean flow is altered; (b) the viscosity of the fluid in the near wall region changes thereby affecting the perturbation field; (c) thirdly an interface is introduced which is an additional source of vortical perturbations. Therefore, the stability of the boundary is affected in a complex manner by the wall film. The objective of this work is to explain the effect of an immiscible wall film on the stability of boundary layers in the presence of vortical disturbances. In order to achieve this objective, more specific questions are

raised and addressed:

a) How does the wall-film alter the modal stability of the boundary layer ?

b) What is the effect of the wall film on penetration of free-stream vortical disturbances into the shear ?

c) How does the wall film affect the transient growth of perturbations ?

In this thesis, each subsequent chapter (except for the last one) addresses one of these questions in their respective order. The general scheme in all the chapters is to first examine the special case of a single-fluid boundary layer. Thereafter, the effect of the wall film is investigated by varying the viscosity of the lower fluid.

The three questions on linear stability of boundary layers are addressed using the Orr-Sommerfeld and Squire equations for the single fluid boundary layer. The pair of Orr-Sommerfeld and Squire equations is applicable under the parallel flow assumption. This assumption though valid for bounded flows like Couette and Poiseuille flow, is only approximately true for boundary layers when $\frac{\lambda_x}{\delta}\frac{d\delta}{dx} \ll 1$, where λ_x is the streamwise wavelength of the perturbation and δ is the boundary layer thickness. The non-parallel effects are therefore not accounted for in the current formulation. However, the non-parallel effects are $O(\sqrt{Re_x^{-1}})$ (Herbert, 1997) for the modal instabilities, where Re_x is the Reynolds number based on downstream distance, x. Therefore the the non-parallel effects alter the results only quantitatively. The physical mechanism and hence the qualitative behavior are captured by the Orr-Sommerfeld and Squire equations. Cossu *et al.* (2009) have justified the use of the parallel flow assumption for computing the growth of the algebraic instability by pointing out the similarity in the results of Butler & Farrell (1992) and Andersson *et al.* (1999). The former used the Orr-Sommerfeld and Squire equations to compute optimal disturbances and predicted that streamwise independent structures lead to maximum energy growth. They also reported that the maximum amplification in energy is proportional to $Re_{\delta^*}^2$. Later, Andersson *et al.* (1999) incorporated the non-parallel effects and arrived at the same conclusion, though the scaling factor for maximum growth was found to be half of that predicted by Butler & Farrell (1992). Therefore, the focus of this work is to predict the qualitative effect of the wall film on the instabilities. Inferences from the quantitative results should be regarded as preliminary in nature.

Since the current formulation is based on linear theory, the non-linear effects such

as mean flow distortion and modal interactions, which are crucial in latter stages of transition are also absent in this study. However, it is generally acknowledged that the growth of streaks in boundary layers is essentially due to the transient growth mechanism, which is within the purview of linear theory (Trefethen *et al.*, 1993; Zaki & Durbin, 2005). The non-linear interactions constantly feed energy into the low-frequency modes which potentially amplify owing to the linear mechanism (Jacobs & Durbin, 2001).

While analyzing the two-fluid boundary layers, the interface equation and linearized matching conditions are included in the formulation. The linearization of the interfacial boundary conditions is valid under the assumption, $k|A| \ll 1$ where k is the magnitude of the perturbation wavenumber vector and $|A|$ is the amplitude of the perturbation (Miles, 1959). This assumption is necessary in order to ensure that the velocity perturbations arising due to interface deformation are within the bounds of linear theory. Large amplification of interface deformation owing to transient growth could therefore quickly lead to non-linear interactions.

1.6 Overview

This thesis is organized into five chapters. In this chapter the study of linear stability theory was motivated. Subsequently the literature was reviewed to identify the various instabilities present in boundary layers. Finally, three questions were posed in order to assess the effect of a wall film on boundary layer stability, which are to be answered in the following chapters.

Chapter two deals with the exponential instabilities present in two-fluid boundary layers. At first, the equations governing the mean flow are examined. Thereafter the Orr-Sommerfeld and Squire eigenvalue problem for two-fluid boundary layers is formulated and the associated exponential instabilities are reported. In order to classify the various instabilities, the kinetic energy equation for infinitesimal perturbations is derived and all the terms are computed (Boomkamp & Miesen, 1996). To conclude, the effect of viscosity stratification on the various instabilities is investigated.

The exponential instabilities are expected to be dominant only at low free-stream disturbance levels. If the free-stream turbulence intensity is moderate, the algebraic instability dominates which is three dimensional in nature. The continuous spectrum modes are vital contributors to the amplification of the algebraic instability and hence

the focus of chapter three. The extent to which these free-stream disturbances get ingested into the boundary layer depends on a selectivity mechanism. Low-frequency disturbances are allowed to perturb the boundary layer more efficiently compared to the high-frequency disturbances. Although it is evident from experimental observations that free-stream disturbances affect the boundary layer stability (Hernon *et al.*, 2007), a physical description of the receptivity process is lacking in the literature.

In order to explain the selectivity mechanism, a piecewise linear approximation of the Blasius profile is developed and analytical expressions for continuous modes are obtained in three asymptotic limits. The asymptotic results are compared to the numerically obtained continuous modes for a Blasius profile. The asymptotic analysis provides insight into modal penetration, based on which a penetration mechanism is proposed for continuous modes. A norm to quantify the penetration of continuous modes into the boundary layer is also defined. The asymptotic analysis is extended further to the two-fluid boundary layer and the effect of viscosity stratification and film thickness is evaluated using the penetration depth norm.

In chapter four, the temporal evolution of linear perturbations from specific initial conditions is described. An initial boundary value problem is formulated in terms of normal velocity, interface displacement and normal vorticity perturbations to study the growth of the algebraic instability. The initial boundary value problem is solved using the eigenfunctions of the Orr-Sommerfeld, interface and Squire equations. The evolution of a streamwise oriented vortex is traced, which is constituted using a continuous Orr-Sommerfeld mode and the interface mode. The coupling coefficient proposed by Zaki & Durbin (2005) and the amplification of the algebraic instability are computed at different viscosity ratios and film thicknesses. Finally, the optimal disturbances are computed in order to examine the effect of general initial conditions and establish the stability of the boundary layer. Chapter five comprises of a summary and the key results of this work.

Chapter 2

Modal stability

2.1 Introduction

The growth of the Tollmien–Schlichting wave governs the natural transition process in a Blasius boundary layer (Schubauer & Skramstad, 1948). The introduction of a wall film alters the stability of the boundary layer by introducing additional unstable modes. The soft mode and the Tollmien–Schlichting mode have been reported extensively in the literature on two-fluid boundary layers. For instance, Craik (1966) identified slow waves and fast waves (based on the group velocity) in his experiments on air-water flows with water as the wall film. The fast waves (Tollmien–Schlichting wave) appeared for thicker film thicknesses and slow waves (soft mode) were observed upon reduction in the film thickness. Craik concluded from his theoretical analysis that the slow waves have their origin in the tangential stress perturbations introduced by air at the interface. However, he had considered only the flow in the thin film in his analysis. Miesen & Boersma (1995) included the perturbation field in the air in their analysis and obtained better agreement with the experimental results of Craik (1966).

Similarly, Kao & Park (1972) reported the existence of shear (Tollmien–Schlichting wave) and interfacial (soft mode) waves in their experiments on two-layered Poiseuille flow of oil over water with equal thicknesses. The shear waves had a critical layer deep inside the water and traveled faster than the mean interfacial velocity. The interfacial waves were however damped and did not affect the natural transition process. Moreover, recent experiments of Ozgen *et al.* (2002) captured the fast waves of Craik but found little evidence for the slow-interfacial waves.

The dominance of the fast shear mode (Tollmien–Schlichting wave) over the slow

interfacial mode (soft mode) in the experiments can be understood in terms of mode competition. Yecko *et al.* (2002) performed linear stability analysis of plane mixing layers and found that the liquid mode dominates over the interfacial mode for viscosity ratios of $O(1)$. However, the shear mode dominates at very low viscosity ratios. In the context of two-fluid boundary layers, the instability observed in the experiments of Hendrickson & Hill (1987) was suggested to be an interfacial mode by Yih (1990) based on his asymptotic analysis. Later, Yih's result was shown to be incorrect by the numerical investigation of Ozgen *et al.* (1998), who revealed that the shear mode is the most dominant instability.

However, all these investigations considered the flow with the more viscous fluid being present in the film. No experimental evidence exists of either the short wavelength instability (Hooper & Boyd, 1983) or the high Reynolds number instability (Hooper & Boyd, 1987). In this chapter, the regime in which these instabilities exist is identified and their growth rates are computed to establish the most dominant mode in each regime. Furthermore, there exists a need to distinguish the modes from one another. For instance, if two modal instabilities are present in the same regime, how would one differentiate one from the other? Boomkamp & Miesen (1996) suggested that the instabilities can be discerned based on the mechanism which transfers energy to the perturbation. Finally, the effect of viscosity stratification on the growth rate of the various modes is investigated.

This chapter is arranged into seven sections. The following section presents the mean-flow equations for the two-fluid boundary layer followed by the formulation of the two-fluid eigenvalue problem. The governing equations and boundary conditions are stated in §3, followed by a discussion on the regimes of various instabilities observed in two-fluid boundary layer. Thereafter, the kinetic energy equation is derived and the energy budget for the different types of modes is reported. The penultimate section presents the effect of viscosity stratification, followed by the conclusions of this chapter.

2.2 The base flow

A schematic representation of the base flow in a two-fluid boundary layer is shown in figure 2.1. The fluid densities, ρ_j, and viscosities, μ_j, change across the interface, where the associated subscript $j = T, B$ denotes the top and bottom fluids respectively. The film-thickness is denoted by δ_B and the viscosity and density ratios are expressed as

$\mu_{BT} \equiv \mu_B/\mu_T$ and $\rho_{BT} \equiv \rho_B/\rho_T$. Therefore the kinematic viscosity, $\nu_j = \frac{\mu_j}{\rho_j}$, and ν_{BT} refers to $\frac{\mu_{BT}}{\rho_{BT}}$. The Blasius-like mean flow profile is obtained by solving the two-fluid boundary layer equations following the approach of Nelson *et al.* (1995). In boundary layer coordinates (ξ, ζ), the mean-flow satisfies,

$$F\partial_\zeta^2 F + \nu_j \partial_\zeta^3 F - \xi \left(\partial_\zeta F \frac{\partial \partial_\zeta F}{\partial \xi} - \partial_\zeta^2 F \frac{\partial F}{\partial \xi} \right) = 0, \tag{2.1}$$

where $\xi = \left(\frac{U_\infty x}{2\nu_T}\right)^{1/2}$, $\zeta = y\left(\frac{U_\infty}{2\nu_T x}\right)^{1/2}$, and $F = \frac{\Psi}{(2\nu_T x U_\infty)^{1/2}}$ with Ψ as the streamfunction and $\partial_\zeta \equiv \frac{\partial}{\partial \zeta}$. The interface height $\zeta^* = \delta_B \left(\frac{U_\infty}{2\nu_T x}\right)^{1/2}$ is governed by the standard kinematic condition,

$$\frac{\partial \zeta^*}{\partial \xi} = \frac{1}{\xi}\left(\frac{V}{U} - \zeta^*\right), \tag{2.2}$$

where U and V are the mean streamwise and wall-normal velocities at the interface, respectively. Continuity of velocity and stress are enforced at $\zeta = \zeta^*$, according to,

$$[F] = 0 \quad ; \qquad [\partial_\zeta F] = 0 \quad ; \qquad [\mu \partial_\zeta^2 F] = 0, \tag{2.3}$$

where [.] denotes the change across the interface, $(.)_T - (.)_B$. In addition, $F(\xi, \zeta)$ must satisfy the boundary conditions,

$$F(\xi, 0) = 0, \quad \partial_\zeta F(\xi, 0) = 0, \quad \lim_{\zeta \to \infty} \partial_\zeta F(\xi, \zeta) = 1. \tag{2.4}$$

Equation 2.1, and the associated boundary and interface conditions, are solved according to the approach described in Schlichting (1987, pp 187-191) but here for the two-fluid problem. The iterative procedure ensures convergence of the interface height and velocity profile at every downstream location, ξ. The solution at large ξ agrees with the asymptotic behavior described in Nelson *et al.* (1995), and provides the mean profile for the present analysis. In the following subsection the effect of variation in viscosity of the film on the base flow is investigated.

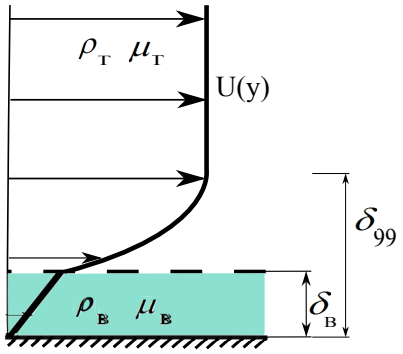


Figure 2.1: Schematic of the base flow of a two-fluid boundary layer.

2.2.1 Viscosity stratification effects on base flow

Figure 2.2(a) shows the effect of viscosity ratio, μ_{BT} on the mean shear distribution. As the viscosity ratio μ_{BT} is reduced the mean shear is strengthened in the lower fluid and is weakened in the upper fluid. This effect can be understood by noticing the linear velocity profile of the flow in the lower fluid and shear stress continuity at the interface. The viscous term dominates over the inertia terms in equation 2.1 inside the bottom fluid as the film-thickness, ζ^*, tends to zero in the limit $\xi \to \infty$, thereby rendering the flow locally to be a low Reynolds number flow (Nelson *et al.*, 1995). As a result, the velocity profile in the wall film resembles Couette flow driven by the shear stress exerted by upper fluid at the interface. The shear stress continuity in equation 2.3 requires that the ratio of mean velocity gradients across the interface be inversely proportional to μ_{BT}. Therefore as the viscosity ratio μ_{BT} is reduced the mean shear in the bottom fluid increases. The strengthening of mean shear in the lower layer affects the boundary layer thickness, δ_{99} as well. Figure 2.2(b) shows that the boundary layer thickness reduces with reduction in μ_{BT}. Since δ_{99} is a function of μ_{BT}, its use as a lengthscale for stability calculations leads to lack of correspondence between the results for different values of μ_{BT}. Therefore, the boundary layer thickness of the Blasius profile, $\delta_{SF} \equiv 4.9\sqrt{\frac{\nu x}{U_\infty}}$, is used as the lengthscale for two-fluid stability calculations to ensure comparability of results, where the subscript SF stands for single-fluid.

2.3 The linear perturbation equations

The linearized Navier-Stokes equations govern the stability of a base flow with respect to infinitesimal perturbations. Further by assuming a parallel base flow, the linearized

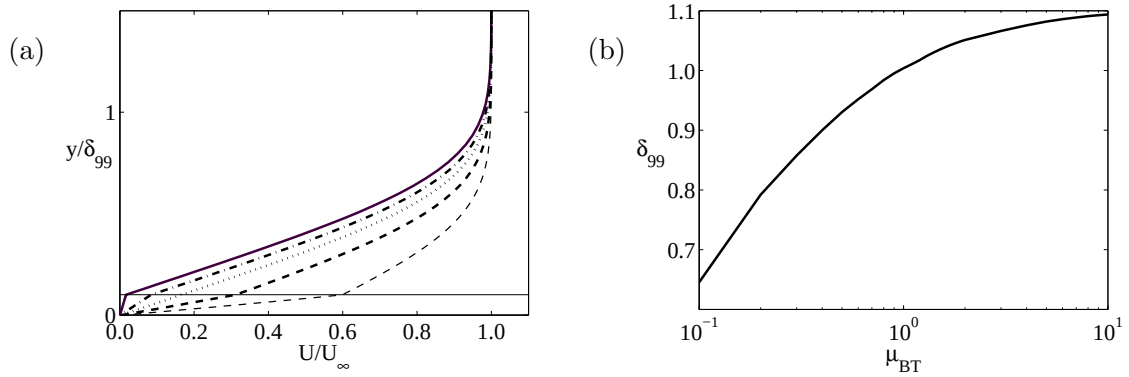


Figure 2.2: (a) The mean velocity profile at different viscosity ratios. ——, $\mu_{BT} = 10$; — · —, $\mu_{BT} = 2$; · · · ·, $\mu_{BT} = 1$; - - -, $\mu_{BT} = 0.5$; - - -, $\mu_{BT} = 0.2$. $\rho_{BT} = 1, \delta_B = 0.1$ (b) The variation in boundary layer thickness with viscosity ratio μ_{BT}.

Navier-Stokes equations can be reduced to a pair of equations for normal velocity and normal vorticity (see for example Schmid & Henningson (2001) for the derivation). The parallel flow assumption also allows accommodation of wavelike solutions in the streamwise, spanwise and temporal directions. Thus the system of partial differential equations is reduced to a system of ordinary differential equations commonly known as the Orr-Sommerfeld and Squire equations. Moreover, the system of ordinary differential equations can be reduced to an eigenvalue problem by imposing homogeneous boundary conditions that determine the stability of a base flow.

The eigenvalue problem comprising of the Orr-Sommerfeld and Squire equations can be used to study either the temporal or the spatial stability of a base flow. In the temporal problem, the base flow is perturbed with a disturbance of particular wavelength in the streamwise and spanwise directions initially and the time response of the system is calculated. In the spatial problem the inflow into a domain is perturbed with a disturbance of particular frequency and the downstream evolution of the perturbation is studied. The temporal case is investigated in this chapter, since it is a linear eigenvalue problem. The spatial counterpart is a non-linear eigenvalue problem (Schmid & Henningson, 2001; Haj-Hariri, 1988; Danabasoglu & Biringen, 1990).

The stability analysis of the Blasius boundary layer involved perturbing the velocity and pressure field. In two-fluid flows a general disturbance perturbs the interface, in addition to the velocity and pressure field and therefore must be accounted for in the stability analysis. In the following subsection the theoretical formulation for the two-fluid

stability problem is described.

2.3.1 Governing equations and boundary conditions

The problem of interest requires determining the stability of a base flow $[U_j(y)\ 0\ 0]$ with respect to a linear perturbation, $\mathbf{u} = [\mathbf{u}\ \mathbf{v}\ \mathbf{w}]^{\mathbf{T}}$ and an infinitesimal displacement of the interface, f, from its mean location y_f. The stability problem can be described completely in terms of v, f and normal vorticity $\eta \equiv \frac{\partial u}{\partial z} - \frac{\partial w}{\partial x}$.

$$\frac{\partial}{\partial t}\begin{bmatrix}\nabla^2 v_j \\ \mathrm{f} \\ \eta_j\end{bmatrix} = \begin{bmatrix} d_y^2 U_j \frac{\partial}{\partial x} + \nu_j \nabla^4 - U_j \frac{\partial}{\partial x}\nabla^2 & 0 & 0 \\ \mathcal{C}_v & -U(y_f)\frac{\partial}{\partial x} & 0 \\ d_y U_j \frac{\partial}{\partial z} & 0 & \nu_j \nabla^2 \eta - U_j \frac{\partial}{\partial x} \end{bmatrix}\begin{bmatrix} v_j \\ \mathrm{f} \\ \eta_j \end{bmatrix} \quad (2.5)$$

where the operator $\mathcal{C}_v v \equiv v(y_f)$. While presenting the results, lengths are non-dimensionalized by the Blasius boundary layer thickness, and velocities by the free-stream speed U_∞, so that ν_j is effectively $1/Re_j$ where $Re_j \equiv \frac{U_\infty \delta_{SF}}{\nu_j}$ is the Reynolds number of the respective fluid.

The wall and free-stream boundary conditions require that the perturbation vanish at $y = 0$ and $y \to \infty$ respectively. In addition velocity and stress continuity need to be maintained at the interface. The interfacial conditions at $y = y_f$ (Yih, 1967; Yecko & Zaleski, 2005) are as follows,

$$[u] = -\left[\frac{dU}{dy}\right]\mathrm{f}; \qquad [v] = 0; \qquad [w] = 0,$$

$$[\tau_{xy}] = -\left[\mu\frac{d^2U}{dy^2}\right]\mathrm{f}; \qquad [\tau_{zy}] = 0; \qquad [\tau_{yy}] = \sigma\nabla^2\mathrm{f}. \quad (2.6)$$

where, $[u]$ is the jump in u across the interface, for instance. The normal mode assumption is invoked along the x, z and t axes as these directions are homogeneous,

$$\begin{bmatrix} v_j \\ \mathrm{f} \\ \eta_j \end{bmatrix} = \begin{bmatrix} \phi_j(y) \\ f \\ \chi_j(y) \end{bmatrix} e^{i(k_x x + k_z z - \omega t)}. \quad (2.7)$$

Substituting the normal mode assumption (equation 2.7) into equation 2.5 leads to

the following eigenvalue problem,

$$-i\omega \begin{bmatrix} d_y^2 - k^2 & 0 & 0 \\ 0 & 1 & 0 \\ 0 & 0 & 1 \end{bmatrix} \begin{bmatrix} \phi_j \\ f \\ \chi_j \end{bmatrix} = \begin{bmatrix} \mathscr{L}_j & 0 & 0 \\ \mathscr{C}_v & \mathscr{I} & 0 \\ \mathscr{C}_j & 0 & \mathscr{S}_j \end{bmatrix} \begin{bmatrix} \phi_j \\ f \\ \chi_j \end{bmatrix} \tag{2.8}$$

where,

$$\begin{aligned} \mathscr{L}\phi_j &\equiv ik_x d_y^2 U_j \phi_j + \nu_j (d_y^2 - k^2)^2 \phi_j - ik_x U_j (d_y^2 - k^2)\phi_j \\ \mathscr{C}_v \phi_j &\equiv \phi_j(y_f) \\ \mathscr{I} f &\equiv -ik_x U_j(y_f) f \\ \mathscr{C}\phi_j &\equiv ik_z d_y U_j \phi_j \\ \mathscr{S}\chi_j &\equiv \nu_j (d_y^2 - k^2)\chi_j - ik_x U \chi_j \end{aligned}$$

The no-slip and no-penetration boundary conditions are imposed on the eigenfunctions ϕ and χ at the wall and in free-stream,

$$\begin{aligned} \phi_B(0) = 0; \qquad d_y\phi_B(0) = 0; \qquad \chi_B(0) = 0 \\ \phi_T(y \to \infty) = 0; \quad d_y\phi_T(y \to \infty) = 0; \quad \chi_T(y \to \infty) = 0 \end{aligned} \tag{2.9}$$

The normal mode assumption reduces the velocity and stress continuity conditions 2.6 at $y = y_f$ to the following conditions,

$$[\phi] = 0; \quad [d_y\phi] = ik_x[d_y U]f; \quad [\mu(d_y^2 + k^2)\phi] = ik_x[\mu d_y^2 U]f;$$

$$\left[\rho\Big(- i\omega d_y\phi + ik_x(U d_y\phi - \phi d_y U) - \nu(d_y^3 - 3k^2 d_y)\phi\Big)\right] = \sigma k^4 f, \tag{2.10}$$

and,

$$[\chi] = -ik_z[d_y U]f; \quad [\mu_T d_y \chi] = -ik_z[\mu d_y^2 U]f. \tag{2.11}$$

The surface tension, σ, is represented by the non-dimensional parameter $We \equiv \frac{\rho_T U_\infty^2 \delta_{99}}{\sigma}$ in the results which signifies the ratio of inertial to capillary forces.

The eigenvalue problem 2.8 is split into two individual eigenvalue problems, as the coupling term, $\mathscr{C}_j$ does not affect the eigenvalues. This simplification is possible as there exists one way coupling between the Orr-Sommerfeld, the interface equation and the Squire equations. That is, *only* the normal velocity and interface equations force the Squire equation. Further, by examining the characteristic equation for 2.8 it is concluded,

$$(\mathscr{L}_j\phi_j + i\omega_{os}(d_y^2 - k^2)\phi_j + \mathscr{C}_v\phi_j + \mathscr{I}f + i\omega_{os}f)(\mathscr{S}\chi_j + i\omega_{sq}\chi_j) \quad = \quad 0.$$

This characteristic equation clearly demonstrates that the eigenvalues of the Orr-Sommerfeld, interface and the Squire equations are independent of the coupling term $\mathscr{C}_j$. Hence, the eigenvalues of each equation can be found independently by solving the corresponding homogeneous problem. Therefore each Orr-Sommerfeld eigenmode is associated with a normal velocity and a particular normal vorticity eigenfunction denoted by $[\phi_j \ f \ \chi_j^P]^T$ whereas each Squire eigenmode is associated with only a normal vorticity eigenfunction denoted by $[0 \ 0 \ \chi^H]^T$ (Schmid & Henningson, 2001). Hereafter, the eigenfunctions of the Squire equation, χ^H, are referred to as homogeneous Squire eigenfunctions and the normal vorticity component of the Orr-Sommerfeld modes, χ^P, as the particular Squire eigenfunctions. Hence the following eigenvalue problem results for the normal velocity and interface displacement $[\phi_j \ f]^T$,

$$-i\omega_{os}\begin{bmatrix} d_y^2 - k^2 & 0 \\ 0 & 1 \end{bmatrix}\begin{bmatrix} \phi_j \\ f \end{bmatrix} \quad = \quad \begin{bmatrix} \mathscr{L}_j & 0 \\ \mathscr{C}_v & \mathscr{I} \end{bmatrix}\begin{bmatrix} \phi_j \\ f \end{bmatrix} \tag{2.12}$$

with interfacial conditions 2.10. The Squire eigenvalue problem reduces to

$$-i\omega_{sq}\chi_j^H \quad = \quad \mathscr{S}\chi_j^H, \tag{2.13}$$

with the following conditions at the interface,

$$[\chi^H] = 0; \quad [\mu d_y\chi^H] = 0 \tag{2.14}$$

on χ^H. The free-stream and the wall boundary conditions remain unaltered as shown in equation 2.9.

2.3.2 The numerical scheme

The eigenmodes of the Orr-Sommerfeld , interface and Squire equations were computed using a spectral method proposed by Orszag (1971). The numerical implementation is detailed in Schmid & Henningson (2001) for Couette and Poiseuille flows. The method was extended to boundary layer flows and is described first for the single-fluid eigenvalue problem. The extension to the two-fluid problem is presented thereafter. The eigenfunctions are continuous across the interface for the single-fluid problem and the interface equation can be dispensed with. The normal velocity eigenfunction, ϕ, is expanded in terms of mapped Chebyshev polynomials,

$$\phi(y) = \sum_{n=0}^{N} a_n T_n(y) \tag{2.15}$$

where a_n is the coefficient of the n^{th} Chebyshev polynomial T_n. The maximum number of Chebyshev polynomials, N, used to achieve convergence was in the range $150 - 200$. The domain was truncated at a large but finite wall-normal location, ℓ. The value of ℓ was chosen such that the results remain unaffected despite further extension of the domain height. A typical value of $\ell = 10$ was found sufficient to meet the criterion.

The grid was generated in the Chebyshev space, $y_{ch} \in [-1, 1]$ using the Gauss-Lobatto points, $y_{ch,k} = cos\left(\frac{\pi k}{N-1}\right)$ and mapped to the physical space $y \in [0, \ell]$. The mapping function

$$y \;=\; C_1 \frac{1 + y_{ch}}{C_2 - y_{ch}} \tag{2.16}$$

was employed, where $C_1 = \frac{y_m \ell}{\ell - 2y_m}$ and $C_2 = 1 + 2\frac{C_1}{\ell}$. In order to resolve the eigenfunctions accurately inside the boundary layer, half the grid points are clustered in the region, $y \in [0, y_m]$ with $y_m \approx \frac{\ell}{4}$.

The expansion in equation 2.15 was substituted into the Orr-Sommerfeld equation and the resulting expression was equated to zero at the mapped Gauss-Lobatto grid points to obtain a system of algebraic equations. The eigenvalues of the discretized system were obtained using the standard mathematical libraries in MATLAB version 7.0. The same procedure was used to compute the eigenvalues of the Squire equation as well. The eigenvalues obtained from the spectral code were validated against results reported

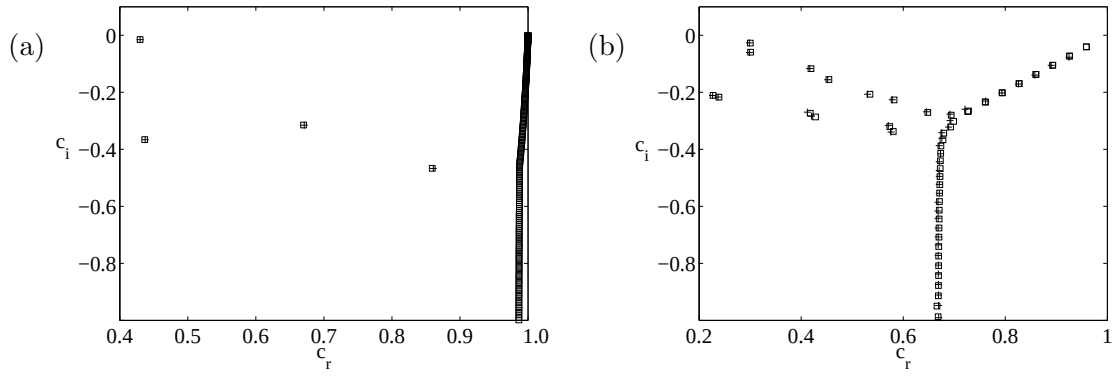


Figure 2.3: Comparison of eigenvalues of Orr-Sommerfeld equation obtained from spectral code to those from literature. (a) Eigenvalues for Blasius boundary layer in Table *A*.4. of Schmid & Henningson (2001, pp 507) $k_x = 0.125, k_z = 0.3, Re_{\delta^*} = 800$. The length-scale is based on displacement thickness, δ^*. (b) Eigenvalues for Poiseuille flow from Figure 1 of Butler & Farrell (1992, pp 1640). $k_x = 1.48, k_z = 0, Re = 5000$. The length-scale is based on half channel width. □: Orr-Sommerfeld eigenvalues from spectral code, +: data from literature.

by Schmid & Henningson (2001); Butler & Farrell (1992) for the Blasius profile (see figure 2.3). In order to solve the eigenvalue problems 2.12 and 2.13 the numerical method was extended to the two-fluid case. Considering the discontinuities in the gradients of the eigenfunctions of Orr-Sommerfeld and Squire equations at the interface (2.10 and 2.14), the eigenfunctions were discretized using separate Chebyshev expansions for each fluid (Boomkamp *et al.*, 1997). Each Chebyshev domain was mapped to the physical space using the non-linear mapping function 2.16. The eigenvalues obtained from the numerical solution were validated against results of Malik & Hooper (2007); Yecko *et al.* (2002); Ozgen *et al.* (1998) for two-fluid Poiseuille flow (see figure 2.4(a - b) and table 2.1), plane mixing layer and two-fluid boundary layer, respectively. In the following subsection the various modal instabilities present in two-fluid boundary layers and the effect of wavenumber and Reynolds number on their growth rate are discussed.

2.3.3 The discrete and continuous spectrum

In this section the eigenvalue spectrum of a Blasius boundary layer is discussed in order to distinguish the discrete and continuous eigenmodes. Such a distinction is necessary because these two classes of modes have distinct origins and affect the boundary layer stability in different ways. Figure 2.5 shows the eigenvalue spectrum of the Blasius

	Orr-Sommerfeld eigenvalues	Squire eigenvalues
Eigenvalue 1(a)	$0.96918601073189 + 0.00604208866655i$	$0.98766995266517 - 0.01372566302651i$
Eigenvalue 1(b)	$0.96918601076110 + 0.00604208869132i$	$0.98766995264539 - 0.01372566304011i$
Eigenvalue 2(a)	$0.28484843890443 - 0.01011185546559i$	$0.95816777060089 - 0.04041796909515i$
Eigenvalue 2(b)	$0.28484843890322 - 0.01011185537559i$	$0.95816777059932 - 0.04041796909526i$
Eigenvalue 3(a)	$0.94259490753582 - 0.05627479656729i$	$0.93845662260597 - 0.05044730483170i$
Eigenvalue 3(b)	$0.94259490753787 - 0.05627479656900i$	$0.93845662258111 - 0.05044730484577i$
Eigenvalue 4(a)	$0.93840674255833 - 0.06477324027322i$	$0.92280220710842 - 0.08882120841495i$
Eigenvalue 4(b)	$0.93840674255152 - 0.06477324026143i$	$0.92280220710899 - 0.08882120841128i$
Eigenvalue 5(a)	$0.37723505341686 - 0.06794412605333i$	$0.86663140299941 - 0.10417748155876i$
Eigenvalue 5(b)	$0.37723505353947 - 0.06794412588336i$	$0.86663140298608 - 0.10417748155628i$
Eigenvalue 6(a)	$0.88115101729715 - 0.10307735555716i$	$0.21406783996782 - 0.11870123022709i$
Eigenvalue 6(b)	$0.88115101729405 - 0.10307735555510i$	$0.21406783998015 - 0.11870123020867i$
Eigenvalue 7(a)	$0.89766085840158 - 0.11125255950915i$	$0.21557185150578 - 0.11938817021499i$
Eigenvalue 7(b)	$0.89766085839054 - 0.11125255951702i$	$0.21557185150586 - 0.11938817021458i$
Eigenvalue 8(a)	$0.85522572479450 - 0.15272511748131i$	$0.88775518818245 - 0.12930728536209i$
Eigenvalue 8(b)	$0.85522572532745 - 0.15272511788305i$	$0.88775518818132 - 0.12930728536050i$
Eigenvalue 9(a)	$0.82665473518114 - 0.16322748841623i$	$0.79851838147823 - 0.16024506404555i$
Eigenvalue 9(b)	$0.82665473503831 - 0.16322748850042i$	$0.79851838177810 - 0.16024506382595i$
Eigenvalue 10(a)	$0.80684188551368 - 0.18995362225777i$	$0.85300543638929 - 0.17371596251881i$
Eigenvalue 10(b)	$0.80684188588084 - 0.18995362229659i$	$0.85300543639136 - 0.17371596252217i$

Table 2.1: Comparison of eigenvalues with column 1 of Table *I* in Malik & Hooper (2007, pp 052102-6). (a) Eigenvalues from Malik & Hooper (2007); (b) Eigevalues from the spectral code. $k_x = 1, k_z = 0, Re = 3000, \mu_{BT} = 0.5$.

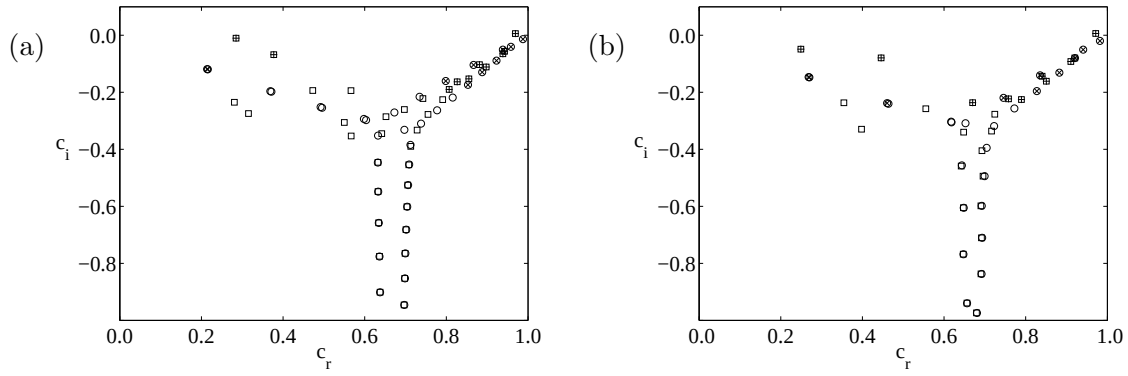


Figure 2.4: Comparison of eigenvalues of Orr-Sommerfeld and Squire equation for two-layered Poiseuille flow obtained from two-phase spectral code to those in Table *I* of Malik & Hooper (2007, pp 052102-6). (a) $k_x = 1, k_z = 0, Re = 3000$. (b) $k_x = 0.5, k_z = 0.5, Re = 3000$. The length-scale is based on half channel width. □: Orr-Sommerfeld eigenvalues from spectral code, +: Orr-Sommerfeld eigenvalues of Malik & Hooper (2007), ○: Squire eigenvalues from spectral code, ×: Squire eigenvalues of Malik & Hooper (2007)

.

boundary layer. The real part of the complex eigenvalue, $c_r = \omega_r/k_x$, is the phase speed of the disturbance and the imaginary part, $c_i = \omega_i/k_x$, is the associated growth rate of the disturbance. Two distinct class of modes can be identified: the discrete and the continuous spectrum. The discrete modes have a phase speed lower than U_∞ whereas the continuous spectrum modes convect at the free-stream velocity. The Tollmien–Schlichting wave belongs to the discrete spectrum and is stable as the eigenvalue spectrum is evaluated at a subcritical Reynolds number, $Re = 1417.8$.

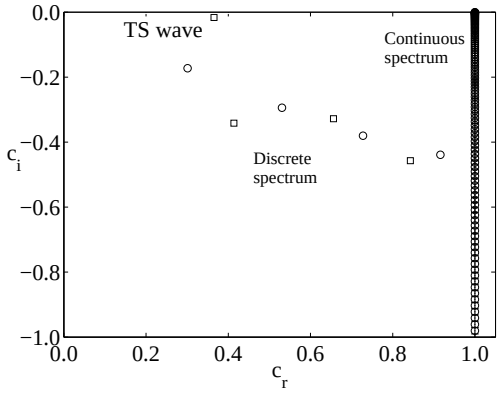


Figure 2.5: The eigenvalue spectrum for the Blasius boundary layer at a subcritical Reynolds number. $k_x = 0.5671, k_z = 0, Re = 1417.8$

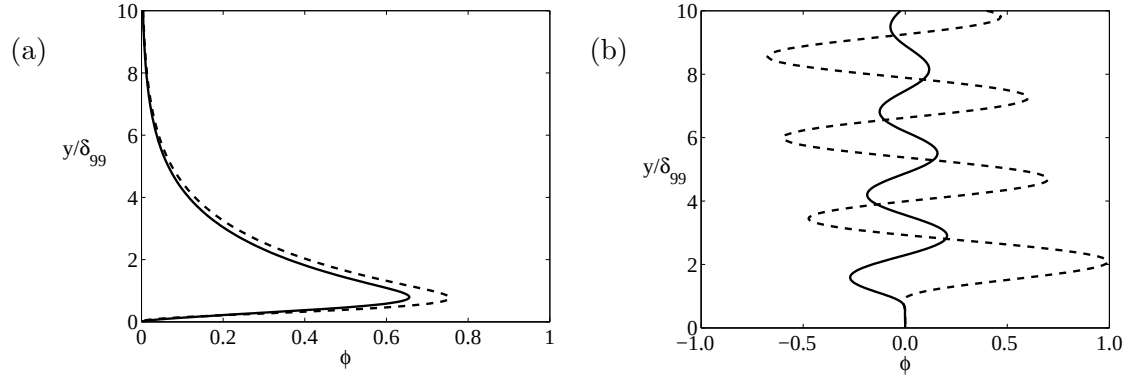


Figure 2.6: (a) Eigenfunction of the Tollmien–Schlichting mode $c = 0.3652 - 0.0165i$ (b) Eigenfunction of a continuous Orr-Sommerfeld mode $c = 1 - 0.0098i$. $k_x = 0.5671, k_z = 0, Re = 1417.8$. ——, real component; - - -, imaginary component.

Figure 2.6 contrasts between the eigenfunctions associated with the Tollmien–Schlichting wave and a continuous Orr-Sommerfeld mode. The eigenfunction of the Tollmien–Schlichting wave peaks inside the boundary layer and decays exponentially in the free-stream as shown in figure 2.6(a). In contrast the eigenfunction of the continuous mode in figure 2.6(b) is oscillatory in the free-stream and decays inside the boundary layer.

The discrete and continuous Squire modes also display the same contrast in the free-stream behavior. Figure 2.7(a) shows that the eigenfunction of a discrete Squire mode is non-zero only between the wall and the boundary layer edge. The continuous Squire eigenfunction in figure 2.7(b) remains oscillatory outside the boundary layer and decays rapidly at the edge of the boundary layer. All Squire modes belong to the stable half of the complex plane (Schmid & Henningson, 2001) and therefore do not affect the modal stability of the boundary layer.

It would seem curious that the discrete and continuous modes, despite being the eigenstates of the same mean flow, have a vastly different free-stream behavior. In order to understand this difference, the Orr-Sommerfeld equation is examined in the free stream ($y \to \infty$) where $U \to U_\infty$ and $d_y U$ and $d_y^2 U$ vanish,

$$\left[(U_\infty k_x - \omega) \left(\frac{d^2}{dy^2} - k_x^2 - k_z^2 \right) + i\nu \left(\frac{d^2}{dy^2} - k_x^2 - k_z^2 \right)^2 \right] \phi_\infty = 0. \qquad (2.17)$$

The constant coefficient equation admits solutions of the form $\phi_\infty \sim e^{\lambda y}$. Substituting

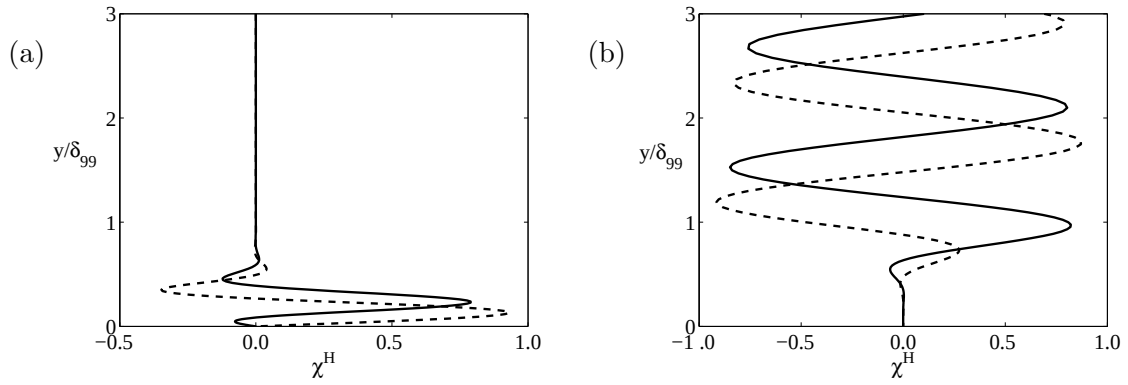


Figure 2.7: (a) Eigenfunction of the discrete Squire mode $c = 0.301 - 0.1726i$ (b) Eigenfunction of a continuous Squire mode $c = 1 - 0.0098i$. $k_x = 0.5671, k_z = 0, Re = 1417.8$. ——, real component; - - -, imaginary component.

$e^{\lambda y}$ in 2.17 and solving for λ yields the following roots,

$$\begin{aligned} \lambda_{1,2} &= \pm\sqrt{k_x^2 + k_z^2 + i\frac{k_x}{\nu}\left(U_\infty - \omega/k_x\right)} \\ \lambda_{3,4} &= \pm\sqrt{k_x^2 + k_z^2}. \end{aligned} \tag{2.18}$$

Therefore the solution in the free stream can be written as $\phi_\infty \sim \sum_{n=1}^{4} \phi_n(y)$ where $\phi_n(y) \equiv C_n e^{\lambda_n y}$. It should be noted that, ϕ_3 grows exponentially and therefore must be excluded from the solution. The eigenfunction, ϕ_1 also exhibits the same behavior. One exception is when λ_1 is purely imaginary which yields the continuous modes. Here the focus is on discrete modes and hence ϕ_1 should be excluded. The solutions ϕ_2 and ϕ_4 decay exponentially in the free stream. Therefore the free-stream solution of the discrete modes comprises of ϕ_2 and ϕ_4 only (Mack, 1976). Gustavsson (1979) considered the initial value problem of the evolution of a three-dimensional disturbance in a boundary layer. He obtained the solution using Fourier and Laplace transforms. While inverting the Laplace transform of the normal velocity component, he found that the discrete modes are the poles which satisfy the condition

$$\phi_2(0)d_y\phi_4(0) - d_y\phi_2(0)\phi_4(0) = 0.$$

The oscillatory behavior of the continuous modes is discussed in the following chapter wherein a detailed analysis of the structure of the continuous modes is presented.

In this section the Orr-Sommerfeld and Squire equations that govern the linear stability

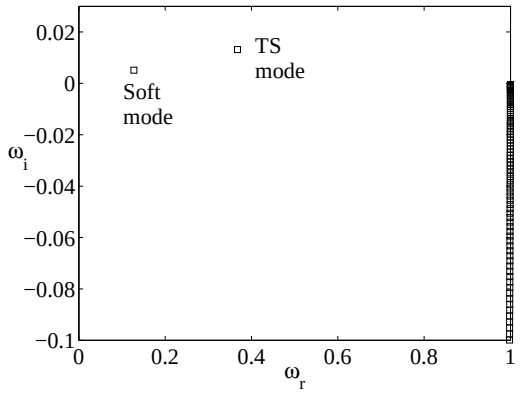


Figure 2.8: Eigenvalue spectrum of a two-fluid boundary layer showing multiple unstable modes. $k_x = 0.9, k_z = 0, Re_T = 2000, \mu_{BT} = 1.5, \delta_B = 0.1$

of a boundary layer were described. The origin of discrete and continuous modes were also discussed. The following section presents the various instabilities which arise in the presence of a wall-film, as well as the regime of dominance of each mode.

2.4 The modal instabilities

Figure 2.8 shows the eigenvalue spectrum of a two-fluid boundary layer at a supercritical Reynolds number. Apart from the stable continuous spectrum there exist the unstable soft and Tollmien–Schlichting modes. The Tollmien–Schlichting mode has a higher growth rate and phase speed compared to the soft mode. The phase speed of the Tollmien–Schlichting mode compared to the soft mode has been reported to be higher in the experiments of Craik (1966) and Kao & Park (1972).

The eigenfunctions corresponding to the Tollmien–Schlichting mode and the soft mode are shown in figure 2.9(a) and (b), respectively. Both the modes decay in the free-stream but are non-zero well outside the boundary layer. At the interface however the soft mode has a sharp jump in the gradient which is absent in the Tollmien–Schlichting mode, indicating that the viscosity jump across the interface affects the soft mode. The short wavelength instability and the high Reynolds number instability also present at the same Reynolds number have a growth rate higher than the Tollmien–Schlichting mode. The corresponding eigenfunctions is shown in figure 2.10(a) and (b) respectively. The short wavelength instability is primarily localized around the interface whereas high Reynolds number instability is primarily located inside the boundary layer. Both the

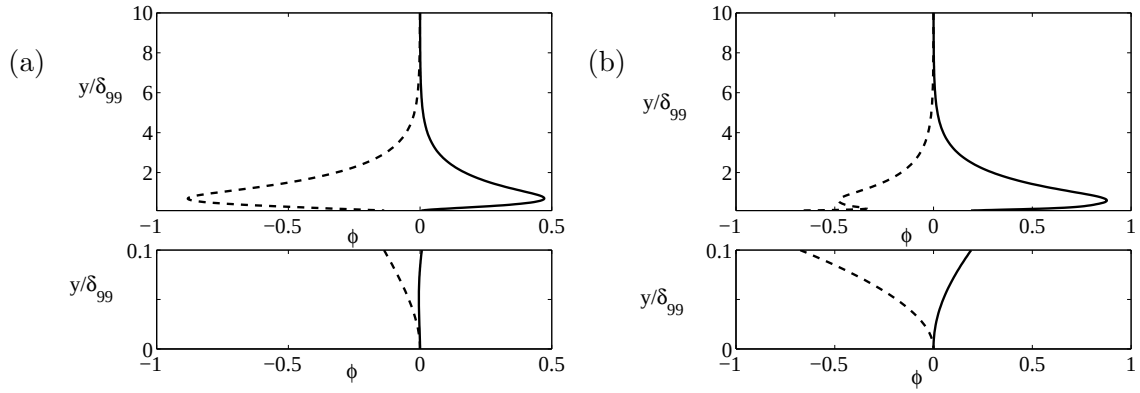


Figure 2.9: Eigenfunctions of modal instabilities (a) Tollmien–Schlichting mode $\omega = 0.3308 + 0.0118i$. (b) The long wavelength instability or the soft mode $\omega = 0.1147 + 0.0046i$. $k_x = 0.9, k_z = 0, Re_T = 2000, We^{-1} = 0, \mu_{BT} = 1.5, \delta_B = 0.1$. ——, real component; - - -, imaginary component.

eigenfunctions show a sharp jump in the gradient across the interface.

The four modal instabilities, (a) Tollmien–Schlichting mode, (b) soft mode, (c) HB(1983) and (d) HB(1987) reported in figures 2.9 and 2.10 are unstable in different regimes. For instance figure 2.11(a) shows three distinct peaks in the growth rate of the unstable modes. The soft mode is a long wavelength instability and is therefore present for $k_x \ll O(1)$. The Tollmien–Schlichting mode is unstable over a limited range of wavenumbers, $k_x \sim O(1)$ and the HB(1983) mode is present for $k_x \gg O(1)$. The short wavelength instability has the highest growth rate. However, all the three instabilities are present only if $\mu_{BT} > 1$ and the Reynolds number is supercritical.

If the viscosity ratio, $\mu_{BT} < 1$, at a supercritical Reynolds number then the HB(1983) and the HB(1987) modes are unstable. Figure 2.11(b) shows two peaks, the first corresponding to HB(1987) mode and the second to HB(1983) mode. The high Reynolds number instability has a wavelength of the order of the film thickness and dominates the short wavelength instability. Figure 2.11(b) also shows that the soft and the Tollmien–Schlichting modes are stable in this configuration.

At subcritical Reynolds numbers, only the soft mode and the HB(1983) mode are present if the lower layer is more viscous than the upper layer. Figure 2.11(c) shows the growth rate of the most unstable mode for this configuration. The soft mode is present at low wavenumbers and has a growth rate much lower than that of the HB(1983) mode. However, the presence of even a small amount of surface tension, $We \sim O(1000)$, is sufficient to stabilize the short wavelength instability. The effect of surface tension on

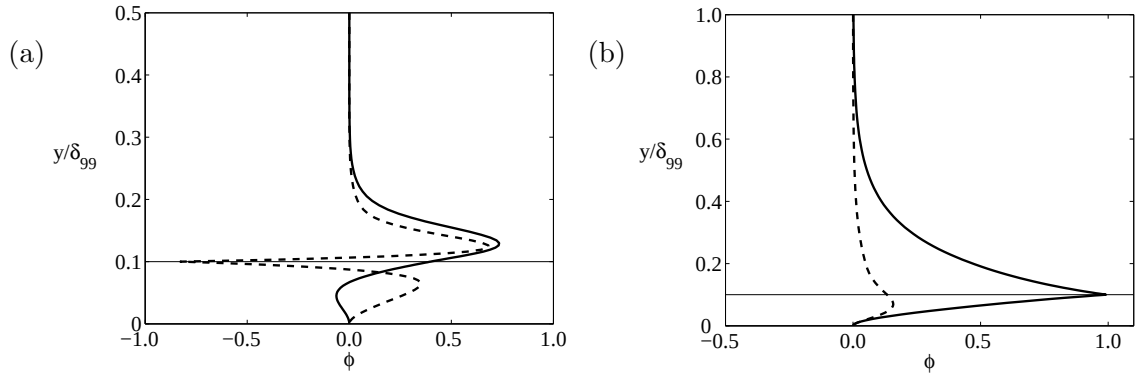


Figure 2.10: Eigenfunctions of modal instabilities (a) The short wavelength instability or HB(1983) $\omega = 2.9656 + 0.0435i$. $k_x = 35, \mu_{BT} = 2.0$ (b) The high Reynolds number instability or HB(1987) $\omega = 1.5059 + 0.0269i$. $k_x = 7.5, k_z = 0, Re_T = 2000, We^{-1} = 0, \mu_{BT} = 0.7, \delta_B = 0.1$. ——, real component; - - -, imaginary component.

the growth rate of the soft mode is negligible as shown in figure 2.11(c). The preferential effect of surface tension on the soft and the HB(1983) mode can be understood by examining the normal stress continuity (equation 2.6). The surface tension force is proportional to the curvature of the interface given by $k_x^2 f$. Hence, curvature of the interface is higher for the short wavelength instability compared to the long wavelength instability and, therefore, the stronger stabilizing effect of surface tension.

Figure 2.11(d) shows the growth rate of the most unstable mode at a subcritical Reynolds number with $\mu_{BT} < 1$. All the instabilities except for the HB(1983) mode are absent in this case. Since it is known that even a small amount of surface tension stabilizes the short wavelength instability, two-fluid boundary layers can be in practice considered stable with respect to modal instabilities in this configuration.

All the exponential instabilities present in a two-fluid boundary layer are summarized in Table 2.2. The short wavelength instability (HB(1983)) is the only unstable mode found when the lower fluid is less viscous than the upper layer and the Reynolds number is subcritical. However, if the viscosity of the bottom fluid is higher than that of the top fluid at a subcritical Reynolds number, the soft mode is also found to be unstable. At supercritical Reynolds numbers with $\mu_{BT} < 1$ the high Reynolds number instability (HB(1987)) is observed along with the short wavelength instability and Tollmien–Schlichting mode. The Tollmien–Schlichting mode was found to be unstable only over a range of viscosity ratios in this configuration. Finally, the soft mode, the Tollmien–Schlichting

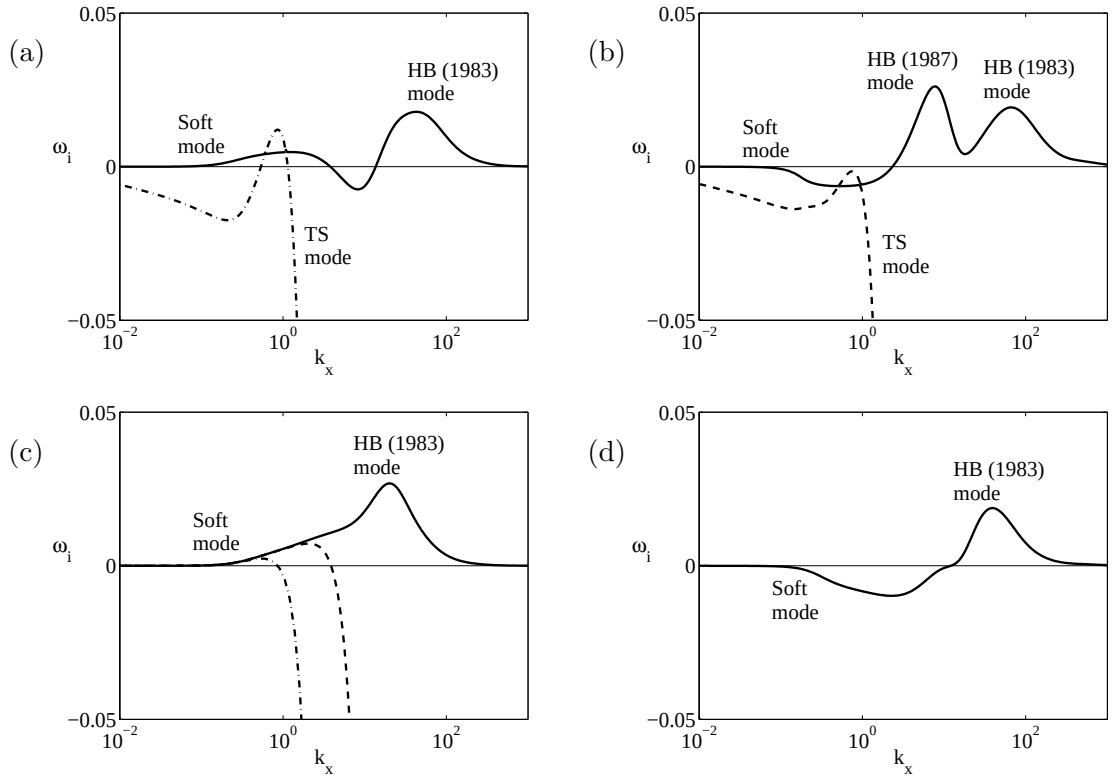


Figure 2.11: Variation in growth rate of modal instabilities with k_x (a) Growth rate of the Tollmien–Schlichting mode, soft mode and short wavelength instability. $Re_T = 2000, \mu_{BT} = 1.5$ (b) Growth rate of the High Reynolds number instability, HB (1983), soft and Tollmien–Schlichting modes . $Re_T = 2000, \mu_{BT} = 0.7$. (c) Stabilization of short wavelength instability by surface tension. ——, $We^{-1} = 0.0$; - - -, $We^{-1} = 0.001$; — · —, $We^{-1} = 0.1$. $Re_T = 600, \mu_{BT} = 1.5$ (d) Growth rate of the soft mode and short wavelength instability. $Re_T = 600, \mu_{BT} = 0.7$. For all cases $k_z = 0, \delta_B = 0.1$

	$\mu_{BT} < 1$	$\mu_{BT} > 1$
$Re < Re_{crit}$	HB(1983) mode	HB(1983) mode Soft mode
$Re > Re_{crit}$	HB(1983) mode HB(1987) mode Tollmien–Schlichting mode	HB(1983) mode Soft mode Tollmien–Schlichting mode

Table 2.2: Modal instability regime map. Here Re_{crit} refers to the critical Reynolds number.

mode and the short wavelength instability are all found to coexist if $\mu_{BT} > 1$ and the Reynolds number is supercritical.

The four instabilities presented in this section have been identified based on the regime in which they are unstable. A more rigorous discernment can be made by examining the kinetic energy equation. A more detailed understanding of nature of the unstable modes is presented in the next section. First, the kinetic energy equation is derived and thereafter the sources of energy contributing to these instabilities are reported. The instabilities are then classified based on the dominant mechanism of energy transfer (Boomkamp & Miesen, 1996).

2.5 The kinetic energy equation

This section describes the derivation of kinetic energy equation for a three-dimensional infinitesimal perturbation from the linearized Navier-Stokes equations. The left hand side of the kinetic energy equation is the material derivative of the kinetic energy of the perturbation. The right hand side of the equation describes the rate of energy transfer to the perturbation by different physical mechanisms like Reynolds stress, work done by shear and normal stress and energy loss due to viscous dissipation.

The continuity equation for a three-dimensional perturbation for incompressible flow is:

$$\frac{\partial u}{\partial x} + \frac{\partial v}{\partial y} + \frac{\partial w}{\partial z} = 0. \tag{2.19}$$

The momentum balance equations are:

$$\rho\frac{Du}{Dt}+\rho v\frac{dU}{dy} = -\frac{\partial p}{\partial x}+\left[\frac{\partial \tau_{xx}}{\partial x}+\frac{\partial \tau_{yx}}{\partial y}+\frac{\partial \tau_{zx}}{\partial z}\right] \quad (2.20)$$

$$\rho\frac{Dv}{Dt} = -\frac{\partial p}{\partial y}+\left[\frac{\partial \tau_{xy}}{\partial x}+\frac{\partial \tau_{yy}}{\partial y}+\frac{\partial \tau_{zy}}{\partial z}\right] \quad (2.21)$$

$$\rho\frac{Dw}{Dt} = -\frac{\partial p}{\partial z}+\left[\frac{\partial \tau_{xz}}{\partial x}+\frac{\partial \tau_{yz}}{\partial y}+\frac{\partial \tau_{zz}}{\partial z}\right] \quad (2.22)$$

where $\tau_{mn} \equiv \mu\epsilon_{mn}$ and $\epsilon_{mn} \equiv \frac{\partial u_m}{\partial x_n}+\frac{\partial u_n}{\partial x_m}$. The current notation is equivalent to that of Tennekes & Lumley (1972, pp 27) with $\tilde{s}_{mn} \equiv \frac{1}{2}\epsilon_{mn}$. Multiplying equation 2.20 with u, equation 2.21 with v, equation 2.22 with w and adding them gives:

$$\begin{aligned}\rho\left(u\frac{Du}{Dt}+v\frac{Dv}{Dt}+w\frac{Dw}{Dt}\right) = & -\rho uv\frac{dU}{dy}-u\frac{\partial p}{\partial x}-v\frac{\partial p}{\partial y}-w\frac{\partial p}{\partial z}\\ & +\mu\Bigg[u\frac{\partial \epsilon_{xx}}{\partial x}+u\frac{\partial \epsilon_{yx}}{\partial y}+u\frac{\partial \epsilon_{zx}}{\partial z}\\ & +v\frac{\partial \epsilon_{xy}}{\partial x}+v\frac{\partial \epsilon_{yy}}{\partial y}+v\frac{\partial \epsilon_{zy}}{\partial z}\\ & +w\frac{\partial \epsilon_{xz}}{\partial x}+w\frac{\partial \epsilon_{yz}}{\partial y}+w\frac{\partial \epsilon_{zz}}{\partial z}\Bigg] \end{aligned} \quad (2.23)$$

The $L.H.S$ of equation 2.23 can be rewritten as,

$$\begin{aligned}\rho\left(u\frac{Du}{Dt}+v\frac{Dv}{Dt}+w\frac{Dw}{Dt}\right) &= \frac{1}{2}\rho\left(\frac{Du^2}{Dt}+\frac{Dv^2}{Dt}+\frac{Dw^2}{Dt}\right)\\ &= \rho\frac{D}{Dt}\left(\frac{u^2+v^2+w^2}{2}\right)\\ &= \rho\frac{D}{Dt}(K.E.).\end{aligned}$$

The right hand side of equation 2.23 is now examined. The terms containing pressure gradient are addressed in the latter part of the derivation. First the viscous terms are

re-written using the following identities,

$$\begin{aligned}
u\frac{\partial \epsilon_{xx}}{\partial x} &= u\frac{\partial}{\partial x}\left(2\frac{\partial u}{\partial x}\right) \\
&= 2\left[\frac{\partial}{\partial x}\left(u\frac{\partial u}{\partial x}\right) - \left(\frac{\partial u}{\partial x}\right)^2\right] \\
&= \frac{\partial}{\partial x}(u\epsilon_{xx}) - 2\left(\frac{\partial u}{\partial x}\right)^2 \\
u\frac{\partial \epsilon_{yx}}{\partial y} &= u\frac{\partial}{\partial y}\left(\frac{\partial u}{\partial y} + \frac{\partial v}{\partial x}\right) \\
&= \left[\frac{\partial}{\partial y}\left(u\frac{\partial u}{\partial y}\right) - \left(\frac{\partial u}{\partial y}\right)^2\right] + \left[\frac{\partial}{\partial y}\left(u\frac{\partial v}{\partial x}\right) - \left(\frac{\partial v}{\partial x}\frac{\partial u}{\partial y}\right)\right] \\
&= \frac{\partial}{\partial y}(u\epsilon_{yx}) - \left(\frac{\partial u}{\partial y}\right)^2 - \left(\frac{\partial v}{\partial x}\frac{\partial u}{\partial y}\right) \\
u\frac{\partial \epsilon_{zx}}{\partial z} &= u\frac{\partial}{\partial z}\left(\frac{\partial u}{\partial z} + \frac{\partial w}{\partial x}\right) \\
&= \left[\frac{\partial}{\partial z}\left(u\frac{\partial u}{\partial z}\right) - \left(\frac{\partial u}{\partial z}\right)^2\right] + \left[\frac{\partial}{\partial z}\left(u\frac{\partial w}{\partial x}\right) - \left(\frac{\partial w}{\partial x}\frac{\partial u}{\partial z}\right)\right] \\
&= \frac{\partial}{\partial z}(u\epsilon_{zx}) - \left(\frac{\partial u}{\partial z}\right)^2 - \left(\frac{\partial w}{\partial x}\frac{\partial u}{\partial z}\right)
\end{aligned} \tag{2.24}$$

Similarly, the remaining viscous terms can be expressed as,

$$\begin{aligned}
v\frac{\partial \epsilon_{xy}}{\partial x} &= \frac{\partial}{\partial x}(v\epsilon_{xy}) - \left(\frac{\partial v}{\partial x}\right)^2 - \left(\frac{\partial v}{\partial x}\frac{\partial u}{\partial y}\right) \\
v\frac{\partial \epsilon_{yy}}{\partial y} &= \frac{\partial}{\partial y}(v\epsilon_{yy}) - 2\left(\frac{\partial v}{\partial y}\right)^2 \\
v\frac{\partial \epsilon_{zy}}{\partial z} &= \frac{\partial}{\partial z}(v\epsilon_{zy}) - \left(\frac{\partial v}{\partial z}\right)^2 - \left(\frac{\partial v}{\partial z}\frac{\partial w}{\partial y}\right)
\end{aligned} \tag{2.25}$$

$$\begin{aligned}
w\frac{\partial \epsilon_{xz}}{\partial x} &= \frac{\partial}{\partial x}(w\epsilon_{xz}) - \left(\frac{\partial w}{\partial x}\right)^2 - \left(\frac{\partial w}{\partial x}\frac{\partial u}{\partial z}\right) \\
w\frac{\partial \epsilon_{yz}}{\partial y} &= \frac{\partial}{\partial y}(w\epsilon_{yz}) - \left(\frac{\partial w}{\partial y}\right)^2 - \left(\frac{\partial w}{\partial y}\frac{\partial v}{\partial z}\right) \\
w\frac{\partial \epsilon_{zz}}{\partial z} &= \frac{\partial}{\partial z}(w\epsilon_{zz}) - 2\left(\frac{\partial w}{\partial z}\right)^2
\end{aligned} \tag{2.26}$$

Adding the above identities (2.24 - 2.26) leads to:

$$\begin{aligned} u\frac{\partial \epsilon_{xx}}{\partial x} + u\frac{\partial \epsilon_{yx}}{\partial y} + u\frac{\partial \epsilon_{zx}}{\partial z} & \\ +v\frac{\partial \epsilon_{xy}}{\partial x} + v\frac{\partial \epsilon_{yy}}{\partial y} + v\frac{\partial \epsilon_{zy}}{\partial z} & = \\ +w\frac{\partial \epsilon_{xz}}{\partial x} + w\frac{\partial \epsilon_{yz}}{\partial y} + w\frac{\partial \epsilon_{zz}}{\partial z} & \end{aligned} \begin{aligned} & \frac{\partial}{\partial x}(u\epsilon_{xx}) + \frac{\partial}{\partial y}(u\epsilon_{yx}) + \frac{\partial}{\partial z}(u\epsilon_{zx}) \\ & -\frac{1}{2}\left[\epsilon_{xx}^2 + \epsilon_{yx}^2 + \epsilon_{zx}^2\right] \\ & +\frac{\partial}{\partial x}(v\epsilon_{xy}) + \frac{\partial}{\partial y}(v\epsilon_{yy}) + \frac{\partial}{\partial z}(v\epsilon_{zy}) \\ & -\frac{1}{2}\left[\epsilon_{xy}^2 + \epsilon_{yy}^2 + \epsilon_{zy}^2\right] \\ & +\frac{\partial}{\partial x}(w\epsilon_{xz}) + \frac{\partial}{\partial y}(w\epsilon_{yz}) + \frac{\partial}{\partial z}(w\epsilon_{zz}) \\ & -\frac{1}{2}\left[\epsilon_{xz}^2 + \epsilon_{yz}^2 + \epsilon_{zz}^2\right]. \end{aligned} \tag{2.27}$$

Multiplying equation 2.19 with pressure, p, and subtracting it from the pressure gradient terms in the kinetic energy equation (2.23) gives:

$$\begin{aligned} -u\frac{\partial p}{\partial x} - v\frac{\partial p}{\partial y} - w\frac{\partial p}{\partial z} & \\ -p\left(\frac{\partial u}{\partial x} + \frac{\partial v}{\partial y} + \frac{\partial w}{\partial z}\right) & = \end{aligned} \quad -\frac{\partial up}{\partial x} - \frac{\partial vp}{\partial y} - \frac{\partial wp}{\partial z}. \tag{2.28}$$

Substituting the viscous (2.27) and pressure (2.28) terms into the kinetic energy equation (2.23) and rearranging the following is obtained:

$$\begin{aligned} \rho\frac{D}{Dt}\left(\frac{u^2+v^2+w^2}{2}\right) = & \underbrace{-\rho uv\frac{dU}{dy}}_{T1} - \underbrace{\frac{\mu}{2}\left[\epsilon_{xx}^2 + \epsilon_{yy}^2 + \epsilon_{zz}^2 + 2\epsilon_{xy}^2 + 2\epsilon_{zx}^2 + 2\epsilon_{yz}^2\right]}_{T2} \\ & \underbrace{\left[\frac{\partial}{\partial x}[u(-p+\tau_{xx})] + \frac{\partial}{\partial y}[u\tau_{yx}] + \frac{\partial}{\partial z}[u\tau_{zx}]\right.}_{T3} \\ & + \frac{\partial}{\partial x}[v\tau_{xy}] + \frac{\partial}{\partial y}[v(-p+\tau_{yy})] + \frac{\partial}{\partial z}[v\tau_{zy}] \\ & \underbrace{\left. + \frac{\partial}{\partial x}[w\tau_{xz}] + \frac{\partial}{\partial y}[w\tau_{yz}] + \frac{\partial}{\partial z}[w(-p+\tau_{zz})]\right]}_{T3} \end{aligned} \tag{2.29}$$

The first term $T1$ is the Reynolds stress term, which transfers energy either to or from the mean flow to the perturbation depending on the sign of this term. The second term, $T2$, is the viscous dissipation. The last term, $T3$, includes the work done by pressure and the viscous stresses. Equation 2.29 is valid in either fluid and in order to obtain energy balance, it is integrated over a control volume, V, denoted by $\iiint_V dV \equiv$

$\int_0^{\lambda_z}\int_0^{\lambda_x}\int_{\ell_l}^{\ell_u} dydxdz$. The control volume, V, has dimensions of a streamwise wavelength, $\lambda_x \equiv \frac{2\pi}{k_x}$, along the x direction and a spanwise wavelength, $\lambda_z \equiv \frac{2\pi}{k_z}$, along the z direction. The wall normal region in V belongs to $[\ell_l, \ell_u]$, where ℓ_u and ℓ_l are the upper and lower limits of the flow being considered. In the particular case of a boundary layer, $\ell_u \to \infty$ and $\ell_l = 0$. Thus,

$$\begin{aligned}
\iiint_V \rho \frac{D}{Dt}\left(\frac{u^2+v^2+w^2}{2}\right) dV &= -\iiint_V \rho uv \frac{dU}{dy} dV \\
&\quad - \iiint_V \frac{\mu}{2}\left[\epsilon_{xx}^2 + \epsilon_{yy}^2 + \epsilon_{zz}^2 + 2\epsilon_{xy}^2 + 2\epsilon_{zx}^2 + 2\epsilon_{yz}^2\right] dV \\
&\quad + \underbrace{\iiint_V \left[\frac{\partial}{\partial x}[u(-p+\tau_{xx})] + \frac{\partial}{\partial y}[u\tau_{yx}] + \frac{\partial}{\partial z}[u\tau_{zx}]\right.}_{I1} \\
&\quad + \frac{\partial}{\partial x}[v\tau_{xy}] + \frac{\partial}{\partial y}[v(-p+\tau_{yy})] + \frac{\partial}{\partial z}[v\tau_{zy}] \\
&\quad \underbrace{\left. + \frac{\partial}{\partial x}[w\tau_{xz}] + \frac{\partial}{\partial y}[w\tau_{yz}] + \frac{\partial}{\partial z}[w(-p+\tau_{zz})]\right] dV}_{I1}
\end{aligned}$$

The last volume integral on the right hand side, $I1$, can be split into six surface integrals by applying the divergence theorem:

$$\begin{aligned}
I1 &= \int_0^{\lambda_z}\int_{\ell_l}^{y_f} [u(-p+\tau_{xx}) + v\tau_{xy} + w\tau_{xz}]\Big|_{x=0}^{x=\lambda_x} dydz + \\
&\quad \int_0^{\lambda_z}\int_{y_f}^{\ell_u} [u(-p+\tau_{xx}) + v\tau_{xy} + w\tau_{xz}]\Big|_{x=0}^{x=\lambda_x} dydz + \\
&\quad \int_0^{\lambda_x}\int_{\ell_l}^{y_f} [u\tau_{zx} + v\tau_{zy} + w(-p+\tau_{zz})]\Big|_{z=0}^{z=\lambda_z} dydx + \\
&\quad \int_0^{\lambda_x}\int_{y_f}^{\ell_u} [u\tau_{zx} + v\tau_{zy} + w(-p+\tau_{zz})]\Big|_{z=0}^{z=\lambda_z} dydx + \\
&\quad \int_0^{\lambda_z}\int_0^{\lambda_x} [u\tau_{yx} + v(-p+\tau_{yy}) + w\tau_{yz}]\Big|_{y=\ell_l}^{y=y_f^-} dxdz + \\
&\quad \int_0^{\lambda_z}\int_0^{\lambda_x} [u\tau_{yx} + v(-p+\tau_{yy}) + w\tau_{yz}]\Big|_{y=y_f^+}^{y=\ell_u} dxdz
\end{aligned}$$

where $[.]\Big|_a^b \equiv [.]\Big|_b - [.]\Big|_a$. The first four surface integrals on the $R.H.S$ vanish due to periodic boundary conditions in the streamwise and spanwise directions. The wall and free-stream boundary conditions ensure $u(\ell_l) = u(\ell_u) = 0, v(\ell_l) = v(\ell_u) = 0, w(\ell_l) = w(\ell_u) = 0$. The interfacial boundary conditions require that there is no jump in w and

τ_{yz} and therefore the term $w\tau_{yz}$ does not contribute to the kinetic energy. As a result, the work done by normal stress, $v(-p+\tau_{yy})$, and tangential stress, $u\tau_{yx}$, at the interface is left unbalanced and hence contributes to the kinetic energy of the perturbation.

$$\begin{aligned}\iiint_V \rho \frac{D}{Dt}\left(\frac{u^2+v^2+w^2}{2}\right) dV &= \iiint_V \rho\left(-u_j v_j \frac{dU}{dy}\right) dV \\ &\quad - \iiint_V \frac{\mu}{2}\left[\epsilon_{xx}^2+\epsilon_{yy}^2+\epsilon_{zz}^2+2\epsilon_{xy}^2+2\epsilon_{zx}^2+2\epsilon_{yz}^2\right] dV \\ &\quad + \int_0^{\lambda_z}\int_0^{\lambda_x} [u\tau_{xy}]\Big|_{y_f^+} - [u\tau_{xy}]\Big|_{y_f^-} dxdz \\ &\quad + \int_0^{\lambda_z}\int_0^{\lambda_x} [v(-p+\tau_{yy})]\Big|_{y_f^+} - [v(-p+\tau_{yy})]\Big|_{y_f^-} dxdz\end{aligned}$$

$$\Rightarrow (KE_T + KE_B) = REY_T + REY_B + DISS_T + DISS_B + TAN + NOR \quad (2.30)$$

where

$$\begin{aligned}KE_T &= \frac{D}{Dt}\int_0^{\lambda_z}\int_0^{\lambda_x}\int_{y_f}^{\ell_u} \rho_T\left(\frac{u^2+v^2+w^2}{2}\right) dydxdz \\ KE_B &= \frac{D}{Dt}\int_0^{\lambda_z}\int_0^{\lambda_x}\int_{\ell_l}^{y_f} \rho_B\left(\frac{u^2+v^2+w^2}{2}\right) dydxdz \\ REY_T &= \int_0^{\lambda_z}\int_0^{\lambda_x}\int_{y_f}^{\ell_u} \rho_B\left(-uv\frac{dU}{dy}\right) dydxdz \\ REY_B &= \int_0^{\lambda_z}\int_0^{\lambda_x}\int_{\ell_l}^{y_f} \rho_B\left(-uv\frac{dU}{dy}\right) dydxdz \\ DISS_T &= -\int_0^{\lambda_z}\int_0^{\lambda_x}\int_{y_f}^{\ell_u} \frac{\mu_T}{2}\left[\epsilon_{xx}^2+\epsilon_{yy}^2+\epsilon_{zz}^2+2\epsilon_{xy}^2+2\epsilon_{zx}^2+2\epsilon_{yz}^2\right] dydxdz \\ DISS_B &= -\int_0^{\lambda_z}\int_0^{\lambda_x}\int_{\ell_l}^{y_f} \frac{\mu_B}{2}\left[\epsilon_{xx}^2+\epsilon_{yy}^2+\epsilon_{zz}^2+2\epsilon_{xy}^2+2\epsilon_{zx}^2+2\epsilon_{yz}^2\right] dydxdz \\ TAN &= \int_0^{\lambda_z}\int_0^{\lambda_x} [u\tau_{xy}]\Big|_{y_f^+} - [u\tau_{xy}]\Big|_{y_f^-} dxdz \\ NOR &= \int_0^{\lambda_z}\int_0^{\lambda_x} [v(-p+\tau_{yy})]\Big|_{y_f^+} - [v(-p+\tau_{yy})]\Big|_{y_f^-} dxdz.\end{aligned}$$

The terms KE_T, KE_B are the rate of change of kinetic energy of the perturbation in the top and the bottom fluid respectively. Hence, if the sum of the two terms is positive, it implies that the mode is unstable. The terms REY_T, REY_B contribute to the perturbation energy by Reynolds stress mechanism. The term TAN is the work done by shear

Mode	TS	Soft	HB (1983)	HB (1987)
ω	$0.3308 + 0.0118i$	$0.1147 + 0.0046i$	$2.9656 + 0.0435i$	$1.5059 + 0.0269i$
TAN	7.7146×10^{-4}	$\underline{0.8134}$	$\underline{0.7599}$	$\underline{0.0181}$
NOR	0	0	0	0
REY_T	$\underline{0.0595}$	$\underline{0.2584}$	0.0122	0.0017
REY_B	7.9305×10^{-4}	0.0019	-0.0036	$\underline{0.0192}$
$DISS_T$	-0.0086	-0.2596	-0.4555	-0.0088
$DISS_B$	-0.0296	-0.7825	-0.3085	-0.0251
KE_T	0.0213	0.0139	0.0039	0.0018
KE_B	0.0017	0.0179	0.0015	0.0032

Table 2.3: Energy terms for different modes of two-fluid boundary layer

stress at the interface. The term NOR is the work done by pressure and viscous normal stress on the interface. The kinetic energy equation for three-dimensional infinitesimal perturbation was derived to classify various unstable modes on the basis of major energy contributing mechanism. In the following subsection the energy contribution from various mechanisms to the four modal instabilities discussed previously is presented.

2.5.1 Discussion

Table 2.3 summarizes the energy contributions to the modal instabilities. The terms which contribute most to the kinetic energy are underlined. Since each instability is driven by different physical phenomena, the modes can be easily distinguished once the terms of the kinetic energy equation are computed. For instance, the Tollmien–Schlichting mode derives energy primarily from the Reynolds stress in the top fluid. The energy contribution from REY_B and TAN terms, though positive, is negligible compared to REY_T. In contrast the soft mode receives energy from the work done by tangential stresses at the interface. Hence, the instability has its origin in viscosity stratification. The Reynolds stress in the top fluid also has a sizable contribution to the instability. The TAN term is also the major source of energy to the HB (1983) mode. The high Reynolds number instability derives energy from the work done by shear stress and Reynolds stress in the bottom fluid. Having identified the primary mechanisms of energy growth, the four instabilities reported in the previous section can be distinguished.

The variation in Reynolds stress, dissipation and kinetic energy in the wall-normal direction of each of the four instabilities is shown in figure 2.12. Figure 2.12(a) shows the energy distribution for the Tollmien–Schlichting mode (shown in figure 2.9(a)). The

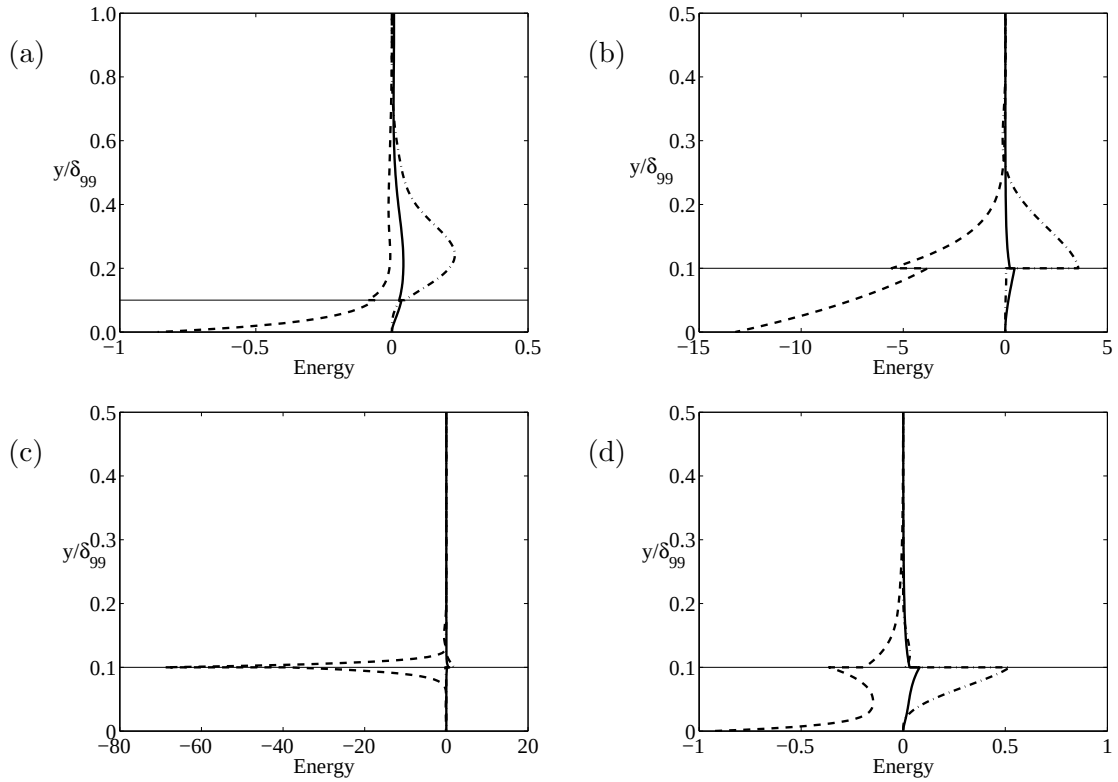


Figure 2.12: Energy distribution of KE (——), REY (— ·—), $DISS$ (- - -) for various modal instabilities (a) Tollmien–Schlichting mode $\omega = 0.3308 + 0.0118i$. $k_x = 0.9, k_z = 0, Re_T = 2000, \mu_{BT} = 1.5, \delta_B = 0.1$ (b) The long wavelength instability or the soft mode $\omega = 0.1147 + 0.0046i$. $k_x = 0.9, k_z = 0, Re_T = 2000, \mu_{BT} = 1.5, \delta_B = 0.1$ (c) The short wavelength instability or HB(1983) $\omega = 2.9656 + 0.0435i$. $k_x = 35, k_z = 0, Re_T = 2000, \mu_{BT} = 2, \delta_B = 0.1$ (d) The high Reynolds number instability or HB(1987) $\omega = 1.5059 + 0.0269i$. $k_x = 7.5, k_z = 0, Re_T = 2000, \mu_{BT} = 0.7, \delta_B = 0.1$

Reynolds stress in the top fluid contributes most to the kinetic energy, whereas dissipation dominates in the bottom fluid . The soft mode also derives energy from the Reynolds stress in the top fluid as shown in figure 2.12(b). The short wavelength instability is dominated by the viscous dissipation term near the interface (see figure 2.12(c)). Figure 2.12(d) shows that the Reynolds stress in the bottom fluid primarily contributes energy to the HB(1987) mode with a negligible contribution from the top fluid.

The evaluation of all the terms of the kinetic energy equation provides insight into the mechanism driving an instability. Having distinguished the modes, the effect of viscosity stratification on the modal instabilities is examined in the following section.

2.6 Viscosity stratification effects

The growth rate of the Tollmien–Schlichting mode is shown in figure 2.13(a) at viscosity ratios $\mu_{BT} = 1, 3, 5$ and 50. The growth rate increases as the viscosity is increased from $\mu_{BT} \in [1, 5]$ and decreases thereafter. The destabilization of the Tollmien–Schlichting mode can be understood by considering the mean shear distribution. As the viscosity of the lower fluid is increased the shear in the top fluid increases (figure 2.2(a)). As a result the Reynolds stress term in the top fluid increases and, hence, the higher growth rate of the Tollmien–Schlichting mode. However, for extremely large viscosity ratios for example $\mu_{BT} = 50$, the mean velocity profile imitates the Blasius profile and as a result the growth rate also approaches that of the single-fluid case.

Figure 2.13(b) shows the growth rate of the soft mode at viscosity ratios $\mu_{BT} = 1, 3, 4$ and 5. In the absence of viscosity stratification ($\mu_{BT} = 1$), the growth rate is trivial at all wavenumbers. An increase in the viscosity ratio causes the growth rate of the soft mode to increase monotonically. The soft mode derives energy from the TAN term. An increase in the viscosity ratio, μ_{BT}, leads to a stronger jump in mean velocity gradient across the interface. As a result, the discontinuity in the streamwise velocity perturbation is enhanced, which in turn leads to a stronger contribution from the TAN term. Thus the growth rate of the soft mode increases with increase with μ_{BT}. The same effect is observed on the ω_i of the short wavelength instability if the viscosity of the wall-film is lowered with $\mu_{BT} < 1$, as shown in figure 2.13(c). The instability is neutrally stable in the absence of viscosity stratification but is destabilized as the viscosity ratio is reduced. Since a reduction in μ_{BT} leads to an increase in the TAN term, which is

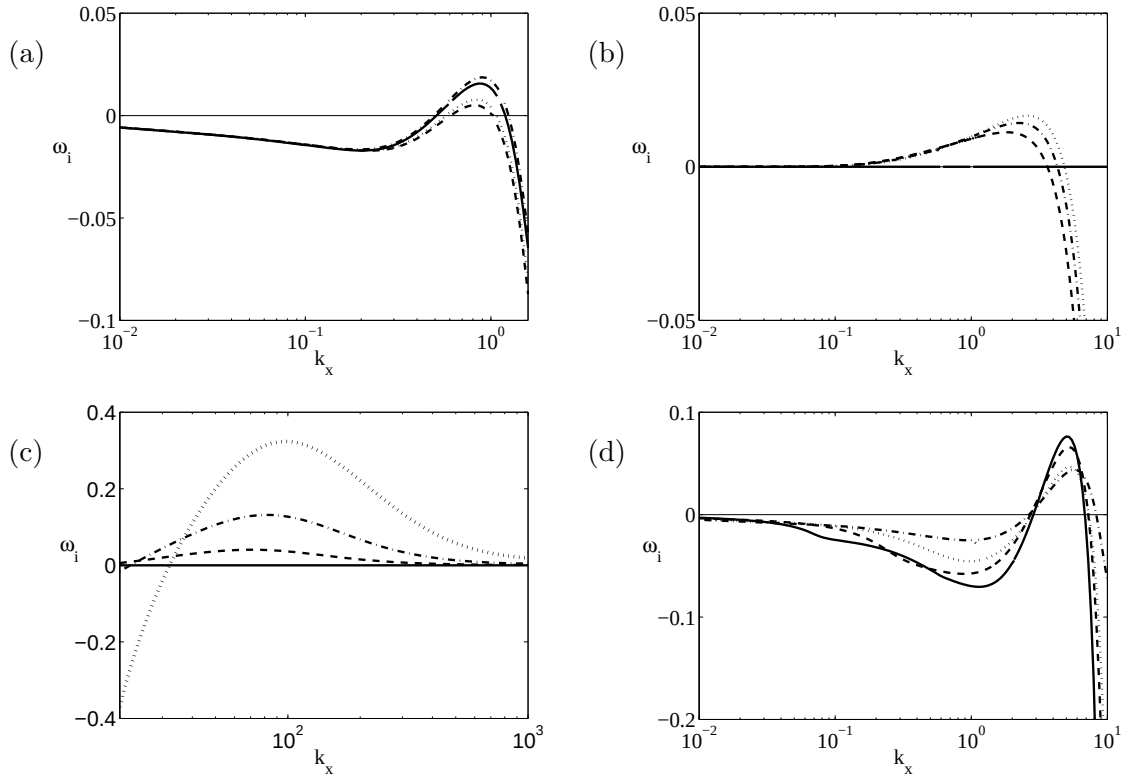


Figure 2.13: Variation in growth rate of modal instabilities with viscosity ratio μ_{BT}. (a) Growth rate of Tollmien–Schlichting mode. - - -, $\mu_{BT} = 1$; ——, $\mu_{BT} = 3$; — ·—, $\mu_{BT} = 5$; ····, $\mu_{BT} = 50$; (b) Growth rate of the soft mode. ——, $\mu_{BT} = 1$; - - -, $\mu_{BT} = 3$; — ·—, $\mu_{BT} = 4$; ····, $\mu_{BT} = 5$. (c) Growth rate of the short wavelength instability. ····, $\mu_{BT} = 0.2$; — ·—, $\mu_{BT} = 0.4$; - - -, $\mu_{BT} = 0.6$; ——, $\mu_{BT} = 1$. (d) Growth rate of HB(1987) mode. ——, $\mu_{BT} = 0.1$; - - -, $\mu_{BT} = 0.2$; ····, $\mu_{BT} = 0.3$; — ·—, $\mu_{BT} = 0.4$; $k_z = 0, Re_T = 2000, \delta_B = 0.1$

the sole contributor to the kinetic energy of this mode, it follows that the growth rate increases with reduction in μ_{BT}.

The effect of viscosity stratification on the high Reynolds number instability is shown in Figure 2.13(d). The mode is destabilized as the viscosity ratio is reduced. In order to understand this observation the terms of the kinetic energy equation are examined again. The HB (1987) mode derives energy from the Reynolds stress in the bottom fluid and the work done by the shear stress at the interface. As the viscosity of the bottom fluid is reduced the mean velocity gradient in the bottom fluid increases as demonstrated in figure 2.2(a). Hence, the Reynolds stress term in the bottom fluid is enhanced, thereby destabilizing the HB (1987) mode. It is also known that the TAN term increases as the viscosity ratio is reduced and hence it enhances the growth rate of this particular mode.

2.7 Conclusion

In this chapter the characteristics of modal instabilities were explored. The single fluid boundary layer possesses only one modal instability, the Tollmien–Schlichting wave. However, introduction of the wall-bounded film introduces three more instabilities, the soft mode, the short wavelength instability and the high Reynolds number instability. The short wavelength instability was found to exist in all regimes discussed but is easily suppressed by the presence of surface tension. Thus among the various regimes investigated, the boundary layer is stable at subcritical Reynolds numbers if the wall-bounded film has a viscosity lower than that of the outer fluid.

The modal instabilities were distinguished based on the primary mechanism of energy transfer from the mean flow to the perturbation. The Tollmien–Schlichting mode and the high Reynolds number instability derive energy from the mean flow by Reynolds stress mechanism. The soft mode and the short wavelength instability obtain energy from the work done by shear-stress at the interface and, therefore, have their origin in viscosity stratification. Finally, the effect of viscosity stratification on the modal instabilities was investigated. A departure from the single-fluid state, that is if $|1 - \mu_{BT}|$ increases, destabilizes all the unstable modes in a two-fluid boundary layer. Having examined in detail the nature of modal instabilities in this chapter, the focus is shifted to the stable branch of the eigenvalue spectrum: the continuous modes, in the following

chapter. The continuous spectrum is most relevant to the growth of the algebraic instability. Since the two-fluid boundary layer is asymptotically stable to long wavelength perturbations when the lower fluid is less viscous, the algebraic instability is likely to dominate under such circumstances. The structure of the continuous spectrum modes is investigated, in order to understand why the long wavelength perturbations are the most potent in triggering the algebraic instability.

Chapter 3

The continuous spectrum

3.1 Introduction

3.1.1 A historical perspective

The existence of the continuous spectrum was the subject of a debate between Case (Case, 1960, 1961) and Lin (Lin, 1961). Case argued that a continuous spectrum of normal modes exists as eigen-solutions to linearized Euler equations. The continuous spectrum modes must be included in the expansion that describes the evolution of a general linear inviscid disturbance, because the discrete modes do not form a complete basis by themselves (Case, 1960). Moreover in the subsequent article Case (1961) has shown that the solution to the inviscid problem is identical to the leading order solution to the viscous problem except for the boundaries where there would be viscous corrections. However, as pointed out later by (Lin, 1961), a major assumption underlying Case's seminal work was the independence of the initial condition of viscosity. Lin reasoned that a general initial condition would depend on viscosity and the inviscid limit of the viscous initial condition would have a discontinuity in the gradient of the eigenfunction at the critical layer. Hence, in order to represent the discontinuity a continuous spectrum of normal modes is required. Lin demonstrated further, that the viscous Orr-Sommerfeld eigenvalue problem possesses discrete eigenvalues for bounded flows.

However, the question of the presence of the continuous spectrum for unbounded flows remained open. Jordinson (1971) computed the eigenspectrum of the Orr-Sommerfeld equation for a Blasius boundary layer and hypothesized the presence of the continuous spectrum. He commented that the decaying modes form a "gently curving line".

Later Mack (1976) computed the temporal eigenvalues over a range of Reynolds numbers and wavenumbers, and further substantiated the existence of the continuous spectrum by reporting the phase speed and growth rate associated with these modes. These initial investigations were numerical in nature. Formal mathematical characterization of the continuous spectrum, and the analytical expression of its dispersion relation, were later presented by Grosch & Salwen (1978). Gustavsson (1979) studied the temporal evolution of a two-dimensional disturbance in a boundary layer using Fourier-Laplace transforms. He concluded that the continuous spectrum is associated with a branch cut in the complex plane, that is encountered while inverting the Laplace transform.

Since the work of Grosch & Salwen (1978) and Gustavsson (1979) the continuous spectrum modes have been applied to a variety of problems. For instance, the continuous modes along with the discrete modes form a complete basis (Salwen & Grosch, 1981). Therefore an arbitrary disturbance can be expressed as a superposition of Orr-Sommerfeld eigenfunctions. The completeness of Orr-Sommerfeld and the Squire eigenfunctions has been applied in computations of the evolution of linear perturbations in boundary layers, and in the synthesis and analysis of disturbances. Jacobs & Durbin (2001) used the continuous modes to generate a turbulent inflow field to simulate the transitional flow on a flat plate without a leading edge. Salwen & Grosch (1981) solved the initial value problem for the evolution of a two-dimensional disturbance using an expansion in terms of the continuous and discrete eigenfunctions. Zaki & Durbin (2005) applied a similar expansion in order to solve the initial value problem of Squire response to a three-dimensional Orr-Sommerfeld continuous mode. In the context of perturbation analysis, Tumin (2003) proposed a multi-mode decomposition of the flow field in transition simulations using continuous modes. This approach can identify the most dominant modes in the proceedings of transition.

The continuous spectrum has also been frequently studied in the context of the phenomenon of shear-sheltering (Jacobs & Durbin, 1998; Maslowe & Spiteri, 2001; Zaki & Durbin, 2005; Zaki & Saha, 2009). The following subsection elaborates on the shear-sheltering phenomenon and briefly reviews the literature on this topic.

3.1.2 The shear-sheltering phenomenon

The ability of free-stream vortical disturbances to penetrate boundary layers is curtailed by the mean shear – an inviscid phenomenon known as *shear-sheltering*. At finite Reynolds numbers, however, the sheltering mechanism is less effective and vortical disturbances permeate the shear. The implications are significant in many engineering and environmental flows: For instance, laminar boundary layers become prone to bypass transition even at moderate levels of free-stream turbulence (Morkovin, 1969). In atmospheric flows, vortical disturbances due to thermal convection in clouds can penetrate the surface layer and induce high-speed gusts (Nakamura *et al.*, 1996). In two-fluid shear flows, free-stream disturbances which reach the two-fluid interface appreciably affect the amplification of interfacial modes (Belcher & Hunt, 1998).

The ability of shear to selectively filter high-frequency vortical perturbations is relevant to both laminar and turbulent flows. In the former, the shear shelters the laminar flow from external vortical forcing. A similar filtering influences the interaction of small and large scale eddies in turbulent motion (Hunt & Durbin, 1999). A scale disparity is, however, required for shear-sheltering to be effective. These conditions were satisfied in the work of Grosch & Salwen (1978) where the computed eigenfunctions were high-frequency and, hence, filtered by the mean shear. Their eigenfunctions decayed exponentially at the edge of the boundary layer. Craik (1991) arrived at a similar conclusion by carrying out inviscid analysis of mode shapes using a piecewise linear mean flow. Despite the difference in Reynolds numbers, both Grosch & Salwen (1978) and Craik (1991) considered the same asymptotic limit where the shear dominates the remaining terms in the Orr-Sommerfeld equation.

Jacobs & Durbin (1998) studied the effect of shear sheltering on the continuous Orr-Sommerfeld modes for a piece-wise linear, infinitely deep boundary layer. Their analysis demonstrated that penetration is inversely proportional to the Reynolds number and the disturbance frequency. Further investigations of mode shapes were primarily numerical, and include Maslowe & Spiteri (2001) who examined the effect of pressure gradient on the continuous modes. The importance of shear sheltering is also documented experimentally. Hernon *et al.* (2007) have demonstrated that the penetration of free-stream vortical disturbances into a transitional boundary layer indeed agrees with the theoretical prediction of Jacobs & Durbin (1998).

Recent studies of stability of two-fluid shear flows, for instance mixing layers (Yecko & Zaleski, 2005), highlight the dependence of transient amplification on modal penetration, and, in turn, on the frequency-dependence of shear-sheltering. However, the shape of the continuous spectrum modes in two-fluid flows, and the influence of wall-bounded film on shear-sheltering have never been addressed in the literature. Instead, the majority of the literature has focused on the discrete Tollmien–Schlichting and interfacial instability waves (Yih, 1967; Hooper & Boyd, 1983, 1987). In that context, the work of Charru & Hinch (2000) perhaps bears most relevance to the current investigation. They aimed to classify the various *interfacial* waves based on their extent of penetration into the surrounding fluids. A "phase-diagram" of penetration regimes was developed based on the model problem of Couette flow over a wavy-wall. Their analysis, however, only considered two-dimensional, neutral waves due to an infinitesimal displacement of the solid-fluid or fluid-fluid boundary. Since their base flow is bounded, only discrete modes were relevant. The behavior of free-stream vortical modes, or the continuous spectrum eigenfunctions, and their ability to penetrate two-fluid shear flows was not discussed. This issue is addressed herein, and a quantitative measure of penetration and its dependence on modal and flow parameters is presented. The analysis takes into account the decay rate of the free-stream vortical disturbance. This is shown to have a significant effect on both modal penetration and the structure of the eigenfunction across the interface.

Due to the importance of the continuous spectrum in studies of single- and two-fluid boundary layers, it is essential to understand the physical mechanisms that determine the structure of these eigenmodes. Shear sheltering is one contributing element. While the literature includes interesting observations related to shear-sheltering, questions regarding its physical interpretation and effectiveness remain unanswered. For instance, previous studies suggest that shear-sheltering is most pronounced in relation to small-scale, or high-frequency, disturbances particularly at high Reynolds number. This view is however inconsistent with the observation that perturbations with high wall-normal wavenumbers can effectively penetrate boundary layers (Zaki & Durbin, 2005). Therefore, in this work, a clear physical explanation of the mechanics of shear-sheltering is sought. A detailed description of the structure of the continuous modes of the Orr-Sommerfeld equation is provided. The continuous modes are then classified in terms of

their ability to penetrate and perturb the boundary layer. The present approach relies on asymptotic analysis of the governing equation for a piece-wise linear profile, both in single- and two-fluid boundary layers. These asymptotic solutions are then compared to the numerical solution of the Orr-Sommerfeld equation for smoothly varying mean flow profiles to demonstrate the validity of the piece-wise linear approximation.

This chapter is divided into seven sections. The formulation of the single-fluid problem, and the closed-form eigen-solution for the piece-wise linear mean flow, are presented in section two. The relevant asymptotic regimes are examined in section three, and are followed by a discussion of the physical mechanism of shear-sheltering. The formulation of the two-fluid problem is given in section four. The associated asymptotic regimes, in case of viscosity stratification, are derived in section five. The effect of wall-bounded film on the continuous modes is evaluated numerically in section six, followed by concluding remarks in the last section.

3.2 The single-fluid theoretical formulation

3.2.1 The continuous spectrum

The study of penetration of vortical modes into shear regions has as a starting point the linear perturbation equations. Since the focus of this chapter is the continuous spectrum of the Orr-Sommerfeld equation, the characteristic dispersion relation for continuous modes is derived following Grosch & Salwen (1978); Gustavsson (1979); Jacobs & Durbin (1998); Zaki & Durbin (2005). The Orr-Sommerfeld equation requires four boundary conditions. At solid surfaces, the perturbation and its gradient must vanish,

$$\phi(0) = 0 \qquad ; \qquad \left.\frac{d\phi}{dy}\right|_0 = 0.$$

In semi-bounded flows, the Orr-Sommerfeld equation possesses a finite number of discrete modes, and a spectrum of continuous eigenvalues. The discrete modes are obtained by requiring that the perturbation decays in the free stream, $\phi_\infty \to 0$. Grosch & Salwen (1978) introduced the continuous spectrum by relaxing this free stream condition. Instead they only required that the perturbation remains bounded,

$$|\phi| < \infty \qquad ; \qquad |d_y\phi| < \infty.$$

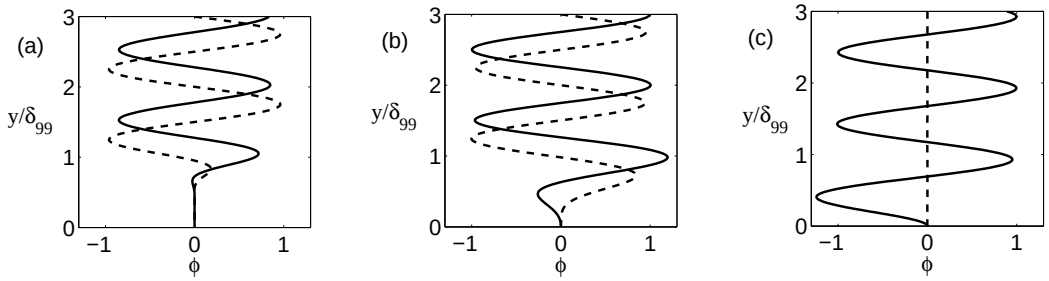


Figure 3.1: Example of continuous mode shapes for the Blasius boundary layer in three different regimes. Left to right: the sheltered regime $k_xRe = 800\pi, k_y = 2\pi, k_z = 4\pi$, the intermediate regime $k_xRe = 50\pi, k_y = 2\pi, k_z = \pi$, and the diffusive regime $k_xRe = \pi/100, k_y = 2\pi, k_z = \pi$. ——, real component; - - -, imaginary component.

In order to ensure that the perturbation is bounded, it would suffice to construct an oscillatory solution. By examining the free-stream solutions of the Orr-Sommerfeld equation (2.17) one concludes that if $\lambda_{1,2}^2 = -k_y^2$, the eigenfunction $\phi_{1,2}(y \to \infty) \sim e^{\pm ik_y y}$ where k_y is any positive real number. In addition, this assumption implies that the continuous modes have a contribution from ϕ_1 along with ϕ_2 and ϕ_4 which are used to construct the discrete modes. The dispersion relation for the continuous modes is thus obtained as,

$$-k_y^2 = k_x^2 + k_z^2 + i\frac{k_x}{\nu}\left(U_\infty - \omega/k_x\right)$$

which can be solved for the eigenvalues. In the temporal problem,

$$\omega = k_x U_\infty - i\nu\left(k_x^2 + k_z^2 + k_y^2\right). \tag{3.1}$$

Assuming the dispersion relation 3.1, the continuous modes are obtained by numerical solution of the Orr-Sommerfeld equation. The solution algorithm is an extension of the spectral collocation method of Orszag (1971): Chebyshev polynomials were used to expand the eigenfunctions in the wall-normal direction. Since the polynomials are valid in the domain $[-1, 1]$, non-linear mapping was incorporated to extend the method to semi-infinite domains. The boundedness condition in the free-stream was enforced according to the method proposed by Jacobs & Durbin (1998).

The numerical and analytical results presented herein are for three-dimensional disturbances. This choice is motivated by the importance of oblique waves in the transient growth phenomenon in shear flows. Many transient growth studies report that waves

with spanwise wavelength on the order of the shear or boundary layer thickness are the amplified the most (for e.g. Butler & Farrell, 1992). Therefore, the value of $k_z \sim \pi$ is selected for the numerical evaluation of solutions and subsequent discussion. The shapes of three continuous modes for a Blasius base flow are shown in figure 3.1. The mode shapes suggest that penetration of the vortical mode into the boundary layer is dependent on parameters of the mean flow and of the eigenmode considered. The three modes epitomize three regimes: a sheltered regime where the free-stream vorticity does not penetrate the boundary layer (figure 3.1-a); an intermediate regime where the vortical perturbation penetrates the boundary layer, but not sufficiently to influence the near-wall region (figure 3.1-b); and a diffusive regime where the oscillatory free-stream behavior of the perturbation persists deep inside the boundary layer to the vicinity of the wall (figure 3.1-c). In order to investigate those asymptotic regimes, a piece-wise linear base flow is considered in the analyses.

3.2.2 Analytical solution for piece-wise linear profile

The numerical solution of the *fourth order* Orr-Sommerfeld equation demonstrates the dependence of the shape of continuous modes on frequency, wave-number, and Reynolds number. However, the mechanisms that determine the structure of the eigenfunction are not evident. Therefore, in order to derive the relevant asymptotic regimes, a piecewise linear mean flow profile is assumed, and the Orr-Sommerfeld equation is thus reduced to a second order vorticity equation. This simplification enables us to identify the parameters which determine the structure of the continuous modes. A similar approach was adopted by Craik (1991) in order to explain the results of Grosch & Salwen (1978) for a Blasius profile. First, the closed form solutions of the vorticity equation are presented, followed by a discussion of the dominant balance of the terms in the equation.

A transformed wall-normal coordinate $Y = y - \delta_{BL}$ is adopted, and the analysis is carried out in a frame translating with the free-stream velocity, $\mathscr{U}(Y) = U(Y) - U_\infty$ as shown in figure 3.2. The mean flow is therefore,

$$\begin{aligned} \mathscr{U}(Y) &= 0, & Y > 0, \\ \mathscr{U}(Y) &= \tau Y, & 0 \geq Y \geq -\delta_{BL}, \end{aligned} \tag{3.2}$$

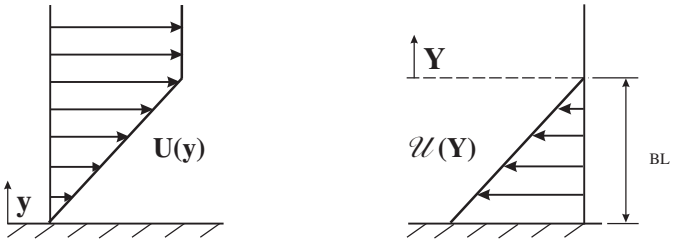


Figure 3.2: Schematic of the single-fluid piecewise linear mean velocity profile. At right, the mean velocity profile is shown in a frame translating at U_∞.

where δ_{BL} is the single fluid boundary layer thickness and $\tau = U_\infty/\delta_{BL}$.

Using the piece-wise linear profile, and the dispersion relation 3.1, the final linear stability equations have the form,

$$d_Y^2\psi + k_y^2\psi = 0, \qquad Y > 0, \tag{3.3}$$

$$d_Y^2\psi + k_y^2\psi - \frac{ik_x\tau}{\nu}Y\psi = 0, \qquad 0 \geq Y \geq -\delta_{BL}, \tag{3.4}$$

where $\psi \equiv (d_Y^2 - k^2)\phi$. For two-dimensional disturbances, $\psi = \frac{\partial}{\partial x}(\partial v/\partial x - \partial u/\partial y)$ is a measure of the spanwise vorticity of a two-dimensional eigenmode. It should be noted that the Orr-Sommerfeld equation 3.4 in terms of ψ is identical to the homogeneous Squire equation for normal vorticity. Therefore, the shape of the continuous Orr-Sommerfeld and Squire modes are similar. In addition, asymptotic analyses performed in subsequent sections using 3.4 are also valid for the Squire equation.

For the piece-wise linear profile, apart from the free stream and wall boundary conditions, four interface conditions are required in order to match the solutions across the edge of the boundary layer. These conditions are derived from continuity of velocity and stresses,

$$\begin{aligned} \phi(0^+) - \phi(0^-) &= 0 \quad ; \quad d_Y\phi(0^+) - d_Y\phi(0^-) = \frac{k_x\tau\phi(0)}{k_xU(0) - \omega} \\ d_Y^2\phi(0^+) - d_Y^2\phi(0^-) &= 0 \quad ; \quad d_Y^3\phi(0^+) - d_Y^3\phi(0^-) = 3k^2\frac{k_x\tau\phi(0)}{k_xU(0) - \omega}. \end{aligned} \tag{3.5}$$

In the free-stream, equation 3.3 is solved for ψ_{FS} and in turn ϕ_{FS} (note: throughout this chapter, subscripts $m = 1, 2, 3, 4$ will be reserved for the integration constants in the

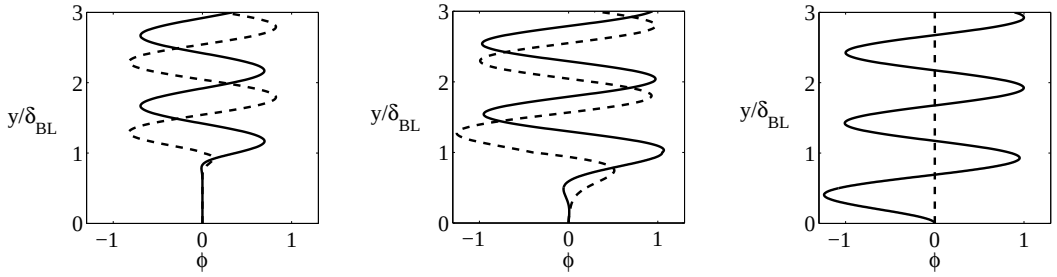


Figure 3.3: Example of continuous mode shapes for piecewise linear profile in three different regimes: (left to right) convective shear-sheltering regime $k_xRe = 800\pi, k_y = 2\pi, k_z = 4\pi$, convective-diffusive regime $k_xRe = 50\pi, k_y = 2\pi, k_z = \pi$ and diffusive regime $k_xRe = \pi/100, k_y = 2\pi, k_z = \pi$. ——, real component; - - -, imaginary component.

free-stream, while $m \geq 5$ will be used for the solution inside the boundary layer),

$$\psi_{FS} = C_1' \exp(-ik_yY) + C_2' \exp(ik_yY), \tag{3.6}$$

$$\phi_{FS} = C_1 \exp(-ik_yY) + C_2 \exp(ik_yY) + C_3 \exp(-kY) + C_4 \exp(kY), \tag{3.7}$$

In order to maintain boundedness of the eigenfunction in the free-stream, $C_4 = 0$. Inside the boundary layer, the solution to 3.4 yields,

$$\psi = C_5 Ai[\mathscr{Z}(Y)] + C_6 Bi[\mathscr{Z}(Y)], \tag{3.8}$$

$$\begin{aligned}\phi = {} & \exp(-kY) \int_{-\delta_{BL}}^{Y} \exp(ks)(C_5 Ai[\mathscr{Z}(s)] + C_6 Bi[\mathscr{Z}(s)])ds \\ & + \exp(kY) \int_{Y}^{0} \exp(-ks)(C_5 Ai[\mathscr{Z}(s)] + C_6 Bi[\mathscr{Z}(s)])ds \\ & + C_7 \exp(-kY) + C_8 \exp(kY),\end{aligned} \tag{3.9}$$

where $\mathscr{Z}(Y) = \exp(i5\pi/6)(\frac{k_x\tau}{\nu})^{\frac{1}{3}}(Y + \frac{ik_y^2\nu}{k_x\tau})$. The constants of integration C_m are given in the appendix A.1.1.

Three continuous Orr-Sommerfeld eigenfunctions evaluated using the above analytic solution are shown in figure 3.3. Similar to the Blasius eigenfunctions of figure 3.1, three degrees of modal penetration are observed. These are not, however, evident in the exact analytical expressions 3.8 and 3.9 where the solution is in terms of integrals of the Airy functions. In the following section, the Orr-Sommerfeld equation 3.4 inside the boundary layer is revisited,

$$d_Y^2\psi + k_y^2\psi - \frac{ik_x\tau}{\nu}Y\psi = 0. \tag{3.4}$$

and asymptotic solutions are derived based on the relative magnitude of the convective term, $\frac{ik_x\tau}{\nu}Y$, and diffusive term, k_y^2. The objective is to explain the different mechanisms governing vortical mode penetration inside the boundary layer. Three limits are considered and will be referred to as,

(a) the convective, shear-sheltered regime, $\frac{k_x\tau\delta_{BL}}{k_y^2\nu} \gg 1$

(b) the diffusive regime, $\frac{k_x\tau\delta_{BL}}{k_y^2\nu} \ll 1$

(c) and the convective-diffusive regime, $\frac{k_x\tau\delta_{BL}}{k_y^2\nu} \sim O(1)$

3.3 Asymptotic solutions in the single-fluid boundary layer

3.3.1 The convective shear-sheltered regime

Hunt (1977) and coworkers investigated the interaction of vortical disturbances with shear flows. Their inviscid rapid distortion theory (RDT) solution demonstrated that free-stream vortical disturbances with a finite streamwise wavelength are simply convected, and do not penetrate the shear. The result was disconcerting because it did not allow any interaction of the free-stream disturbances with the boundary layer shear. The inability of the shear region to sustain a vortical solution is due to the inviscid assumption. When $\nu = 0$, the vorticity equation 3.4 reduces to, $ik_x(c - U(Y))\psi = 0$. A non-trivial solution requires that the phase speed of the vortical disturbance equals that of the base flow. For the continuous spectrum modes, $c = U_\infty$, and therefore these disturbances can only be sustained in the free-stream.

Jacobs & Durbin (1998) incorporated the effect of viscosity in their analysis of the continuous modes. They demonstrated that viscous theory allows for vortical penetration into the shear, and that the penetration depth is proportional to $(\nu/\omega\tau)^{1/3}$. Zaki & Durbin (2005) extended this analysis in order to incorporate the modal decay rate.

All the above analyses only considered high-frequency disturbances in an infinitely deep boundary layer. The effect of the wall on modal penetration was not included. Here, a finite thickness boundary layer is considered in order to demonstrate both shear sheltering and the blocking effect of the wall. A small parameter, $\epsilon_s \equiv \frac{k_y^2\nu}{k_x\tau\delta_{BL}} \ll 1$, is defined; subscript s denotes the shear-sheltered regime. Equation 3.4 can be expressed

in terms of the small parameter,

$$\epsilon_s d_Y^2 \psi + \epsilon_s k_y^2 \psi - k_y^2 \frac{iY}{\delta_{BL}} \psi \quad = \quad 0.$$

A series expansion, $\psi = \epsilon_s^0 \psi_0 + \epsilon_s^1 \psi_1 + \epsilon_s^2 \psi_2 + \cdots$, yields trivial solutions for all powers of ϵ_s. This solution, while possibly valid in the bulk of the shear, can not match free stream vorticity, nor can it satisfy the wall boundary conditions; indeed $\psi = 0$ in the near-wall region violates both the no-penetration and no-slip boundary conditions. Therefore, an *edge* and a *wall* layer develop in these regions of the shear in order to satisfy the free-stream matching and wall boundary conditions, respectively.

In the edge layer, a scaled coordinate $Y_e \equiv Y/\delta_e$, and $\psi_e \equiv \psi(Y)$ are introduced, and the governing equation becomes,

$$\frac{\epsilon_s}{\delta_e^2} \frac{d^2 \psi_e}{dY_e^2} + \epsilon_s k_y^2 \psi_e - i k_y^2 \frac{\delta_e}{\delta_{BL}} Y_e \psi_e \quad = \quad 0. \tag{3.10}$$

Balance of the dominant terms implies that $\delta_e \sim O\left(\nu/k_x\tau\right)^{1/3}$. To leading order, this scaling yields,

$$\frac{d^2 \psi_e}{dY_e^2} - iY_e \psi_e \quad = \quad 0,$$

and hence the solution is given by,

$$\psi_e = C_{e_1} Ai[\exp(i5\pi/6)Y_e] + C_{e_2} Bi[\exp(i5\pi/6)Y_e]. \tag{3.11}$$

In the limit $Y_e \to \infty$, the edge layer solution ψ_e must asymptotically match the trivial solution in the bulk of the shear, which leads to $C_{e_2} = 0$.

In the wall layer, the scaled coordinate $Y_w \equiv \left(\delta_{BL} + Y\right)/\delta_w$, and $\psi_w \equiv \psi(Y)$ are introduced. The governing equation re-written in terms of wall co-ordinates is therefore,

$$\frac{1}{\delta_w^2} \frac{d^2 \psi_w}{dY_w^2} + \frac{ik_x\tau}{\nu} (\delta_{BL}(1 - i\epsilon_s) - \delta_w Y_w)\psi_w \quad = \quad 0. \tag{3.12}$$

Expanding ψ_w in powers of ϵ_s and balancing the leading order terms gives $\delta_w \sim O\left(\sqrt{\frac{\nu}{k_x\tau\delta_{BL}}}\right)$.

To leading order, the governing equation is,

$$\frac{d^2\psi_w}{dY_w^2} + i\psi_w = 0. \tag{3.13}$$

The leading order solution is therefore,

$$\psi_w(Y_w) = C_{w_1}\exp(\frac{1}{\sqrt{2}}(1-i)Y_w) + C_{w_2}\exp(-\frac{1}{\sqrt{2}}(1-i)Y_w). \tag{3.14}$$

The above expression must asymptotically match the trivial solution in the bulk of the shear, $\lim_{Y_w\to\infty}\psi_w(Y_w) = 0$ and therefore $C_{w_1} = 0$.

A uniformly valid vorticity eigenfunction can be expressed in terms of the bulk, edge, and wall layer solutions. To leading order, in the shear region $Y \in [-\delta_{BL}, 0]$, the continuous mode is given by,

$$\psi = C_{e_1}Ai[\varsigma(Y)] + C_{w_2}\exp(-\zeta(\delta_{BL}+Y)), \tag{3.15}$$

where $\varsigma(Y) = \exp(i5\pi/6)(\frac{k_x\tau}{\nu})^{1/3}Y$ and $\zeta = \frac{(1-i)}{\sqrt{2}\delta_w}$. The normal velocity eigenfunction inside the boundary layer is therefore,

$$\begin{aligned}\phi = {} & C_5\exp(-kY) + C_6\exp(kY) + C_{w_2}\exp(-\zeta(\delta_{BL}+Y)) + \\ & C_{e_1}\Bigg[exp(-kY)\int_{-\delta_{BL}}^{Y} exp(ks)Ai[\varsigma(s)]ds + \\ & \exp(kY)\int_{Y}^{0} exp(-ks)Ai[\varsigma(s)]ds\Bigg].\end{aligned} \tag{3.16}$$

The constants of integration can be evaluated using the boundary and matching conditions, and are given in appendix A.1.2. The eigenfunction 3.16 is comprised of an exponentially decaying component and an integral of the Airy function which is decaying for $Y < 0$. The coefficient of the exponentially growing component is very small according to A.3 and therefore its contribution is negligible.

A comparison of the mode shapes from the shear-sheltered asymptotic limit and the exact eigenfunction 3.9 is not included because the two solutions coincide nearly identically in this regime. Instead, figures 3.4 and 3.5 compare the eigenfunctions ϕ and ψ for a piecewise linear profile to those obtained for a Blasius mean flow. The eigenfunction ϕ is oscillatory in the free-stream and decays rapidly inside the boundary

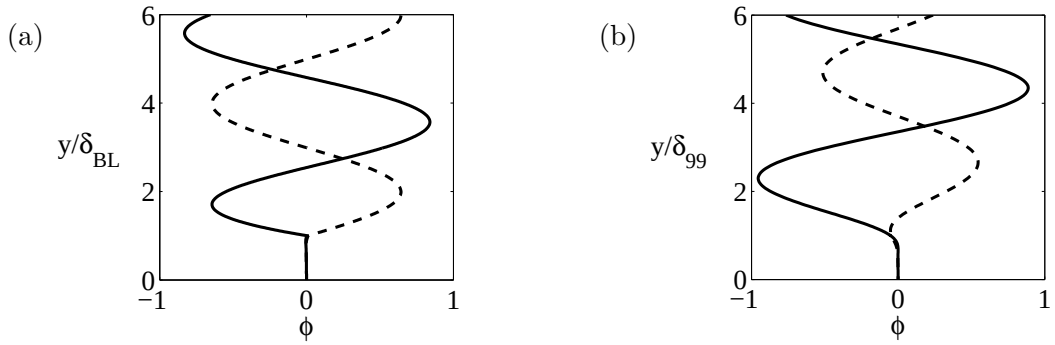


Figure 3.4: Continuous mode shape in convective shear-sheltered regime for (a) piecewise linear profile and (b) Blasius boundary layer. ——, real component; - - -, imaginary component. $k_x Re = 1000\pi/3, k_y = \pi/2, k_z = \pi/3$.

layer indicating the strong influence of shear, $\epsilon_s \equiv k_y^2 \nu / k_x \tau \delta_{BL} \ll 1$. The decay in the eigenfunction of the piece-wise linear profile is more rapid near the edge of the boundary layer due to the higher level of shear in comparison to the Blasius mean flow.

More insight into the structure of these vortical modes can be gathered from figure 3.5. In the free-stream the vorticity ψ is oscillatory. Inside the boundary layer, shown in the bottom pane of figure 3.5, three regions can be clearly identified:

a) the outer layer near the edge of the boundary layer,

b) the bulk, or central region, which is devoid of any significant vortical disturbance,

c) and the wall layer where vorticity is again non-zero.

The scaling of these layers is captured by the above derived asymptotic solutions. The outer layer is a measure of the extent of penetration of the free-stream vorticity into the shear. Its thickness is $\delta_e \propto (\nu/k_x\tau)^{1/3}$. Beyond δ_e, the shear prevents further penetration of the free-stream mode. The vortical disturbance in the outer layer is convected downstream, and imposes a normal velocity "boundary-condition" on the bulk of the shear. As a result, an exponentially small, irrotational perturbation field is setup in that region. While this inviscid mechanism is relevant to the other asymptotic regimes discussed in this work, it is most discernible in the shear-sheltered eigenfunctions. In this limit, viscous penetration of the free-stream disturbance is inhibited and, as a result, the contribution of the inviscid mechanism to the eigenfunction inside the shear is more evident. An example of the streamlines is shown in figure 3.6. In the vicinity of the wall, vorticity is generated in order to satisfy the no-slip and no-penetration boundary conditions. The wall layer is in fact a Stokes layer whose lengthscale is $\delta_w \sim \sqrt{\nu/\Omega}$,

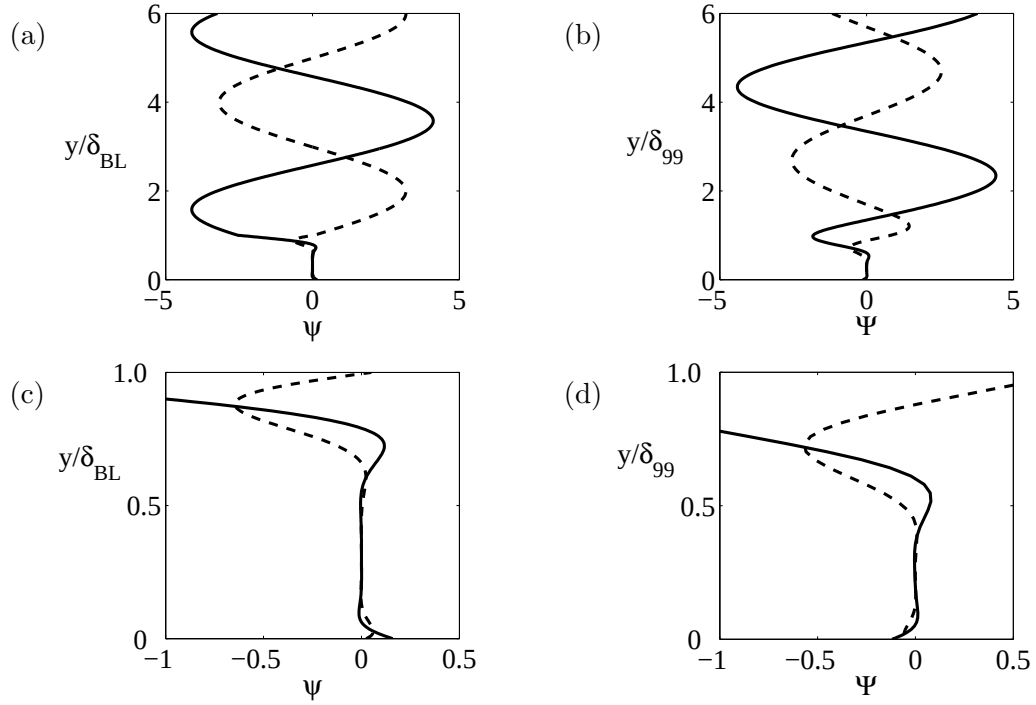


Figure 3.5: Spanwise vorticity in the convective shear-sheltered regime. At left eigenfunction for piecewise linear profile and at right eigenfunction for Blasius boundary layer. The bottom figures show the eigenfunction ψ inside the boundary layer. ——, real component; - - -, imaginary component. $k_x Re = 1000\pi/3, k_y = \pi/2, k_z = \pi/3$.

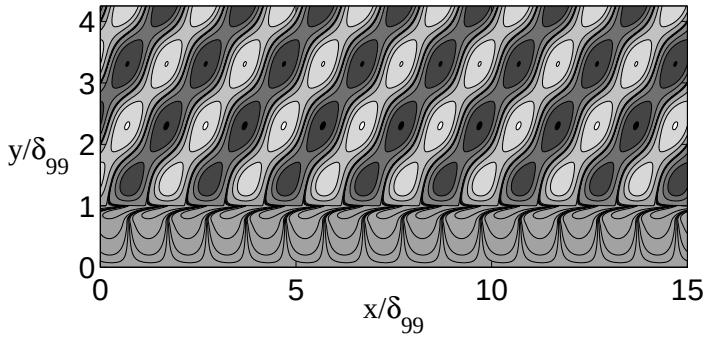


Figure 3.6: Streamlines of a continuous mode with $k_x Re = 1000\pi, k_y = \pi, k_z = 0$

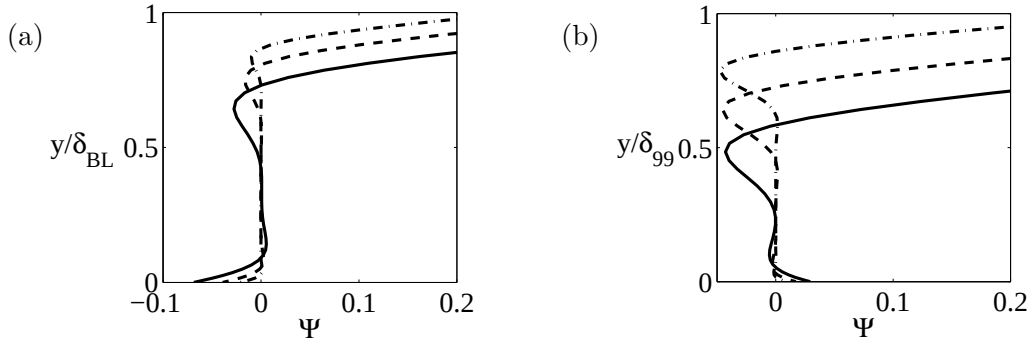


Figure 3.7: Effect of Reynolds number on the edge and wall layer for (a) piecewise linear profile and (b) Blasius boundary layer. $k_x = \pi, k_y = \pi, k_z = \pi$. ——, Re = 100; - - -, Re = 200 ; — · —, Re = 1000.

where $\Omega \equiv k_x U_\infty$ is the frequency of oscillation of the free stream.

The effect of viscosity on the edge- and wall-layer thicknesses is shown in figure 3.7. This behavior is captured by the expressions for the length-scales δ_w and δ_e. It is instructive to consider two sources of vorticity: the first in the free-stream and the second at the wall. At low viscosity, scaling δ_{BL} by the edge-layer $\delta_e \propto (\nu/k_x\tau)^{1/3}$, the boundary layer appears deeper and hence, there is no overlap between the free-stream and wall-generated vorticity. Lowering the viscosity causes the sources to move further apart, thus widening the inner core. In the limit $\nu \to 0$, the influence of the wall becomes insignificant.

It is important to note that the decay of the eigenfunction inside the boundary layer is due to the sheltering effect of the shear, and is *not* a wall-blocking phenomenon. This can be further verified by considering the limit of infinite shear, $\delta_{BL} \to \infty$. In this limit,

the eigenfunction 3.16 reduces to,

$$\begin{aligned}\phi &= C_5 \exp(kY) + C_{e_1}\Big[exp(-kY)\int_{-\infty}^{Y} exp(ks)Ai[\varsigma(s)]ds + \\ &\quad \exp(kY)\int_{Y}^{0} exp(-ks)Ai[\varsigma(s)]ds\Big], \end{aligned} \tag{3.17}$$

or equivalently $\psi = C_{e_1} Ai[\varsigma(Y)]$. A similar expression for ψ was obtained by Jacobs & Durbin (1998) for the infinitely deep boundary layer. The normal velocity eigenfunction 3.17 is composed of an exponentially decaying component and the integral of first Airy function which is also decaying. Therefore, in the absence of a solid boundary, the normal velocity is exponentially small but not exactly zero. A solid boundary at finite Y forces ϕ to be zero and, therefore, spanwise vorticity, ψ, must be generated at the wall in order to satisfy the boundary conditions. The extent of diffusion of this wall-vorticity into the shear is the thickness of the wall-layer, δ_w, as demonstrated by 3.12.

3.3.2 The diffusive regime

The reciprocal of the shear-sheltered limit is the diffusive regime. In this regime, the filtering effect of the shear is ineffective, and the oscillatory free-stream vortical disturbances persist deep into the boundary layer (figure 3.3 c). As the name suggests, the viscosity dominates the convective term in the continuous-mode vorticity equation 3.4. A small parameter $\epsilon_d \equiv \frac{k_x \tau \delta_{BL}}{k_y^2 \nu} \ll 1$ can be defined. The vorticity equation 3.4 can therefore be expressed in terms of ϵ_d,

$$\frac{1}{k_y^2} d_Y^2 \psi + \psi - \epsilon_d \frac{iY}{\delta_{BL}} \psi = 0.$$

Assuming a power series solution, $\psi \sim \psi_0 + \epsilon_d \psi_1 + \epsilon_d^2 \psi_2 + \cdots$, the governing equation to leading order has the form,

$$\frac{1}{k_y^2} d_Y^2 \psi + \psi = 0. \tag{3.18}$$

The above equation resembles the governing equation for Stokes second problem. However, unlike the real frequency of oscillation in the Stokes problem, the continuous eigenfunctions are purely decaying in time. The oscillatory behavior of the continuous modes is in the wall-normal direction due to k_y dependence in the free-stream. Therefore, due

to the difference in the free-stream flow conditions, the two problems are distinct.

The solution to the leading order vorticity equation, and the corresponding wall-normal velocity perturbation ϕ are, respectively,

$$\begin{aligned} \psi &= C_5' \exp(-ik_y Y) + C_6' \exp(ik_y Y), \\ \phi &= C_5 \exp(-ik_y Y) + C_6 \exp(ik_y Y) + C_7 \exp(-kY) + C_8 \exp(kY). \end{aligned} \tag{3.19}$$

The constant C_5 through C_8 are obtained by satisfying the wall boundary conditions and matching conditions at the edge of the boundary layer, and are provided in appendix A.1.3. For $k_x = 0$, the similarity between the above expression for ϕ and the free-stream eigenfunction 3.7 can be exploited in order to derive a uniformly valid solution for $Y \in [-\delta_{BL}, \infty)$,

$$\begin{aligned} \phi = C \exp(-k\delta_{BL}) \Bigg[\exp(-kY) &- \frac{1}{2}\left(1 + \frac{k}{ik_y}\right) \exp(k\delta_{BL} - ik_y(\delta_{BL} + Y)) \\ &- \frac{1}{2}\left(1 - \frac{k}{ik_y}\right) \exp(k\delta_{BL} + ik_y(\delta_{BL} + Y)) \Bigg], \end{aligned} \tag{3.20}$$

where C is the arbitrary amplitude of the free-stream vortical mode.

The most conspicuous attribute of the modes is their ability to preserve the free-stream oscillatory nature throughout the boundary layer shear, and up to the wall. This behavior is characteristic of streamwise elongated, or low-k_x, vortical modes, as suggested by the scaling parameter, $\epsilon_d \equiv k_x \tau \delta_{BL} / k_y^2 \nu$. The expression for ϵ_d also suggests that high-k_y belong to the diffusive regime, and can therefore penetrate the boundary layer. This observation is consistent with Zaki & Durbin (2005).

Figure 3.8 compares the mode shapes obtained from the asymptotic solution 3.20 for a piecewise linear profile to that obtained for a Blasius boundary layer. In addition to the similarity in the mode shape, good quantitative agreement is also observed. This agreement can be explained by noting that the terms associated with the mean flow in the Orr-Sommerfeld equation (the convective and mean curvature term) are an order of magnitude smaller than the viscous and transient terms. The leading order Orr-Sommerfeld equation is therefore independent of the mean flow chosen and hence a good quantitative agreement is observed between the eigenfunctions shown in figure 3.8.

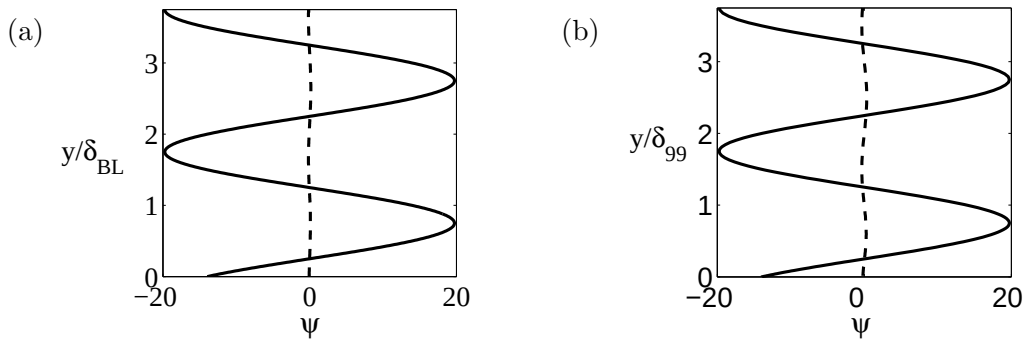


Figure 3.8: Continuous mode shapes in the diffusive regime. At left, eigenfunctions for piecewise linear profile and at right eigenfunctions for Blasius boundary layer. ——, real component; - - -, imaginary component. $k_x Re = \frac{\pi}{10}, k_y = \pi, k_z = \pi$.

3.3.3 The convective-diffusive regime

Free-stream vortical modes which partially penetrate the boundary layer shear (figure 3.3-b) do not fall within the premise of the fully-sheltered convected disturbances or of the fully-penetrating viscous regime. Instead, in the convective-diffusive regime, both the convective and the viscous terms in the vorticity equation 3.4 are of comparable magnitude throughout the bulk of the shear, $k_x \tau \delta_{BL} \sim k_y^2 \nu$. The structure of the eigenfunctions is examined by considering solutions of the vorticity equation in the outer region of the boundary layer, as well as in the vicinity of the wall.

Near the edge of the boundary layer, $Y \to 0$, the vorticity equation 3.4 is approximated, to lowest order in Y, by the diffusion dominated limit,

$$\frac{d^2\psi_e^0}{dY^2} + k_y^2 \psi_e^0 \quad = \quad 0,$$

whose solution is given according to,

$$\psi_e^0 \quad = \quad \underbrace{C_{e_1} \exp(ik_y Y)}_{\psi_{e_1}^0} + \underbrace{C_{e_2} \exp(-ik_y Y)}_{\psi_{e_2}^0}. \tag{3.21}$$

This oscillatory solution mimics exactly the free-stream eigenfunction, and shear-sheltering is negligible near the edge of the boundary layer. The influence of the uniform shear is therefore *not* local but, as suggested by the convective term $k_x \tau Y$, cumulative with increased depth within the boundary layer.

In order to demonstrate the influence of the shear on the wall-normal decay of the eigenfunction, a correction is sought for each of the two independent solutions, $\psi^0_{e_1}$ and $\psi^0_{e_2}$ (the procedure is outlined for $\psi^0_{e_1}$ only). The corrected solution $\psi_{e_1} = \psi^0_{e_1} + \psi^1_{e_1}$, where $\psi^1_{e_1} \ll \psi^0_{e_1}$, is substituted in the vorticity equation 3.4, and the following equation for $\psi^1_{e_1}$ is obtained,

$$\frac{d^2\psi^1_{e_1}}{dY^2} + k_y^2\psi^1_{e_1} - \frac{ik_x\tau Y}{\nu}C_{e_1}e^{+ik_yY} = 0,$$

with the homogeneous boundary conditions $\psi^1_{e_1} = d_Y\psi^1_{e_1} = 0$ at $Y = 0$. The correction term is therefore,

$$\psi^1_{e_1} = C_{e_1}e^{ik_yY}\left[\frac{k_x\tau}{2k_y\nu}\left(\frac{Y^2}{2} - \frac{Y}{2ik_y} - \frac{1-e^{-2ik_yY}}{4k_y^2}\right)\right].$$

A similar procedure yields the correction $\psi^1_{e_2}$ and, finally, the asymptotic behavior of the vorticity eigenfunction near $Y = 0$ can be expressed as,

$$\begin{aligned}\psi_e(Y) = \quad & \underbrace{C_{e1}e^{ik_yY}}_{\psi^0_{e_1}} \quad + \underbrace{C_{e_1}e^{ik_yY}\left[\frac{k_x\tau}{2k_y\nu}\left(\frac{Y^2}{2} - \frac{Y}{2ik_y} - \frac{1-e^{-2ik_yY}}{4k_y^2}\right)\right]}_{\psi^1_{e_1}} \\ & + \underbrace{C_{e2}e^{-ik_yY}}_{\psi^0_{e_2}} \quad + \underbrace{C_{e_2}e^{-ik_yY}\left[-\frac{k_x\tau}{2k_y\nu}\left(\frac{Y^2}{2} + \frac{Y}{2ik_y} - \frac{1-e^{2ik_yY}}{4k_y^2}\right)\right]}_{\psi^1_{e_2}}. \quad (3.22)\end{aligned}$$

The constants C_{e1} and C_{e2} are obtained by matching the vorticity and its gradient at the edge of the boundary layer. These constants have been provided in appendix A.1.4.

In the approximate solution 3.22, both $\psi^0_{e_1}$ and $\psi^0_{e_2}$ are oscillatory and only account for the diffusive term. The decay of the eigenfunction inside the boundary layer is due to an incomplete cancellation by the increasing amplitudes of $\psi^1_{e_1}$ and $\psi^1_{e_2}$ inside the shear, $Y < 0$. The decay of the solution inside the boundary layer is captured in figure 3.9. The figure compares the exact and asymptotically-derived vorticity eigenfunctions. The two solutions are in good quantitative agreement in the region $0 > Y > 0.6$. The oscillation of the eigenfunction near the edge of the boundary layer, and the gradual decay in the amplitude of oscillation due to the cumulative effect of the shear are captured by 3.22.

The near-wall behavior of the eigenfunction is derived by considering the limit $Y \rightarrow$

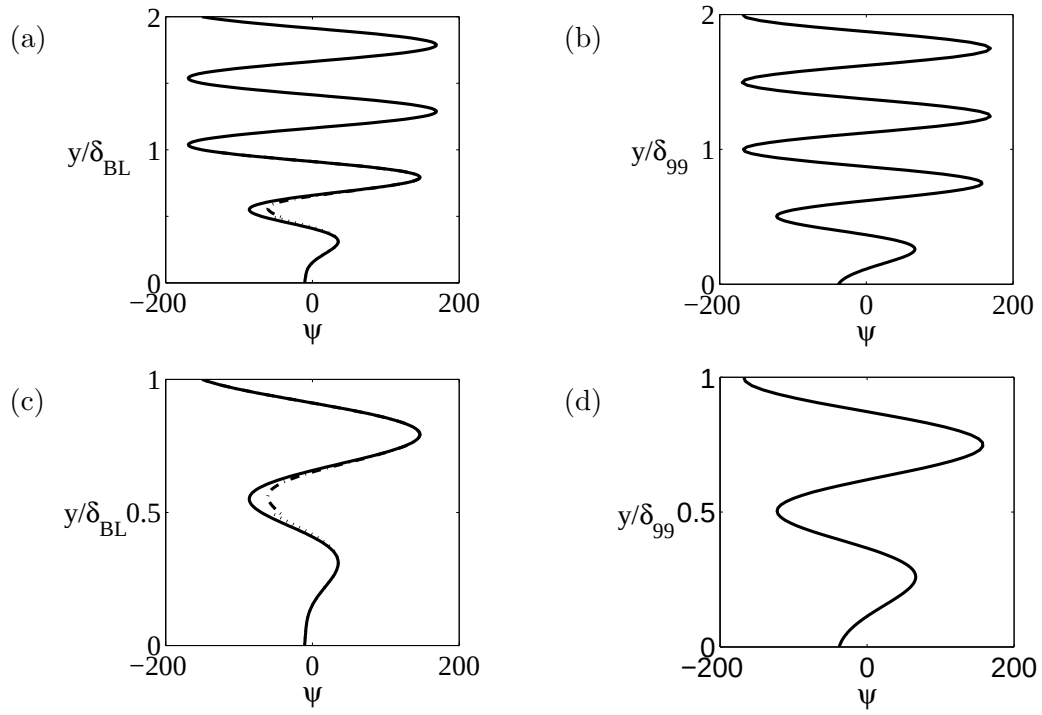


Figure 3.9: Spanwise vorticity in convective-diffusive regime. At left, real(ψ) for a piecewise linear profile and at right, real(ψ) for a Blasius boundary layer. ——, Exact analytical solution; — · —, Oscillatory solution; · · · ·, Exponential wall solution; $k_x Re = 50\pi, k_y = 4\pi, k_z = \pi$.

$-\delta_{BL}$ of the vorticity equation 3.4,

$$\frac{d^2\psi_w^0}{dY^2} + \left(k_y^2 + i\frac{k_x\tau\delta_{BL}}{\nu}\right)\psi_w^0 \quad = \quad 0.$$

The lowest order approximation of the vorticity eigenfunction is therefore composed of a growing and a decaying exponential,

$$\psi_w^0 \quad = \quad \underbrace{C_{w_1}\exp(i\kappa_w(Y+\delta_{BL}))}_{\psi_{w_1}^0} + \underbrace{C_{w_2}\exp(-i\kappa_w(Y+\delta_{BL}))}_{\psi_{w_2}^0}, \tag{3.23}$$

where $\kappa_w = \sqrt{k_y^2 + i\,(k_x\tau\delta_{BL}/\nu)}$. The cumulative effect of the shear over the boundary layer, $ik_x\tau\delta_{BL}/\nu$ determines the deviation of the solution from a purely oscillatory form. In a manner similar to the solution in edge layer, a corrected eigenfunction $\psi_w = \psi_w^0 + \psi_w^1$ is obtained in the wall-region,

$$\begin{aligned}
\psi_w(Y) = \quad & C_{w1}e^{ik_w(Y+\delta_{BL})} + C_{w2}e^{-ik_w(Y+\delta_{BL})} \\
+ \quad & C_{w1}e^{ik_w(Y+\delta_{BL})}\left[\frac{k_x\tau}{2k_w\nu}\left(\frac{(Y+\delta_{BL})^2}{2} - \frac{(Y+\delta_{BL})}{2ik_w} - \frac{1-e^{-2ik_w(Y+\delta_{BL})}}{4k_w^2}\right)\right] \\
+ \quad & C_{w2}e^{-ik_w(Y+\delta_{BL})}\left[\frac{-k_x\tau}{2k_w\nu}\left(\frac{(Y+\delta_{BL})^2}{2} + \frac{(Y+\delta_{BL})}{2ik_w} - \frac{1-e^{2ik_w(Y+\delta_{BL})}}{4k_w^2}\right)\right].
\end{aligned}$$

The constants C_{w_1} and C_{w_2} are given in appendix A.1.4, and are obtained by imposing continuity of vorticity and its gradient at the wall. Agreement between the asymptotic wall-layer solution ψ_w and the exact eigenfunction is shown in figure 3.9.

3.3.4 Discussion

The propensity of a vortical free-stream mode to penetrate the boundary layer is enhanced by viscosity and limited by the shear. The filtering effect of the shear is, however, wavenumber dependent. In the limit $\epsilon_s \equiv \frac{k_y^2\nu}{k_x\tau\delta_{BL}} \ll 1$, shear-sheltering is most effective. Therefore, high-k_x, or short streamwise-wavelength, vortical modes can not penetrate the boundary layer. In the reciprocal limit of long streamwise-wavelength, $\epsilon_d \equiv \frac{k_x\tau\delta_{BL}}{k_y^2\nu} \ll 1$, the eigenfunction preserves its free-stream oscillatory nature and amplitude deep into the boundary layer.

A physical interpretation of shear-sheltering is proposed by considering the relative

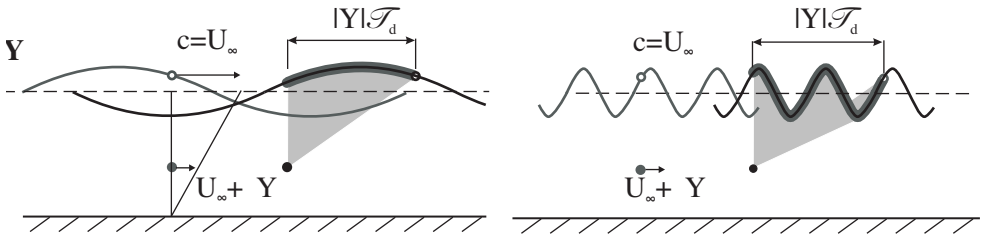


Figure 3.10: Schematic of modal penetration for low- and high-frequency free-stream vortical perturbations.

motion of a free-stream vortical mode and a point P within the shear (figure 3.10). The vortical mode at the edge of the boundary layer convects downstream at $c = U_\infty$, and point P has speed $U(p) = U_\infty + \tau Y$. The influence of the free-stream disturbance reaches P by wall-normal diffusion *only*. Within the diffusion time-scale, $\mathscr{T}_d \equiv 1/k_y^2\nu$, the free-stream boundary condition which affects P varies due to the relative motion of the wave and the shear flow. As a result, point P is exposed to n wavelengths of the free-stream disturbance, where n is given by,

$$n \;=\; \frac{(c - U\,(p))\,\mathscr{T}_d}{1/k_x} = \frac{k_x\tau|Y|}{k_y^2\nu}.$$

The definition of n is a ratio of two time-scales: The numerator defines the relative streamwise convection, or shear, time-scale according to $\mathscr{T}_s \equiv 1/k_x\tau\delta_{BL}$, and the denominator defines the wall-normal diffusion time-scale $\mathscr{T}_d \equiv 1/k_y^2\nu$. For low-$k_x$, or streamwise elongated waves, $n \to 0$ and the perturbation at the edge of the boundary layer appears seemingly steady relative to point P, over the diffusion time scale $\mathscr{T}_d$. As a result, a free-stream vortical mode diffuses effectively into the boundary layer shear in this limit. On the other hand, for short waves, n tends to ∞ and the edge condition appears to be changing very rapidly with respect to point P. The net effect over the time scale $\mathscr{T}_d$ is a near-zero edge condition relative to point P. As a result, the penetration of high-k_x vortical modes is limited. The filtering effect of high-frequencies is enhanced by the shear, $n \propto k_x\tau Y$, and hence the terminology "shear-sheltering". The precise mechanism is due to the difference in convective speeds between the free-stream perturbation and the flow inside the boundary layer. Therefore, shear-sheltering is cumulative, and n increases with depth.

When the convection and diffusion terms are approximately equal, $n \sim O(1)$, and the perturbation is able to partially penetrate the boundary layer, but decays due to the

cumulative influence of the shear. Therefore, the vorticity eigenfunctions in this regime are oscillatory near the edge of the boundary layer and exponentially decaying in the near-wall region.

The exact analytical expression 3.8 for $\psi(y)$ captures the change in the eigenfunction from oscillatory to exponential decay,

$$\psi = C_5 Ai\left[\mathscr{Z}(Y)\right] + C_6 Bi\left[\mathscr{Z}(Y)\right]. \tag{3.8}$$

The ratio of the convective and diffusive time scales, $\mathscr{T}_s/\mathscr{T}_d$, appears in the argument of the Airy function,

$$\mathscr{Z}(Y) = \exp\left(i5\pi/6\right)\left(\frac{Y}{\delta_e} + i\frac{\mathscr{T}_s\delta_{BL}}{\mathscr{T}_d\delta_e}\right).$$

The ratio $\mathscr{T}_s/\mathscr{T}_d$ determines the phase of $\mathscr{Z}(Y)$, and in turn the behavior of the Airy solution. In the viscous regime, the diffusive time scale is much shorter than the convective time scale, $\mathscr{T}_d \ll \mathscr{T}_s$. As a result, $|phase(\mathscr{Z})| > \pi/3$, and the first and second Airy functions are both oscillatory. In the shear-sheltered regime, $\mathscr{T}_d \gg \mathscr{T}_s$. Therefore, $i\mathscr{T}_s\delta_{BL}/\mathscr{T}_d\delta_e \to 0$ and $(|phase(\mathscr{Z})| \sim \pi/6) < \pi/3$. In this region of the complex plane, $Ai(\mathscr{Z})$ is monotonically decreasing, and $Bi(\mathscr{Z})$ is increasing. The coefficient of the latter, C_6, is negligible in the sheltered regime, and the overall behavior of the vorticity eigenfunction is captured by the decaying $Ai(\mathscr{Z})$.

The shear-sheltered solution is also recovered in the limit of vanishing kinematic viscosity. In this limit, $\mathscr{T}_d \to \infty$ and $\delta_e \to 0$. Since $\mathscr{T}_d \propto 1/\nu$ and $\delta_e \propto \nu^{1/3}$, their product tends to infinity. As a result, the same limit $(|phase(\mathscr{Z})| \sim \pi/6) < \pi/3$ is obtained and the eigenfunction is exponentially decaying.

3.3.5 Penetration depth

In order to quantify the propensity of a continuous vortical mode to permeate the boundary layer, a penetration depth norm is defined,

$$d \equiv \int_0^{\delta_{BL}} \frac{|\phi|}{|\phi|_\infty}\, dy,$$

where $|\phi|_\infty$ is the free-stream amplitude of the eigenfunction. Figure 3.11 shows the variation of d continuous modes with $k_x Re$ for various k_y. In the limit $k_x Re \to \infty$

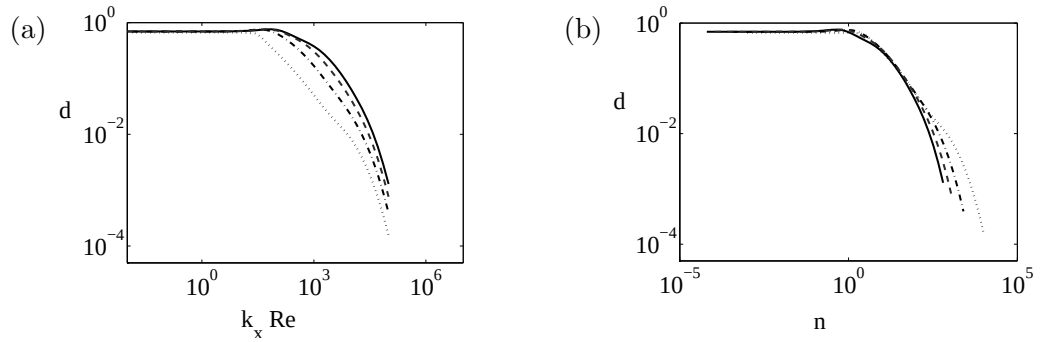


Figure 3.11: Variation in penetration depth with (a) k_xRe and (b) $n \equiv \frac{\mathscr{T}_d}{\mathscr{T}_s} = k_xRe/k_y^2$. ——, $k_y = 4\pi$; - - -, $k_y = 3\pi$; — · —, $k_y = 2\pi$; · · · ·, $k_y = \pi$.

penetration depth tends to zero. The same behavior is observed whether $k_x \to \infty$ and Re remains finite, or the opposite. In the first case, the boundary layer appears infinitely deep when scaled by the disturbance wavelength, and hence penetration is negligible. When $Re \to \infty$ and k_x is finite, viscous effects can be ignored and no means of vortical mode penetration in the boundary layer is present. As k_xRe is reduced, penetration increases due to the increase in $\mathscr{T}_s$ compared to $\mathscr{T}_d$. The change in the behavior of the penetration depth curve near $k_xRe \sim O(10)$ marks the convective-diffusive regime where both time-scales become comparable. At lower k_xRe, the diffusive regime is reached and d does not change significantly; the oscillatory solution prevails deep inside the boundary layer. Penetration increases with k_y due to the reduction of the diffusive time-scale. In the viscous regime, however, d is maximum and saturates independent of the wall-normal wavenumber. Motivated by the discussion of the convective and diffusive time-scales, the penetration curves are plotted against $n = \mathscr{T}_d/\mathscr{T}_s$ in figure 3.11-b. Residual dependence of penetration on n is observed in the sheltered regime where penetration is negligible. However, the penetration curves collapse in the diffusive ($\mathscr{T}_d/\mathscr{T}_s < 1$) and the convective-diffusive ($\mathscr{T}_d/\mathscr{T}_s \sim O(1)$) regimes.

3.4 The two-fluid theoretical formulation

The shape of the continuous spectrum modes and their ability to penetrate a single-fluid boundary layer depend on the disturbance wave-number, the intensity of the mean shear, and the kinematic viscosity of the fluid. In two-fluid boundary layers, both the mean shear and viscosity are discontinuous across the two-fluid interface. In addition,

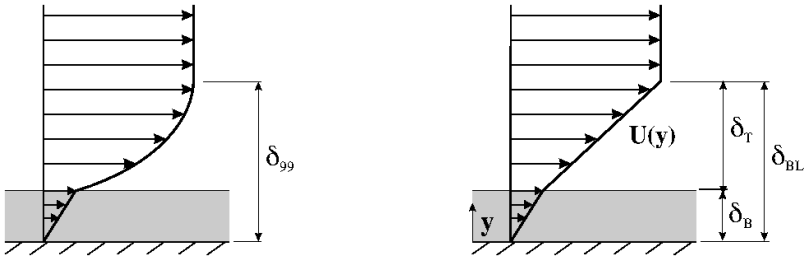


Figure 3.12: Schematic of the two-fluid mean velocity profile.

the density discontinuity and surface tension appear in the interfacial stress conditions and can, therefore, affect the ability of free-stream disturbances to penetrate the lower film. In order to investigate the dependence of mode-shape on these parameters, analyses similar to those carried out in the context of single-fluid boundary layers are presented for the two-fluid problem. The analysis begins from equations 2.10 and 2.12. First, an exact analytical expression of the eigenfunction is derived assuming the piece-wise linear mean flow, similar to the treatment of single-fluid boundary layer. The exact solution is subsequently explained by considering possible asymptotic limits.

Similar to the single-fluid problem, the continuous spectrum is obtained from the free stream behavior of the Orr-Sommerfeld equation. Therefore, the dispersion relation retains the same form,

$$-k_y^2 = k_x^2 + k_z^2 + i\frac{k_x}{\nu_T}\left(U_\infty - \omega/k_x\right).$$

Note, however, that the decay rate of the eigenvalue,

$$\omega = k_x U_\infty - i\nu_T\left(k_x^2 + k_z^2 + k_y^2\right), \tag{3.24}$$

is determined solely by the viscosity of the top fluid, ν_T.

3.4.1 The piecewise linear mean flow

For the purpose of the asymptotic analyses of relevant regimes and mechanisms of modal penetration into the shear, a piece-wise linear mean flow is assumed which mimics the base flow described in section 2.2. The asymptotic results are compared to the behavior of numerically computed continuous modes for a two-fluid boundary layer.

A schematic of the two-fluid boundary layer profile used in this study is shown in

figure 3.12. The piece-wise linear approximation to the mean profile, which is used in the analytical derivations, is defined according to,

$$\begin{aligned} U(y) &= \tau_B y & 0 < y < \delta_B, \\ U(y) &= \tau_B \delta_B + \tau_T (y - \delta_B) & \delta_B < y < \delta_{BL}, \\ U(y) &= U_\infty & y > \delta_{BL}, \end{aligned} \tag{3.25}$$

where,

$$\begin{aligned} \delta_{BL} &= \delta_{SF} + \delta_B \left(1 - \frac{\mu_T}{\mu_B}\right), \\ \tau_T &= \frac{U_\infty}{\delta_T + \frac{\mu_T}{\mu_B}\delta_B} = \frac{U_\infty}{\delta_{SF}}, \\ \tau_B &= \frac{\mu_T \tau_T}{\mu_B}. \end{aligned}$$

The single fluid boundary layer thickness, δ_{SF}, is the unit lengthscale and the film thickness, δ_B, is a parameter. As the viscosity ratio $\mu_{BT} \to \infty$, the shear in the bottom fluid vanishes, $\tau_B \to 0$. However τ_T remains constant indicating that the shear predominantly resides in the top fluid and the lower film mimics a solid wall. Conversely, as the viscosity ratio is reduced, the shear increases in the lower layer. For $\frac{\mu_B}{\mu_T} < \delta_B/\delta_{SF}$, the shear is entirely limited to the wall film ($\delta_T = 0, \tau_T = 0$ and $\tau_B = U_\infty/\delta_B$).

3.4.2 Analytical solution for piece-wise linear profile

An exact expression for the eigenfunction of the piece-wise linear mean profile is sought. Similar to the single-fluid problem, an equation for ψ is derived for each layer of the mean flow,

$$\begin{aligned} d_Y^2 \psi_{FS} + k_y^2 \psi_{FS} &= 0, & Y \geq 0, \\ d_Y^2 \psi_T + k_y^2 \psi_T - \frac{i k_x \tau_T}{\nu_T} Y \psi_T &= 0, & 0 \geq Y \geq -\delta_T, \\ \nu_B d_Y^2 \psi_B + \left[\nu_T \left(k_x^2 + k_y^2 + k_z^2\right) - \nu_B \left(k_x^2 + k_z^2\right)\right] \psi_B & \\ + i k_x \left(\tau_T \delta_T - \tau_B \left(Y + \delta_T\right)\right) \psi_B &= 0, & -\delta_T \geq Y \geq -\delta_{BL}. \end{aligned} \tag{3.26}$$

It is important to note that the viscosity of the top fluid, ν_T, appears in the vorticity equation of the bottom fluid because the temporal decay rate of the continuous mode

is determined by the free-stream behavior in the top fluid. As a result, the mode shape in the bottom fluid is expected to depend on the viscosity ratio, even in the absence of density stratification and surface tension, which only appear in the interface stress conditions.

The eigenmodes in the free stream, $Y > 0$, and in the outer boundary layer, $-\delta_T < Y < 0$, retain the same functional form as in the single-fluid problem (3.6 through 3.9). In the lower film, $-\delta_T \geq Y \geq -\delta_{BL}$, the solution for ψ_B and ϕ_B are, respectively,

$$\psi_B = C_9 Ai[\mathscr{X}(Y)] + C_{10} Bi[\mathscr{X}(Y)], \tag{3.27}$$

$$\begin{aligned}\phi_B = {} & \frac{\exp(-kY)}{2k} \int_{-\delta_{BL}}^{Y} \exp(ks)(C_9 Ai[\mathscr{X}(s)] + C_{10} Bi[\mathscr{X}(s)])ds \\ & + \frac{\exp(kY)}{2k} \int_{Y}^{-\delta_T} \exp(ks)(C_9 Ai[\mathscr{X}(s)] + C_{10} Bi[\mathscr{X}(s)])ds \\ & + C_{11} \exp(-kY) + C_{12} \exp(kY)\end{aligned} \tag{3.28}$$

where

$$\mathscr{X}(Y) = \exp\left(i5\pi/6\right) \left(\frac{k_x \tau_B}{\nu_B}\right)^{1/3} \left(Y + \frac{i\gamma\nu_B}{k_x \tau_B}\right)$$

and

$$\gamma = \frac{\nu_T k_y^2}{\nu_B} + \left(\frac{\nu_T}{\nu_B} - 1\right)\left(k_x^2 + k_z^2\right) + \frac{ik_x\delta_T}{\nu_B}\left(\tau_T - \tau_B\right).$$

The constants C_1 through C_{12} are selected such that the solution satisfies the boundedness condition in the free stream, no-slip at the wall, and the interface conditions 2.10. Analytical expressions for the constants are too complex, and are not provided. Instead, the constants are evaluated by numerical solution of the system of equations representing the boundary conditions. This linear system of equations is provided in appendix A.2.1.

An example of the two-fluid eigenfunctions, for both a piece-wise linear and a two-fluid boundary layer mean flow profile, is shown in figure 3.13. Properties of the top fluid were chosen to ensure that the disturbance penetrates the outer shear and reaches the interface. Based on the outer flow, the eigenfunctions therefore belong to the diffusive regime, $k_x \tau_T \delta_{SF} \ll k_y^2 \nu_T$. The three viscosity ratios shown in figure 3.13 reflect three asymptotic limits of the eigenfunction in the wall film. These limits bear resemblance to the asymptotic regimes of single-fluid boundary layers, and can be determined from the ratio of convective and diffusive terms in equation 3.26,

(a) the convective, shear-sheltered regime, $k_x \tau_B \delta_B \gg \nu_T k_y^2 + (\nu_T - \nu_B)(k_x^2 + k_z^2)$

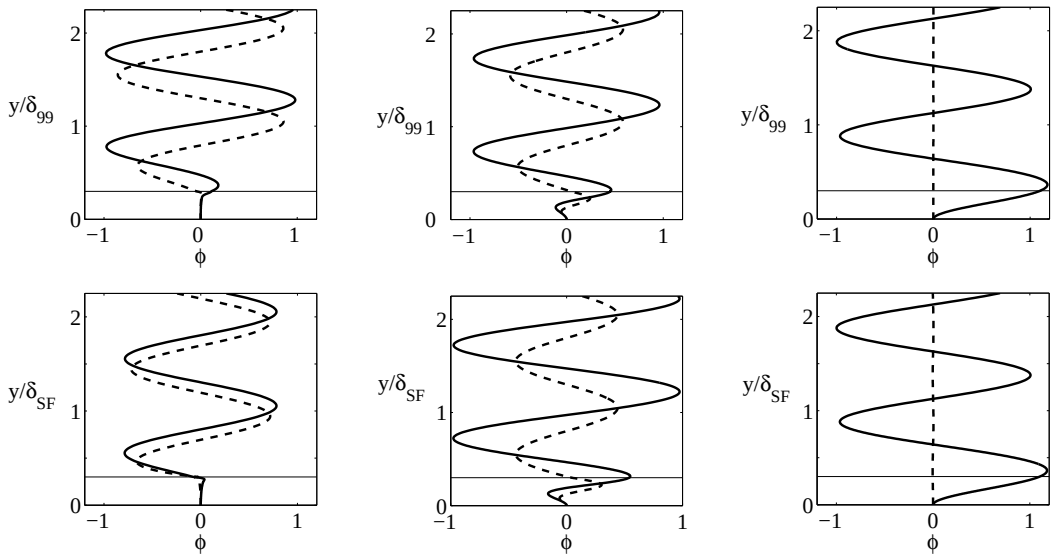


Figure 3.13: Example of continuous mode shape for two-fluid boundary layer (top figures) and piecewise linear profile (bottom figures) in three different regimes: (left to right) convective shear-sheltering regime $k_x Re_T = 4000\pi, k_y = 2\pi, k_z = \pi, \delta_B = 0.3, \mu_{BT} = 0.1$, convective-diffusive regime $k_x Re_T = 50\pi, k_y = 2\pi, k_z = \pi, \delta_B = 0.3, \mu_{BT} = 0.3$ and diffusive regime $k_x Re_T = \pi/100, k_y = 2\pi, k_z = \pi, \delta_B = 0.3, \mu_{BT} = 0.75$. ——, real component; - - -, imaginary component.

(b) the diffusive regime, $k_x(\tau_T\delta_T + \tau_B\delta_B) \ll \nu_T k_y^2 + (\nu_T - \nu_B)(k_x^2 + k_z^2)$

(c) and the convective-diffusive regime, $k_x\tau_B\delta_B \approx \nu_T k_y^2 + (\nu_T - \nu_B)(k_x^2 + k_z^2)$.

In order to realize conditions (a) and (c) for the shear-sheltered and convective-diffusive regimes, respectively, the viscosity of the bottom fluid must be much smaller than the top fluid, $\nu_B \ll \nu_T$. As a result, the shear can be assumed to be restricted to the bottom layer. In the shear-sheltered regime, where viscosity is not significant, the two-fluid eigenfunctions are expected to bear resemblance to the single-fluid problem. However, in the other two limits, where viscous effects are appreciable, the behavior of the two-fluid eigenfunctions is likely to be affected. Indeed, it is shown that eigenfunctions become dependent on the viscosity ratio, and not the viscosity of the bottom fluid *per se*.

3.5 Asymptotic solutions in the two-fluid boundary layer

3.5.1 The convective shear-sheltered regime

Our investigation of the convective-sheltered regime assumes an oscillatory solution in the top fluid, and the shear is restricted to the bottom layer. Therefore, the following simplifications are adopted, $\tau_T = 0$, $\delta_T = 0$, $\delta_B = \delta_{BL}$ and $\tau_B = U_\infty/\delta_{BL}$. In this limit, the vorticity equation 3.26 reduces to,

$$\epsilon_s \nu_B d_Y^2 \psi_B + \left(\nu_T \left(k_x^2 + k_y^2 + k_z^2\right) - \nu_B \left(k_x^2 + k_z^2\right)\right) \left(\epsilon_s - \frac{iY}{\delta_B}\right) \psi_B \quad = \quad 0,$$

where

$$\epsilon_s \equiv \frac{\nu_T(k_x^2 + k_y^2 + k_z^2) - \nu_B(k_x^2 + k_z^2)}{k_x \tau_B \delta_{BL}} \ll 1.$$

A series expansion, $\psi_B = \epsilon_s^0 \psi_{B0} + \epsilon_s^1 \psi_{B1} + \epsilon_s^2 \psi_{B2} + \cdots$, yields trivial solutions for all powers of ϵ_s. The trivial solution is only valid in the bulk of the lower-fluid.

Similar to the single-fluid boundary layer, an edge-layer exists, here near the two-fluid interface. The solution in the edge-layer satisfies the interfacial conditions, and asymptotically matches the trivial solution in the bulk of the lower fluid. The vorticity equation is expressed in terms of the edge coordinate, $Y_e \equiv Y/\delta_e$, and the dominant balance yields an edge layer thickness, $\delta_e \sim O\left(\nu_B/k_x\tau_B\right)^{1/3}$. The leading order behavior of the eigenfunction, ψ_{B_e}, is given according to,

$$\psi_{B_e} = C_{e_1} Ai[\exp(i5\pi/6)Y_e] + C_{e_2} Bi[\exp(i5\pi/6)Y_e]. \tag{3.29}$$

Since ψ_{B_e} must match the trivial solution in the limit $Y_e \to \infty$, the constant C_{e_2} must be identically zero and, as a result, $\psi_{B_e} = C_{e_1} Ai[\exp(i5\pi/6)Y_e]$.

A wall layer also exists in the vicinity of the solid boundary in order to satisfy the no-slip and no-penetration conditions. The vorticity equation is expressed in terms of the wall-coordinate, $Y_w \equiv (\delta_{BL} + Y)/\delta_w$. The dominant balance yields a wall-layer thickness $\delta_w \sim O\left(\sqrt{\frac{\nu_B}{k_x\tau_B\delta_{BL}}}\right)$, and the following leading order solution for ψ_{B_w} is obtained,

$$\psi_{Bw}(Y_w) \quad = \quad C'_{w_1} \exp\left(\frac{1}{\sqrt{2}}(1-i)Y_w\right) + C'_{w_2} \exp\left(-\frac{1}{\sqrt{2}}(1-i)Y_w\right). \tag{3.30}$$

Since the solution in the wall-layer must match the trivial solution in the bulk of the

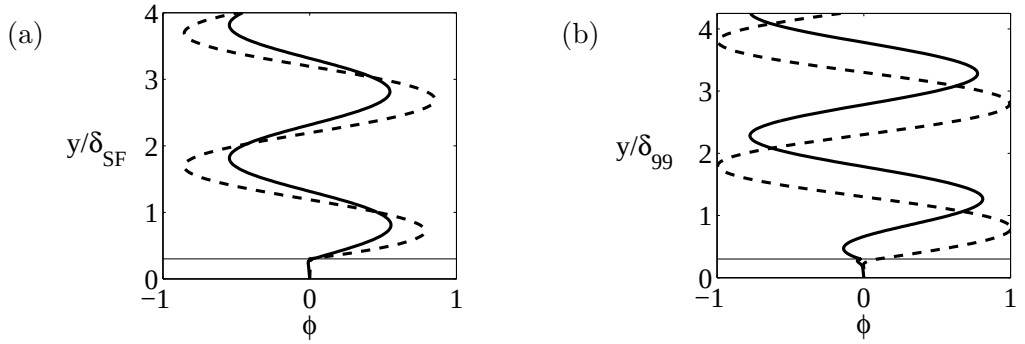


Figure 3.14: Continuous mode shape in convective shear-sheltering regime. At left, eigenfunction for a piecewise linear profile and at right,eigenfunction for a two-fluid boundary layer. ——, real component; - - -, imaginary component. $k_x Re_T = 500\pi, k_y = \pi, k_z = \pi, \delta_B = 0.3, \mu_{BT} = 0.1$.

bottom fluid, $\psi_{B_w}(Y_w \to \infty) = 0$, therefore $C'_{w_1} = 0$.

A uniformly valid approximation of the eigenfunction is sought in the bottom fluid, $Y \in [-\delta_{BL}, 0]$. The solution combines the edge, bulk, and wall-layer solutions. To leading order, the vorticity eigenfunction is given according to,

$$\psi_B = C_{e_1} Ai[z(Y)] + C'_{w_2} \exp(-\zeta(\delta_{BL} + Y)), \tag{3.31}$$

where $z(Y) = exp\,(i5\pi/6) \left(\frac{k_x \tau_B}{\nu_B}\right)^{1/3} Y$ and $\zeta = \frac{1-i}{\sqrt{2}\delta_w}$. The corresponding vertical velocity eigenfunction, in the bottom fluid, is therefore,

$$\begin{aligned} \phi_B = & \frac{C_{e_1}}{2k} \Big[exp(-kY) \int_{-\delta_{BL}}^{Y} exp(ks) Ai[z(s)] ds + \\ & \exp(kY) \int_{Y}^{0} exp(ks) Ai[z(s)] ds \Big] + \\ & C_{w_2} \exp(-\zeta(\delta_{BL} + Y)) + C_9 \exp(-kY) + C_{10} \exp(kY), \end{aligned} \tag{3.32}$$

The constants of integration form a system of algebraic equations and it is provided in appendix A.2.2.

An example of a vertical velocity eigenfunction, ϕ, which penetrates the top fluid, but is sheltered by the shear in the bottom layer is shown in figure 3.14. The behavior is consistent among the piece-wise linear and two-fluid boundary layer eigenfunctions. Figure 3.15 shows the vorticity of the same mode, ψ. In the lower fluid, there exists a three-layer structure similar to that observed in the single-fluid boundary layer.

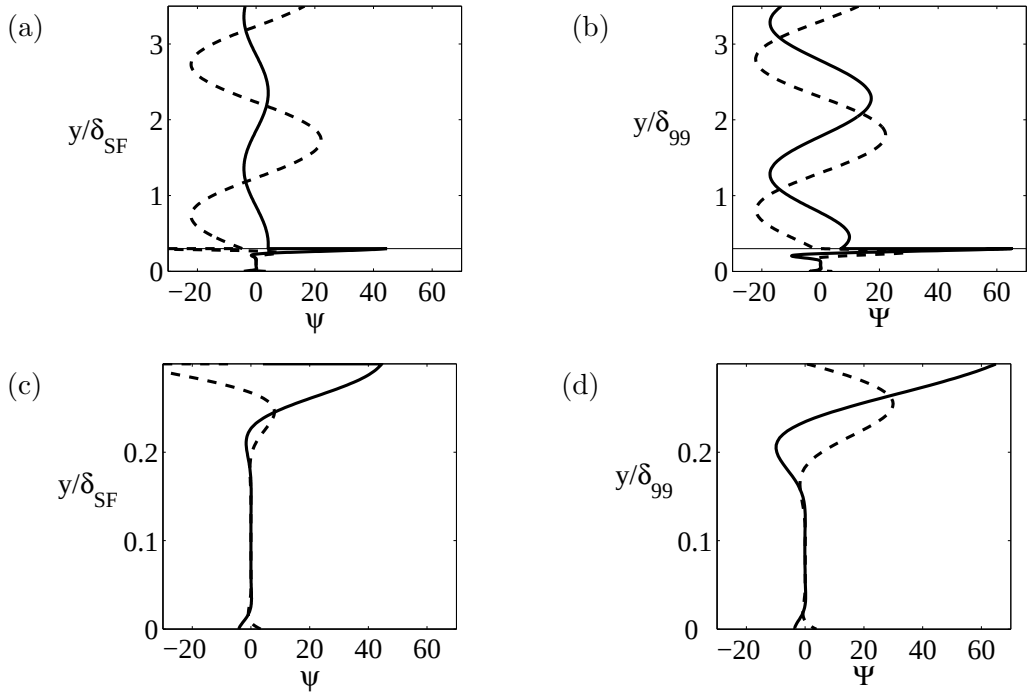


Figure 3.15: Spanwise vorticity in convective shear-sheltering regime with three layered structure. At left, eigenfunction for a piecewise linear profile and at right,eigenfunction for a two-fluid boundary layer. ——, real component; - - -, imaginary component. $k_x Re_T = 500\pi, k_y = \pi, k_z = \pi, \delta_B = 0.3, \mu_{BT} = 0.1$.

A noticeable difference between the two-fluid and the previously derived single-fluid eigenfunctions is the sharp discontinuity in ψ at the interface. This discontinuity arises due to the interface conditions, even when both fluids have equal densities and surface tension is ignored. The normal velocity eigenfunction shows that $\phi \to 0$ at the interface which implies that the interface displacement is negligible. The interface, therefore, resembles a rigid membrane which prevents free-stream vortical disturbances from entering the bottom fluid.

3.5.2 The diffusive regime

In the diffusive regime, viscous effects dominate the convective term in the vorticity equation 3.26 of the bottom fluid. Therefore, the small parameter ϵ_d is defined as the ratio of the convective to viscous terms,

$$\epsilon_d \equiv \frac{k_x(\tau_T\delta_T + \tau_B\delta_B)}{\nu_T k_y^2 + (\nu_T - \nu_B)(k_x^2 + k_z^2)} \ll 1.$$

In terms of ϵ_d, the vorticity equation 3.26 can be expressed as,

$$\frac{\nu_B}{\nu_T(k_x^2 + k_y^2 + k_z^2) - \nu_B(k_x^2 + k_z^2)} d_Y^2\psi_B + \psi_B + i\epsilon_d \frac{\tau_T\delta_T - \tau_B(Y + \delta_T)}{\tau_T\delta_T + \tau_B\delta_B}\psi_B = 0.$$

A series solution of ψ in powers of ϵ_d is assumed. The leading order term in the expansion is governed by the following equation,

$$\frac{\nu_B}{\nu_T(k_x^2 + k_y^2 + k_z^2) - \nu_B(k_x^2 + k_z^2)} d_Y^2\psi_B + \psi_B = 0, \tag{3.33}$$

and the leading order solution is, therefore,

$$\begin{aligned} \psi_B &= C_9' \exp(-i\kappa_d Y) + C_{10}' \exp(i\kappa_d Y), \\ \phi_B &= C_9 \exp(-i\kappa_d Y) + C_{10} \exp(i\kappa_d Y) + C_{11} \exp(-kY) + C_{12} \exp(kY). \end{aligned}$$

where $\kappa_d = \sqrt{\frac{\nu_T}{\nu_B}(k_x^2 + k_y^2 + k_z^2) - (k_x^2 + k_z^2)}$. The constants C_1 through C_{12} are obtained by constructing a system of equations representing the wall, free stream, and interface conditions 3.5 and solving it numerically as described in Appendix A.2.3.

In contrast to the single-fluid eigenfunctions, the two-fluid solution predicts an effective wall-normal wavenumber κ_d, which differs from the free-stream value k_y. The

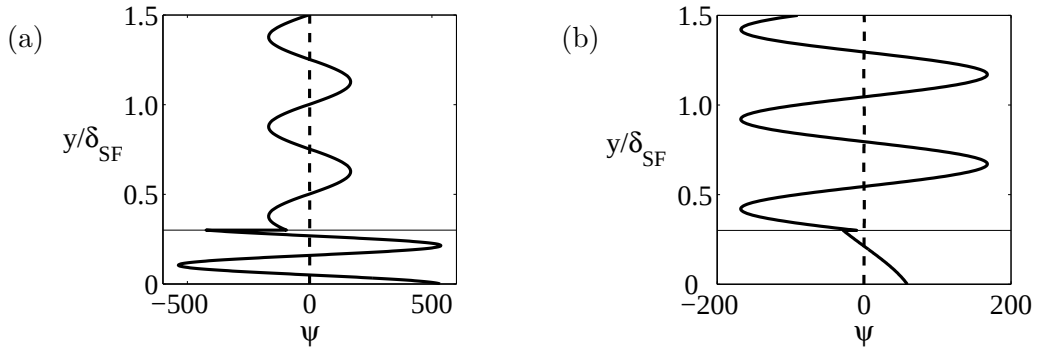


Figure 3.16: Change in nature of spanwise vorticity from oscillatory to exponential in the film at different ratios of ν_B/ν_T. ——, real component; - - -, imaginary component. $k_x Re_T = \frac{\pi}{10}, k_y = 4\pi, k_z = \pi, \delta_B = 0.3$. (a) $\nu_B/\nu_T = 0.2$. (b)$\nu_B/\nu_T = 5$.

definition of κ_d indicates that the solution changes from oscillatory to exponential behavior at a critical viscosity ratio, $(\nu_B/\nu_T)_c = (k_x^2 + k_y^2 + k_z^2)/(k_x^2 + k_z^2)$. For a viscosity ratio ν_B/ν_T lower than the critical value, an oscillatory solution is obtained; for ν_B/ν_T greater than the critical ratio, the solution is exponential. This change in the character of the solution is demonstrated in figure 3.16, where ψ is plotted at sub- and super-critical viscosity ratios.

The change in the wall-normal wavenumber, $\kappa_d \neq k_y$, is due to a mismatch in dissipation and diffusion in the streamwise and spanwise directions: The continuous mode decay rate is determined by the free-stream viscosity, and is proportional to $\nu_T \left(k_x^2 + k_z^2\right)$. In the lower fluid, however, diffusion is proportional to $\nu_B \left(k_x^2 + k_z^2\right)$. The mismatch between the modal decay rate and diffusion in the bottom fluid causes the distortion of the wall-normal wavenumber; this distortion ensures that the diffusion term in the bottom fluid O-S equation maintains the correct modal decay rate, set by the free stream.

For instance, consider a bottom fluid with lower viscosity than the free stream. The streamwise and spanwise diffusion in this layer will therefore be smaller than the free-stream values. As a result, the effective wall normal wavenumber κ_d in the bottom fluid must be greater than k_y, in order to match the free stream prescribed modal decay rate.

The change in the wall-normal wavenumber is significant in correctly explaining penetration of vortical disturbances in two-fluid boundary layer. In the single fluid problem, it was shown that modal penetration into the shear is proportional to $k_y^2 \nu / k_x \tau \delta$, where k_y^2 is a parameter, and low viscosity implies weak penetration, while higher viscosity

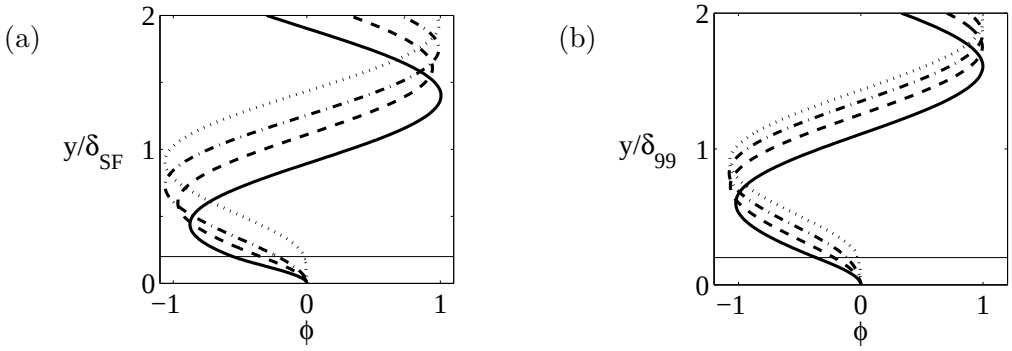


Figure 3.17: Effect of ν_{BT} on penetration of continuous modes for (a) piecewise linear profile and (b) two-fluid boundary layer. $k_x Re_T = \frac{\pi}{10}, k_y = \pi, k_z = \pi, \delta_B = 0.2$. ——, $\mu_{BT} = 0.5$; - - -, $\mu_{BT} = 1$; — · —, $\mu_{BT} = 2(\nu_{r\,crit})$; · · · ·, $\mu_{BT} = 10$.

enhances penetration. This dependence is not, however, preserved in the two-fluid problem. Instead, the expression for penetration must be updated to account for the modified wave-number, $\kappa_d^2 \nu_B / k_x \tau \delta$. A reduction of ν_B, alone, would reduce penetration. However, the associated increase in κ_d causes a net increase in penetration at lower ν_B. Conversely, an increase in ν_B and the associated reduction in κ_d cause an overall reduction in penetration, opposite to the prediction for a single-fluid shear flow. These observations are confirmed in figure 3.17 where the eigenfunction is plotted at various viscosity ratio; higher ν_B is shown to reduce modal penetration.

The thin-film solution

The effect of a thin film on continuous modes which belong to the diffusive regime is further examined in this section. It is assumed that $\kappa_d \delta_B \ll 1$ and $k\delta_B \ll 1$, so that the thickness of the film can be considered as a small parameter. Under these assumptions the vorticity equation 3.33 for the bottom fluid reduces to,

$$d_Y^2 \psi_B = 0$$

the solution to which is,

$$\psi_B = C_9^{'} + C_{10}^{'}(Y - \delta_{BL}). \tag{3.34}$$

Integrating equation 3.34 twice gives the normal velocity,

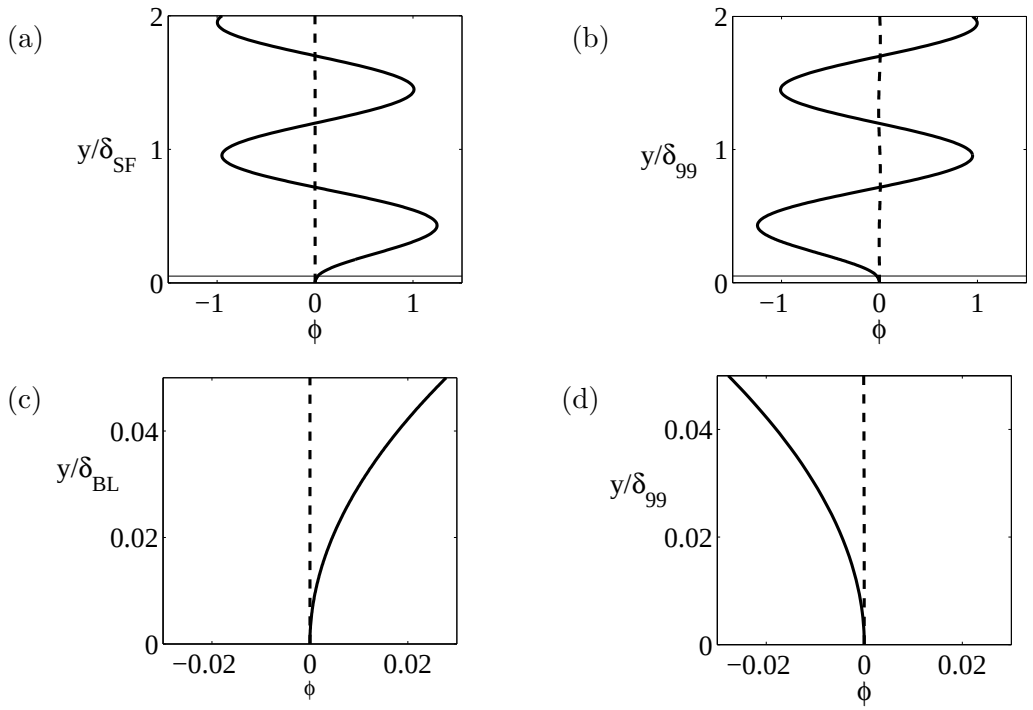


Figure 3.18: Eigenfunction ϕ, $k_x Re_T = \frac{\pi}{10}, k_y = 2\pi, k_z = \pi, \delta_B = 0.05, \mu_{BT} = 2$. At left, eigenfunction for a piecewise linear profile and at right,eigenfunction for a two-fluid boundary layer. ——, real component; - - -, imaginary component

$$\phi_B = C_{11} + C_{12}(Y + \delta_{BL}) + C_9(Y + \delta_{BL})^2 + C_{10}(Y + \delta_{BL})^3.$$

The wall boundary conditions require, $\phi_B(-\delta_{BL}) = d_Y\phi_B(-\delta_{BL}) = 0$. The constants, C_{11} and C_{12}, therefore must be zero in order to satisfy the no-slip and no-penetration conditions at the wall. Hence, the expression for normal velocity reduces to,

$$\phi_B = C_9(Y + \delta_{BL})^2 + C_{10}(Y + \delta_{BL})^3.$$

The constants C_9, C_{10} are given in appendix A.2.5 and are obtained by satisfying the interfacial matching conditions 2.10. Figure 3.18 shows a good agreement between the eigenfunction, ϕ obtained from analytical solution for the piecewise linear profile and the numerical solution for the two-fluid boundary layer profile.
The leading order solution for ψ_B is linear. The same can be observed in figure 3.19 where the vorticity is linear inside the film. A similar result was obtained by Charru & Hinch (2000), who derived asymptotic solutions of the vorticity equation for two-dimensional perturbations in Couette flow over a wavy wall. Under the long wavelength assumption (referred to as the shallow viscous regime therein), they obtained a vorticity eigenfunction which was linear. The present order of magnitude analysis reveals that the dominant term in the vorticity equation is wall normal diffusion and that the vorticity is linear. It implies that the effect of the viscous diffusion can be felt in the entire film and the convection of vorticity is negligible at the leading order.

3.5.3 The convective-diffusive regime

In this regime, both the viscous and convective terms in the vorticity equation 3.26 of the bottom fluid are of the same order,

$$\nu_T(k_x^2 + k_y^2 + k_z^2) - \nu_B(k_x^2 + k_z^2) \approx k_x\tau_B\delta_{BL}.$$

If a fully penetrating solution is assumed in the outer fluid, the above condition necessitates that τ_B is sufficiently large; here the shear is assumed to be restricted to the near-wall region and, as a result, the interface is located at $Y = 0$.

The asymptotic behavior of the solution near the interface is derived by considering

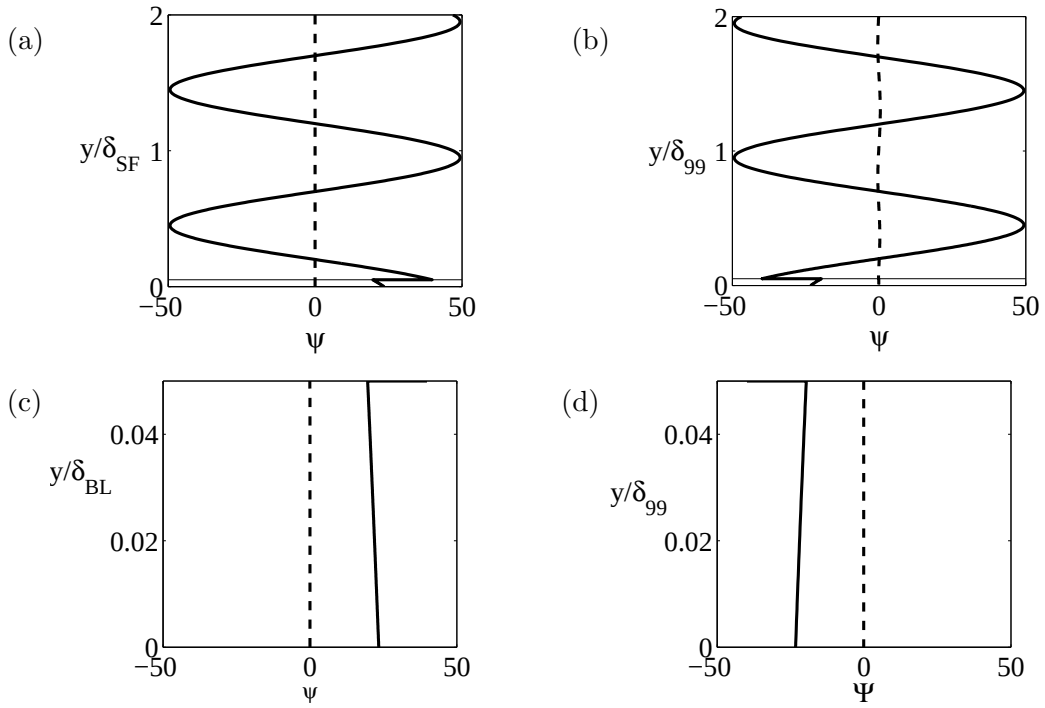


Figure 3.19: Spanwise vorticity ψ, $k_x Re_T = \frac{\pi}{10}, k_y = 2\pi, k_z = \pi, \delta_B = 0.05, \mu_{BT} = 2$. At left, eigenfunction for a piecewise linear profile and at right,eigenfunction for a two-fluid boundary layer. ——, real component; - - -, imaginary component

the limit $Y \to 0$ of the vorticity equation 3.26, which yields,

$$\nu_B \frac{d^2\psi^0_{Be}}{dY^2} + (\nu_T(k_x^2 + k_y^2 + k_z^2) - \nu_B(k_x^2 + k_z^2))\psi^0_{Be} \quad = \quad 0,$$

The solution near the interface is, therefore,

$$\psi^0_{Be} \quad = \quad \underbrace{C_{e_1} \exp(i\kappa_e Y)}_{\psi^0_{Be_1}} + \underbrace{C_{e_2} \exp(-i\kappa_e Y)}_{\psi^0_{Be_2}}, \tag{3.35}$$

where $\kappa_e = \sqrt{\frac{\nu_T}{\nu_B}(k_x^2 + k_y^2 + k_z^2) - (k_x^2 + k_z^2)}$. The effect of the shear on the wall-normal decay of the eigenfunction is not captured in this expression. Therefore, similar to the analysis of the single-fluid problem, corrections to the two linearly independent solutions $\psi^0_{Be_{\{1,2\}}}$ are sought. The governing equations for the correction terms are obtained by substituting $\psi_{Be_{\{1,2\}}} = \psi^0_{Be_{\{1,2\}}} + \psi^1_{Be_{\{1,2\}}}$ in the full vorticity equation, which yields

$$\frac{d^2\psi^1_{Be_{\{1,2\}}}}{dY^2} + \kappa_e^2 \psi^1_{Be\{1,2\}} - \frac{ik_x\tau_B Y}{\nu_B} C_{e\{1,2\}} e^{\pm i\kappa_e Y} \quad = \quad 0$$

with the homogeneous boundary conditions $\psi^1_{Be_{\{1,2\}}} = d_Y\psi^1_{Be_{\{1,2\}}} = 0$ at $Y = 0$. Analytic solutions for $\psi^1_{Be_{\{1,2\}}}$ are obtained, and the final expression for the eigenfunction near the interface is given according to,

$$\begin{aligned} \psi_{Be} = \quad & \underbrace{C_{e1}e^{i\kappa_e Y}}_{\psi^0_{Be_1}} + \quad \underbrace{C_{e1}e^{ik_e Y}\left[\frac{k_x\tau_B}{2k_e\nu_B}\left(\frac{Y^2}{2} - \frac{Y}{2i\kappa_e} - \frac{1 - e^{-2i\kappa_e Y}}{4\kappa_e^2}\right)\right]}_{\psi^1_{Be_1}} \\ & + \underbrace{C_{e2}e^{-i\kappa_e Y}}_{\psi^0_{Be_2}} + \quad \underbrace{C_{e2}e^{-ik_e Y}\left[-\frac{k_x\tau_B}{2k_e\nu_B}\left(\frac{Y^2}{2} + \frac{Y}{2i\kappa_e} - \frac{1 - e^{2i\kappa_e Y}}{4k_e^2}\right)\right]}_{\psi^1_{Be_2}} \end{aligned} \tag{3.36}$$

The constants C_{e1} and C_{e2} are calculated by enforcing continuity of ψ and its gradient at $Y = 0$ and are provided in appendix A.2.4. The above solution in the edge layer is compared to the exact analytical expression 3.27 in figure 3.20, and good quantitative agreement is observed. The wall-normal oscillation due to $\psi^0_{Be_{\{1,2\}}}$ is similar to that in the diffusive regime, at the modified wall-normal wavenumber, $\kappa_e = \kappa_d$. The decay of the solution inside the bottom fluid, away from the interface, is due to the cancellation by $\psi^1_{Be_{\{1,2\}}}$, where the influence of the shear is cumulative and increases with distance

from the interface.

In the vicinity of the wall, the behavior of ψ is described by the limit $Y \to -\delta_{BL}$ of equation 3.26 for the bottom fluid. To lowest order in y, the governing equation becomes,

$$\nu_B \frac{d^2\psi^0_{B_w}}{dY^2} + (\nu_T(k_x^2+k_y^2+k_z^2) - \nu_B(k_x^2+k_z^2) + ik_x\tau_B\delta_{BL})\psi^0_{B_w} = 0,$$

and has the solution,

$$\psi^0_{Bw} = \underbrace{C_{w_1}\exp(i\kappa_w(Y+\delta_{BL}))}_{\psi^0_{Bw_1}} + \underbrace{C_{w_2}\exp(-i\kappa_w(Y+\delta_{BL}))}_{\psi^0_{Bw_2}}, \tag{3.37}$$

where

$$\kappa_w = \sqrt{\frac{\nu_T}{\nu_B}(k_x^2+k_y^2+k_z^2) - (k_x^2+k_z^2) + i\frac{k_x\tau_B\delta_{BL}}{\nu_B}}.$$

Correction terms to ψ^0_{Bw} can be obtained using a similar procedure to the edge layer. The corrected solution in the near-wall region is therefore,

$$\begin{aligned}
\psi_{Bw} = \quad & C_{w1}e^{ik_w(Y+\delta_{BL})} + C_{w2}e^{-ik_w(Y+\delta_{BL})} \\
+ \quad & C_{w1}e^{ik_w(Y+\delta_{BL})}\left[\frac{k_x\tau_B}{2k_w\nu_B}\left(\frac{(Y+\delta_{BL})^2}{2} - \frac{(Y+\delta_{BL})}{2ik_w} - \frac{1-e^{-2ik_w(Y+\delta_{BL})}}{4k_w^2}\right)\right] \\
+ \quad & C_{w2}e^{-ik_w(Y+\delta_{BL})}\left[\frac{-k_x\tau_B}{2k_w\nu_B}\left(\frac{(Y+\delta_{BL})^2}{2} + \frac{(Y+\delta_{BL})}{2ik_w} - \frac{1-e^{2ik_w(Y+\delta_{BL})}}{4k_w^2}\right)\right].
\end{aligned}$$

The constants C_{w1} and C_{w2} are obtained by imposing wall-boundary conditions on ψ and its gradient. These constants are given in appendix A.2.4. The wall solution accurately captures the exact solution in the near wall region as shown in figure 3.20.

The complex κ_w implies that the solution is oscillatory and also decaying. The deviation of the solution from the purely oscillatory form in the edge-layer is characteristic of the convective-diffusive regime. This deviation is due to the term $k_x\tau_B\delta_{BL}/\nu_B$, which is the cumulative effect of shear sheltering over the depth of the boundary layer as discussed in the single-fluid problem and shown in figure 3.20.

It was demonstrated in the viscous regime that penetration is enhanced at low ν_B due to the modified wavenumber, $\kappa_d > k_y$. A similar effect can be observed in the convective-diffusive regime: The definition of κ_w indicates that for low ν_B modal penetration is enhanced by the modified wavenumber, $\Re(\kappa_w) > k_y$. However, the exponential decay

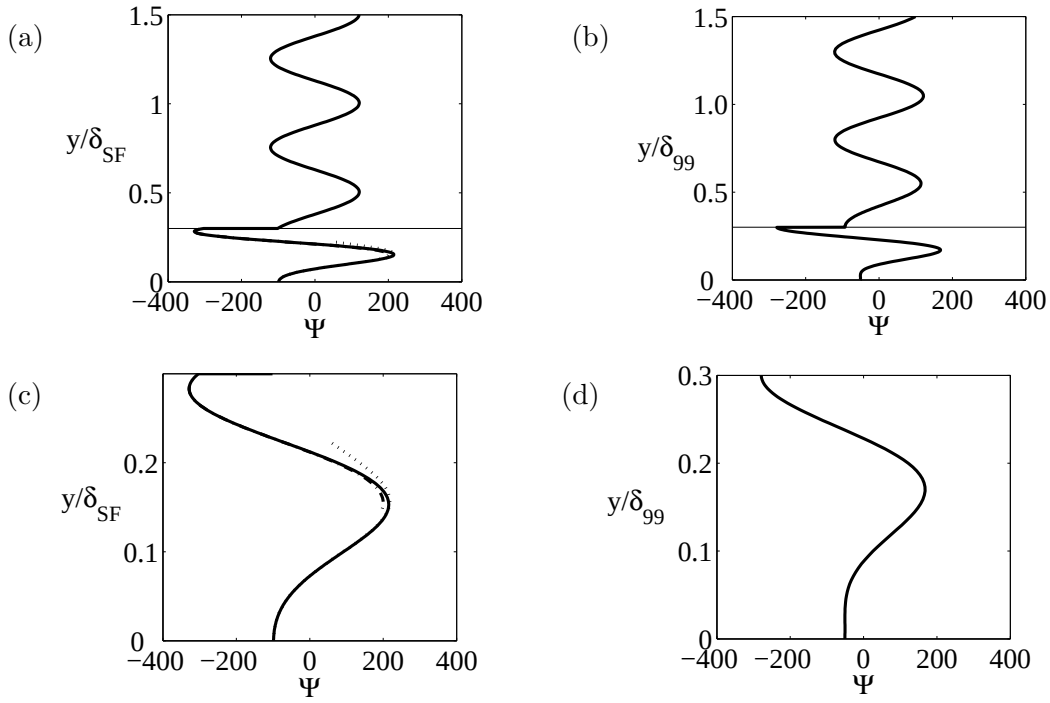


Figure 3.20: Structure of spanwise vorticity in convective-diffusive regime, showing the edge- and wall-layer solutions for piecewise linear profile. The real part of the exact analytical solution (——), the asymptotic solution in the edge-layer (— · —), and the asymptotic solution in the wall-layer (· · · ·) are compared. $k_x Re_T = 50\pi, k_y = 4\pi, k_z = \pi, \delta_B = 0.3, \mu_{BT} = 0.3$.

rate is also increased for small ν_B. Therefore, it is not clear whether a lower viscosity film enhances or reduces the penetration of the vortical disturbance into the bottom fluid. Further discussion of the dependence of penetration on viscosity ratio is therefore presented in the next section, and is explained in light of the above derived asymptotic solutions.

3.6 Discussion

In this chapter, asymptotic solutions were derived for the continuous spectrum modes of single and two-fluid boundary layers. The competition between the convective and diffusive terms in the Orr-Sommerfeld equations delineated the various possible asymptotic regimes, and a physical interpretation of shear-sheltering was provided. In the single-fluid problem, it was shown that penetration of the vortical disturbance into the boundary layer was enhanced by viscosity, and limited by the shear. The influence of

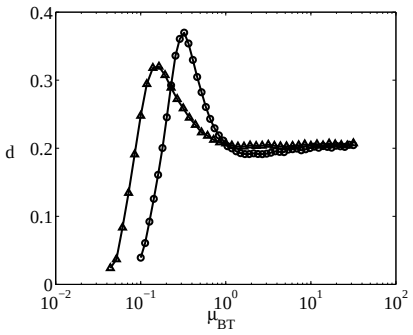


Figure 3.21: Variation of penetration depth with viscosity ratio where $k_x Re_T = \frac{1}{100}, k_y = \frac{\pi}{4}, k_z = \pi$, $\circ$ $\delta_B = 0.3$, $\triangle$ $\delta_B = 0.2$

introducing a fluid of different viscosity near the wall is complex. For instance, a low viscosity film enhances shear sheltering and, as a result, can suppress the eigenfunction in the bottom fluid. However, another competing mechanism emerges due to viscosity stratification: an increase in the *apparent* wall-normal wavenumber can result in enhanced penetration of the vortical mode at low viscosity. This competition suggests an optimal viscosity ratio exists, whereby penetration of the disturbances in the two-fluid boundary layer is maximum. The effect of viscosity and density ratio is investigated to identify whether such a ratio exists or not. The effect of viscosity ratio is examined first as it affects the mean flow, governing equation, and boundary conditions. Finally a brief note on the surface tension effects is presented at the end of this section.

3.6.1 Viscosity stratification effects

The effect of viscosity ratio on penetration depth, d, for the continuous modes of the two-fluid boundary layer is shown in figure 3.21. Indeed an optimal viscosity ratio, $\mu^\star_{BT} \equiv (\mu_B/\mu_T)^\star$, exists where d is maximum. The optimal viscosity ratio is less than unity, indicating maximum modal penetration into the shear takes place when the lower fluid is less viscous, contrary to the results from the single fluid analysis.

In the limit $\mu_{BT} \gg 1$, the bottom fluid simulates the influence of a solid wall. As a result, the penetration d asymptotes to the single fluid limit. A reduction in the viscosity of the lower fluid, $\mu^\star_{BT} < \mu_{BT} < 1$, is observed to increase penetration. Despite an expected reduction in $d \propto \mu_B$, penetration in fact increases due the modified wavenumber, $\kappa_d > k_y$, as discussed in the diffusive regime 3.5.2. Upon further reduction of μ_B, the

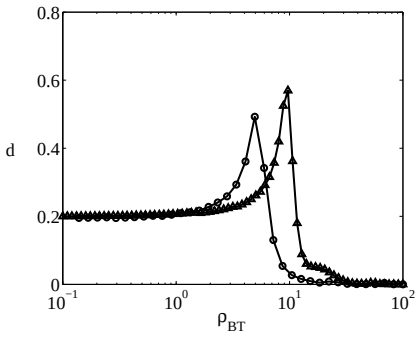


Figure 3.22: Variation of penetration depth with density ratio where $k_x Re_T = \frac{1}{100}, k_y = \frac{\pi}{4}, k_z = \pi, \mu_{BT} = 1, We^{-1} = 0$, $\circ$ $\delta_B = 0.3$, $\triangle$ $\delta_B = 0.2$

convective term becomes appreciable, and the eigenfunction falls within the convective-diffusive regime (§3.5.3). Due to shear sheltering, d decays for $\mu_{BT} < \mu^{\star}_{BT}$. The influence of the shear continues to amplify for smaller μ_{BT} ratios, and the eigenfunctions transitions into the shear-sheltered regime (§3.5.1). In this limit, the vortical modes are unable to significantly perturb the interface, which resembles a stiff membrane.

3.6.2 Density stratification

In the eigenvalue problem, the density ratio appears in the normal stress interface condition, and implicitly in the O-S equation via the kinematic viscosity. In order to isolate the effect of density, it is assumed that the dynamic viscosities of the two fluids are identical, $\mu_B = \mu_T$, and surface tension is ignored. The dependence of penetration d on density ratio, $\rho_{BT} = \rho_B/\rho_T$, is shown in figure 3.22. An optimal ratio exists, and directly corresponds to the optimal $\mu^{\star}_{BT}$. The optimal density ratio is always observed for $\rho_{BT} > 1$ which implies that heavier fluids tend to enhance penetration. Less dense fluids do not affect the penetration significantly. Since gravitational effects are not considered here, the density ratio must satisfy the assumption $|\rho_{BT} - 1| \ll U_\infty^2/(g\delta_{99})$ to ensure that gravity does not play an important role.

The first asymptotic limit in figure 3.22 is $\rho_{BT} \ll 1$. This regime corresponds to the previously considered limit of $\mu_{BT} \gg 1$ in figure 3.21. In that regime, it was shown that the bottom fluid acts as a highly viscous, or solid surface, and as a result penetration is limited to the single-fluid behavior.

In the limit of large density ratio, figure 3.22 shows that penetration d is negligible,

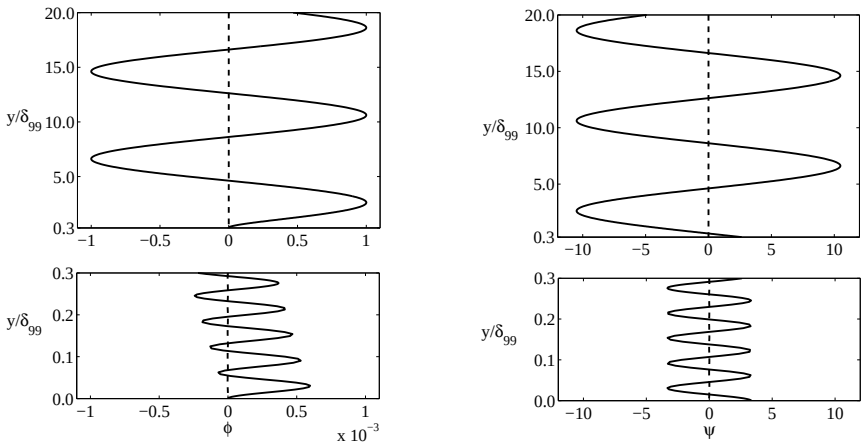


Figure 3.23: High frequency oscillations in mode shape for an extremely dense film. ——, real component; - - -, imaginary component. $k_x Re_T = 1/100, k_y = \pi/4, k_z = \pi, \delta_B = 0.3, \rho_{BT} = 1000$. Note, ϕ is plotted on separate scales in the top and bottom fluids

even for low-k_x eigenfunctions which can effectively penetrate single-fluid boundary layers. Intuitively, this is not surprising since the density of the bottom fluid is very large and expels external perturbations. An example of an eigenfunction from this limit is shown in figure 3.23. The amplitudes of both ψ and ϕ are significantly reduced across the interface. It is curious, however, that their wall-normal wavenumber increases.

An explanation can be provided from the Orr-Sommerfeld equation and the normal stress condition across the interface. In order to simplify the analysis, the low-k_x disturbances are considered where shear-sheltering is ineffective; any decay in the eigenfunction can not, therefore, be attributed to the shear. In addition, it is assumed $1/\rho_{BT} = \epsilon_R$, and therefore the equation for ψ reduces to,

$$\frac{\epsilon_R}{\delta_R^2}\frac{d^2\psi_B}{dY_R^2} + \left(\left(k_x^2 + k_y^2 + k_z^2\right) - \epsilon_R\left(k_x^2 + k_z^2\right)\right)\psi_B \quad = \quad 0,$$

where $Y_R = Y/\delta_R$. From the balance of the dominant terms, $\delta_R \sim O\left(\frac{\epsilon_R}{k_x^2+k_y^2+k_z^2}\right)^{1/2}$, and the solution to the governing equation is therefore,

$$\psi_B \quad = \quad C_1 \exp(-i\kappa_R Y) + C_2 \exp(i\kappa_R Y), \tag{3.38}$$

where $\kappa_R = \sqrt{\frac{1}{\epsilon_R}\left(k_x^2 + k_y^2 + k_z^2\right)}$. The solution exhibits an oscillation at the modified

wavenumber, $\kappa_R \gg k_y$, consistent with figure 3.23. This solution, *per se*, does not explain the reduction of the amplitude of the eigenfunction across the interface — an issue addressed by considering the normal stress condition.

In the limit of $1/\rho_{BT} = \epsilon_R$, the interface stress condition 2.10 is expressed in the form,

$$\left(k_x^2 + k_y^2 + k_z^2\right) d_Y \phi_T + \epsilon_R \left(d_Y^3 \phi_T - d_Y^3 \phi_B\right) = 0.$$

A comparison of the free-stream behavior of the eigenfunction and the solution in the bottom fluid, 3.38, shows that $(d_Y^3 \phi_T \sim k_y^3 \phi_T) \ll (d_Y^3 \phi_B \sim \kappa_R^3 \phi_B)$. Therefore, the normal stress condition can be simplified,

$$\left(k_x^2 + k_y^2 + k_z^2\right) d_Y \phi_T = \epsilon_R d_Y^3 \phi_B.$$

Assuming oscillatory solution in both the top and bottom fluids, the interface condition indicates that

$$\phi_B \sim \sqrt{\frac{\epsilon_R k_y^2}{k_x^2 + k_y^2 + k_z^2}} \phi_T,$$

which explains the reduction in the amplitude of the eigenfunction observed in figure 3.23.

3.6.3 Surface tension

Surface tension appears in the normal stress interface condition only. In order to isolate its effect, it is assumed that the density and viscosity of the two fluid are identical. Therefore, the normal stress boundary condition reduces to,

$$d_Y^3 \phi_T - d_Y^3 \phi_B = -\left(\frac{\sigma}{\nu_T}\right) k^4 f. \tag{3.39}$$

The stress condition hints to the dependence of mode shapes on surface tension; the eigenfunction is fully defined by the solution to the O-S equation. For low surface tension, $\sigma \sim \epsilon_\sigma$, the stress condition recovers the single-fluid behavior where $d_y^3 \phi$ is continuous across a "virtual" interface. In the opposite limit of large $\sigma \to \infty$, the interface deformation must tend to zero, $f \to 0$, in order to maintain boundedness in the normal stress condition. Since the interface displacement is trivial, the normal velocity

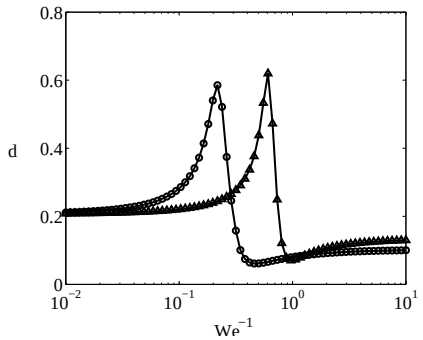


Figure 3.24: Variation of penetration depth with surface tension where $k_x Re_T = \frac{1}{100}, k_y = \frac{\pi}{4}, k_z = \pi, \mu_{BT} = 1, \rho_{BT} = 1, \circ\ \delta_B = 0.3, \triangle\ \delta_B = 0.2$

at the interface also tends to zero. This is consistent with physical intuition: at high surface tension, the interface is expected to resemble a rigid membrane which prevents any perturbation from the upper layer to penetrate into the lower fluid and vice-versa.

The limits of low and high surface tension are observed in figure 3.24 where penetration d is plotted as a function of inverse Weber number. At low surface tension, the single-fluid limit is recovered, and is common among the two curves which correspond to two different film thicknesses. In the opposite limit, $We^{-1} >> 1$, penetration is reduced below the single fluid limit. In this regime, the bottom fluid is shielded from the external vortical perturbation and, therefore, the asymptotic value of d is dependent on the film thickness. For the intermediate values of We^{-1}, a maximum is observed in the penetration depth. This observation suggests that elasticity of the interface due to surface tension constructively enforces the penetration of the free-stream vortical disturbance into the shear.

3.7 Conclusion

The penetration of free-stream vortical disturbances into single and two-fluid boundary layers was examined using analytical and asymptotic solution of the Orr-Sommerfeld equation. Three asymptotic regimes were identified, and are determined by the ratio of the diffusive to the convective terms in the vorticity equation. In the shear-sheltering regime, the oscillatory free-stream disturbances are simply convected by the outer flow, and decay exponentially at the edge of the boundary layer. In the viscous regime, the

oscillatory solution persists towards the wall. In the intermediate regime, both wall-normal diffusion and the accumulative effect of shear-sheltering with increased depth causes a gradual decay of the oscillatory eigenfunction. The analytical solutions were complemented by a physical interpretation of shear sheltering, which contrasts low- and high-frequency modes, and their ability to penetrate the shear.

The analysis of the two-fluid Orr-Sommerfeld equation was guided by findings from the single-fluid problem. The extent of penetration of vortical modes into the lower film was shown *not* to depend on the viscosity of the film *per se*, but on the viscosity ratio for the following reason: The decay rate of the continuous modes is determined by the free-stream viscosity which does not match that of the lower fluid. A modified wall-normal wavenumber, which is proportional to the viscosity ratio, therefore emerges and ensures that decay rate in the bottom layer matches that set by the free stream. Lower viscosity films caused the modified wavenumber, κ_d, to increase which in turn lead to deeper penetration. This is contrary to the single-fluid boundary layer where lower viscosities enhance shear sheltering, and hence reduce penetration of the continuous modes.

This chapter revealed that long wavelength perturbations penetrate the deepest into the boundary layer and therefore couple most effectively to the mean shear. Penetration depth of continuous modes, though a vital link between the algebraic instability and free-stream disturbances is only one factor. The linear amplification of disturbances depends also on, how effectively the normal vorticity equation is forced by the normal velocity component. For instance, the eigenfunction of the Tollmien–Schlichting wave is non-trivial inside the boundary layer and should ideally couple efficiently with the mean shear. However, the Tollmien–Schlichting wave is still unable to cause any significant short-time growth: a fact which will be better understood in the following chapter where the mechanisms driving transient amplification of disturbances are examined. Moreover, the presence of the interface can potentially alter the short-time dynamics of the system. Hence, having examined in detail the effects of the wall-bounded film on the eigenfunctions of the continuous modes, the influence on transient growth of linear perturbation is explored in the following chapter.

Chapter 4

Transient growth of linear perturbations

4.1 Introduction

The previous chapter explained how the free-stream vortical disturbances penetrate the boundary layer shear. Zaki & Durbin (2005, 2006) have shown that the penetration of free-stream normal velocity disturbances into mean shear can lead to generation of normal vorticity perturbation by a vorticity tilting mechanism. The tilting mechanism can be understood by referring to the inviscid vorticity transport equation (Panton, 1996, pp 329) which shows that vorticity can be generated by stretching or straining of vortex lines. The generation of the vorticity in this equation can also be linked to the Orr mechanism as the disturbance growth is algebraic. The linearized form of the inviscid vorticity transport equation for a parallel mean flow is (Butler & Farrell, 1992),

$$\frac{D\eta}{Dt} = -\frac{dU}{dy}\frac{\partial v}{\partial z} \tag{4.1}$$

In the present context, equation 4.1 shows that the mean flow vortex lines along the spanwise direction, $\frac{dU}{dy}$, are strained by the normal velocity perturbation, $\frac{\partial v}{\partial z}$, thereby generating a wall-normal vorticity perturbation, η.

The wall-normal vorticity generated by tilting of mean vorticity is manifested in the growth of streamwise velocity fluctuations for low frequency modes since $\eta \approx ik_z u$. These streamwise velocity fluctuations resemble the streaks observed in boundary layer transition (Zaki & Durbin, 2005) and a study of their temporal amplification indicates which perturbations are most likely to exhibit growth. The streaks observed in a boundary layer are generated by the linear vorticity tilting mechanism (Zaki & Durbin, 2005;

Trefethen *et al.*, 1993). The amplification of the streaks occurs over a time-scale much shorter than the growth of the Tollmien–Schlichting wave. Hence, the temporal evolution from specific initial conditions must be traced in order to predict streak amplification. The aim of this chapter is to:
(a) study the effect of a wall film on the transient evolution of linear perturbations, and (b) unveil the physical mechanisms governing the transient amplification of perturbations in a two-fluid boundary layer.
Though the physical problem warrants a spatial investigation as conducted by Andersson *et al.* (1999); Zaki & Durbin (2005), numerous researchers (Ellingsen & Palm, 1975; Gustavsson, 1979; Landahl, 1980; Salwen & Grosch, 1981; Butler & Farrell, 1992; Reddy & Henningson, 1993; Trefethen *et al.*, 1993; Schmid & Henningson, 2001; Schmid, 2007) have focused on the temporal counterpart to study the linear amplification mechanism as both yield similar qualitative results. Moreover, the computational cost is significantly reduced as the temporal analysis requires the solution of a linear eigenvalue problem compared to the spatial equivalent which requires the solution of a fourth order nonlinear eigenvalue problem. Indeed, the work of Lasseigne *et al.* (1999) demonstrates that the growth rates obtained from a temporal analysis match those of a spatial simulation under specific scaling laws. Therefore, the present investigation is restricted to the temporal amplification of the linear perturbations in a boundary layer.

4.1.1 The initial value problem

The work of Ellingsen & Palm (1975) and Landahl (1980) demonstrated the need to consider the evolution of linear perturbations from initial conditions. The Orr-Sommerfeld eigenvalue problem reveals only the long time stability of the system. The solution to the initial value problem describing the temporal evolution of perturbations is therefore necessary to determine the short time behavior. Investigation of the initial value problem for bounded flows by Gustavsson & Hultgren (1980); Gustavsson (1981); Benney & Gustavsson (1981) indicated that short time transient growth of perturbations could be attributed to a resonance mechanism. The authors argued that the initial value problem could be viewed as a forced response problem where the normal vorticity is driven by the normal velocity component of the perturbation. Therefore resonance between the discrete Orr-Sommerfeld and Squire eigenvalue spectra results in short time growth

of normal vorticity of the form $te^{-i\omega t}$ where ω is the resonant eigenvalue (Gustavsson & Hultgren, 1980). Eventually, at long time, $t > 1/\omega_i$, viscous dissipation present in the system overcomes the algebraic growth and thereafter the stability is governed by the leading eigenmode. However, such occurrences of direct resonance in bounded flows between Orr-Sommerfeld and Squire eigenvalues exist only for specific values of wavenumber and Reynolds number.

For semi- and un-bounded flows, the continuous spectrum of the Orr-Sommerfeld and Squire equations overlap completely and therefore infinitely many instances of resonance can occur. Zaki & Durbin (2005, 2006) studied the temporal evolution of normal vorticity forced by a continuous Orr-Sommerfeld mode in a laminar boundary layer. Their solution explicitly demonstrated that the resonant Squire mode grows as $te^{-i\omega t}$. The extent of amplification is determined by the forcing term, $-\frac{dU}{dy}\frac{\partial v}{\partial z}$, in equation 4.1, which is the coupling between normal velocity perturbation and mean shear and hence representative of the vorticity tilting mechanism. This coupling is governed by the penetration depth of the continuous Orr-Sommerfeld mode and the mean shear distribution. The effect of viscosity stratification on penetration depth was evaluated in the previous chapter. It was shown that there exists an optimum value, for which penetration of continuous modes is maximized. For viscosity ratios lower than the optimum penetration of continuous modes is inhibited due to the shear-sheltering mechanism. The mean shear distribution, on the other hand, is also affected by introduction of a thin film. Films with viscosity lower than the outer fluid absorb the mean shear due to the tangential stress continuity at the interface. As a result the shear is weaker in the top fluid and stronger inside the film. The coupling between mean shear and normal velocity fluctuations therefore depends on the viscosity ratio. Hence, the viscosity ratio of the system would affect the efficacy of the vorticity tilting mechanism in causing temporal amplification of linear perturbations.

The wall film not only alters the mean shear distribution but also introduces a jump in mean vorticity across the the interface. Hence, the displacement of the interface from its mean location also generates normal vorticity perturbations. The extent to which the displacement of the interface affects the stability of the boundary layer, must therefore be accounted for in any short time energy amplification study.

The temporal evolution of normal velocity, interface displacement and normal vorticity is obtained by solving an initial value problem. The solution to the initial value problem describes the evolution of normal velocity, interfacial deformation and normal vorticity from any given initial condition. It is demonstrated that the potency of the vorticity tilting mechanism in causing transient amplification is reduced by the introduction of low-viscosity thin wall-film. The investigation also reveals that the thin film viscosity can enhance the energy growth due to interface displacement. This mechanism is referred to as the interface deformation mechanism. Due to the opposing effect of viscosity stratification on the two mechanisms, there exists a competition which leads to an optimal viscosity ratio for minimal transient amplification.

The effectiveness of the two mechanisms depends not only on the viscosity ratio but also on the initial conditions. In order to understand which initial conditions lead to large energy amplification arising from each mechanism, the optimal disturbances are computed following Malik & Hooper (2007). In addition, the effect of viscosity stratification and film thickness is also investigated by computing the transient amplification curves.

This chapter is divided into five sections. This first section introduced the motivation for the investigation carried out in this chapter. The initial value problem that describes the evolution of a single Fourier component of a linear disturbance is formulated in section two. The solution is expanded in terms of the normal modes of the Orr-Sommerfeld and Squire equations. The coefficients of these modes are computed using the adjoint eigenfunctions. Section three examines the boundary layer response to an initial condition corresponding to a streamwise oriented vortex at different viscosity ratios. In order to construct a streamwise oriented vortex, a continuous Orr-Sommerfeld mode and the interfacial mode are excited initially (see figure 4.1). In order to evaluate the influence of the interface deformation mechanism, the asymptotic behavior of the interface mode is analyzed under the long wavelength approximation. The results indicate the presence of a critical viscosity ratio where the dominant linear mechanism for amplification changes from vorticity tilting to the interface deformation mechanism. In section four, the optimal perturbations are computed and the effects of viscosity stratification and film thickness are evaluated. The last section comprises concluding remarks on the present investigation.

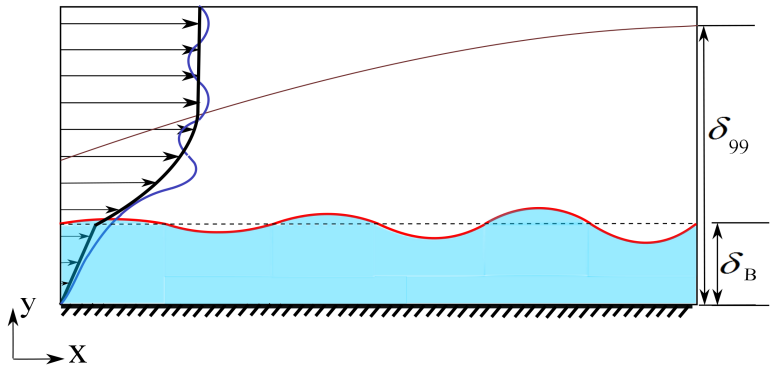


Figure 4.1: Schematic of a two-fluid boundary layer under the influence of a continuous mode and an interface mode.

4.2 The initial value problem

The physical problem of interest is the temporal evolution of an infinitesimal disturbance in a laminar, incompressible two-fluid boundary layer. Under the parallel mean flow approximation, the system of equations governing the evolution of a linear perturbation is,

$$\frac{\partial}{\partial t}\begin{bmatrix}\nabla^2 v_j \\ \mathrm{f} \\ \eta_j\end{bmatrix} = \begin{bmatrix} d_y^2 U_j \frac{\partial}{\partial x} + \nu_j \nabla^4 - U_j \frac{\partial}{\partial x}\nabla^2 & 0 & 0 \\ \mathcal{C}_v & -U(y_f)\frac{\partial}{\partial x} & 0 \\ d_y U_j \frac{\partial}{\partial z} & 0 & \nu_j \nabla^2 \eta - U_j \frac{\partial}{\partial x} \end{bmatrix} \begin{bmatrix} v_j \\ \mathrm{f} \\ \eta_j \end{bmatrix}$$

where, $\mathcal{C}_v v \equiv v(y_f)$.

No-slip and no-penetration boundary conditions are imposed at the wall. Homogeneous boundary conditions are imposed on v, $\frac{\partial v}{\partial y}$ and η in the free-stream (see conditions 2.9). In addition, continuity of velocity and stresses is applied at the interface as shown in 2.6.

In order to solve the set of coupled partial differential equations, the Fourier transform is introduced in the streamwise and the spanwise directions. The dependent variables can be expressed as,

$$\begin{aligned} v_{j,\vec{k}}(y,t) &= \int_{-\infty}^{\infty}\int_{-\infty}^{\infty} v_j(\vec{x},t)e^{-ik_x x}e^{-ik_z z}dxdz \\ f_{\vec{k}}(t) &= \int_{-\infty}^{\infty}\int_{-\infty}^{\infty} \mathrm{f}(x,z,t)e^{-ik_x x}e^{-ik_z z}dxdz \\ \eta_{j,\vec{k}}(y,t) &= \int_{-\infty}^{\infty}\int_{-\infty}^{\infty} \eta_j(\vec{x},t)e^{-ik_x x}e^{-ik_z z}dxdz \end{aligned}$$

The system of equations which governs the evolution of a Fourier component with wavenumber $\vec{k} \equiv (k_x, k_z)$ is,

$$\frac{\partial}{\partial t}\begin{bmatrix} \nabla^2 v_{j,\vec{k}} \\ f_{\vec{k}} \\ \eta_{j,\vec{k}} \end{bmatrix} = \begin{bmatrix} \mathscr{L}_j & 0 & 0 \\ \mathscr{C}_v & \mathscr{I} & 0 \\ \mathscr{C}_j & 0 & \mathscr{S}_j \end{bmatrix} \begin{bmatrix} v_{j,\vec{k}} \\ f_{\vec{k}} \\ \eta_{j,\vec{k}} \end{bmatrix} \tag{4.2}$$

with the Fourier transformed operators, $\mathscr{L}_j, \mathscr{I}, \mathscr{C}_v, \mathscr{C}_j, \mathscr{S}_j$ defined as,

$$\begin{aligned} \mathscr{L}_j v_{j,\vec{k}} &\equiv ik_x\partial_y^2 U_j v_{j,\vec{k}} + \nu_j(\partial_y^2 - k^2)^2 v_{j,\vec{k}} - ik_x U_j(\partial_y^2 - k^2)v_{j,\vec{k}} \\ \mathscr{C}_v v_{\vec{k}} &\equiv v_{\vec{k}}(y_f) \\ \mathscr{I} f_{\vec{k}} &\equiv -ik_x U(y_f) \\ \mathscr{C}_j v_{j,\vec{k}} &\equiv ik_z \partial_y U_j \\ \mathscr{S}_j \eta_{j,\vec{k}} &\equiv \nu_j(\partial_y^2 - k^2)\eta_{j,\vec{k}} - ik_x U_j \eta_{j,\vec{k}}. \end{aligned}$$

The boundary conditions at the wall and in the free-stream in Fourier space are as follows,

$$\begin{aligned} v_{B,\vec{k}} = 0; \quad \partial_y v_{B,\vec{k}} = 0; \quad \eta_{B,\vec{k}} = 0; \ y = 0 \\ v_{T,\vec{k}} = 0; \quad \partial_y v_{T,\vec{k}} = 0; \quad \eta_{T,\vec{k}} = 0; \ y \to \infty \end{aligned}$$

and the matching conditions at the interface $y = y_f$ are,

$$[v_{\vec{k}}] = 0; \quad [\partial_y v_{\vec{k}}] = ik_x[d_y U]f_{\vec{k}}; \quad [\mu(\partial_y^2 + k^2)v_{\vec{k}}] = ik_x[\mu d_y^2 U]f_{\vec{k}};$$

$$\left[\rho\Big(- i\omega\partial_y v_{\vec{k}} + ik_x(U\partial_y v_{\vec{k}} - v_{\vec{k}} d_y U) - \nu(\partial_y^3 - 3k^2\partial_y)v_{\vec{k}}\Big)\right] = \sigma k^4 f_{\vec{k}}.$$

In order to solve the initial boundary value problem, the eigenfunctions of the Orr-Sommerfeld, interface and Squire equations discussed in section 2.3 are used. The use of eigenfunctions to solve the initial boundary value problem is motivated by the fact that each eigenfunction satisfies equation 4.2 along with the boundary conditions.

4.2.1 The evolution of normal velocity and interface disturbance

For semi-bounded domains, the eigenspectra of the Orr-Sommerfeld and Squire equations consist of a finite number of discrete modes and a continuous spectrum. The corresponding eigenfunctions form a complete basis for a single fluid boundary layer (Salwen & Grosch, 1981). In this section the completeness of the Orr-Sommerfeld and Squire eigenfunctions is assumed in order to describe the evolution of the perturbation field due to a specific initial condition. However, the solution derived here is general and can be extended to any arbitrary initial condition.

A normal velocity perturbation forces the Squire equation and generates normal vorticity by tilting of mean vorticity. In addition, the interfacial boundary conditions also force the Squire equation for two-fluid flows. The normal vorticity however, does not affect the evolution of either the normal velocity perturbation or the interfacial displacement. The one way coupling present in the system of equations (4.2) allows a convenient splitting into two individual initial value problems. Hence, the evolution of the normal velocity perturbation and interfacial displacement can be obtained independent of normal vorticity disturbance. The evolution of normal vorticity can then be obtained, as the response to the forcing due to normal velocity and interfacial displacement.

The normal velocity and the interface equations form a homogeneous sub-system which is not affected by the normal vorticity and is therefore solved first. The homogeneous sub-system of equations is as follows,

$$\frac{\partial}{\partial t}\begin{bmatrix}\nabla^2 v_{j,\vec{k}}(y,t)\\ f_{\vec{k}}(t)\end{bmatrix} = \begin{bmatrix}\mathscr{L}_j & 0\\ \mathscr{C}_v & \mathscr{I}\end{bmatrix}\begin{bmatrix}v_{j,\vec{k}}(y,t)\\ f_{\vec{k}}(t)\end{bmatrix} \tag{4.3}$$

The solution is expanded in terms of the eigenfunctions of the sub-system for a given

wavenumber vector $\vec{k}$.

$$\begin{bmatrix} v_{\vec{k}}(y,t) \\ f_{\vec{k}}(t) \end{bmatrix} = \sum_{n=1}^{Nos_{\vec{k}}} a_{\vec{k},n}(t) \begin{bmatrix} \phi_{\vec{k},n}(y) \\ f_{\vec{k},n} \end{bmatrix} + \int_{k_y} a_{\vec{k},k_y}(t) \begin{bmatrix} \phi_{\vec{k},k_y}(y) \\ f_{\vec{k},k_y} \end{bmatrix} dk_y. \tag{4.4}$$

The summation is performed over all the discrete modes (the number of discrete modes equals $Nos_{\vec{k}}$) and an integration is performed over the continuous spectrum.

In order to derive the amplitude functions, $a_{\vec{k},n}, a_{\vec{k},k_y}$ in equation 4.4, Salwen & Grosch (1981) used the eigenfunctions of the adjoint Orr-Sommerfeld equation. The adjoint Orr-Sommerfeld eigenfunctions, $\begin{bmatrix} \phi^\dagger \\ f^\dagger \end{bmatrix}$, satisfy the following bi-orthogonality condition (see appendix D for the derivation of adjoint problem and the definition of the bi-orthogonality condition D.14),

$$\begin{aligned} \left\langle \begin{bmatrix} \phi^\dagger_{\vec{k},m} \\ f^\dagger_{\vec{k},m}\delta(y-y_f) \end{bmatrix}, \begin{bmatrix} \rho(d_y^2-k^2) & 0 \\ 0 & 1 \end{bmatrix} \begin{bmatrix} \phi_{\vec{k},n} \\ f_{\vec{k},n} \end{bmatrix} \right\rangle &= \delta_{mn} \\ \left\langle \begin{bmatrix} \phi^\dagger_{\vec{k},k_y'} \\ f^\dagger_{\vec{k},k_y'}\delta(y-y_f) \end{bmatrix}, \begin{bmatrix} \rho(d_y^2-k^2) & 0 \\ 0 & 1 \end{bmatrix} \begin{bmatrix} \phi_{\vec{k},k_y} \\ f_{\vec{k},k_y'} \end{bmatrix} \right\rangle &= \delta(k_y-k_y') \end{aligned} \tag{4.5}$$

where, $\langle X, Y\rangle \equiv \int_0^\infty X^* Y dy$ and $\dagger, *$ denote the adjoint variable and the conjugate transpose respectively. The inner product between the bi-orthogonality condition (4.5) and equation 4.4 leads to

$$\begin{aligned} a_{\vec{k},n}(t) &= \left\langle \begin{bmatrix} \phi^\dagger_{\vec{k},n} \\ f^\dagger_{\vec{k},n}\delta(y-y_f) \end{bmatrix}, \begin{bmatrix} \rho(\partial_y^2-k^2) & 0 \\ 0 & 1 \end{bmatrix} \begin{bmatrix} v_{\vec{k}}(y,t) \\ f_{\vec{k}}(t) \end{bmatrix} \right\rangle \\ a_{\vec{k},k_y}(t) &= \left\langle \begin{bmatrix} \phi^\dagger_{\vec{k},k_y} \\ f^\dagger_{\vec{k},k_y}\delta(y-y_f) \end{bmatrix}, \begin{bmatrix} \rho(\partial_y^2-k^2) & 0 \\ 0 & 1 \end{bmatrix} \begin{bmatrix} v_{\vec{k}}(y,t) \\ f_{\vec{k}}(t) \end{bmatrix} \right\rangle. \end{aligned} \tag{4.6}$$

Substituting equation 4.4 into 4.3 and using the bi-orthogonality condition (4.5) yields

the following ordinary differential equations for the expansion coefficients,

$$\begin{aligned}
\frac{d}{dt}a_{\vec{k},n}(t) &= \left\langle \begin{bmatrix} \phi^{\dagger}_{\vec{k},n} \\ f^{\dagger}_{\vec{k},n}\delta(y-y_f) \end{bmatrix}, \begin{bmatrix} \rho\mathscr{L}_j & 0 \\ \mathscr{C}_v & \mathscr{I} \end{bmatrix} \begin{bmatrix} v_{\vec{k}}(y,t) \\ f_{\vec{k}}(t) \end{bmatrix} \right\rangle \\
\frac{d}{dt}a_{\vec{k},k_y}(t) &= \left\langle \begin{bmatrix} \phi^{\dagger}_{\vec{k},k_y} \\ f^{\dagger}_{\vec{k},k_y}\delta(y-y_f) \end{bmatrix}, \begin{bmatrix} \rho\mathscr{L}_j & 0 \\ \mathscr{C}_v & \mathscr{I} \end{bmatrix} \begin{bmatrix} v_{\vec{k}}(y,t) \\ f_{\vec{k}}(t) \end{bmatrix} \right\rangle.
\end{aligned}$$

Using equation 4.4 to replace $\begin{bmatrix} v_{\vec{k}}(y,t) \\ f_{\vec{k}}(t) \end{bmatrix}$ and then applying equations 4.5 and 4.6 reduces the ordinary differential equations to,

$$\begin{aligned}
\frac{d}{dt}a_{\vec{k},n}(t) &= -i\omega_{\vec{k},n}a_{\vec{k},n}(t) \\
\frac{d}{dt}a_{\vec{k},k_y}(t) &= -i\omega_{\vec{k},n}a_{\vec{k},k_y}(t).
\end{aligned}$$

Finally, the expansion coefficients can be expressed as,

$$\begin{aligned}
a_{\vec{k},n} &= \left\langle \begin{bmatrix} \phi^{\dagger}_{\vec{k},n} \\ f^{\dagger}_{\vec{k},n}\delta(y-y_f) \end{bmatrix}, \begin{bmatrix} \rho(d_y^2-k^2) & 0 \\ 0 & 1 \end{bmatrix} \begin{bmatrix} v_{\vec{k}}(y,0) \\ f_{\vec{k}}(0) \end{bmatrix} \right\rangle e^{-i\omega_{\vec{k},n}t} \\
a_{\vec{k},k_y} &= \left\langle \begin{bmatrix} \phi^{\dagger}_{\vec{k},k_y} \\ f^{\dagger}_{\vec{k},k_y}\delta(y-y_f) \end{bmatrix}, \begin{bmatrix} \rho(d_y^2-k^2) & 0 \\ 0 & 1 \end{bmatrix} \begin{bmatrix} v_{\vec{k}}(y,0) \\ f_{\vec{k}}(0) \end{bmatrix} \right\rangle e^{-i\omega_{\vec{k},k_y}t}
\end{aligned}$$

The initial condition on normal velocity must be specified before the forced Squire response can be solved. A normal velocity disturbance in general consists of a superposition of Orr-Sommerfeld modes. Here, the focus is on the normal vorticity due to a particular Orr-Sommerfeld mode. The general case of Squire response to a spectrum of Orr-Sommerfeld eigenfunction can then be found by superposing all the individual solutions. Therefore, for the initial condition, a particular Orr-Sommerfeld mode, $\omega_{\vec{k},\tilde{k}_y}$, is prescribed,

$$a_{\vec{k},n}(0) = 0; \quad a_{\vec{k},k_y}(0) = A\delta(k_y - \tilde{k}_y)$$

where, A is the initial amplitude of the normal velocity perturbation. Therefore the

vertical velocity and interface height are,

$$\begin{bmatrix} v_{j,\vec{k}} \\ f_{\vec{k}} \end{bmatrix} = A \begin{bmatrix} \phi_{j,\vec{k},\tilde{k}_y} \\ f_{\vec{k},\tilde{k}_y} \end{bmatrix} e^{-i\omega_{\vec{k},\tilde{k}_y} t} \tag{4.7}$$

In the next subsection the solution to the initial value problem for the evolution of normal vorticity perturbation is derived. It is assumed that the normal vorticity perturbation is forced by a continuous Orr-Sommerfeld mode with frequency $\omega_{\vec{k},\tilde{k}_y}$. The solution for the case of forcing due to any discrete mode (including the interface mode) can be obtained by merely replacing the subscript $\tilde{k}_y$ by n.

4.2.2 The evolution of normal vorticity perturbation

Zaki & Durbin (2005) proposed the solution to the forced Squire equation for a single-fluid boundary layer, in terms of the eigenfunctions of the Squire modes. The Squire modes, χ^H, satisfy the homogeneous Squire equation,

$$(-i\omega + ik_x U_j)(d_y^2 - k^2)\chi_j^H - \nu_j(d_y^2 - k^2)\chi_j^H = 0, \tag{4.8}$$

and homogeneous interfacial conditions,

$$\begin{aligned} \chi_T^H - \chi_B^H &= 0, \\ \mu_T d_y \chi_T^H - \mu_B d_y \chi_B^H &= 0, \end{aligned}$$

since there is neither any normal velocity nor any interface displacement associated with Squire modes. For a two-fluid boundary layer the normal vorticity is discontinuous across the interface and needs to satisfy the following interfacial jump conditions,

$$[\eta_{\vec{k}}] = -ik_z[d_y U]f_{\vec{k}} \quad ; \quad [\mu\partial_y\eta_{\vec{k}}] = -ik_z[\mu d_y^2 U]f_{\vec{k}} \tag{4.9}$$

However, the homogeneous Squire eigenfunctions are continuous across the interface and the discontinuous normal vorticity cannot be expressed as a summation of homogeneous Squire eigenfunctions. In order to satisfy the jump conditions implicitly, a

continuous function, Ψ, is defined where,

$$\Psi_{j,\vec{k}}(y,t) \equiv \eta_{j,\vec{k}}(y,t) + ik_z d_y U_j f_{\vec{k}}(t) g(y). \tag{4.10}$$

The function $g(y)$ must be continuous and differentiable over the interval $[0,\infty)$ in order for Ψ to be continuous and satisfy the interfacial jump conditions. Moreover, $g(y)$ should equal unity at the interface and zero at the wall. The choice of $g(y)$ does not affect our results and any $g(y)$ which satisfies the above conditions can serve the purpose of solving the initial value problem. In this particular case, $g(y) = \frac{y}{y_f} e^{y_f - y}$ is used. Thus the interfacial boundary conditions on Ψ are identical to those on χ^H,

$$[\Psi_{\vec{k}}] = 0 \quad ; \quad [\mu \partial_y \Psi_{\vec{k}}] = 0 \tag{4.11}$$

The equation governing Ψ can be derived by substituting equation 4.10 into the Squire equation,

$$\frac{\partial}{\partial t}\Psi_{j,\vec{k}} - \mathscr{S}_j \Psi_{j,\vec{k}} \;\; = \;\; \mathscr{F}_j e^{-i\omega_{\vec{k},\tilde{k}_y} t}, \tag{4.12}$$

where the forcing term $\mathscr{F}_j$ is,

$$\begin{aligned} \mathscr{F}_j = \;\; -ik_z A \Bigg[\;\; & d_y U_j \Big(\phi_{j,\vec{k},\tilde{k}_y}(y) - \phi_{j,\vec{k},\tilde{k}_y}(y_f) g(y) \Big) \\ & + \nu_j \left(d_y^2 - k^2 \right) \Big(d_y U_j g(y) \Big) f_{\vec{k},\tilde{k}_y} \Bigg] \end{aligned}$$

Following Zaki & Durbin (2005) Ψ is expanded in terms of the homogeneous Squire eigenfunctions,

$$\Psi_{\vec{k}}(y,t) = \sum_{m=1}^{Nsq_{\vec{k}}} b_{\vec{k},m}(t) \chi^H_{\vec{k},m}(y) + \int_{k_y} b_{\vec{k},k_y}(t) \chi^H_{\vec{k},k_y}(y) dk_y. \tag{4.13}$$

The amplitude functions, $b_{\vec{k},m}(t), b_{\vec{k},k_y}(t)$, can be derived using the biorthogonality condition satisfied by the adjoint Squire eigenfunctions, $\chi^{H\dagger}$, (see Appendix E for the derivation of the adjoint Squire eigenfunctions and the biorthogonality condition E.14),

$$\langle \chi^{H\dagger}_{\vec{k},m}, \rho \chi^H_{\vec{k},n} \rangle = \delta_{mn} \quad ; \quad \langle \chi^{H\dagger}_{\vec{k},k'_y}, \rho \chi^H_{\vec{k},k_y} \rangle = \delta(k_y - k'_y). \tag{4.14}$$

The inner product of the adjoint eigenfunctions with expansion 4.13 yields the amplitude functions,

$$\begin{aligned} b_{\vec{k},m}(t) &= \langle \chi^{H\dagger}_{\vec{k},m}, \rho\Psi_{\vec{k}}(y,t)\rangle \\ b_{\vec{k},k_y}(t) &= \langle \chi^{H\dagger}_{\vec{k},k_y}, \rho\Psi_{\vec{k}}(y,t)\rangle \end{aligned} \tag{4.15}$$

Substituting in the expansion 4.13 into equation 4.12 and using conditions 4.14, leads to,

$$\begin{aligned} \frac{d}{dt}b_{\vec{k},m}(t) &= \langle \chi^{H\dagger}_{\vec{k},m}, \rho\mathscr{S}_j\Psi_{\vec{k}}(y,t)\rangle + \langle \chi^{H\dagger}_{\vec{k},m}, \rho\mathscr{F}_j\rangle e^{-i\omega_{\vec{k},\tilde{k}_y}t} \\ \frac{d}{dt}b_{\vec{k},k_y}(t) &= \langle \chi^{H\dagger}_{\vec{k},k_y}, \rho\mathscr{S}_j\Psi_{\vec{k}}(y,t)\rangle + \langle \chi^{H\dagger}_{\vec{k},k_y}, \rho\mathscr{F}_j\rangle e^{-i\omega_{\vec{k},\tilde{k}_y}t} \end{aligned}$$

Using the expansion 4.13 to replace Ψ and then applying condition 4.15,

$$\begin{aligned} \frac{d}{dt}b_{\vec{k},m}(t) &= -i\omega_{\vec{k},n}b_{\vec{k},n}(t) + \langle \chi^{H\dagger}_{\vec{k},m}, \rho\mathscr{F}_j\rangle e^{-i\omega_{\vec{k},\tilde{k}_y}t} \\ \frac{d}{dt}b_{\vec{k},k_y}(t) &= -i\omega_{\vec{k},k_y}b_{\vec{k},k_y}(t) + \langle \chi^{H\dagger}_{\vec{k},k_y}, \rho\mathscr{F}_j\rangle e^{-i\omega_{\vec{k},\tilde{k}_y}t} \end{aligned} \tag{4.16}$$

Equation 4.16 is a first order ordinary differential equation and can be solved analytically for the amplitude functions,

$$b_{\vec{k},m}(t) = b_{\vec{k},m}(0)e^{-i\omega_{\vec{k},m}t} - \langle \chi^{H\dagger}_{\vec{k},m}, \rho\mathscr{F}_j\rangle \left[\frac{e^{-i\omega_{\vec{k},\tilde{k}_y}t} - e^{-i\omega_{\vec{k},m}t}}{i\omega_{\vec{k},\tilde{k}_y} - i\omega_{\vec{k},m}}\right] \tag{4.17}$$

Since the continuous spectrum of the Squire and the Orr-Sommerfeld equations overlap, there exists a continuous Squire mode which resonates with the forcing Orr-Sommerfeld mode. Therefore, for non-resonant Squire modes $k_y \neq \tilde{k}_y$

$$b_{\vec{k},k_y}(t) = b_{\vec{k},k_y}(0)e^{-i\omega_{\vec{k},k_y}t} - \langle \chi^{H\dagger}_{\vec{k},k_y}, \rho\mathscr{F}_j\rangle \left[\frac{e^{-i\omega_{\vec{k},\tilde{k}_y}t} - e^{-i\omega_{\vec{k},k_y}t}}{i\omega_{\vec{k},\tilde{k}_y} - i\omega_{\vec{k},k_y}}\right] \tag{4.18}$$

and for the resonant mode, $k_y = \tilde{k}_y$, the expression 4.18 reduces to

$$b_{\vec{k},k_y}(t) = b_{\vec{k},k_y}(0)e^{-i\omega_{\vec{k},k_y}t} - \langle \chi^{H\dagger}_{\vec{k},k_y}, \rho\mathscr{F}_j\rangle t\left[e^{-i\omega_{\vec{k},\tilde{k}_y}t}\right] \tag{4.19}$$

The normal vorticity η can be obtained from Ψ using equation 4.10. A summary of the

entire solution to the initial value problem is presented in the following subsection in order to highlight the key steps.

4.2.3 Summary of the solution to the initial value problem

The initial value problem involving v, f and η was decomposed into two distinct initial value problems. In the first problem, the temporal evolution of v and f was obtained. The second problem described the evolution of normal vorticity forced by v and f. The system of equations governing the first problem is,

$$\frac{\partial}{\partial t}\begin{bmatrix}\nabla^2 v_{j,\vec{k}}\\ f_{\vec{k}}\end{bmatrix} = \begin{bmatrix}\mathscr{L}_j & 0\\ \mathscr{C}_v & \mathscr{I}\end{bmatrix}\begin{bmatrix}v_{j,\vec{k}}\\ f_{\vec{k}}\end{bmatrix}$$

In order to obtain the solution to the initial value problem it was assumed that the eigenfunctions of the Orr-Sommerfeld and the interface equations form a complete basis. The solution is therefore written as,

$$\begin{bmatrix}v_{\vec{k}}\\ f_{\vec{k}}\end{bmatrix} = \sum_{n=1}^{Nos_{\vec{k}}} a_{\vec{k},n}(t)\begin{bmatrix}\phi_{\vec{k},n}(y)\\ f_{\vec{k},n}\end{bmatrix} + \int_{k_y} a_{\vec{k},k_y}(t)\begin{bmatrix}\phi_{\vec{k},k_y}(y)\\ f_{\vec{k},k_y}\end{bmatrix} dk_y.$$

where,

$$a_{\vec{k},n} = \left\langle \begin{bmatrix}\phi^{\dagger}_{\vec{k},n}\\ f^{\dagger}_{\vec{k},n}\delta(y-y_f)\end{bmatrix}, \begin{bmatrix}\rho(d_y^2-k^2) & 0\\ 0 & 1\end{bmatrix}\begin{bmatrix}v_{\vec{k}}(y,0)\\ f_{\vec{k}}(0)\end{bmatrix}\right\rangle e^{-i\omega_{\vec{k},n}t}$$

$$a_{\vec{k},k_y} = \left\langle \begin{bmatrix}\phi^{\dagger}_{\vec{k},k_y}\\ f^{\dagger}_{\vec{k},k_y}\delta(y-y_f)\end{bmatrix}, \begin{bmatrix}\rho(d_y^2-k^2) & 0\\ 0 & 1\end{bmatrix}\begin{bmatrix}v_{\vec{k}}(y,0)\\ f_{\vec{k}}(0)\end{bmatrix}\right\rangle e^{-i\omega_{\vec{k},k_y}t}$$

In order to solve the forced normal vorticity equation, a particular continuous Orr-Sommerfeld mode is prescribed as the forcing function,

$$\begin{bmatrix}v_{j,\vec{k}}\\ f_{\vec{k}}\end{bmatrix} = A\begin{bmatrix}\phi_{j,\vec{k},\tilde{k}_y}\\ f_{\vec{k},\tilde{k}_y}\end{bmatrix} e^{-i\omega_{\vec{k},\tilde{k}_y}t}$$

Since the normal vorticity equation is forced at the interface, a variable $\Psi_{j,\vec{k}}(y,t) \equiv \eta_{j,\vec{k}}(y,t) + ik_z d_y U_j f_{\vec{k}}(t) g(y)$ was defined to homogenize the interfacial boundary condition. The equation governing the evolution of Ψ is,

$$\frac{\partial}{\partial t}\Psi_{j,\vec{k}} - \mathscr{S}_j \Psi_{j,\vec{k}} = \mathscr{F}_j e^{-i\omega_{\vec{k},\tilde{k}_y} t},$$

The variable Ψ was expanded in terms of the homogeneous Squire eigenfunctions,

$$\Psi_{\vec{k}} = \sum_{m=1}^{Nsq_{\vec{k}}} b_{\vec{k},m}(t)\chi_{\vec{k},m}(y) + \int_{k_y} b_{\vec{k},k_y}(t)\chi_{\vec{k},k_y}(y)dk_y.$$

where,

$$\begin{aligned}
b_{\vec{k},m}(t) &= b_{\vec{k},m}(0)e^{-i\omega_{\vec{k},m}t} - \langle \chi^{\dagger}_{\vec{k},m}, \rho\mathscr{F}_j\rangle \left[\frac{e^{-i\omega_{\vec{k},\tilde{k}_y}t} - e^{-i\omega_{\vec{k},m}t}}{i\omega_{\vec{k},\tilde{k}_y} - i\omega_{\vec{k},m}}\right] \\
b_{\vec{k},k_y}(t) &= b_{\vec{k},k_y}(0)e^{-i\omega_{\vec{k},k_y}t} - \langle \chi^{\dagger}_{\vec{k},k_y}, \rho\mathscr{F}_j\rangle \left[\frac{e^{-i\omega_{\vec{k},\tilde{k}_y}t} - e^{-i\omega_{\vec{k},k_y}t}}{i\omega_{\vec{k},\tilde{k}_y} - i\omega_{\vec{k},k_y}}\right]; \; k_y \neq \tilde{k}_y \\
b_{\vec{k},k_y}(t) &= b_{\vec{k},k_y}(0)e^{-i\omega_{\vec{k},k_y}t} - \langle \chi^{\dagger}_{\vec{k},k_y}, \rho\mathscr{F}_j\rangle t \left[e^{-i\omega_{\vec{k},\tilde{k}_y}t}\right]; \qquad k_y = \tilde{k}_y
\end{aligned}$$

4.3 The amplification of linear disturbances

4.3.1 The single-fluid boundary layer

The results for a single fluid boundary layer are introduced first in order to explain the mechanism of vorticity tilting. A streamwise oriented vortex is prescribed as the initial condition, since it is the optimal disturbance in shear flows (Butler & Farrell, 1992). An Orr-Sommerfeld mode with $k_x << 1$ and $k_z \sim O(1)$ is chosen so that the mode is nearly perpendicular to the mean flow and comprises only of v and w components. Moreover, the initial condition imposed on normal vorticity is $\eta_{\vec{k}}(y,0) = 0$ to ensure u perturbation does not arise due to normal vorticity. Figure 4.2(a) shows that the normal velocity perturbation decays monotonically with time. The monotonic decay is due to the presence of only one continuous Orr-Sommerfeld mode in the initial condition as can be seen in equation 4.7. However the monotonically decreasing normal velocity generates a strong normal vorticity response as shown in figure 4.2(b-c). Initially normal vorticity is absent in the system, however as time progresses, the normal velocity perturbation

generates normal vorticity by tilting the mean vorticity. Figure 4.2(c) shows that the normal vorticity response peaks over a time-scale, $t_{max} = O(Re/(k_x^2+k_y^2+k_z^2))$, associated with the decay rate of the forcing Orr-Sommerfeld mode. On a time-scale much larger than t_{max}, the normal velocity perturbation is virtually absent and there is no mechanism to generate normal vorticity. Therefore viscous dissipation dominates over long time-scales and causes η to decay.

The shape of the normal vorticity response is similar to the forcing induced by the tilting term, $d_yU\phi$. In the free-stream, mean vorticity is absent and therefore no normal vorticity is generated. Within the boundary layer the mean vorticity, d_yU, increases towards the wall contrary to the normal velocity perturbation which decays inside the boundary layer. Therefore, the tilting term, $d_yU\phi$ shown in figure 4.3 peaks inside the boundary layer ($y \approx 0.5\delta_{99}$) and hence the Squire response. This observation is consistent with optimal perturbations computed by Luchini (2000) and experimental results of Matsubara & Alfredsson (2001) who reported that the maximum u_{rms} is observed at $y \approx 0.5\delta_{99}$.

The extent of amplification of normal vorticity is a function of the forcing due to the tilting term and the decay rate of the Orr-Sommerfeld mode. The tilting mechanism causes normal vorticity to grow linearly with time whilst the decay rate of the Orr-Sommerfeld mode decides the time-scale over which the viscous decay occurs. Therefore, the two competing phenomena decide the amplitude of the streaks. In order to quantify the propensity of the normal velocity perturbations to generate streaks, Zaki & Durbin (2005) had proposed the coupling coefficient, $\theta \equiv \left| \frac{\langle \chi^{H\dagger}, \mathscr{C}\phi_{\tilde{k}_y} \rangle}{\omega_i} \right|$ for continuous modes with wall normal wavenumber $\tilde{k}_y$ and decay rate ω_i. Figure 4.4 shows the contours of the coupling coefficient optimized over $\tilde{k}_y$. The coupling coefficient reduces with increasing k_x, as the modes with high k_x do not penetrate deep into the boundary layer. For $k_x \ll 1$ there exists a variation in coupling coefficient with k_z. The coupling coefficient increases with k_z for $k_z < 1$ as $\theta \propto k_z$. However modes with $k_z \gg 1$, have a large decay rate and therefore the coupling coefficient decreases with further increase in k_z. Hence an optimal k_z exists, as can be seen in figure 4.4. The optimal $k_z \sim O(\pi)$ corresponds to a lengthscale of the order of the boundary layer thickness. Matsubara & Alfredsson (2001) also report that streamwise elongated streaky structures with spanwise scales approximately equal to the Blasius boundary layer thickness are present in transitional

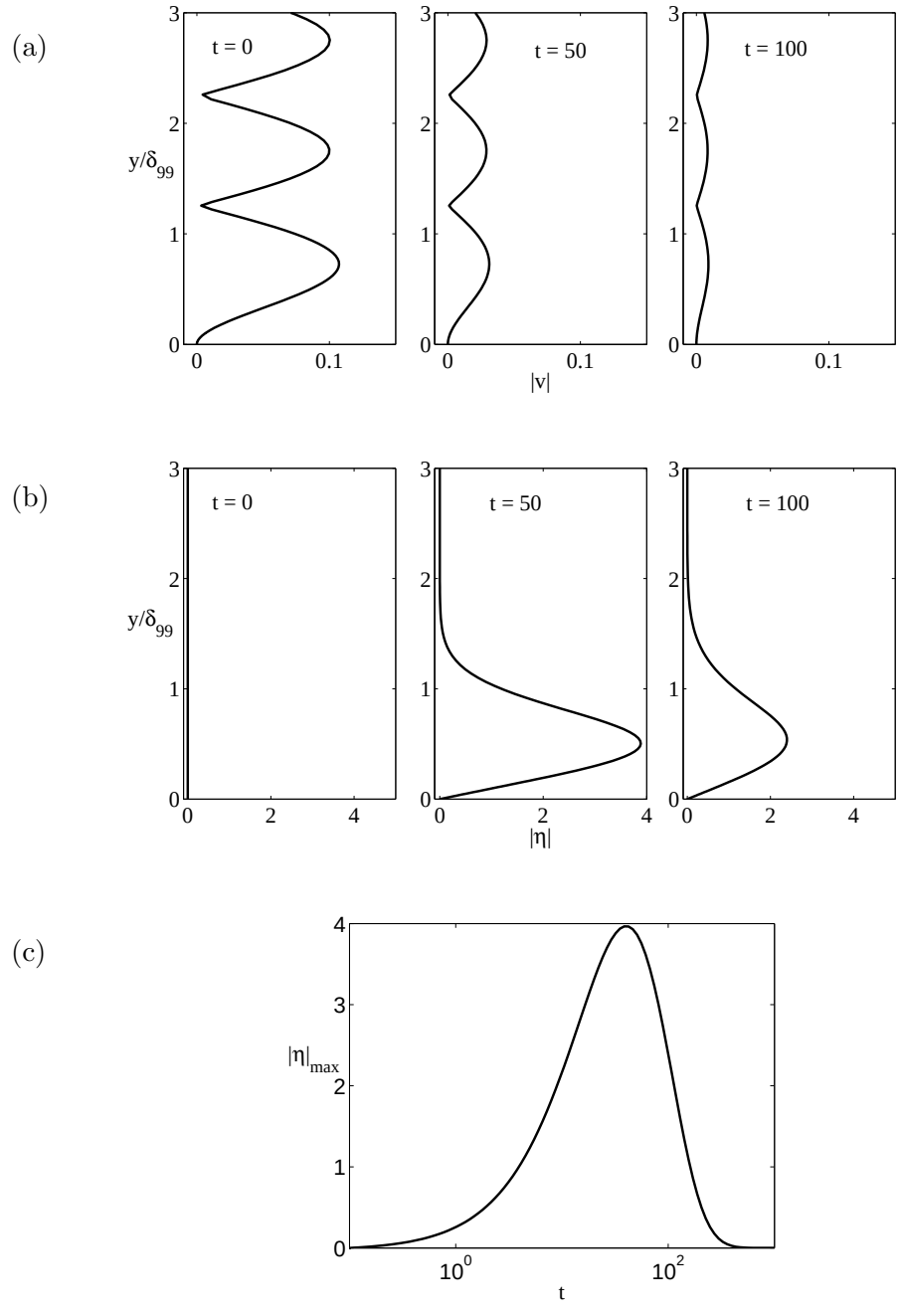


Figure 4.2: (a) Normal velocity, (b) Normal vorticity at short time, (c) $|\eta|_{max}(t) \equiv \max_y |\eta_{\vec{k}}(y,t)|$. $k_x = 0.001, k_y = \pi, k_z = \pi, Re = 800, \mu_{BT} = 1$.

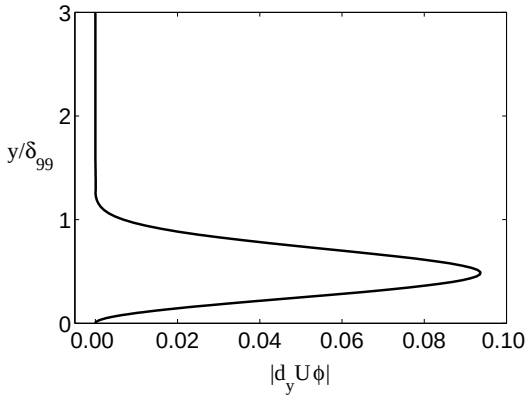


Figure 4.3: Tilting term, $|d_y U\phi|$ for a single-fluid boundary layer. $k_x = 0.001, k_y = \pi, k_z = \pi, Re = 800$.

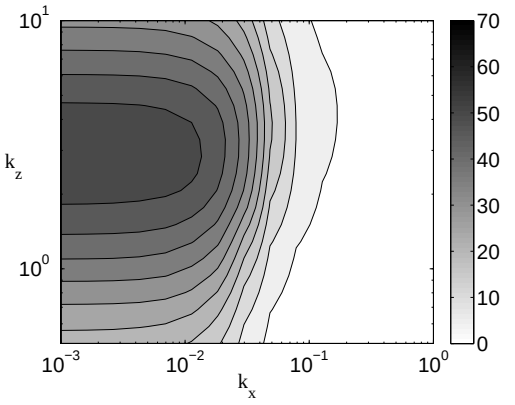


Figure 4.4: Coupling coefficient, θ for a single-fluid boundary layer. $Re = 800$. Contour levels correspond to $0 \leq \theta \leq 70$ at an increment of 5

flows. The coupling coefficient therefore indicates the propensity of free-stream modes to generate streaks by the vorticity tilting mechanism.

4.3.2 The two-fluid boundary layer

The previous subsection described the evolution of a streamwise oriented vortex in a single-fluid boundary layer. In this section the same initial condition is considered for a two-fluid boundary layer. The presence of interface deformation requires a jump in the normal vorticity perturbation across the interface. A streamwise oriented vortex has no normal vorticity, and therefore in order to prescribe $\eta_{\vec{k}}(y, 0) = 0$ as the initial condition, the interface deformation, $f_{\vec{k}}$, is initially set to zero. Each continuous Orr-Sommerfeld mode has a non-trivial $f_{\vec{k},\tilde{k_y}}$, associated with it. The interface mode is added to the initial perturbation field with an amplitude such that the interface displacement due

to the continuous Orr-Sommerfeld mode and the interface mode cancel out exactly. The solution to the initial value problem was described for a continuous Orr-Sommerfeld mode, however it can be applied to the interfacial mode as well. The individual solutions due to the two forcing modes are superimposed to obtain the complete solution.

The normal velocity profile shown in figure 4.5(a) is oscillatory in the free-stream and decays inside the boundary layer similar to the single-fluid boundary layer. The entire normal velocity field decays with time owing to viscous dissipation. At long time there is almost no normal velocity present because the continuous Orr-Sommerfeld mode undergoes viscous decay and the normal velocity associated with the interface mode is negligible.

$$f_{\vec{k}}(t) \quad = \quad A_{\vec{k},\tilde{k}_y} f_{\vec{k},\tilde{k}_y} e^{-i\omega_{\vec{k},\tilde{k}_y} t} + A_{\vec{k},int} f_{\vec{k},int} e^{-i\omega_{\vec{k},int} t}. \tag{4.20}$$

The time evolution of the interface displacement shown in figure 4.5(b) can be understood by examining equation 4.20. The two amplitudes $A_{\vec{k},\tilde{k}_y}$ and $A_{\vec{k},int}$ in equation 4.20 were chosen such that the interface displacement is zero at $t = 0$. However this cancellation is no longer maintained at a later time since the continuous Orr-Sommerfeld mode decays much faster than the interfacial mode. Therefore the interface displacement, which is the difference between the individual interfacial displacements of the two modes, also increases. At long time only the interface mode is present and therefore interfacial displacement should decay as $e^{-i\omega_{\vec{k},int} t}$. A detailed discussion of the asymptotic behavior of the interface mode in the limit $k_x \delta_{99} \to 0$ is presented in the subsequent subsection 4.3.3. The asymptotic analysis reveals that the interface mode is neutrally stable to leading order and therefore the interface displacement seems to achieve an asymptotic value at long time as shown in figure 4.5(b).

Figure 4.6(a) shows the normal vorticity response as a result of the forcing due the interfacial and continuous Orr-Sommerfeld mode. The free-stream solution is trivial at all instants of time. Normal vorticity is generated by the vorticity tilting mechanism, whereby the normal velocity component of the perturbation tilts the mean vorticity and generates perturbation vorticity. Since there is no mean vorticity in the free-stream, no normal vorticity is generated. However, inside the boundary layer the normal

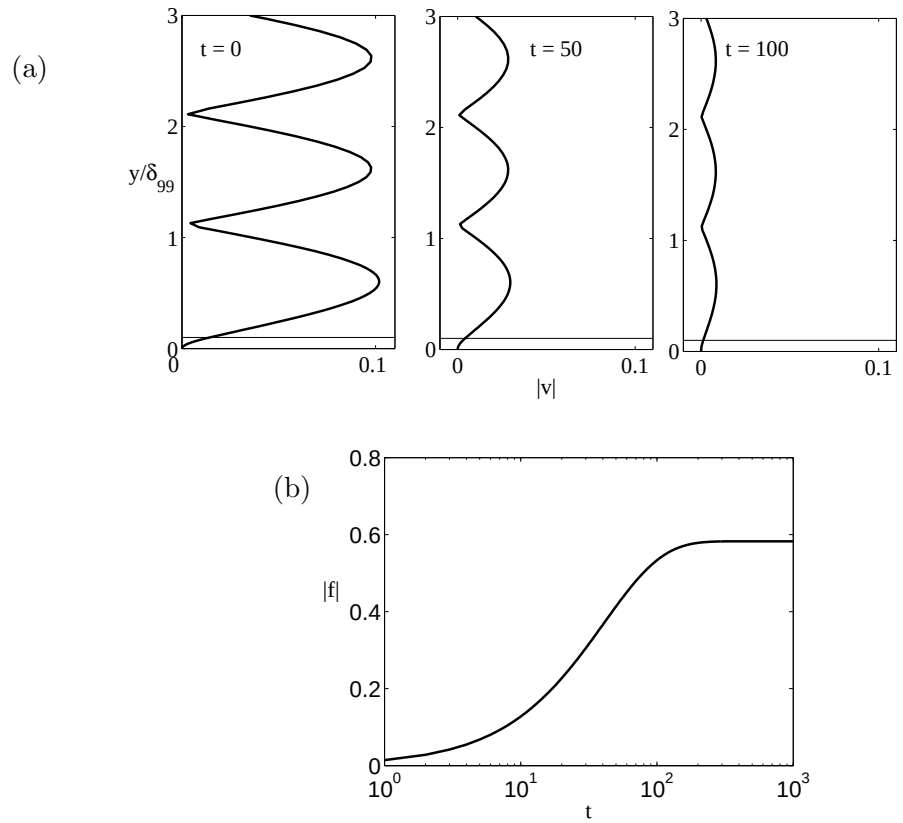


Figure 4.5: (a) Normal velocity, (b) Interface displacement at different instants of time. $k_x = 0.001, k_{y,cont} = \pi, \omega_{int} = 3.7296 \times 10^{-4} - 3.7170 \times 10^{-7} i, k_z = \pi, Re = 800, \mu_{BT} = 0.3, \delta_B = 0.1$.

velocity perturbation tilts the mean vorticity to generate normal vorticity perturbation. The normal vorticity perturbation initially amplifies with time on a time-scale $t_{vort} \sim O(Re/(k_x^2+k_y^2+k_z^2))$ due to the vorticity tilting mechanism and then decays due to viscous dissipation.

Thereafter the normal velocity perturbation ceases to exist and the normal vorticity equation is driven purely by the displacement of the interface. At long time, a jump in normal vorticity is observed across the interface and the vorticity field fades away with distance from the interface as shown in figure 4.6(b). The long time normal vorticity field is identical to the particular normal vorticity, χ^P, associated with the interface mode. The neutrally stable interface mode generates normal vorticity by virtue of the jump in mean vorticity across the interface. The jump in normal vorticity is proportional to $(1-\mu_{BT})d_yU_T(y_f)f_{\vec{k}}(t)$ and hence the increase in the interface deformation with time (as shown in figure 4.5(b)) leads to an increase in the normal vorticity field. It should be noted that this mechanism of energy amplification is absent in single-fluid boundary layers as there is no jump in mean vorticity across the interface. As $(1-\mu_{BT})$ increases, the jump in mean vorticity is enhanced, which results in the generation of larger normal vorticity perturbation due to interface deformation. The vorticity generated by the interfacial displacement is referred to as the interface deformation mechanism.

The continuous Orr-Sommerfeld mode resonantly forces the Squire equation and equation 4.19 explicitly shows initial algebraic growth with time for the resonant Squire mode. The inner product, $|\langle \chi^{\dagger}_{\vec{k},k_y}, \rho\mathscr{F}\rangle|$ for the continuous Orr-Sommerfeld and interface modes is shown in figure 4.7. The resonant mode and the near resonance modes contain maximum energy and hence contribute to the linear amplification with time. This resonance mechanism for the initial growth in normal vorticity was suggested by Gustavsson & Hultgren (1980); Gustavsson (1981); Benney & Gustavsson (1981); Zaki & Durbin (2005).

The energy density of the boundary layer, $E_{bl}(t)$ (see appendix C for derivation),

$$E_{bl}(t) \equiv \frac{1}{4k^2\delta_{99}}\left[\rho_B\int_0^{y_f}(|\partial_y v_{\vec{k}}|^2+k^2|v_{\vec{k}}|^2+|\eta_{\vec{k}}|^2)dy + \rho_T\int_{y_f}^{\delta_{99}}(|\partial_y v_{\vec{k}}|^2+k^2|v_{\vec{k}}|^2+|\eta_{\vec{k}}|^2)dy\right]$$

and the energy contribution from normal velocity,

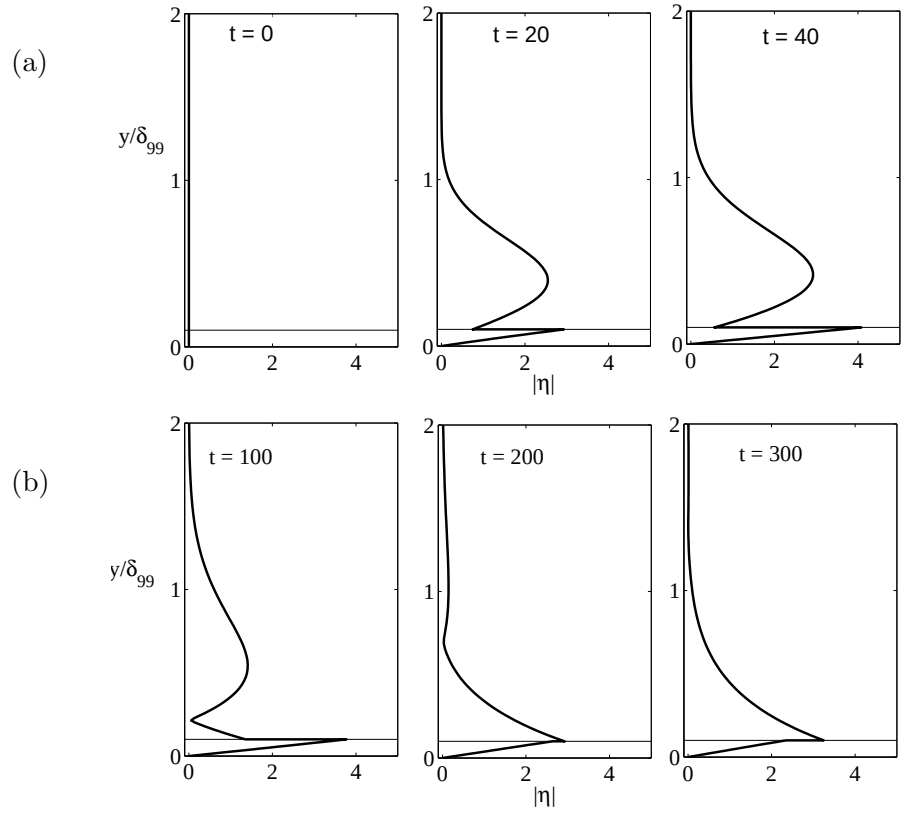


Figure 4.6: (a) Normal vorticity response at short time, (b) Normal vorticity response inside the boundary layer at long time. $k_x = 0.001, k_{y,cont} = \pi, \omega_{int} = 3.7296 \times 10^{-4} - 3.7170 \times 10^{-7} i, k_z = \pi, Re = 800, \mu_{BT} = 0.3, \delta_B = 0.1$.

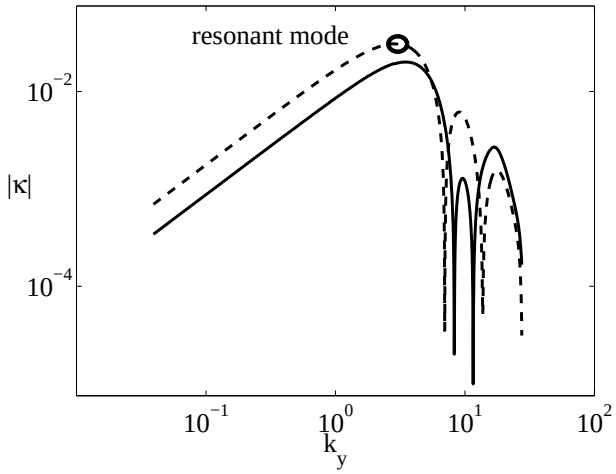


Figure 4.7: Projection of forcing $\kappa \equiv |\langle \chi^{\dagger}_{\tilde{k},k_y}, \rho\mathscr{F}\rangle|$ on the homogeneous Squire eigenfunctions. ——, interfacial mode; - - -, continuous Orr-Sommerfeld mode. $k_x = 0.001, k_{y,cont} = \pi, \omega_{int} = 3.7296 \times 10^{-4} - 3.7170 \times 10^{-7} i, k_z = \pi, Re = 800, \mu_{BT} = 0.3, \delta_B = 0.1$.

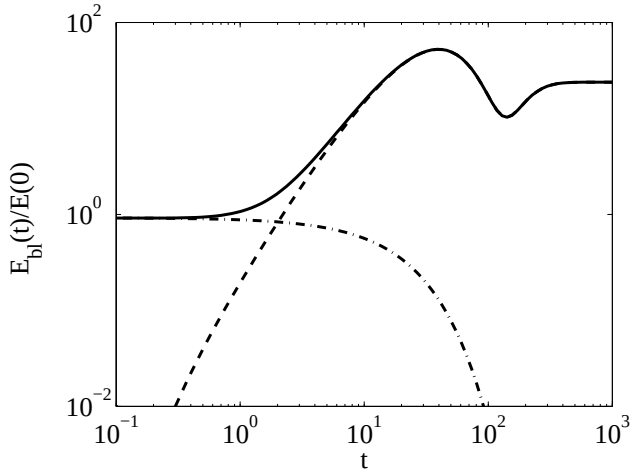


Figure 4.8: Variation in energy with time. ——, $\frac{E_{bl}(t)}{E(0)}$; - - -, $\frac{E_\eta(t)}{E(0)}$; — · —, $\frac{E_v(t)}{E(0)}$. $k_x = 0.001, k_{y,cont} = \pi, \omega_{int} = 3.7296 \times 10^{-4} - 3.7170 \times 10^{-7} i, k_z = \pi, Re = 800, \mu_{BT} = 0.3, \delta_B = 0.1$.

$$E_v(t) \equiv \frac{1}{4k^2\delta_{99}}\left[\rho_B \int_0^{y_f} k^2|v_{\vec{k}}|^2 + |\partial_y v_{\vec{k}}|^2 dy + \rho_T \int_{y_f}^{\delta_{99}} k^2|v_{\vec{k}}|^2 + |\partial_y v_{\vec{k}}|^2 dy\right]$$

and normal vorticity,

$$E_\eta(t) \equiv \frac{1}{4k^2\delta_{99}}\left[\rho_B \int_0^{y_f} |\eta_{\vec{k}}|^2 dy + \rho_T \int_{y_f}^{\delta_{99}} |\eta_{\vec{k}}|^2 dy\right]$$

are also computed and shown in figure 4.8. The energy density presented in the results, $E_{bl}(t)$, is normalized by the initial energy density, $E(0)$, of the entire domain which is given by,

$$\begin{aligned} E(0) \quad \equiv \quad & \frac{1}{4k^2\ell}\Bigg[\rho_B \int_0^{y_f} (|d_y v_{\vec{k}}(y,0)|^2 + k^2|v_{\vec{k}}(y,0)|^2 + |\eta_{\vec{k}}(y,0)|^2) dy + \\ & \rho_T \int_{y_f}^{\ell} (|d_y v_{\vec{k}}(y,0)|^2 + k^2|v_{\vec{k}}(y,0)|^2 + |\eta_{\vec{k}}(y,0)|^2) dy\Bigg]. \end{aligned}$$

In addition, the amplitude of the inteface mode is set equal to the negative of the continuous mode at $t = 0$, in order to ensure that there is no interface deformation.

Figure 4.8 reveals that initially at $t \sim 0(1)$, the Orr-Sommerfeld mode contains all the energy as $E \approx E_v$. As time proceeds the normal vorticity component E_η amplifies and for $t > O(10)$ it is approximately equal to the total energy of the system. Figure 4.6 shows that the amplification of normal vorticity is initially due to the vorticity

tilting caused by the continuous Orr-Sommerfeld mode and the vorticity at long time is due to the particular vorticity of the interface mode. Both the mechanisms generate normal vorticity simultaneously and their individual effects must be distinguished. The interfacial mode was chosen to demonstrate the role of the latter mechanism. The long-time normal vorticity generated by the interface mode is purely by virtue of interface deformation. This is illustrated by figure 4.5 which shows that the normal velocity decays on a much smaller time-scale than that of the interface displacement. Hence, the neutrally stable mode leads to amplification of η despite the absence of any normal velocity perturbation at long time.

If, however, two continuous modes were chosen, the interface deformation would have initially increased, but $f_{\vec{k}}(t)$ would tend to zero on the time-scale of the decay of normal velocity. In the absence of interface displacement, there would be no forcing acting on the normal vorticity equation. In that case, it would be impossible to distinguish the normal vorticity generated by the normal velocity (tilting of mean vorticity) and that by interface deformation.

The analysis of the single-fluid system demonstrated that the propensity of the vorticity tilting mechanism to generate normal vorticity can be estimated by the coupling coefficient. However, the ability of the interface mode to generate normal vorticity still remains to be explored. In the following subsection the asymptotic behavior of the interface mode is examined in the long wavelength limit in order to evaluate the effect of viscosity stratification on the interface deformation mechanism.

4.3.3 Long wavelength limit of the interface mode

The normal vorticity at long time is caused by the interface mode. In this subsection the effect of viscosity stratification on the interface mode is considered by assuming the absence of surface tension and density stratification. The long wavelength approximation $k_x\delta_{99} \to 0$ is introduced in the following analysis in order to examine streamwise oriented vortices which lead to large transient amplification. In addition, we assume that the ratio of convective to viscous terms, $\frac{k_x U_\infty \delta_{99}^2}{\nu_T} \ll 1$ and that $\frac{k_z^4 \nu \delta_{99}^2}{k_x U_\infty} \sim O(1)$. The zeroth and first order solutions are presented here to demonstrate that a) the energy associated with the interface mode increases as the viscosity of the wall-film is reduced and b) the eigenvalue of the interface mode, ω_{int}, is $O(k_x\delta_{99})$. The frequency is assumed to be of the form,

$\omega_{int} = \omega_0 + k_x\delta_{99}\omega_1 + (k_x\delta_{99})^2\omega_2 ...$. The eigenfunction for normal velocity and interface displacement is also expanded in powers of $k_x\delta_{99}$,

$$\begin{bmatrix} \phi_j(y) \\ f \\ \chi_j^P(y) \end{bmatrix}_{int} = \begin{bmatrix} \phi_{0j}(y) \\ f_0 \\ \chi_{0j}^P(y) \end{bmatrix} + k_x\delta_{99} \begin{bmatrix} \phi_{1j}(y) \\ f_1 \\ \chi_{1j}^P(y) \end{bmatrix} + ... \tag{4.21}$$

Substituting the expansion in the Orr-Sommerfeld and the interface equations leads to,

$$-i\omega_0 \begin{bmatrix} d_y^2 - k_z^2 & 0 \\ 0 & 1 \end{bmatrix} \begin{bmatrix} \phi_{0j}(y) \\ f_0 \end{bmatrix} = \begin{bmatrix} \mathscr{L}_{0j} & 0 \\ \mathscr{C}_v & 0 \end{bmatrix} \begin{bmatrix} \phi_{0j}(y) \\ f_0 \end{bmatrix}$$

where, $\mathscr{L}_{0j} = \nu_j(d_y^2 - k_z^2)^2$. To leading order, the interfacial boundary conditions on the normal velocity perturbation reduce to,

$$[\phi_0] = 0,$$

$$[d_y\phi_0] = 0,$$

$$[\mu(d_y^2 + k_z^2)\phi_0] = 0,$$

$$[\mu(d_y^3 - 3k_z^2 d_y)\phi_0] = 0.$$

The interfacial boundary conditions on ϕ_0 are independent of f_0 but the interface equation depends on $\phi_0(y_f)$. This implies that there exists only one way coupling between ϕ_0 and f_0 and that the eigenvalues of the Orr-Sommerfeld equation and the interface equation are independent of each other at the leading order. Therefore the interface mode does not have any normal velocity perturbation associated with it at this order. The frequency of the interface mode, ω_{int}, must be $O(k_x)$ as $\omega_0 = 0$. The interface displacement, f_0 is normalized to 1 and the mode essentially represents a standing wave with a spanwise corrugation. The particular normal vorticity eigenfunction associated with the interface mode is found by solving the reduced Squire equation,

$$(d_y^2 - k_z^2)\chi_{0j}^P = 0. \tag{4.22}$$

with the following boundary conditions on χ_0^P,

$$\begin{aligned}
\chi_{0T}^P &= 0; & y \to \infty \\
\chi_{0T}^P - \chi_{0B} &= -ik_z(d_yU_T - d_yU_B)f_0; & y = y_f \\
d_y\chi_{0T}^P - \mu_{BT}d_y\chi_{0B}^P &= -ik_z(d_y^2U_T - \mu_{BT}d_y^2U_B)f_0; & y = y_f \\
\chi_{0B}^P &= 0; & y = 0.
\end{aligned}$$

The normal vorticity eigenfunction, χ_0^P , is of the form,

$$\begin{aligned}
\chi_{0T}^P &= C'_{01}e^{-k_z(y-y_f)} \\
\chi_{0B}^P &= C'_{05}(e^{k_zy} - e^{-k_zy}).
\end{aligned}$$

and the constants of integration, C'_{01}, C'_{05}, are provided in the appendix B.

The first order solution is derived in order to estimate the eigenvalue, ω_{int}. At this order, the normal velocity and interface equations are,

$$\begin{aligned}
\mathscr{L}_{0j}\phi_{1j} &= 0 \\
-i\omega_1 f_0 &= -i\frac{U(y_f)}{\delta_{99}}f_0 + \phi_1(y_f)
\end{aligned}$$

with boundary conditions at $y = y_f$,

$$[\phi_1] = 0; \qquad [d_y\phi_1] = i[d_yU]\frac{f_0}{\delta_{99}};$$

$$[\mu(d_y^2 + k_z^2)\phi_1] = i[\mu d_y^2U]\frac{f_0}{\delta_{99}}; \qquad [\mu(d_y^3 - 3k_z^2d_y)\phi_1] = 0.$$

and homogeneous boundary conditions at the wall and in the free-stream. At first order, the eigenvalue, ω_1 is obtained as

$$\omega_1\delta_{99} = U(y_f) - \frac{(d_yU_T - d_yU_B)(A_{22} - A_{21}y_f) + \frac{1}{2k_z}(d_y^2U_T - \mu_{BT}d_y^2U_B)(A_{11}y_f - A_{12})}{A_{11}A_{22} - A_{12}A_{21}}e^{-k_zy_f}$$

μ_{BT}	numerical $((\omega_r \times 10^{-4}) + i(\omega_i \times 10^{-7}))$	$(\omega_1 \times 10^{-4})$	relative error
0.8	$1.935350331561870 - i0.4455883723948942$	1.935359183163306	4.5×10^{-6}
0.6	$2.391576424560320 - i1.209020897504407$	2.391596160134414	8.2×10^{-6}
0.4	$3.135429548509259 - i2.565568584057602$	3.135493253726059	2.0×10^{-5}
0.3	$3.729609123630786 - i3.732050600085042$	3.729650401002743	1.1×10^{-5}
0.2	$4.682419680538698 - i5.523622827466344$	4.682482537747204	1.3×10^{-5}
0.1	$6.929987214889351 - i7.727603430474145$	6.930047347643953	8.6×10^{-6}

Table 4.1: Comparison of asymptotically and numerically obtained eigenvalue ω_{int}. $k_x = 0.001, k_z = \pi, Re_T = 800, \mu_{BT} = 0.3, \delta_B = 0.1$. ω_r and ω_i are the real and imaginary parts of ω_{int} respectively.

and the eigenfunction, ϕ_1 is,

$$\begin{aligned} \phi_{1T} &= (C_{11} + C_{13}y)e^{-k_z y}, \\ \phi_{1B} &= (C_{15} + C_{17}y)e^{-k_z y} + (C_{16} + C_{18}y)e^{-k_z y}. \end{aligned} \tag{4.23}$$

The constants of integration, C_{ij} and other constants $A_{11}, A_{12}, A_{21}, A_{22}$ are provided in appendix B. The eigenvalue at the first order is purely real, hence the growth rate of the interface mode is $O((k_x\delta_{99})^2)$ and therefore it is almost neutrally stable in this limit. The eigenvalues obtained from the asymptotic expansion are compared to their numerical counterparts in table 4.1. The relative error between the real parts is also computed and is found to be $O(10^{-5})$. Since the eigenfunction, $[\phi\ f\ \chi^P]^T_{int}$ can be scaled by any arbitrary constant, the solution should depend only on one constant. In this case, f_0 was set to unity in order to derive the zeroth order solution. However, at the first order, f_1 is still undetermined. Since there exists an extra degree of freedom, f_1 is set to 0. The choice of f_1 does not affect the overall solution and this assertion in confirmed *a posteriori*. The associated particular normal vorticity, χ^P_{1j}, at the first order is found by solving,

$$-\nu_j(d_y^2 - k_z^2)\eta^P_{1j} = \mathscr{H}_{1j} \tag{4.24}$$

with boundary conditions,

$$\begin{aligned}
\chi^P_{1T} &= 0; && y \to \infty \\
\chi^P_{1T} - \chi_{1B} &= 0; \qquad y = y_f \\
d_y\chi^P_{1T} - \mu_{BT} d_y \chi^P_{1B} &= 0; \quad y = y_f \\
\chi^P_{1B} &= 0; && y = 0.
\end{aligned}$$

where $\mathscr{H}_{1j} \equiv -ik_z d_y U_j \phi_{1j} + i\left(\omega_1 - \frac{U_j}{\delta_{99}}\right)\chi^P_{0j}$. The solution can be written as,

$$\begin{aligned}
\chi^P_{1T} &= \frac{e^{k_z y}}{-2k_z}\int_y^\infty \mathscr{H}_{1T} e^{-k_z s} ds + \left(C'_{12} + \frac{1}{-2k_z}\int_{y_f}^y \mathscr{H}_{1T} e^{k_z s} ds\right) e^{-k_z y} \\
\chi^P_{1B} &= 2C'_{13} sinh(k_z y) + \frac{e^{k_z y}}{2k_z}\int_0^y \mathscr{H}_{1B} e^{-k_z s} ds - \frac{e^{-k_z y}}{2k_z}\int_0^y \mathscr{H}_{1B} e^{k_z s} ds
\end{aligned}$$

The constants C'_{12}, C'_{13} are provided in appendix B. The normal velocity eigenfunction of the interface mode in equation 4.23 is compared to the numerical solution of the eigenvalue problem 2.12 for the interface mode in figure 4.9(a). There is a good agreement between the asymptotically and numerically computed eigenfunctions. The normal vorticity eigenfunction associated with the interface mode, $\chi^P_0 + k_x\delta_{99}\chi^P_1$, which is shown in figure 4.9(b) corresponds to a unit interface displacement. Furthermore, figure 4.9(c) demonstrates that indeed setting $f_1 = 0$ does not affect the results significantly, since χ^P_1 and $\chi - \chi^P_0$ are the same order of magnitude. A non-zero value of f_1 would have implied that the eigenfunction χ^1_P is discontinuous.

The jump in normal vorticity across the interface in figure 4.9(b) is proportional to the term $d_y U_T - d_y U_B$. Therefore as the viscosity ratio, μ_{BT}, is reduced, the jump in normal vorticity increases due to an increase in the discontinuity of the mean flow gradient. As a result the energy of the interface mode, E_η, increases with reduction in μ_{BT} as shown in figure 4.10.

4.3.4 Viscosity stratification effects

The previous section illustrated the effect of viscosity stratification on the interface mode. Two competitive mechanisms driving the normal vorticity response emerged, firstly the

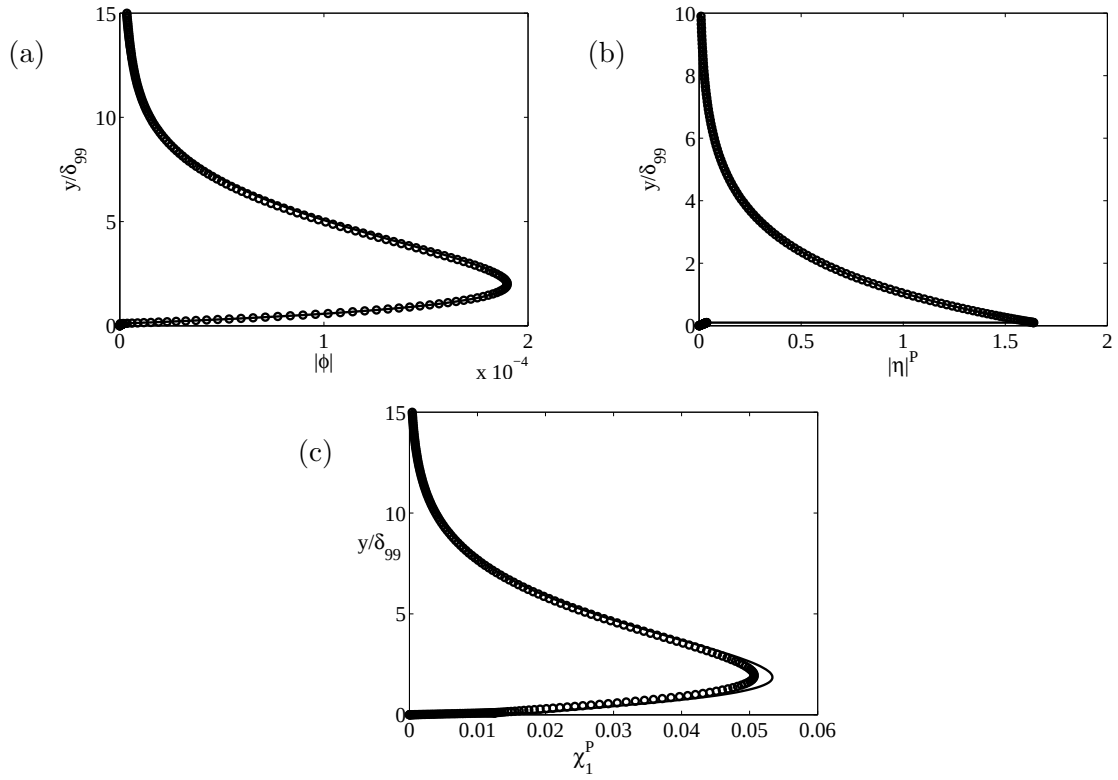


Figure 4.9: Comparison of numerical and asymptotic results for the interface mode. (a) Normal velocity eigenfunction ——, $k_x\delta_{99}\phi_1$, ∘ numerical solution of the eigenvalue problem. (b) Normal vorticity eigenfunction, ——, $\chi_0 + k_x\delta_{99}\chi_1$, ∘ numerical solution of the eigenvalue problem. (c) Comparison of χ_1 (——) with $\chi - \chi_0$ (∘) where χ is the numerically evaluated solution of the Squire equation. $k_x = 0.0001, k_z = \pi/6, Re_T = 800, \mu_{BT} = 0.3, \delta_B = 0.1$.

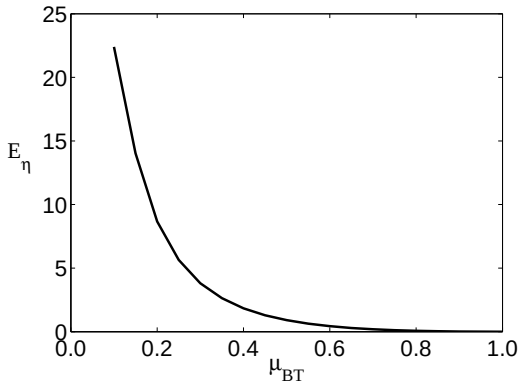


Figure 4.10: Energy, E_η of the interface mode as a function of the viscosity ratio computed from the asymptotically computed from the normal vorticity eigenfunction, χ^P. $k_x = 0.001, k_z = \pi, Re_T = 800, \delta_B = 0.1$

vorticity tilting mechanism and secondly the interface deformation mechanism. A reduction in viscosity ratio, μ_{BT} , increases the energy of the interface mode and hence the neutral interfacial wave generates large amplitude normal vorticity for small viscosity ratios. The effect of viscosity stratification on the vorticity tilting mechanism must also be evaluated. Figure 4.11(a) shows the Squire response at the time of maximum amplification in $E(t)$. The peak in normal vorticity response associated with the vorticity tilting mechanism reduces as the viscosity ratio μ_{BT} is reduced. This observation is further clarified by figure 4.11(b) which shows the maximum normal vorticity in both fluids at different viscosity ratios. The maximum normal vorticity in the top fluid decreases for $\mu_{BT} > 0.3$ and increases for $\mu_{BT} < 0.3$. On the contrary, the maximum normal vorticity in the bottom fluid increases with reduction in μ_{BT}. The normal velocity response inside the wall-film is driven by the interface deformation mechanism. The maximum is observed at the interface and as the viscosity ratio is reduced the jump in normal vorticity increases. As a result, the maximum normal vorticity in the bottom fluid increases. In the case of the top fluid however, the tilting of mean vorticity and the interface deformation mechanism both contribute to the growth of normal vorticity. For viscosity ratios greater than 0.3 the vorticity tilting mechanism is able to generate a stronger vorticity response in the top fluid compared to the interface deformation mechanism. The effect of viscosity ratio variation on the vorticity tilting mechanism is indicated by the strength of the coupling between mean shear and normal velocity shown in figure 4.12(a - b). It is observed that this coupling is weakened for $\mu_{BT} < 1$ and therefore, it can be concluded that the temporal amplification due to the vorticity tilting mechanism is reduced by lowering μ_{BT}.

The energy amplification curves are examined further to estimate the extent to which energy amplification is attenuated. Figure 4.13(a) shows the amplification curves for $E(t)$ for various viscosity ratios. As the viscosity ratio, μ_{BT} is reduced, the magnitude of the first peak in $E(t)$ is reduced whereas that of the second peak increases.

The first peak in figure 4.13 is determined by the strength of the forcing term, $\mathscr{C}$ (Zaki & Durbin, 2005). This term is affected by the mean shear distribution and the variation in ϕ with viscosity stratification. As μ_{BT} is reduced the shear in the bottom fluid increases and the shear in the top fluid is reduced in order to maintain the mean shear stress continuity at the interface. The shape of ϕ in a two-fluid boundary layer

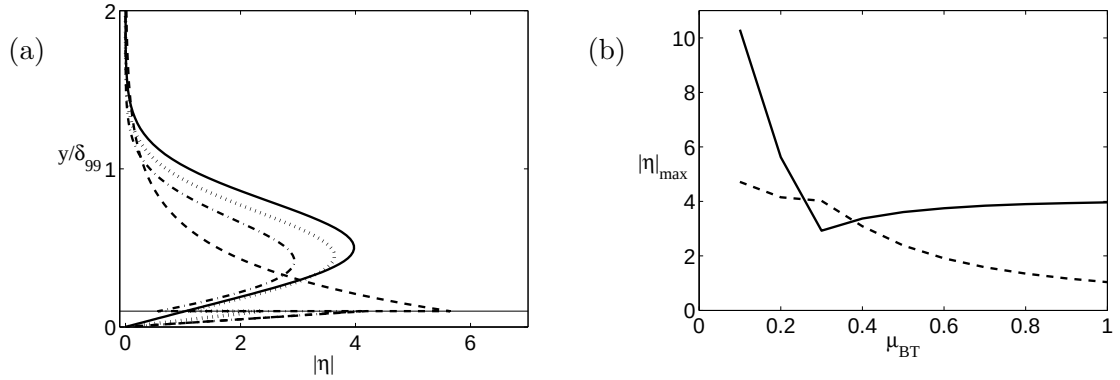


Figure 4.11: (a) Squire response in a two-fluid boundary layer at the time of maximum amplification in energy. $\delta_B = 0.1$ ——, $\mu_{BT} = 1$; $\cdots$, $\mu_{BT} = 0.5$; — $\cdot$ —, $\mu_{BT} = 0.3$; - - -, $\mu_{BT} = 0.2$. (b) Maximum normal vorticity in each fluid at the instant of maximum energy amplification ($t = t_{max}$). - - -, $\max_{y\in[0,y_f)} |\eta_k(y, t_{max})|$; ——, $\max_{y\in(y_f,\infty)} |\eta_k(y, t_{max})|$; $k_x = 0.001, k_y = \pi, k_z = \pi, Re = 800$

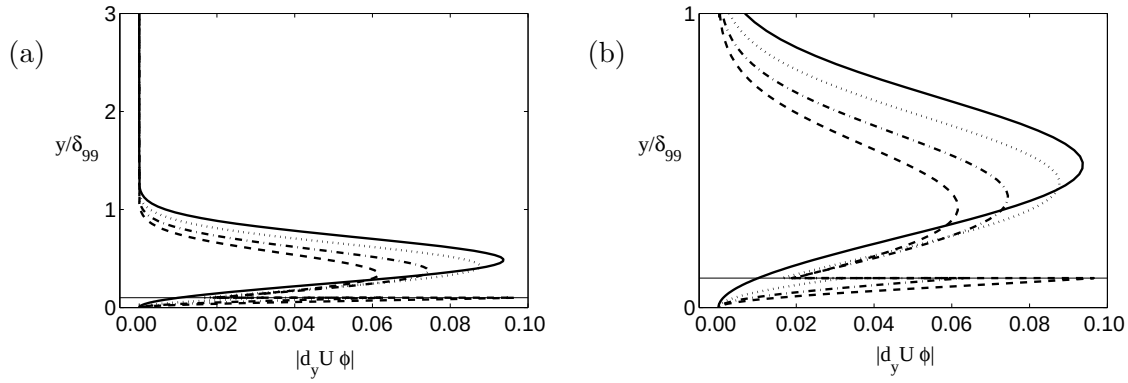


Figure 4.12: (a)Tilting term, $|d_y U\phi|$ for a two-fluid boundary layer (b) Tilting term, $|d_y U\phi|$ inside the boundary layer. $\delta_B = 0.1$ ——, $\mu_{BT=1}$; $\cdots$, $\mu_{BT} = 0.5$; — $\cdot$ —, $\mu_{BT} = 0.3$; - - -, $\mu_{BT} = 0.2$. $k_x = 0.001, k_y = \pi, k_z = \pi, Re = 800$.

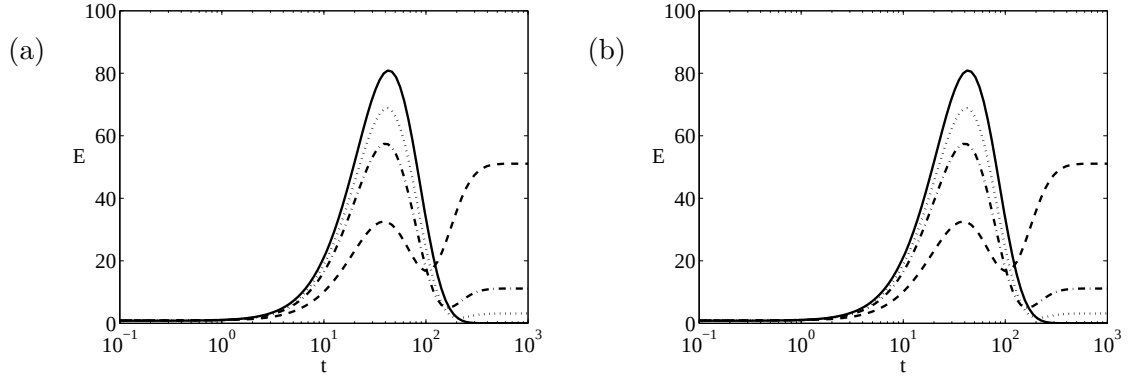


Figure 4.13: Energy amplification for various viscosity ratios (a) $\delta_B = 0.1$ ——, $\mu_{BT} = 1$; · · · ·, $\mu_{BT} = 0.5$; — · —, $\mu_{BT} = 0.3$; - - -, $\mu_{BT} = 0.2$. (b) $\delta_B = 0.05$ ——, $\mu_{BT} = 1$; · · · ·, $\mu_{BT} = 0.3$; — · —, $\mu_{BT} = 0.2$; - - -, $\mu_{BT} = 0.1$. $k_x = 0.001, k_y = \pi, k_z = \pi, Re = 800$.

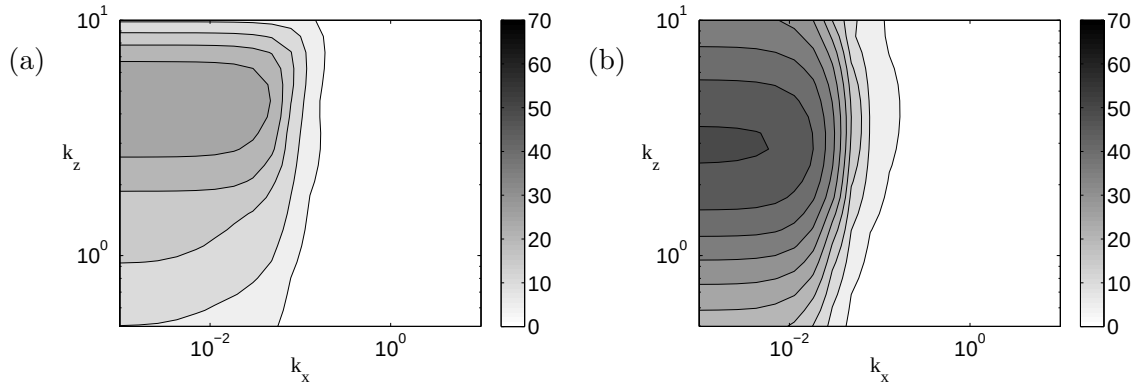


Figure 4.14: Coupling coefficient contours, θ for a two-fluid boundary layer,(a) $\mu_{BT} = 0.1$. (b) $\mu_{BT} = 0.5$. $Re_T = 800$. Contour levels correspond to $0 \leq \theta \leq 70$ at an increment of 5.

was discussed in detail in the previous chapter. It was reported that the penetration of normal velocity perturbation into the boundary layer is inhibited for viscosity ratios lower than $\mu_{BT}*$ due to the presence of stronger shear in the bottom fluid. Lowering of the viscosity ratio strengthens the mean shear in the bottom fluid, a region where $|\phi| \to 0$ due to the no-penetration boundary condition. Moreover, since the shear in the top fluid is weakened where the normal velocity remains oscillatory the coupling between the two decreases further. Therefore the overall forcing term $\mathscr{C}$ is reduced in strength as the viscosity ratio is reduced and hence the reduction in the first peak in figure 4.13. The coupling coefficients in figure 4.14 show that the optimum value is significantly reduced as the viscosity ratio is reduced when compared to the single fluid peak in figure 4.4.

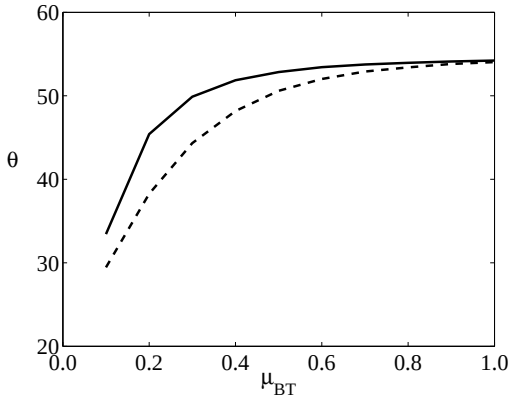


Figure 4.15: Optimum coupling coefficient, θ_{opt} for a two-fluid boundary layer. ——, $\delta_B = 0.05$ - - -, $\delta_B = 0.1$. $Re_T = 800$

Figures 4.13(a) and (b) also show that a critical viscosity ratio exists for each film thickness where the energy amplification due to the interface deformation mechanism exceeds that due to the vorticity tilting mechanism. A film thickness of $0.1\delta_{99}$ shows a higher critical viscosity ratio compared to $0.05\delta_{99}$. For a given viscosity ratio a thicker film absorbs the mean shear to a greater extent and therefore the coupling between mean shear and normal velocity is weaker. This implies that the vorticity tilting mechanism is expected to be weaker for a thicker film. This prediction is substantiated by figure 4.15 which shows that the coupling coefficient, optimized over all k_x, k_y and k_z, is higher for the thinner film. Since the interface deformation mechanism is enhanced by lowering the viscosity ratio the critical viscosity is higher for the thicker film.

The streamwise oriented vortices used as an initial condition to the initial value problem lead to temporal amplification in two-fluid boundary layers. This temporal amplification is reduced by introducing a thin film for a specific initial condition. However such a conclusion cannot be generalized to all initial conditions unless the optimal perturbation which leads to maximum temporal amplification is examined. Reduction in streak amplitude due to the presence of low viscosity wall-films can be asserted only if a reduction in the temporal amplification of optimal perturbations is observed. Moreover, the solution to the initial value problem indicated presence of a critical viscosity ratio, μ_{crit}, below which the interface deformation mechanism can dominate over the vorticity tilting mechanism. Hence, μ_{crit} is defined as the viscosity ratio at which energy amplification is minimum. In the following section a non-modal analysis of two-fluid boundary layers is conducted to answer the following questions:

(a) What is the critical viscosity ratio at which energy amplification because of the interface deformation mechanism exceeds that of the vorticity tilting mechanism ?
(b) What initial condition leads to maximum transient growth and what is the extent of amplification achieved ?

4.4 Optimal disturbances

The maximum transient amplification of perturbation energy achievable, optimized over all initial conditions, is computed by the method proposed by Reddy & Henningson (1993). The energy norm for a single-fluid system leads to a convergent series in terms of the eigenfunctions of the Orr-Sommerfeld and Squire equations. Convergence here refers to the norm reaching to a finite value upon inclusion of larger number of eigenfunctions. For a two-fluid boundary layer the energy norm presents non-convergence problems. The non-convergence of the energy norm is related to perturbation energy growth caused by the work done by stresses across the interface. Hence, convergence can be achieved by accounting for the energy associated with the interface (South & Hooper, 1999). Numerous norms have been proposed to achieve convergence for different flow configurations: for instance South & Hooper (1999) proposed the h-norm for two-layer Poiseuille flow, Yecko & Zaleski (2005) proposed a norm including the energy associated with surface tension in a mixing layer. Neither of the norms lead to convergence for a two-fluid boundary layer. The M-norm suggested by Malik & Hooper (2007) for two-layer Poiseuille flow leads to convergence for a two-fluid boundary layer and is therefore used in this work. A further discussion on convergence of the kinetic energy and the M-norm is presented in appendix F.

An infinitesimal disturbance, $q \equiv [v_{\vec{k}}\ \eta_{\vec{k}}\ f_{\vec{k}}]^T$, present in the mean flow can be expressed in terms of the eigenfunctions of the Orr-Sommerfeld and Squire equations,

$$q(y,t) \quad = \quad \lim_{N\to\infty} \sum_{n=1}^{N} K_n(t) q_n(y) \tag{4.25}$$

assuming that the eigenfunctions of equation 2.8, $q_n \equiv [\phi_{\vec{k},n}\ \chi_{\vec{k},n}\ f_{\vec{k},n}]^T$, form a complete basis. The system of ordinary differential equations governing the time varying coefficients, $K_n(t)$, is obtained by substituting 4.25 into equation 4.2 and using equations 2.8

and 4.5,

$$\frac{d}{dt}K_n(t) \quad = \quad -i\omega_n K_n(t).$$

Therefore, $K_n(t) = K_n(0)e^{-i\omega_n t}$. For computational purposes, the series 4.25 is truncated at a sufficiently large but finite value of $N \approx 150$. A measure of disturbance energy, $\|q\|_E$, is defined as follows,

$$\begin{aligned}\|q\|_E \quad \equiv \quad & \frac{1}{4k^2\ell}\Bigg[\rho_B \int_0^{y_f} (|d_y v_{\vec{k}}|^2 + k^2|v_{\vec{k}}|^2 + |\eta_{\vec{k}}|^2)dy + \\ & \rho_T \int_{y_f}^{\infty} (|d_y v_{\vec{k}}|^2 + k^2|v_{\vec{k}}|^2 + |\eta_{\vec{k}}|^2)dy + k^2\mathscr{M}|(\frac{1}{\mu_{BT}} - 1)||f_{\vec{k}}|^2\Bigg] \end{aligned} \tag{4.26}$$

where $\mathscr{M} = 0.2$ (Malik & Hooper, 2007). The value of $\mathscr{M}$ is chosen such that the change in disturbance energy $\|q\|_E$ is less than 0.1% with an increase in N in the expansion 4.25. The maximum transient amplification at time t is defined as,

$$G(t) \equiv \max_{q_0} \frac{\|q\|_E}{\|q_0\|_E}. \tag{4.27}$$

where q_0 is $q(y, 0)$. In order to compute the transient amplification curve, $G(t)$, the expansion 4.25 is substituted into 4.26, which yields

$$\|q\|_E \quad = \quad \|K^*\Lambda^* M \Lambda K\|_E$$

where the elements of M are defined as follows,

$$\begin{aligned} M_{m,n} \quad = \quad & \frac{1}{4k^2\ell}\Bigg[\rho_B \int_0^{y_f} (d_y\phi_m^* d_y\phi_n + k^2\phi_m^*\phi_n + \chi_m^*\chi_n)dy + \\ & \rho_T \int_{y_f}^{\infty} (d_y\phi_m^* d_y\phi_n + k^2\phi_m^*\phi_n + \chi_m^*\chi_n)dy + k^2\mathscr{M}\left|\frac{1}{\mu_{BT}} - 1\right| f_m^* f_n\Bigg] \end{aligned}$$

where the subscripts m, n denote the eigenmodes of equation 2.8. The column vector, K, contains all the coefficients, $K_n(0)$, and Λ is a diagonal matrix comprising of elements, $\Lambda_{n,n} = e^{-i\omega_n t}$. Since M is hermitian and positive definite, it can be factorized as, $M = F^*F$ and the expression for disturbance energy can be further simplified to,

$$\|q\|_E \quad = \quad \|F\Lambda K\|_2.$$

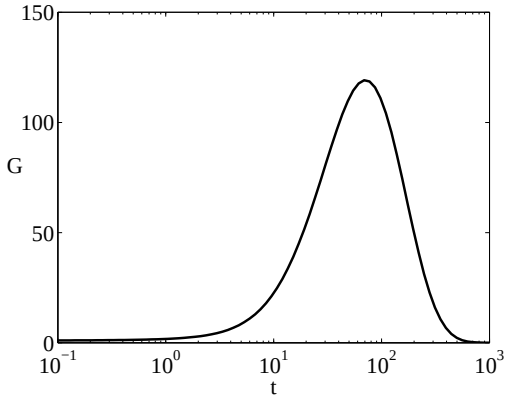


Figure 4.16: Maximum energy amplification, $G(t)$ for a single fluid boundary layer. $k_x = 0.001, k_z = 2, Re = 800$

Hence the transient amplification curve, $G(t)$, can be expressed as,

$$\begin{aligned} G(t) &= \max_{q_0} \frac{\|F\Lambda K\|_2}{\|FK\|_2} \\ &= \max_{q_0} \frac{\|F\Lambda F^{-1}FK\|_2}{\|FK\|_2} \\ &= \|F\Lambda F^{-1}\|_2. \end{aligned} \tag{4.28}$$

The current objective is to identify optimal disturbances which lead to maximum transient growth at a target time in two-fluid boundary layers.

4.4.1 The single-fluid boundary layer

The maximum amplification curve, $G(t)$, in figure 4.16 shows that the energy amplifies on the time-scale $O(10^2)$. At a longer time $t > 100$ there is no amplification as all the modes are stable. The only amplification mechanism present in the system is the vorticity tilting mechanism which can lead to a maximum amplification on the $O(10^2)$. Each point on the curve, $G(t)$, corresponds to a different initial condition. The quantity $G_{max} \equiv \max_t G(t)$ is defined in order to estimate the maximum growth achievable and the associated initial condition is denoted as the optimal disturbance.

The vector plot in figure 4.17 shows the initial condition corresponding to G_{max}. The optimal disturbance is a streamwise oriented vortex present inside the boundary layer. Streamwise oriented vortices have also been reported as the optimal disturbance

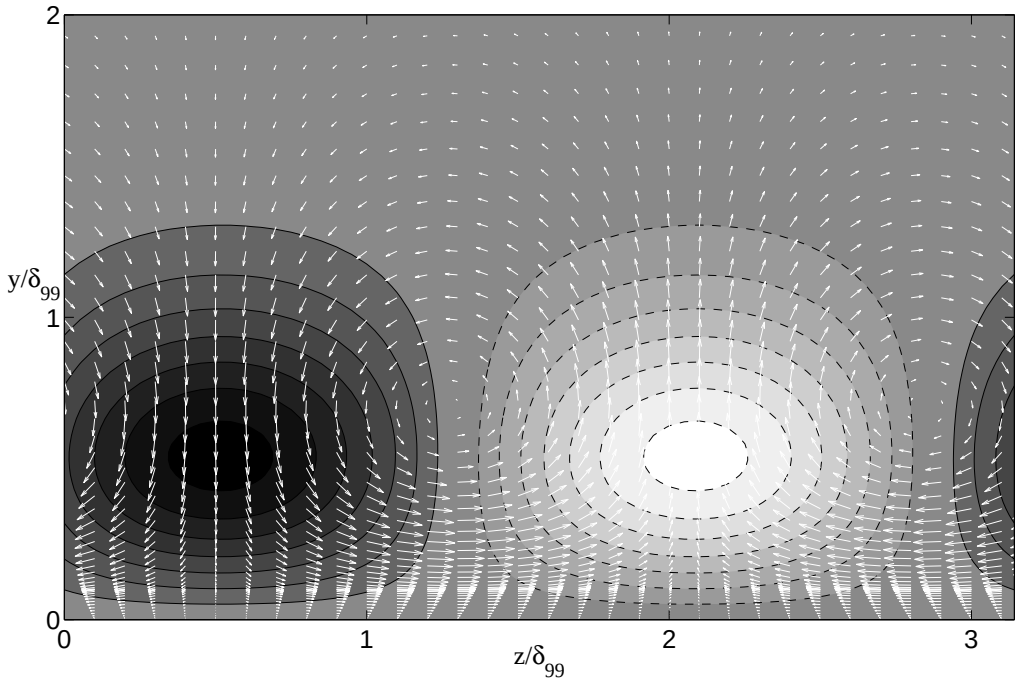


Figure 4.17: Optimal perturbation which gives rise to maximum amplification. The velocity vector plot shows the initial disturbance field comprising of primarily (v, w) components. The contour plot shows the contours of streamwise velocity at the instant of maximum amplification ($t = 75.6$) with solid and dashed lines denoting positive and negative velocity fluctuations respectively. Contour levels are from $[-5, 5]$ with a spacing of 0.5. $k_x = 0.001, k_z = 2, Re = 800$.

by Butler & Farrell (1992) at a supercritical Reynolds number for streamwise independent perturbations. The contour plot shows the streamwise velocity perturbation field at the instant of maximum amplification. The location of maximum streamwise velocity perturbation coincides with the regions of upwelling and downwelling in the initial condition. As a result the strongest response occurs at the location where normal velocity perturbation is maximum.

The eigenvalue spectrum consists only of the continuous spectrum as shown in figure 4.18(a). Hultgren & Gustavsson (1981) have shown that the Laplace transform of the normal velocity equation does not possess any discrete poles, rather a branch cut corresponding to the continuous spectrum in the limit $k_x\delta_{99} \to 0$. The corresponding

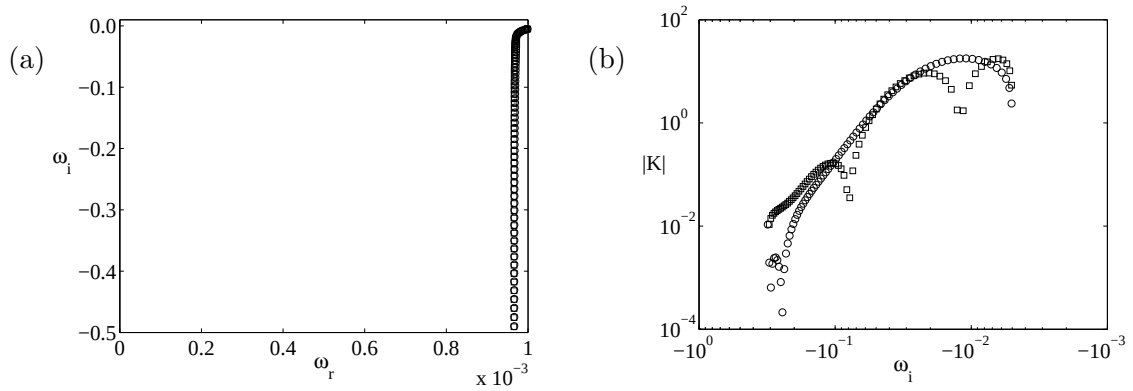


Figure 4.18: (a) Eigenvalue spectrum for a single fluid boundary layer, $k_x = 0.001, k_z = 2, Re = 800$. (b) Projection spectrum for a single fluid boundary layer, $k_x = 0.001, k_z = 2, Re = 800$. □: Orr-Sommerfeld modes. ○: Squire modes.

projection spectrum showing the amplitude, K_n, of each mode in figure 4.18(b) reveals that energy-containing scales have a decay rate on the $O(10^{-2})$. From the dispersion relation for the continuous modes, 3.1, it is concluded that the length-scale, $1/k_y$ of energy-containing modes is $O(\delta_{99})$. Since the vorticity tilting mechanism depends on the mean shear, $d_y U$, which varies on $O(\delta_{99})$, the energy-containing scales are likely to be of the same order.

Figure 4.19 shows the contours of G_{max} for a single-fluid boundary layer. The contours of G_{max} are similar to those of the coupling coefficient in figure 4.4. The coupling coefficient therefore qualitatively predicts the variation in energy amplification with k_x and k_z due to the vorticity tilting mechanism. Perturbations with a large streamwise lengthscale generate strong amplification, an observation consistent with transient growth characteristics of shear flows (Butler & Farrell, 1992). An optimum spanwise wavenumber, $k_z \sim O(\delta_{99})$, which leads to maximum amplification in kinetic energy is also observed. The quantity G_{opt} is defined as $\max_{(k_x,k_z)} G_{max}$ and the corresponding wavenumber as (k_x^o, k_z^o). The energy amplification, G_{opt}, is the same order as that observed in the initial value problem.

Having examined the maximum amplification caused by the tilting of mean vorticity, the focus is shifted to the optimal perturbations for a two-fluid boundary layer in the following subsection. In order to evaluate the combined effect of the two competing mechanisms, results are presented for a viscosity ratio near μ_{crit}.

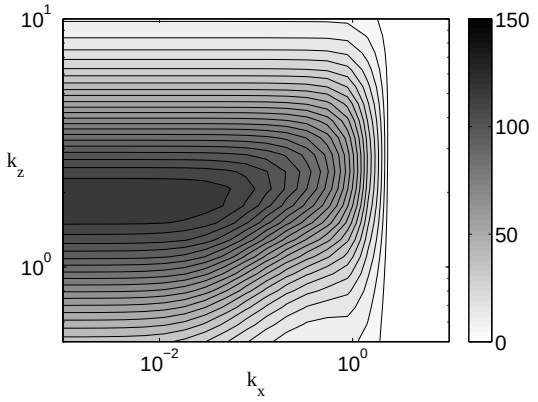


Figure 4.19: Contours of G_{max} for a single fluid boundary layer, $Re = 800$. Contour levels correspond to $0 \leq \theta \leq 150$ at an increment of 5.

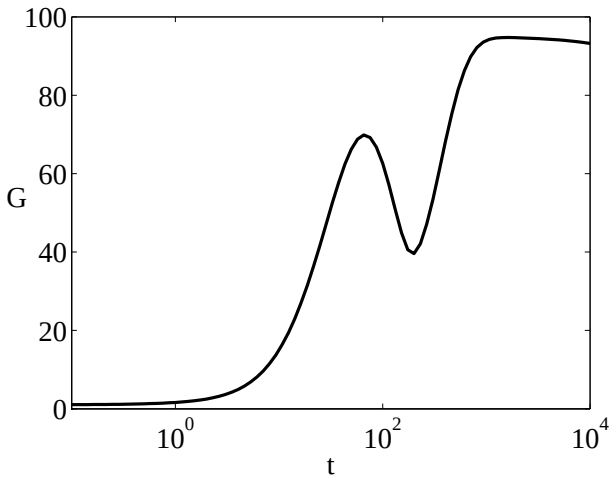


Figure 4.20: Maximum energy amplification, $G(t)$ for a two-fluid boundary layer. $k_x = 0.001, k_z = 2, Re = 800, \mu_{BT} = 0.3, \delta_B = 0.1$.

4.4.2 The two-fluid boundary layer

Figure 4.20 shows the variation in the energy amplification envelope with time for a two-fluid boundary layer near the critical viscosity ratio. Two distinct peaks in energy amplification can be observed, the first on a time-scale $O(10^2)$ and the second on a time-scale $O(10^3)$. These time-scales correspond to the vorticity tilting mechanism and the interface deformation mechanism respectively, as was observed in figure 4.13(a). The energy amplification due to the interface deformation mechanism exceeds that due to the vorticity tilting mechanism at this viscosity ratio.

The corresponding eigenvalue spectrum is shown in figure 4.21. There exists an interfacial mode along with the continuous spectrum. The initial amplitudes of each

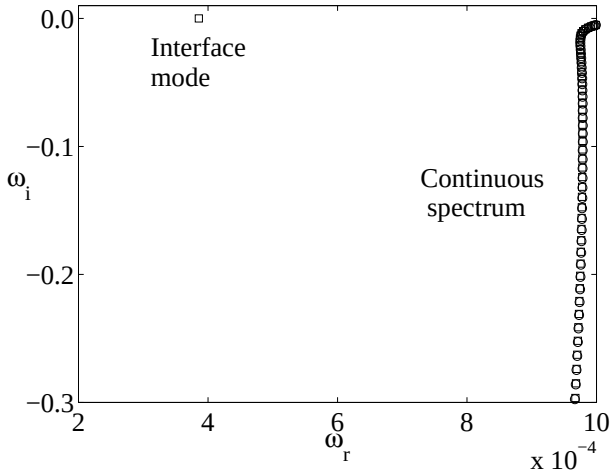


Figure 4.21: Eigenvalue spectrum. $k_x = 0.001, k_z = 2, Re = 800, \mu_{BT} = 0.3, \delta_B = 0.1$. □: Orr-Sommerfeld modes. ○: Squire modes.

of these eigenmodes corresponding to the first peak in figure 4.20 are shown in figure 4.22. The interface mode is almost neutrally stable and has an amplitude on the same order as the energy-containing scales. The energy-containing modes for the two-fluid boundary layer are also $O(\delta_{99})$ similar to the single-fluid boundary layer. Since the decay rate depends on Reynolds number and wavenumber which are identical to that of the single-fluid boundary layer the wall-normal scale remains unaltered.

The vector plot in figure 4.23 shows the initial perturbation velocity field for the optimal disturbance. The free-stream is virtually disturbance free and the disturbance varies on a scale $O(\delta_{99})$ as suggested by the amplitudes of the energy-containing scales. The optimal disturbance is a streamwise oriented vortex located inside the boundary layer. The contours of streamwise velocity perturbation field are shown at the instant of maximum amplification. The location of maximum u perturbation coincides with regions of upwelling and downwelling indicating the dominance of vorticity tilting mechanism.

The projection spectrum for the optimal disturbance corresponding to the second peak is quite similar to that of the first peak as shown in figure 4.24. The modes with high amplitudes have a length-scale $O(\delta_{99})$ in this case as well. The neutrally stable interface mode also has an amplitude on the same order as the high amplitude modes. The relative contribution from the interface mode is only marginally higher for this case. It was found that $|K_{int}|/\max_n |K_n| = 0.34, 0.37$ for the optimal disturbances of the first and second peaks respectively. The initial perturbation velocity field in figure 4.25 shows

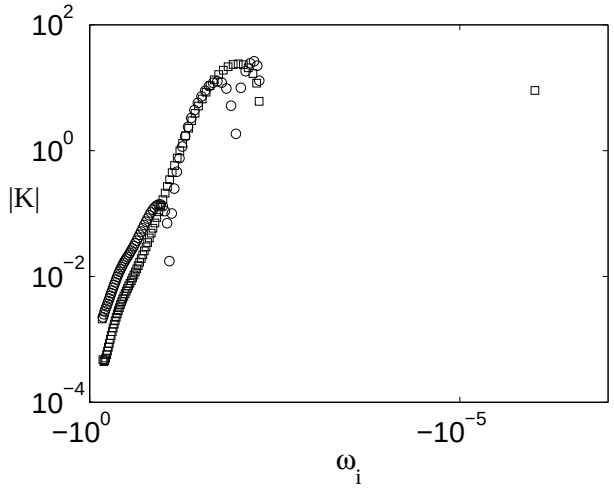


Figure 4.22: Projection spectrum, K_n,. $k_x = 0.001, k_z = 2, Re = 800, \mu_{BT} = 0.3, \delta_B = 0.1$. □: Orr-Sommerfeld modes. ○: Squire modes. $k_x = 0.001, k_z = 2, Re = 800, \mu_{BT} = 0.3, \delta_B = 0.1$.

that the optimal perturbation is also a streamwise oriented vortex in the top fluid. Inside the film however, there exists a strong w perturbation unlike the optimal disturbance for the first peak. The streamwise velocity perturbation contours at the instant of maximum amplification are quite unlike those in figure 4.23. The location of maximum u perturbation do not coincide with the region of upwelling and downwelling. Instead they originate from the interface, a signature of the interface deformation mechanism. There exists a phase change across the interface due to the jump in mean velocity gradient. An upward displacement of the interface requires the less viscous lower fluid to slow down and the top fluid to accelerate, since the mean gradient of the film is higher than that of the upper layer. The difference in the initial conditions is further highlighted by the displacement of the interface as shown in figure 4.26(a). Figure 4.26(b) shows that the ratio of interfacial displacements, $\frac{|f(t)|}{|f(0)|}$, due to the optimal disturbance of the second peak is an order of magnitude lower than that due to the first peak for $t > 1$.

In the following section, the effect of variation in viscosity on the maximum temporal amplification is examined. The investigation is restricted to low viscosity films ($\mu_{BT} \leq 1$) to ensure the absence of modal instabilities. In order to remove the effects of density stratification and surface tension, the density ratio is chosen as unity and the We^{-1} is set to zero respectively. However density stratification and surface tension can affect transient growth; for example see Yecko & Zaleski (2005) and Yecko (2008) for the cases

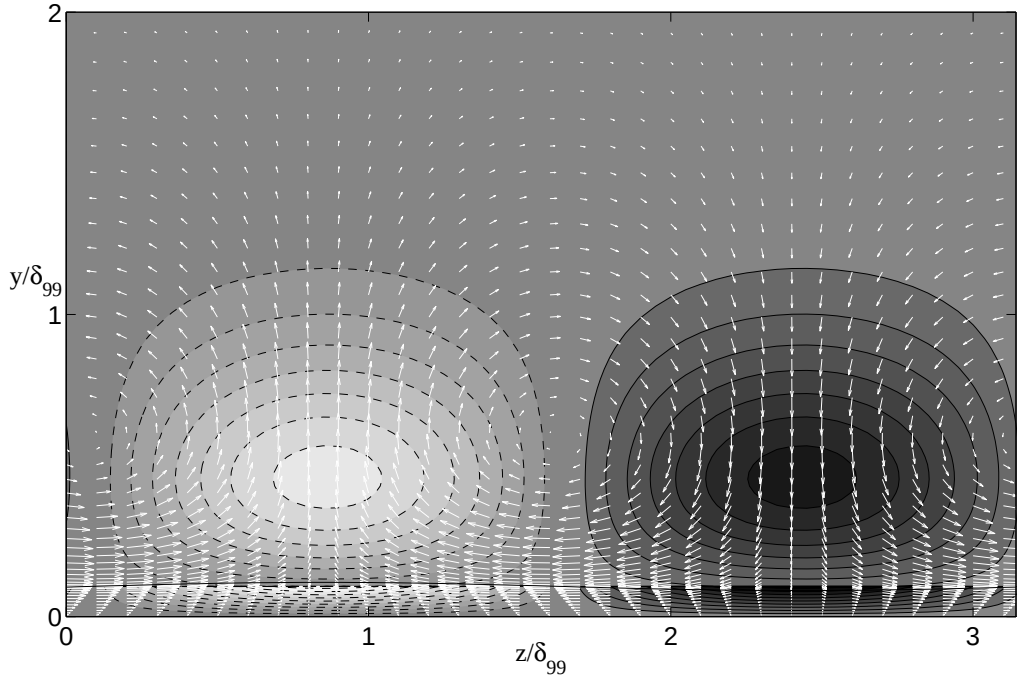


Figure 4.23: Optimal perturbation for the first peak. The velocity vector plot shows the initial disturbance field comprising of primarily (v, w) components. The contour plot shows the contours of streamwise velocity at the instant of maximum amplification ($t = 69.5$). The solid and dashed lines denote positive and negative velocity fluctuations respectively. Contour levels are from $[-5, 5]$ with a spacing of 0.5. $k_x = 0.001, k_z = 2, Re = 800, \mu_{BT} = 0.3, \delta_B = 0.1$.

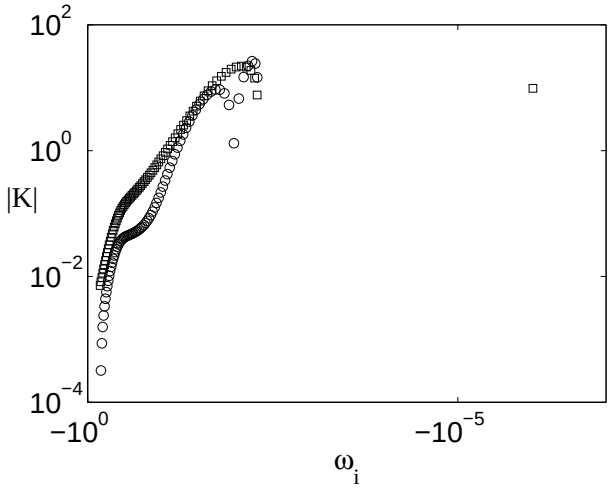


Figure 4.24: Projection spectrum, K_n,. $k_x = 0.001, k_z = 2, Re = 800, \mu_{BT} = 0.3, \delta_B = 0.1$. □: Orr-Sommerfeld modes. ○: Squire modes. $k_x = 0.001, k_z = 2, Re = 800, \mu_{BT} = 0.3, \delta_B = 0.1$.

of mixing layer and channel flow respectively.

4.4.3 Viscosity stratification effects

Figure 4.27 shows the envelope of maximum transient amplification achievable at any instant of time for various viscosity ratios. The single fluid boundary layer shows a single peak whereas the two-fluid boundary layers show two peaks. Multiple peaks for $G(t)$ in two-fluid flows have been reported by other researchers as well (Yecko & Zaleski, 2005; Olsson & Henningson, 1995). The first peak in $G(t)$ reduces with reduction in viscosity ratio μ_{BT} whereas the second peak increases. This observation is in accord with the fact that the vorticity tilting mechanism is weakened and the interface deformation mechanism is strengthened by reduction in μ_{BT}.

It is observed that the amplification due to the tilting of mean vorticity near the critical viscosity ratio is reduced by a factor of two compared to the single-fluid case. This implies that the strongest streaks can at best be only half as strong as those observed in single-fluid boundary layers. Since the vorticity tilting mechanism for streak generation is weakened sufficiently, it is plausible that the downstream non-linear breakdown may not occur by this route. The time-scale on which the interface deformation mechanism becomes significant is large and it is unclear whether it would affect transition.

The maximum amplification factor, G_{max}, is computed over a range of streamwise

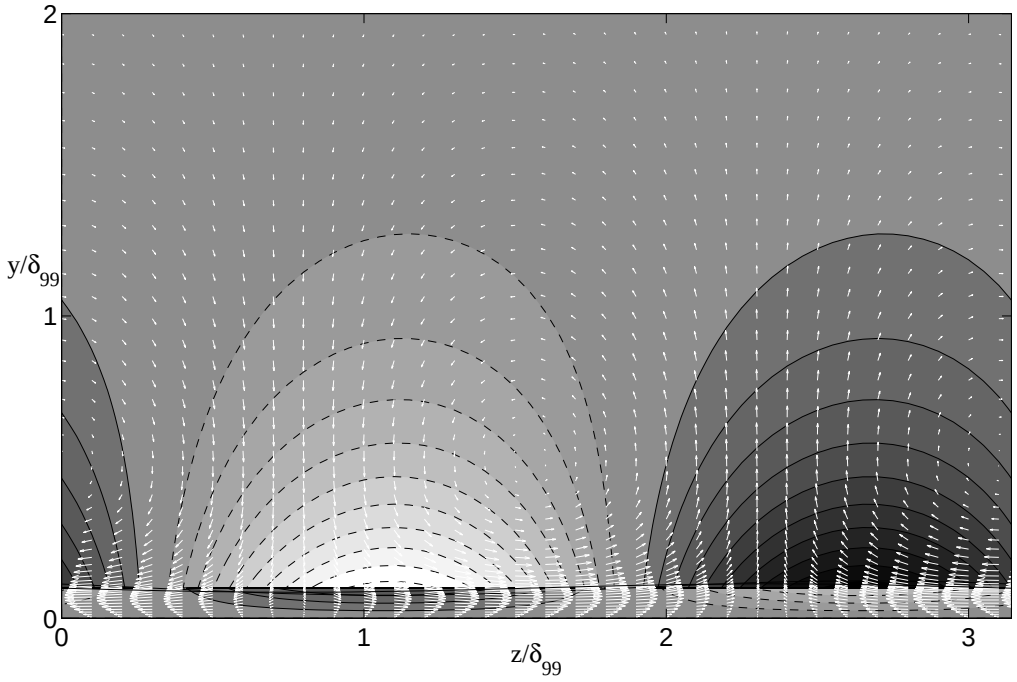


Figure 4.25: Optimal perturbation for the second peak. The velocity vector plot shows the initial disturbance field comprising of primarily (v, w) components. The contour plot shows the contours of streamwise velocity at the instant of maximum amplification ($t = 1624$). The solid and dashed lines denote positive and negative velocity fluctuations respectively. Contour levels are from $[-5, 5]$ with a spacing of 0.5. $k_x = 0.001, k_z = 2, Re = 800, \mu_{BT} = 0.3, \delta_B = 0.1$.

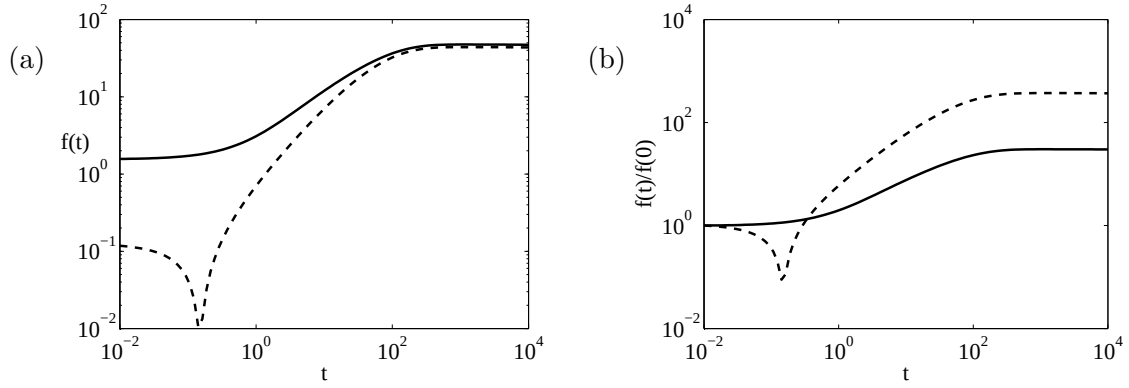


Figure 4.26: Variation in interfacial displacement of the optimal disturbance with time. (a)$|f(t)|$. (b) $\frac{|f(t)|}{|f(0)|}$. $k_x = 0.001, k_z = 2, Re = 800, \mu_{BT} = 0.3, \delta_B = 0.1$. - - -, First peak; ——, Second peak

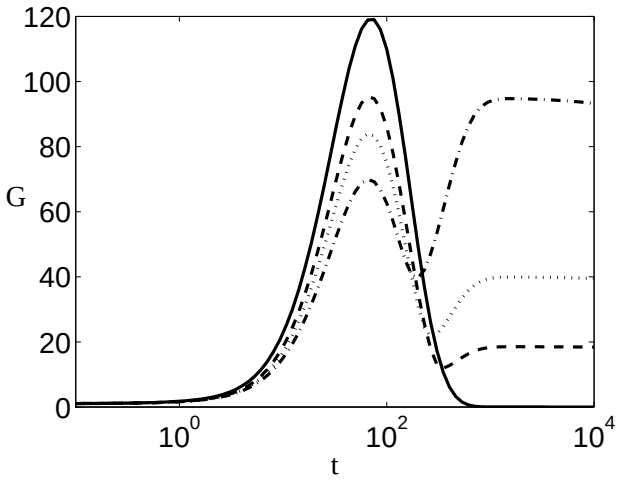


Figure 4.27: Variation in $G(t)$ with μ_{BT}. $k_x = 0.001, k_z = 2, Re = 800, \delta_B = 0.1$.——, $\mu_{BT} = 1$; - - -, $\mu_{BT} = 0.5$; · · · ·, $\mu_{BT} = 0.4$; — · —, $\mu_{BT} = 0.3$

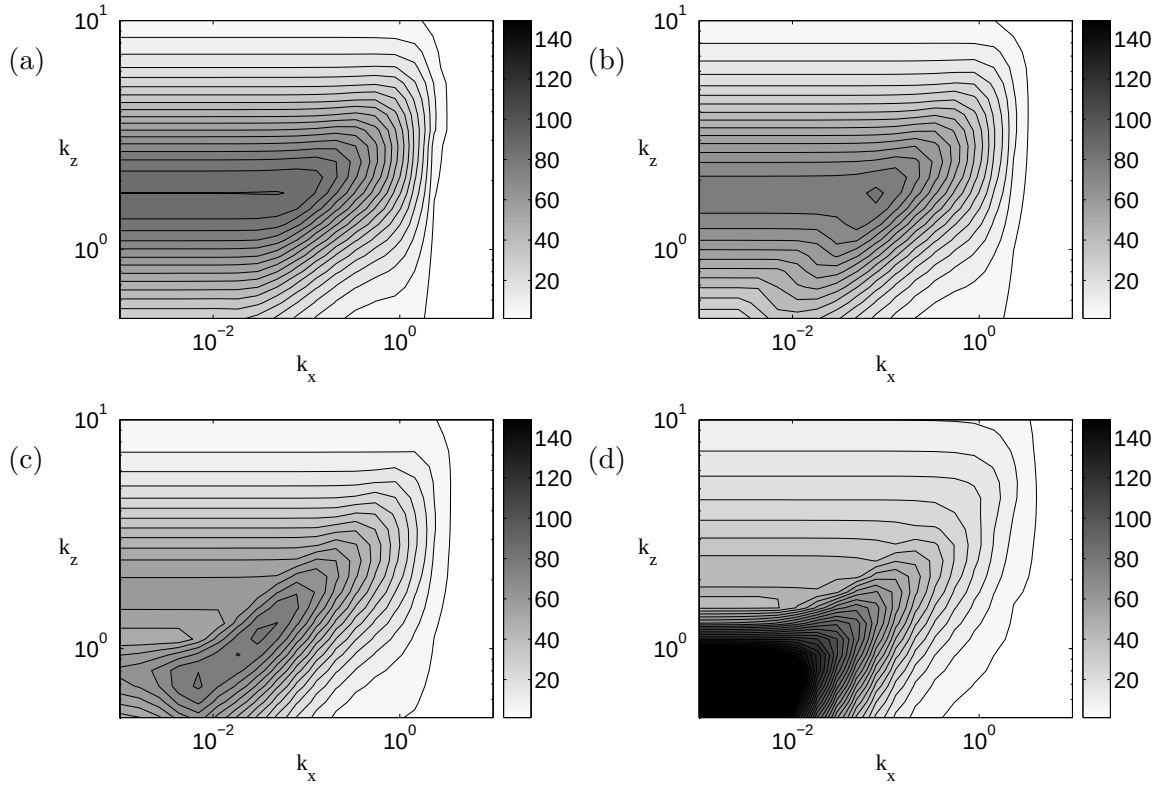


Figure 4.28: Contours of G_{max} at various viscosity ratios. (a) $\mu_{BT} = 0.5$. (b) $\mu_{BT} = 0.4$. (c) $\mu_{BT} = 0.3$. (d) $\mu_{BT} = 0.2$. $Re = 800, \delta_B = 0.1$.

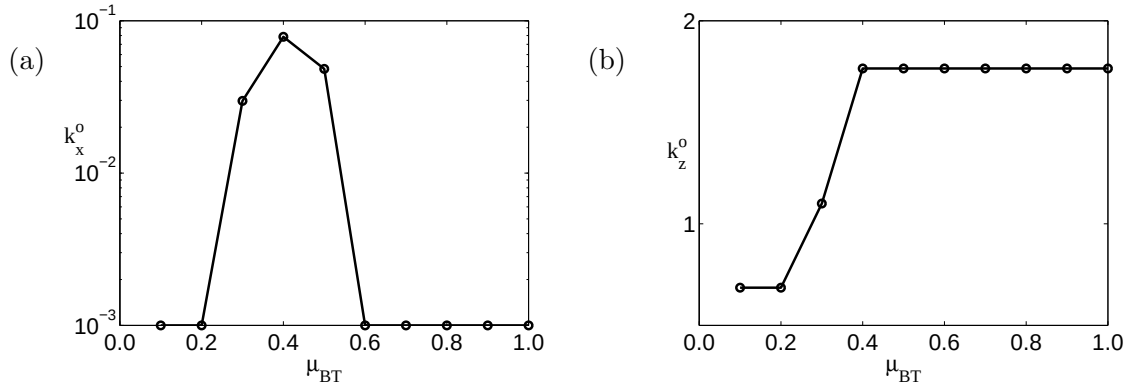


Figure 4.29: Locus of (a) k_x^o and (b) k_z^o as a function of μ_{BT}. $Re = 800, \delta_B = 0.1$.

and spanwise wavenumbers to identify the regime of dominance of both energy growth mechanisms. Figures 4.28(a)-(d) show the contour plots of G_{max} at four different viscosity ratios near μ_{crit}. At the viscosity ratio $\mu_{BT} = 0.5$ (figure 4.28 a) the contours are identical to those for a single-fluid boundary layer (see figure 4.19). This shows that, the tilting of mean vorticity dominates at this viscosity ratio. As the viscosity ratio is reduced to $\mu_{BT} = 0.4$ (figure 4.28 b), the contours change slightly for $k_x \ll O(1)$ and $k_z \sim O(1)$ and the contours are distorted further for $\mu_{BT} = 0.3$ (figure 4.28 c). Figure 4.28(c) shows the emergence of two distinct regions, where each mechanism is dominant. It can also be inferred from figures 4.28(b) and 4.28(c) that the interface deformation mechanism is most dominant for $k_x \ll O(1)$ and $k_z \sim O(1)$. This conclusion is confirmed in figure 4.28(d) where G_{max} due to the interface deformation mechanism at $\mu_{BT} = 0.2$ exceeds that due to the vorticity tilting mechanism for a single-fluid boundary layer. Figures 4.29(a-b) show the locus of optimal wavenumbers, (k_x^o, k_z^o), at different viscosity ratios. The optimum streamwise wavenumber for both mechanisms is $O(10^{-3})$ except for viscosity ratios near $\mu_{crit} \approx 0.3$ where k_x^o increases by two orders of magnitude. The optimal spanwise wavenumber is found to be $1.7652, 0.6854$ for the vorticity tilting and interface deformation mechanisms respectively.

Finally, G_{opt} is presented for a range of viscosity ratios for two different film thicknesses in figure 4.30. The maximum amplification, G_{opt}, reduces gradually for viscosity ratios $0.6 < \mu_{BT} < 1$. As the viscosity ratio is reduced further G_{opt} decreases sharply, similar to the behavior of the optimum coupling coefficient in figure 4.15. However as μ_{crit} is approached, the energy of the interface mode increases sharply as reported in figure 4.9(b), showing how the dominant linear mechanism for temporal amplification

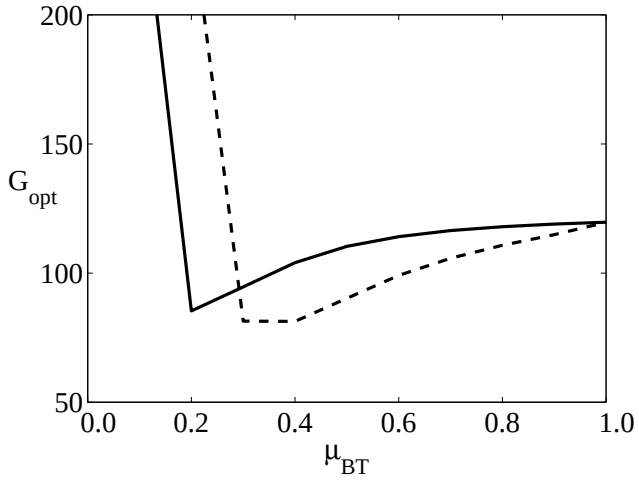


Figure 4.30: Variation in G_{opt} with μ_{BT}. $Re = 800$. ——, $\delta_B = 0.1$; - - -, $\delta_B = 0.05$

changes its nature. The critical viscosity ratio is a function of the film thickness and a thinner film has a lower critical viscosity ratio compared to a thicker film. This conclusion also agrees with the observation that thicker films have lower coupling coefficients and that the interface deformation mechanism is dominant at low viscosity ratios. The extent to which G_{opt} is reduced is nearly equal for both film thicknesses.

It is instructive to consider the implication of reduction in G_{opt} on the transition Reynolds number. A heuristic inference is drawn based on the transition prediction scheme of Andersson *et al.* (1999) who suggested

$$Re_T Tu^2 = K/G_{opt}.$$

The transitional Reynolds number Re_T and the turbulent intensity Tu are related to the maximum transient growth G_{opt} by an empirical constant evaluated from experiments of Voke & Yang (1995); Roach & Brierley (1992). Figure 4.30 shows that G_{opt} is reduced nearly to two-thirds of the single-fluid value at the critical viscosity ratio. The transition prediction formula indicates that the transition Reynolds number could be increased by a factor of 50% for the optimal viscosity ratio for the same turbulence intensity. This estimate is however very crude and more accurate predictions could be sought from direct numerical simulations.

4.5 Conclusion

In this chapter, the temporal growth of linear perturbations in a two-fluid boundary layer was examined. In order to study the evolution from any initial condition, an initial value problem was formulated in terms of the normal velocity, vorticity and interface displacement. The solution to the initial value problem was obtained in terms of the Orr-Sommerfeld and Squire modes. The evolution of a streamwise oriented vortex was traced using the solution to the initial value problem. In order to construct the streamwise oriented vortex, the interface and a continuous mode were used with amplitudes such that the resulting interface deformation is zero. It was found that the normal velocity decays monotonically with time, whereas the displacement of the interface increases initially before decay sets in. The normal vorticity response amplified initially due to tilting of mean vorticity and later due to growth of interface displacement. In this analysis, these disturbance generation mechanisms were referred to as (a) the vorticity tilting mechanism and (b) the interface deformation mechanism respectively.

The asymptotic analysis in section 4.3.3 revealed that the normal velocity associated with the interface mode is $O(k_x\delta_{99})$ in the long-wavelength limit. This implies that the normal velocity associated with the continuous mode is much higher than that of the interface mode. Since the tilting of mean vorticity depends on the coupling between mean shear and normal velocity, the normal vorticity generation due to this mechanism was observed only on a short time-scale, $O(Re/(k_x^2 + k_y^2 + k_z^2))$, associated with the viscous decay of the continuous mode. In order to quantify the potency of the mechanism, a coupling coefficient suggested by Zaki & Durbin (2005) was used. The coupling coefficient indicated that, as the viscosity ratio μ_{BT} is reduced, the coupling between mean shear and normal velocity is weakened. As a result, the normal vorticity amplified. Thicker films tend to absorb the mean shear to a greater extent, thereby rendering the mechanism less effective in causing energy amplification for low viscosity films. It was also reported that long wavelength disturbances with spanwise wavelength of approximately two boundary layer thicknesses lead to maximum transient growth due to this mechanism.

The interface mode is neutrally stable to leading order in the long-wavelength limit, whereas the continuous modes decay on a much shorter time-scale. As a result, the interfacial displacement, which is initially zero, increases and is finite at long time. In

order to compensate for the discontinuity in the mean velocity gradient, a normal vorticity perturbation develops at the interface for $t \gg O(Re/(k_x^2 + k_y^2 + k_z^2))$. It was found that the energy, E_η, associated with the interface mode increases as μ_{BT} decreases and hence the energy amplification due to this mechanism. The competition between the two mechanisms gives rise to a critical viscosity ratio at which energy amplification is minimum. Computation of the optimal disturbances revealed that thinner films have a lower μ_{crit} and G_{opt} can be reduced to two-thirds its value for a Blasius boundary layer.

Chapter 5

Conclusions

5.1 Summary and key results

The linear stability of boundary layers plays a vital role in explaining the events which precede the onset of transition. The focus of this work has been to assess the extent to which the stability of a boundary layer is affected by a wall-film. In order to investigate the linear stability of the flow, three criteria were identified:

a) The modal stability of two-fluid boundary layers.

b) The extent of vortical mode penetration into the boundary layer.

c) The transient amplification of linear disturbances, or the non-modal stability.

In the following subsections the key results are briefly summarized. The section thereafter, includes a discussion of how the findings of the current work relate to laminar flow control.

5.1.1 Modal stability

In chapter 2 the modal stability of boundary layers was examined. The Orr-Sommerfeld and Squire equations which govern the linear stability of a viscous parallel flow were solved and the various exponentially unstable modes were reported. In order to classify the various instabilities, the kinetic energy equation was derived and the dominant mechanisms which transfer energy to the perturbation from the mean flow were

identified.

The two-fluid boundary layer exhibited three more modal instabilities in addition to the Tollmien–Schlichting wave. These were the soft mode, short wavelength instability and high Reynolds number instability. The soft mode was found to be unstable only when the lower fluid was more viscous than the upper layer. In contrast, the high Reynolds number instability existed for wall films which are less viscous than the outer stream. The short wavelength instability is present in both configurations but is stabilized in the presence of surface tension. The soft mode and short wavelength instability derive energy primarily from the work done by the shear stress at the interface. The high Reynolds number instability and the Tollmien–Schlichting wave obtain energy from the work done by Reynolds stress in the bottom and top fluids respectively.

Investigation of viscosity stratification effects revealed that the growth rate of the unstable modes is enhanced by a departure from the single fluid case. The Tollmien–Schlichting mode was destabilized as the viscosity of the lower fluid was increased. On the other hand, the high Reynolds number instability was destabilized as the viscosity of the bottom fluid was reduced. These were due to a greater contribution from the Reynolds stress mechanism. The growth rate of the soft mode and the short wavelength instability also increased with an increase in the viscosity of the bottom fluid. The destabilization is accounted for by the increase in the work done by the shear stress at the interface.

5.1.2 Modal penetration

In order to understand the ability of free-stream vortical modes to penetrate the boundary layer shear, the eigenfunctions of the continuous spectrum were examined in Chapter 3. A piecewise linear mean flow was assumed to simplify the fourth order Orr-Sommerfeld equation into a second order vorticity equation. The asymptotic analysis of the vorticity equation revealed three asymptotic regimes of penetration: a) The convective shear-sheltered regime, b) The diffusive regime and c) The convective-diffusive regime. Asymptotic solutions were derived for each regime in order to obtain further insight into the structure of these vortical modes inside the boundary layer. A physical mechanism of penetration was proposed based on the insight derived from the asymptotic analysis of the vorticity equation. Finally a norm was defined to quantify the penetration of the

continuous modes into the boundary layer.

An approach similar to the single-fluid boundary layer was adopted for the two-fluid case. A piecewise linear mean flow which imitated the two-fluid boundary layer and its variation with viscosity ratio was used to obtain the analytical solution to the Orr-Sommerfeld equation. The asymptotic solutions to the vorticity equation were obtained and the penetration regimes were identified based on the magnitude of the convective and diffusive terms. The effect of viscosity and density stratification and surface tension were evaluated numerically using the penetration depth norm.

The shear-sheltering phenomenon was explored within the framework of continuous modes of the Orr-Sommerfeld equation. The asymptotic analysis of the vorticity equation revealed that shear sheltering is the outcome of a competition between the filtering effect of mean shear and the diffusive effect of viscosity. The sheltering effect was found to be most conspicuous in the shear dominated regime, where the free-stream vorticity could penetrate only into a thin layer at the edge of the boundary layer. In the diffusion dominated limit, viscosity enhanced penetration and the free-stream oscillatory behavior was retained by the vortical modes inside the boundary layer. The convective-diffusive regime was found to exist when the convective and diffusive terms were of the same order and the modes were characterized by the partial penetration inside the boundary layer. The essence of vortical mode penetration is captured by two time-scales: a) the convective time-scale and b) the diffusive time-scale. A smaller convective time-scale implies that the vortical disturbances are convected downstream before viscosity can cause any wall-normal diffusion. Whereas, if the diffusive time-scale is smaller, then the free-stream appears to be nearly steady and the vorticity penetrates into the boundary layer.

The analysis of two-fluid boundary layer revealed the presence of a modified wall-normal wavenumber in the bottom fluid which enhances penetration in the diffusive regime. The modified wavenumber emerges in order to maintain the decay rate of the vortical mode which is prescribed by the viscosity of the outer stream. The convective shear-sheltered regime and the convective-diffusive regime were characterized by negligible and partial penetration for vortical modes respectively. These regimes exist only when the shear is located entirely inside the bottom fluid.

The investigation of viscosity and density stratification revealed the presence of

an optimum viscosity ratio for which penetration is maximum. Viscosity ratios lower than the optimal level enhance shear-sheltering and reduce the penetration of vortical modes. Increase in surface tension lead to an increase in penetration over a range of Weber numbers. However, very high surface tension caused penetration to reduce as the interface acts like a stiff membrane which resists being perturbed.

5.1.3 Non-modal stability

The non-modal stability of boundary layers was analyzed in Chapter 4 by examining the transient growth experienced by linear perturbations. Each eigenmode of the Orr-Sommerfeld and Squire equations assumes a harmonic behavior in time and is inadequate by itself to describe the temporal evolution of a general perturbation. The evolution of a general perturbation is described by a superposition of the Orr-Sommerfeld and Squire modes.

The temporal evolution of normal velocity, interface displacement and normal vorticity was analyzed by solving the initial value problem. The solution was expanded in terms of the eigenfunctions of the normal velocity, interface and homogeneous Squire equations with time varying coefficients. The adjoint problem was formulated in order to obtain the adjoint eigenfunctions which satisfy the orthogonality condition. The time varying coefficients were computed using the orthogonality property of the adjoint eigenfunctions. The normal vorticity equation was solved as a forced response problem and a transformed variable was introduced to homogenize the interfacial boundary conditions. The solution to the initial value problem can be used to describe the evolution of any general perturbation for a known wavenumber vector (k_x, k_z). In order to identify the initial condition which lead to maximum transient growth, and draw bounds on the amplification of energy of the system, the optimal disturbances were computed.

The solution to the initial value problem revealed the existence of two mechanisms which lead to amplification of normal vorticity, a) the vorticity tilting mechanism and b) the interface deformation mechanism. The former mechanism is driven by the normal velocity which tilts the mean spanwise vorticity into the wall-normal direction. It occurs on a time-scale which corresponds to the viscous decay of the normal velocity component. As the viscosity of the wall-bounded film was reduced the mechanism's potency to cause transient growth decreased. The dependence of transient growth on wavenumber was

explained based on the coupling coefficient proposed by Zaki & Durbin (2005). It was found that the coupling between mean shear and normal velocity is inhibited by lower viscosity film. In addition, it was found that thicker films are more effective in reducing transient growth due to the tilting of mean vorticity.

The interface deformation mechanism is driven by the jump in mean vorticity across the interface. The normal vorticity generated is proportional to the displacement of the interface and the mechanism becomes dominant at long time, only after the normal velocity perturbation has decayed. A reduction in viscosity of the film causes a stronger jump in mean vorticity across the interface and therefore this mechanism is dominant at low viscosity ratios.

The competition between the two vorticity generating mechanisms leads to an optimal viscosity ratio which is found by computing the optimal disturbances. The initial condition leading to maximum energy amplification for the vorticity tilting mechanism is a streamwise oriented vortex. The location of maximum streamwise velocity perturbation corresponds to the regions of upwelling and downwelling. The optimal disturbance associated with the latter mechanism is also a streamwise oriented vortex with an initial interfacial displacement, an order of magnitude higher than that of vorticity tilting mechanism. The location of maximum streamwise velocity perturbation lies in the vicinity of the interface. It was found that the maximum transient amplification is reduced by a factor of approximately two-thirds at μ_{crit} compared to the single-fluid case. It is plausible that the transition route may be altered, if transient amplification is the dominant instability mechanism in the linear stage.

5.2 Discussion

The main conclusions of this thesis indicate that the linear stability of a boundary layer is altered significantly by an immiscible wall-film. If the bottom fluid is more viscous, the flow is asymptotically unstable at all Reynolds numbers. On the contrary, a lower viscosity film enhances the asymptotic stability at low Reynolds numbers in the presence of small surface tension. The growth of the algebraic instability is also reduced over a range of viscosity ratios in this configuration. Thus, the linear stability of a boundary layer is enhanced by the introduction of lower viscosity wall-film.

Delay in transition by stabilization of the boundary layer is achieved by control

techniques for instance, wall heating/cooling (Lauchle & Gurney, 1984) and wall suction (Joslin, 1998). Since the boundary layer profile is fuller (that is a higher velocity gradient near the wall) compared to a single-fluid boundary layer the flow is inviscidly more stable. Moreover, passive flow control techniques often tend to make the mean velocity profile fuller to enhance the linear stability. Perhaps the most similar technique to the present case is wall heating/cooling. Wall heating leads to a lowering of viscosity near the wall for liquids whereas cooling leads to the same effect for gases. Liepmann & Fila (1947) who performed experiments on transition on a heated flat plate exposed to air, concluded that wall heating causes the transition location to move upstream. The authors argued that since wall heating increases the near-wall viscosity, an inflection point is introduced in the flow thereby rendering the flow inviscidly unstable. Similarly, the experimental results of Strazisar *et al.* (1977) report a reduction in spatial growth rates of instabilities for boundary layers in water due to wall heating. Lauchle & Gurney (1984) demonstrated that the transitional Reynolds number could be increased from 4.5×10^6 to 3.64×10^7 by heating an underwater body. Physical phenomena other than viscosity stratification could also play a significant role in such a case of transition delay, for instance buoyancy. However, such effects can be neglected as long as the Froude number and density ratio satisfy the criterion $|\rho_{BT} - 1| \ll U_\infty^2/(g\delta_{99})$. Also, the stabilization of the primary instability due to viscosity stratification does provide an effective technique to control transition. It is plausible that the introduction of a low viscosity wall-film has an effect similar to wall heating/cooling on the transition process. The results of the current investigation motivate further exploration of low-viscosity wall films as a means to delay transition.

Appendix A

Continuous modes for the piecewise linear boundary layer profile

A.1 Coefficients of the single-fluid eigenfunctions

A.1.1 Analytical solution

The exact analytical solution for ϕ is

$$\begin{aligned}
\phi &= C_1 \exp(-ik_y Y) + C_2 \exp(ik_y Y) + C_3 \exp(-kY),\ Y > 0, \\
\phi &= C_7 \exp(-kY) + C_8 \exp(kY) \\
&\quad + \exp(-kY) \int_{-\delta_{BL}}^{Y} \exp(ks)(C_5 Ai[\mathscr{Z}(s)] + C_6 Bi[\mathscr{Z}(s)])ds \\
&\quad + \exp(kY) \int_{Y}^{0} \exp(-ks)(C_5 Ai[\mathscr{Z}(s)] + C_6 Bi[\mathscr{Z}(s)])ds,\ -\delta_{BL} < Y < 0
\end{aligned}$$

and the coefficients are,

$$
\begin{aligned}
C_5 &= \frac{C_3}{\frac{Ai[\mathscr{Z}(0)]}{k^2+k_y^2} + A^- - A^+ - \lambda\left(\frac{Bi[\mathscr{Z}(0)]}{k^2+k_y^2} + B^- - B^+\right)} \\
C_6 &= \lambda C_5 \\
C_1 &= \frac{1}{2}\Bigg[\frac{k}{ik_y}\Big(C_5(A^- + A^+) + C_6(B^- + B^+)\Big) + \frac{k_x\tau(C_5 Ai[\mathscr{Z}(0)] + C_6 Bi[\mathscr{Z}(0)])}{\nu k_y(k^2+k_y^2)^2} \\
&\quad - \frac{C_5 Ai[\mathscr{Z}(0)] + C_6 Bi[\mathscr{Z}(0)]}{k^2+k_y^2} - C_3\Big(\frac{k}{ik_y} + \frac{k_x\tau}{\nu k_y(k^2+k_y^2)}\Big)\Bigg] \\
C_2 &= \frac{-1}{2}\Bigg[\frac{k}{ik_y}\Big(C_5(A^- + A^+) + C_6(B^- + B^+)\Big) + \frac{k_x\tau(C_5 Ai[\mathscr{Z}(0)] + C_6 Bi[\mathscr{Z}(0)])}{\nu k_y(k^2+k_y^2)^2} \\
&\quad + \frac{C_5 Ai[\mathscr{Z}(0)] + C_6 Bi[\mathscr{Z}(0)]}{k^2+k_y^2} - C_3\Big(\frac{k}{ik_y} + \frac{k_x\tau}{\nu k_y(k^2+k_y^2)}\Big)\Bigg] \\
C_7 &= 0 \\
C_8 &= -(C_5 A^+ + C_6 B^+)
\end{aligned}
\tag{A.1}
$$

where

$$
A^{\pm} = \frac{1}{2k}\int_{-\delta_{BL}}^{0} exp(\pm ks) Ai[\mathscr{Z}(s)] ds \quad , \quad B^{\pm} = \frac{1}{2k}\int_{-\delta_{BL}}^{0} exp(\pm ks) Bi[\mathscr{Z}(s)] ds,
$$

$$
\lambda = \frac{-2kA^+ + \frac{kAi[\mathscr{Z}(0)] - Ai'[\mathscr{Z}(0)]\mathscr{Z}'(0)}{k^2+k_y^2} - \frac{(3k^2+k_y^2)k_x\tau}{i\nu(k^2+k_y^2)^2}(A^- - A^+)}{2kB^+ + \frac{-kBi[\mathscr{Z}(0)] - Bi'[\mathscr{Z}(0)]\mathscr{Z}'(0)}{k^2+k_y^2} + \frac{(3k^2+k_y^2)k_x\tau}{i\nu(k^2+k_y^2)^2}(B^- - B^+)},
$$

and $\mathscr{Z}(Y) = \exp(i5\pi/6)(\frac{k_x\tau}{\nu})^{\frac{1}{3}}(Y - \frac{ik_y^2\nu}{k_x\tau})$

A.1.2 The convective shear sheltered regime

The solution for ϕ is,

$$
\begin{aligned}
\phi &= C_1\exp(-ik_yY) + C_2\exp(ik_yY) + C_3\exp(-kY),\ Y > 0, \\
\phi &= C_5\exp(-kY) + C_6\exp(kY) + C_{w_2}\exp(-\zeta(\delta_{BL}+Y)) + \\
&\quad C_{e_1}\Bigg[exp(-kY)\int_{-\delta_{BL}}^{Y} exp(-ks)Ai[\varsigma(s)]ds \\
&\quad + \exp(kY)\int_{Y}^{0} exp(-ks)Ai[\varsigma(s)]ds\Bigg],\ -\delta_{BL} < Y < 0.
\end{aligned}
$$

and the coefficients are,

$$
\begin{aligned}
C_{e_1} &= C_1\Bigg[\frac{Ai[0]}{k^2+k_y^2} + A^- - A^+ \\
&\quad +\lambda\bigg(-\frac{k_y^2+\zeta^2}{k^2+k_y^2}\exp(\zeta\delta_{BL}) + \frac{k-\zeta}{2k}\exp(-k\delta_{BL}) - \frac{k+\zeta}{2k}\exp(k\delta_{BL})\bigg)\Bigg]^{-1} \qquad \text{(A.2)}\\
C_{w_2} &= \lambda C_{e_1}\\
C_1 &= \frac{1}{2}\bigg(-C_{e_1}\frac{Ai[\varsigma(0)] + Ai'[\varsigma(0)]\frac{\varsigma'}{ik_y}}{k^2+k_y^2} + C_{w_2}(1+\frac{\zeta}{ik_y})\frac{k^2-\zeta^2}{k^2+\zeta^2}\exp(\zeta\delta_{BL})\\
&\quad -\frac{2k^2k_x\tau}{\nu k_y(k^2+k_y^2)^2}\bigg(C_{w_2}\frac{k^2-\zeta^2}{k^2+\zeta^2}\exp(\zeta\delta_{BL}) - C_{e_1}\frac{Ai[0]}{k^2+k_y^2} + C_3\bigg)\bigg)\\
C_2 &= \frac{1}{2}\bigg(-C_{e_1}\frac{Ai[\varsigma(0)] - Ai'[\varsigma(0)]\frac{\varsigma'}{ik_y}}{k^2+k_y^2} + C_{w_2}(1+\frac{\zeta}{ik_y})\frac{k^2-\zeta^2}{k^2+\zeta^2}\exp(\zeta\delta_{BL})\\
&\quad +\frac{2k^2k_x\tau}{\nu k_y(k^2+k_y^2)^2}\bigg(C_{w_2}\frac{k^2-\zeta^2}{k^2+\zeta^2}\exp(\zeta\delta_{BL}) - C_{e_1}\frac{Ai[0]}{k^2+k_y^2} + C_3\bigg)\bigg)\\
C_5 &= -\frac{k+\zeta}{2k}C_{w_2}\exp(k\delta_{BL})\\
C_6 &= -C_{e_1}A^+ - \frac{k-\zeta}{2k}C_{w_2}\exp(-k\delta_{BL}) \qquad \text{(A.3)}
\end{aligned}
$$

where,

$$
\begin{aligned}
A^{\pm} &= \frac{1}{2k}\int_{-\delta_{BL}}^{0} exp(\pm ks)Ai[\varsigma(s)]ds\\
\lambda &= \frac{\frac{1}{k^2+k_y^2}(kAi[0] - Ai'[\varsigma(0)]\varsigma'[0]) - 2kA^+ + \frac{k_x\tau(k_y^2+3k^2)}{i\nu(k^2+k_y^2)^2}(A^- - A^+)}{(k-\zeta)\bigg(e^{-k\delta_{BL}} - \frac{k_y^2+\zeta^2}{k^2+k_y^2}e^{\zeta\delta_{BL}}\bigg) - \frac{k_x\tau(k_y^2+3k^2)}{i\nu(k^2+k_y^2)^2}\bigg(e^{\zeta\delta_{BL}} - \frac{k-\zeta}{2k}e^{-k\delta_{BL}}\bigg)},
\end{aligned}
$$

$\varsigma(Y) = \exp(i5\pi/6)(\frac{k_x\tau}{\nu})^{1/3}(Y)$ and $\zeta = \frac{(1-i)}{\sqrt{2}\delta_w}$.

A.1.3 The diffusive regime

The solution for ϕ is,

$$
\begin{aligned}
\phi &= C_1\exp(-ik_yY) + C_2\exp(ik_yY) + C_3\exp(-kY),\ Y>0,\\
\phi &= C_5\exp(-ik_yY) + C_6\exp(ik_yY) + C_7\exp(-kY) + C_8\exp(kY),\ -\delta_{BL}<Y<0.
\end{aligned}
$$

and the coefficients are,

$$\begin{aligned}
C_5 &= 2\frac{C_3\exp(-ik_y\delta_{BL})}{((-1+\frac{ik_y}{k})+\lambda(1+\frac{ik_y}{k}))\exp(k\delta_{BL})+(-(1+\frac{ik_y}{k})+\lambda(1-\frac{ik_y}{k}))\exp(-k\delta_{BL})}\\
C_6 &= -\lambda C_5\exp(i2k_y\delta_{BL})\\
C_1 &= C_5+\frac{k^2k_x\tau}{\nu k_y(k^2+k_y^2)^2}(C_5+C_6+C_3)\\
C_2 &= C_6-\frac{k^2k_x\tau}{\nu k_y(k^2+k_y^2)^2}(C_5+C_6+C_3)\\
C_7 &= -\frac{\exp(-k\delta_{BL})}{2}\left((1+\frac{ik_y}{k})C_5\exp(ik_y\delta_{BL})+(1-\frac{ik_y}{k})C_6\exp(-ik_y\delta_{BL})\right)\\
C_8 &= -\frac{\exp(k\delta_{BL})}{2}\left((-1+\frac{ik_y}{k})C_5\exp(ik_y\delta_{BL})-(1-\frac{ik_y}{k})C_6\exp(-ik_y\delta_{BL})\right).
\end{aligned}$$

where,

$$\begin{aligned}
\lambda &= \frac{(2k+\alpha)(-1+\frac{ik_y}{k})\exp(k\delta_{BL})+\alpha}{(-2k+\alpha)(1+\frac{ik_y}{k})\exp(k\delta_{BL})+\alpha},\\
\alpha &= \frac{ik_x\tau(3k^2+k_y^2)}{\nu(k^2+k_y^2)^2}.
\end{aligned}$$

A.1.4 The convective-diffusive regime

The oscillatory solution near the edge of the boundary layer is,

$$\begin{aligned}
\psi_e &= C_{e1}e^{ik_yY}\left[1+\frac{k_x\tau}{2k_y\nu}\left(\frac{Y^2}{2}-\frac{Y}{2ik_y}-\frac{1-e^{-2ik_yY}}{4k_y^2}\right)\right]+\\
&\quad C_{e2}e^{-ik_yY}\left[1-\frac{k_x\tau}{2k_y\nu}\left(\frac{Y^2}{2}+\frac{Y}{2ik_y}-\frac{1-e^{2ik_yY}}{4k_y^2}\right)\right] \qquad (A.4)
\end{aligned}$$

and the coefficients are,

$$\begin{aligned}
C_{e1} &= \frac{1}{2}\left(\psi(0)+\frac{1}{ik_y}\frac{d\psi}{dY}(0)\right)\\
C_{e2} &= \frac{1}{2}\left(\psi(0)-\frac{1}{ik_y}\frac{d\psi}{dY}(0)\right)
\end{aligned}$$

where $\psi(0)=C_5Ai[\mathscr{Z}(0)]+C_6Bi[\mathscr{Z}(0)]$ and $\frac{d\psi}{dY}(0)=(C_5Ai'[\mathscr{Z}(0)]+C_6Bi'[\mathscr{Z}(0)])\mathscr{Z}'$. C_5 and C_6 are the constants calculated in the exact analytical solution (A.1).

The wall solution is,

$$\begin{aligned}\psi_w(Y) = & \quad C_{w1}e^{ik_w(Y+\delta_{BL})} + C_{w2}e^{-ik_w(Y+\delta_{BL})} \\ + & \quad C_{w1}e^{ik_w(Y+\delta_{BL})}\left[\frac{k_x\tau}{2k_w\nu}\left(\frac{(Y+\delta_{BL})^2}{2} - \frac{(Y+\delta_{BL})}{2ik_w} - \frac{1-e^{-2ik_w(Y+\delta_{BL})}}{4k_w^2}\right)\right] \\ + & \quad C_{w2}e^{-ik_w(Y+\delta_{BL})}\left[-\frac{k_x\tau}{2k_w\nu}\left(\frac{(Y+\delta_{BL})^2}{2} + \frac{(Y+\delta_{BL})}{2ik_w} - \frac{1-e^{2ik_w(Y+\delta_{BL})}}{4k_w^2}\right)\right].\end{aligned}$$

and the coefficients are

$$\begin{aligned}C_{w1} &= \frac{1}{2}\left(\psi(-\delta_{BL}) + \frac{1}{ik_w}\frac{d\psi}{dy}(-\delta_{BL})\right) \\ C_{w2} &= \frac{1}{2}\left(\psi(-\delta_{BL}) - \frac{1}{ik_w}\frac{d\psi}{dy}(-\delta_{BL})\right)\end{aligned}$$

where $\psi(-\delta_{BL}) = C_5 Ai[\mathscr{Z}(-\delta_{BL})] + C_6 Bi[\mathscr{Z}(-\delta_{BL})]$ and $\frac{d\psi}{dY}(-\delta_{BL}) = (C_5 Ai'[\mathscr{Z}(-\delta_{BL})] + C_6 Bi'[\mathscr{Z}(-\delta_{BL})])\mathscr{Z}'$.

A.2 Coefficient of the two-fluid eigenfunctions

The nature of the solution in the top fluid and the free stream remains unchanged despite the introduction of the film. Therefore the solution is stated in this appendix for the film only in order to avoid repetition. However the matrix containing the constants of integration is provided for the entire domain.

A.2.1 Analytical solution

The exact analytical solution inside the film for a piecewise linear boundary layer is:

$$\begin{aligned}\phi_B \quad = \quad & \frac{\exp(-kY)}{2k}\int_{-\delta_{BL}}^{Y}\exp(ks)(C_9 Ai[\mathscr{X}(s)] + C_{10}Bi[\mathscr{X}(s)])ds \\ & + \frac{\exp(kY)}{2k}\int_{Y}^{-\delta_T}\exp(ks)(C_9 Ai[\mathscr{X}(s)] + C_{10}Bi[\mathscr{X}(s)])ds \\ & + C_{11}\exp(-kY) + C_{12}\exp(kY) \qquad (A.5)\end{aligned}$$

where

$$\mathscr{X}(Y) = \exp(i5\pi/6)\left(\frac{k_x\tau_B}{\nu_B}\right)^{1/3}\left(Y + \frac{i\gamma\nu_B}{k_x\tau_B}\right)$$

and

$$\gamma = \frac{\nu_T k_y^2}{\nu_B} + \left(\frac{\nu_T}{\nu_B} - 1\right)\left(k_x^2 + k_z^2\right) + \frac{ik_x\delta_T}{\nu_B}\left(\tau_T - \tau_B\right).$$

The constants of integration satisfy the following constraints expressed in the form of a matrix:

$$\begin{bmatrix} A_{11} & A_{12} & A_{13} & A_{14} & A_{15} & A_{16} \\ A_{21} & A_{22} & A_{23} & A_{24} & A_{25} & A_{26} \\ A_{31} & A_{32} & A_{33} & A_{34} & A_{35} & A_{36} \\ A_{41} & A_{42} & A_{43} & A_{44} & A_{45} & A_{46} \\ A_{51} & A_{52} & A_{53} & A_{54} & A_{55} & A_{56} \\ A_{61} & A_{62} & A_{63} & A_{64} & A_{65} & A_{66} \end{bmatrix} \begin{bmatrix} C_5 \\ C_6 \\ C_7 \\ C_8 \\ C_9 \\ C_{10} \end{bmatrix} = \begin{bmatrix} 0 \\ 0 \\ 0 \\ 0 \\ 0 \\ 1 \end{bmatrix} \tag{A.6}$$

where

$$\begin{aligned} A_{11} &= [\exp(-k\delta_T)A^+_{\delta_T}] \\ A_{12} &= [\exp(-k\delta_T)B^+_{\delta_T}] \\ A_{13} &= [\exp(-k\delta_T)] \\ A_{14} &= [\exp(k\delta_T)] \\ A_{15} &= -[\exp(k\delta_T)A^-_{\delta_B} - \exp(-k\delta_T)A^+_{\delta_B}] \\ A_{16} &= -[\exp(k\delta_T)B^-_{\delta_B} - \exp(-k\delta_T)B^+_{\delta_B}] \end{aligned}$$

$$
\begin{aligned}
A_{21} &= [(k_x(\tau_T - \tau_B) - k(\omega - k_x U(-\delta_T)))\exp(-k\delta_T)A^+_{\delta_T}] \\
A_{22} &= [(k_x(\tau_T - \tau_B) - k(\omega - k_x U(-\delta_T)))\exp(-k\delta_T)B^+_{\delta_T}] \\
A_{23} &= [(k_x(\tau_T - \tau_B) - k(\omega - k_x U(-\delta_T)))\exp(-k\delta_T)] \\
A_{24} &= [(k_x(\tau_T - \tau_B) + k(\omega - k_x U(-\delta_T)))\exp(k\delta_T)] \\
A_{25} &= -[k(\omega - k_x U(-\delta_T))(A^-_{\delta_B}\exp(k\delta_T) + A^+_{\delta_B}\exp(-k\delta_T))] \\
A_{26} &= -[k(\omega - k_x U(-\delta_T))(B^-_{\delta_B}\exp(k\delta_T) + B^+_{\delta_B}\exp(-k\delta_T))] \\
A_{31} &= [2k^2\exp(-k\delta_T)A^+_{\delta_T} + Ai(\mathscr{Z}(0))] \\
A_{32} &= [2k^2\exp(-k\delta_T)B^+_{\delta_T} + Bi(\mathscr{Z}(0))] \\
A_{33} &= [2k^2\exp(-k\delta_T)] \\
A_{34} &= [2k^2\exp(k\delta_T)] \\
A_{35} &= -[2k^2(\exp(k\delta_T)A^-_{\delta_B} - \exp(-k\delta_T)A^+_{\delta_B}) + Ai(\mathscr{X}(-\delta_T))]\mu_{BT} \\
A_{36} &= -[2k^2(\exp(k\delta_T)B^-_{\delta_B} - \exp(-k\delta_T)B^+_{\delta_B}) + Bi(\mathscr{X}(-\delta_T))]\mu_{BT}
\end{aligned}
$$

$$
\begin{aligned}
A_{41} &= \Big[-k(k_xU(-\delta_T)-\omega)\exp(-k\delta_T)A^+_{\delta_T} - k_x\tau_T\exp(-k\delta_T)A^+_{\delta_T} \\
&\quad +\frac{i}{Re_T}(2k^3\exp(-k\delta_T)A^+_{\delta_T} + \mathscr{Z}'(0)Ai'(\mathscr{Z}'(0))) + \frac{k^4We^{-1}\exp(-k\delta_T)A^+_{\delta_T}}{(k_xU(-\delta_T)-\omega)}\Big] \\
A_{42} &= \Big[-k(k_xU(-\delta_T)-\omega)\exp(-k\delta_T)B^+_{\delta_T} - k_x\tau_T\exp(-k\delta_T)B^+_{\delta_T} \\
&\quad +\frac{i}{Re_T}(2k^3\exp(-k\delta_T)B^+_{\delta_T} + \mathscr{Z}'(0)Bi'(\mathscr{Z}'(0))) + \frac{k^4We^{-1}\exp(-k*\delta_T)B^+_{\delta_T}}{(k_x*U(-\delta_T)-\omega)}\Big] \\
A_{43} &= \Big[-k(k_xU(-\delta_T)-\omega)\exp(-k\delta_T) - k_x\tau_T\exp(-k\delta_T) \\
&\quad +\frac{i}{Re_T}2k^3\exp(-k\delta_T) + \frac{k^4We^{-1}\exp(-k\delta_T)}{(k_x*U(-\delta_T)-\omega)}\Big] \\
A_{44} &= \Big[k(k_xU(-\delta_T)-\omega)\exp(k\delta_T) - k_x\tau_T\exp(k\delta_T) \\
&\quad -\frac{i}{Re_T}2k^3\exp(k\delta_T) + \frac{k^4We^{-1}\exp(k\delta_T)}{(k_xU(-\delta_T)-\omega)}\Big] \\
A_{45} &= -[k((k_xU(-\delta_T)-\omega) - \frac{i}{Re_B}2k^2)(A^-_{\delta_B}\exp(k\delta_T) + A^+_{\delta_B}\exp(-k\delta_T)) \\
&\quad -k_x\tau_B(A^-_{\delta_B}\exp(k\delta_T) - A^+_{\delta_B}\exp(-k\delta_T)) + \frac{i}{Re_B}\mathscr{X}'(0)Bi'(\mathscr{X}'(0))\Big]\rho_{BT} \\
A_{46} &= -[k((k_xU(-\delta_T)-\omega) - \frac{i}{Re_B}2k^2)(B^-_{\delta_B}\exp(k\delta_T) + B^+_{\delta_B}\exp(-k*\delta_T)) \\
&\quad -k_x\tau_B(B^-_{\delta_B}\exp(k\delta_T) - B^+_{\delta_B}\exp(-k\delta_T)) + \frac{i}{Re_B}\mathscr{X}'(0)Bi'(\mathscr{X}'(0))\Big]\rho_{BT}
\end{aligned}
$$

$$
\begin{aligned}
A_{51} &= \frac{1}{(2k(k^2+ky^2))}(kAi(\mathscr{Z}(0)) - \mathscr{Z}'(0)Ai'(\mathscr{Z}'(0)) \\
A_{52} &= \frac{1}{(2k(k^2+ky^2))}(kBi(\mathscr{Z}(0)) - \mathscr{Z}'(0)Bi'(\mathscr{Z}'(0)) \\
A_{53} &= 1 \qquad A_{54} = 0 \\
A_{55} &= 0 \qquad A_{56} = 0
\end{aligned}
$$

$$
\begin{aligned}
A_{61} &= \frac{1}{(2k(k^2+ky^2))}(kAi(\mathscr{Z}(0)) - \mathscr{Z}'(0)Ai'(\mathscr{Z}'(0)) + A^-_{\delta_T} \\
A_{62} &= \frac{1}{(2k(k^2+ky^2))}(kBi(\mathscr{Z}(0)) - \mathscr{Z}'(0)Bi'(\mathscr{Z}'(0)) + B^-_{\delta_T} \\
A_{63} &= 0 \qquad A_{64} = 1 \\
A_{65} &= 0 \qquad A_{66} = 0
\end{aligned}
$$

The constants $C_1, C_2, C_3, C_{11}, C_{12}$ are evaluated as follows,

$$\begin{aligned}
C_1 &= 1 \\
C_2 &= \frac{-1}{2(k^2+k_y^2)}\left(C_5(Ai[\mathscr{Z}(0)] + Ai'[\mathscr{Z}(0)]\frac{\mathscr{Z}'(0)}{ik_y}) + C_6(Bi[\mathscr{Z}(0)] + Bi'[\mathscr{Z}(0)]\frac{\mathscr{Z}'(0)}{ik_y})\right) \\
C_3 &= \frac{1}{2(k^2+k_y^2)}\left(C_5(-Ai[\mathscr{Z}(0)] + Ai'[\mathscr{Z}(0)]\frac{\mathscr{Z}'(0)}{ik_y}) + C_6(-Bi[\mathscr{Z}(0)] + Bi'[\mathscr{Z}(0)]\frac{\mathscr{Z}'(0)}{ik_y})\right) \\
C_{11} &= C_9 A^+_{\delta_B} + C_{10} B^+_{\delta_B}
\end{aligned}$$

where

$$A^{\pm}_{\delta_T} = \frac{1}{2k}\int_{-\delta_T}^{0} \exp(\pm ks) Ai[\mathscr{Z}(s)] ds \qquad B^{\pm}_{\delta_T} = \frac{1}{2k}\int_{-\delta_T}^{0} \exp(\pm ks) Bi[\mathscr{Z}(s)] ds$$
$$A^{\pm}_{\delta_B} = \frac{1}{2k}\int_{-\delta_{BL}}^{-\delta_T} \exp(\pm ks) Ai[\mathscr{X}(s)] ds \qquad B^{\pm}_{\delta_B} = \frac{1}{2k}\int_{-\delta_{BL}}^{-\delta_T} \exp(\pm ks) Bi[\mathscr{X}(s)] ds$$

A.2.2 The convective shear-sheltered regime

The solution for normal velocity in the bottom fluid is of the form,

$$\begin{aligned}
\phi_B &= \frac{C_{e_1}}{2k}\left[exp(-kY)\int_{-\delta_{BL}}^{Y} exp(ks) Ai[z(s)] ds + \right. \\
&\quad \left. \exp(kY)\int_{Y}^{0} exp(ks) Ai[z(s)] ds\right] + \\
&\quad C_{w_2}\exp(-\zeta(\delta_{BL}+Y)) + C_9\exp(-kY) + C_{10}\exp(kY), \qquad \text{(A.7)}
\end{aligned}$$

where $z(Y) \equiv \exp(i5\pi/6)\left(\frac{k_x\tau_B}{\nu_B}\right)^{1/3} Y$ and $\zeta \equiv \frac{1-i}{\sqrt{\frac{2\nu_B}{k_x\tau_B\delta_{BL}}}}$ The constants of integration are evaluated from the following matrix,

$$\begin{bmatrix} A_{11} & A_{12} & A_{13} & A_{14} \\ A_{21} & A_{22} & A_{23} & A_{24} \\ A_{31} & A_{32} & A_{33} & A_{34} \\ A_{41} & A_{42} & A_{43} & A_{44} \end{bmatrix} \begin{bmatrix} C_2 \\ C_3 \\ C_{e_1} \\ C_{w_2} \end{bmatrix} = \begin{bmatrix} -1 \\ -k \\ -k^2 \\ 2k^3 \end{bmatrix} \qquad \text{(A.8)}$$

where,

$$
\begin{aligned}
A_{11} &= 1 \\
A_{12} &= 1 \\
A_{13} &= A^{-}_{\delta_B} - A^{+}_{\delta_B} \\
A_{14} &= \frac{(k+\zeta)}{(2k)}\exp(-k\delta_B) + \frac{(k-\zeta)}{(2k)}\exp(k\delta_B) - \exp(-\zeta\delta_B)
\end{aligned}
$$

$$
\begin{aligned}
A_{21} &= ik_y \\
A_{22} &= -ik_y \\
A_{23} &= \left(k + \frac{k_x\tau_B}{(k_xU(-\delta_T)-\omega)}\right)A^{+}_{\delta_B} + \left(k - \frac{k_x\tau_B}{(k_xU(-\delta_T)-\omega)}\right)A^{-}_{\delta_B} \\
A_{24} &= \left(k_x\frac{\tau_B}{(k_xU(-\delta_T)-\omega)} - \zeta\right)\exp(-\zeta\delta_B) - \left(k_x\frac{\tau_B}{(k_xU(-\delta_T)-\omega)} - k\right)\frac{(k+\zeta)}{(2k)}\exp(-k\delta_B) \\
&\quad -\left(k_x\frac{\tau_B}{(k_xU(-\delta_T)-\omega)} + k\right)\frac{(k-\zeta)}{(2k)}\exp(k\delta_B)
\end{aligned}
$$

$$
\begin{aligned}
A_{31} &= -k_y^2 \\
A_{32} &= -k_y^2 \\
A_{33} &= (1-2\mu_{BT})k^2(A^{+}_{\delta_B} - A^{-}_{\delta_B}) - \mu_{BT}Ai(\mathscr{Z}(0)) \\
A_{34} &= ((1-\mu_{BT})k^2 - \mu_{BT}\zeta^2)\exp(-\zeta\delta_B) \\
&\quad -(1-2\mu_{BT})k^2\left(\frac{(k+\zeta)}{(2k)}\exp(-k\delta_B) + \frac{(k-\zeta)}{(2k)}\exp(k\delta_B)\right) \\
A_{41} &= -ik_y(k_y^2+3k^2) \\
A_{42} &= ik_y(k_y^2+3k^2) \\
A_{43} &= -\mu_{BT}(2k^3(A^{+}_{\delta_B} + A^{-}_{\delta_B}) + Ai'(\mathscr{Z}(0))\mathscr{Z}'(0)) \\
A_{44} &= -\mu_{BT}\left(\zeta(\zeta^2-3k^2)\exp(-\zeta\delta_B) + 2k^3\left[\frac{(k+\zeta)}{(2k)}\exp(-k\delta_B) - \frac{(k-\zeta)}{(2k)}\exp(k\delta_B)\right]\right)
\end{aligned}
$$

where $A^{\pm}_{\delta_B} = \frac{1}{2k}\int_{-\delta_{BL}}^{-\delta_T} \exp(\pm ks) Ai[z(s)]ds$. The other constants, C_1, C_9 and C_{10} are evaluated using the following relations,

$$\begin{aligned} C_1 &= 1 \\ C_9 &= -(C_{e_1} A^{-}_{\delta_B} + \frac{(k-\zeta)}{(2k)} \exp(-k\delta_B) C_{w_2}) \\ C_{10} &= -(C_{w_2} \frac{(k-\zeta)}{(2k)} \exp(k\delta_B)). \end{aligned}$$

A.2.3 The diffusive regime

The eigenfunction inside the film is oscillatory in nature in the diffusive regime and can be expressed as,

$$\phi_B = C_9 \exp(-i\kappa_d Y) + C_{10} \exp(i\kappa_d Y) + C_{11} \exp(-kY) + C_{12} \exp(kY),$$

where $\kappa_d = \sqrt{\frac{\nu_T}{\nu_B}(k_x^2 + k_y^2 + k_z^2) - (k_x^2 + k_z^2)}$. The constants of integration are found using the following constraints written in the form of a matrix,

$$\begin{bmatrix} A_{11} & A_{12} & A_{13} & A_{14} \\ A_{21} & A_{22} & A_{23} & A_{24} \\ A_{31} & A_{32} & A_{33} & A_{34} \\ A_{41} & A_{42} & A_{43} & A_{44} \end{bmatrix} \begin{bmatrix} C_2 \\ C_3 \\ C_9 \\ C_{10} \end{bmatrix} = \begin{bmatrix} -1 \\ -k(k_x U(\delta_T) - \omega) + k_x(\tau_T - \tau_B) \\ -2k^2 \\ 2k^3 \end{bmatrix} \quad \text{(A.9)}$$

where,

$$\begin{aligned} A_{11} &= 1 \\ A_{12} &= 1 \\ A_{13} &= -1 + \exp(\lambda\delta_B)(\frac{(k+\lambda)}{(2k)} \exp(-k\delta_B) + \frac{(k-\lambda)}{(2k)} \exp(k\delta_B)) \\ A_{14} &= -1 + \exp(-\lambda\delta_B)(\frac{(k-\lambda)}{(2k)} \exp(-k\delta_B) + \frac{(k+\lambda)}{(2k)} \exp(k\delta_B)) \end{aligned}$$

$$
\begin{aligned}
A_{21} &= ik_y(k_xU(-\delta_T)-\omega) - k_x(\tau_T-\tau_B)\\
A_{22} &= -ik_y(k_xU(-\delta_T)-\omega) - k_x(\tau_T-\tau_B)\\
A_{23} &= -(k_xU(-\delta_T)-\omega)\Big[\lambda + k\exp(\lambda\delta_B)\Big(-\frac{(k+\lambda)}{(2k)}\exp(-k\delta_B)+\frac{(k-\lambda)}{(2k)}\exp(k\delta_B)\Big)\Big]\\
A_{24} &= -(k_xU(-\delta_T)-\omega)\Big[-\lambda + k\exp(-\lambda\delta_B)\Big(-\frac{(k-\lambda)}{(2k)}\exp(-k\delta_B)+\frac{(k+\lambda)}{(2k)}\exp(k\delta_B)\Big)\Big]\\
A_{31} &= k^2-k_y^2\\
A_{32} &= k^2-k_y^2\\
A_{33} &= -\mu_{BT}((\lambda^2+k^2)-2k^2\exp(\lambda\delta_B)\Big(\frac{(k+\lambda)}{(2k)}\exp(-k\delta_B)+\frac{(k-\lambda)}{(2k)}\exp(k\delta_B))\Big)\\
A_{34} &= -\mu_{BT}((\lambda^2+k^2)-2k^2\exp(-\lambda\delta_B)\Big(\frac{(k-\lambda)}{(2k)}\exp(-k\delta_B)+\frac{(k+\lambda)}{(2k)}\exp(k\delta_B))\Big)\\
A_{41} &= -ik_y(k_y^2+3k^2)\\
A_{42} &= ik_y(k_y^2+3k^2)\\
A_{43} &= -\mu_{BT}\Big[\lambda(\lambda^2-3k^2)+2k^3\exp(\lambda\delta_B)\Big(\frac{(k+\lambda)}{(2k)}\exp(-k\delta_B)-\frac{(k-\lambda)}{(2k)}\exp(k\delta_B)\Big)\Big]\\
A_{44} &= -\mu_{BT}\Big[-\lambda(\lambda^2-3k^2)+2k^3\exp(-\lambda\delta_B)\Big(\frac{(k-\lambda)}{(2k)}\exp(-k\delta_B)-\frac{(k+\lambda)}{(2k)}\exp(k\delta_B)\Big)\Big]
\end{aligned}
$$

where $\lambda=\sqrt{k_x^2+k_z^2-(k_x^2+k_y^2+k_z^2)/\nu_{BT}}$. The constants C_1, C_{11} and C_{12} are computed using the values of the other constants using the following relations,

$$
\begin{aligned}
C_{11} &= -\frac{1}{(2k)}((k+\lambda)\exp(\lambda(\delta_T+\delta_B))C_9+(k-\lambda)\exp(-\lambda(\delta_T+\delta_B))C_{10})\exp(-k(\delta_T+\delta_B))\\
C_{12} &= -\frac{1}{(2k)}((k-\lambda)\exp(\lambda(\delta_T+\delta_B))C_9+(k+\lambda)\exp(-\lambda(\delta_T+\delta_B))C_{10})\exp(k(\delta_T+\delta_B)).
\end{aligned}
$$

A.2.4 The convective-diffusive regime

The oscillatory solution near the interface is,

$$
\begin{aligned}
\psi_{Be} &= C_{e1}e^{ik_eY}\left[1+\frac{k_x\tau_B}{2k_y\nu_B}\left(\frac{Y^2}{2}-\frac{Y}{2ik_e}-\frac{1-e^{-2ik_eY}}{4k_e^2}\right)\right]+\\
&\quad C_{e2}e^{-ik_eY}\left[1-\frac{k_x\tau_B}{2k_e\nu_B}\left(\frac{Y^2}{2}+\frac{Y}{2ik_e}-\frac{1-e^{2ik_eY}}{4k_e^2}\right)\right] \qquad \text{(A.10)}
\end{aligned}
$$

and the coefficients are,

$$C_{e1} = \frac{1}{2}\left(\psi(0) + \frac{1}{ik_y}\frac{d\psi}{dY}(0)\right)$$
$$C_{e2} = \frac{1}{2}\left(\psi(0) - \frac{1}{ik_y}\frac{d\psi}{dY}(0)\right)$$

where $\psi(0) = C_9 Ai[\mathscr{X}(0)] + C_{10} Bi[\mathscr{X}(0)]$ and $\frac{d\psi}{dY}(0) = (C_9 Ai'[\mathscr{X}(0)] + C_{10} Bi'[\mathscr{X}(0)])\mathscr{X}'$. C_9 and C_{10} are the constants calculated in the exact analytical solution 3.27. Here $k_e = \sqrt{\frac{\nu_T}{\nu_B}(k_x^2 + k_y^2 + k_z^2) - (k_x^2 + k_z^2)}$ The wall solution is,

$$\begin{aligned}
\psi_{Bw} = & \quad C_{w1} e^{ik_w(Y+\delta_{BL})} + C_{w2} e^{-ik_w(Y+\delta_{BL})} \\
+ & \quad C_{w1} e^{ik_w(Y+\delta_{BL})} \left[\frac{k_x \tau_B}{2k_w \nu_B}\left(\frac{(Y+\delta_{BL})^2}{2} - \frac{(Y+\delta_{BL})}{2ik_w} - \frac{1-e^{-2ik_w(Y+\delta_{BL})}}{4k_w^2}\right)\right] \\
+ & \quad C_{w2} e^{-ik_w(Y+\delta_{BL})} \left[-\frac{k_x \tau_B}{2k_w \nu_B}\left(\frac{(Y+\delta_{BL})^2}{2} + \frac{(Y+\delta_{BL})}{2ik_w} - \frac{1-e^{2ik_w(Y+\delta_{BL})}}{4k_w^2}\right)\right].
\end{aligned}$$

and the coefficients are

$$C_{w1} = \frac{1}{2}\left(\psi(-\delta_{BL}) + \frac{1}{ik_w}\frac{d\psi}{dy}(-\delta_{BL})\right)$$
$$C_{w2} = \frac{1}{2}\left(\psi(-\delta_{BL}) - \frac{1}{ik_w}\frac{d\psi}{dy}(-\delta_{BL})\right)$$

where $\psi(-\delta_{BL}) = C_9 Ai[\mathscr{X}(-\delta_{BL})] + C_{10} Bi[\mathscr{X}(-\delta_{BL})]$ and $\frac{d\psi}{dY}(-\delta_{BL}) = (C_9 Ai'[\mathscr{X}(-\delta_{BL})] + C_{10} Bi'[\mathscr{X}(-\delta_{BL})])\mathscr{X}'$. Here $k_w = \sqrt{\frac{\nu_T}{\nu_B}(k_x^2 + k_y^2 + k_z^2) - (k_x^2 + k_z^2) + i\frac{k_x \tau_B \delta_{BL}}{\nu_B L}}$.

A.2.5 Thin film solution

The normal velocity eigenfunction is of the following form

$$\begin{aligned}
\phi_T &= C_1 \exp(-ik_y Y) + C_2 \exp(ik_y Y) + C_3 \exp(-kY), \; Y > -\delta_T, \\
\phi_B &= C_9 (Y + \delta_{BL})^2 + C_{10} (Y + \delta_{BL})^3, \qquad -\delta_{BL} < Y < -\delta_T,
\end{aligned}$$

where

$$
\begin{aligned}
C_9 &= \frac{C_{B1}}{2} \\
C_{10} &= -\frac{C_{B2}}{6} \\
C_{B1} &= C_3 \exp(k\delta_T)\left[\frac{\mu_{BT}}{k^2+k_y^2}(1+\lambda\delta_B) + (\frac{(\mu_{BT}-2)k^2}{k^2+k_y^2}+1)(\frac{\delta_B^2}{2}+\frac{\lambda\delta_B^3}{6})\right]^{-1} \\
C_{B2} &= -\lambda C_{B1} \\
C_1 &= -\frac{\exp(-ik_y\delta_T)}{2(k^2+k_y^2)}(\mu_{BT}(C_{B1}-C_{B2}\delta_B) + (\mu_{BT}-2)k^2(\frac{C_{B1}}{2}\delta_B^2 - \frac{C_{B2}}{6}\delta_B^3) \\
&\quad + \frac{\mu_{BT}}{ik_y}(C_{B2} - 3k^2(-C_{B1}\delta_B + \frac{C_{B2}}{2}\delta_B^2)) \\
&\quad + \frac{2k^2}{ik_y}(\frac{-k_x(\tau_T-\tau_B)}{k_xU_{int}-\omega}(\frac{C_{B1}}{2}\delta_B^2 - \frac{C_{B2}}{6}\delta_B^3) + (-C_{B1}\delta_B + \frac{C_{B2}}{2}\delta_B^2))))
\end{aligned}
$$

$$
\begin{aligned}
C_2 &= \frac{\exp(ik_y\delta_T)}{2(k^2+k_y^2)}(-\mu_{BT}(C_{B1}-C_{B2}\delta_B) - (\mu_{BT}-2)k^2(\frac{C_{B1}}{2}\delta_B^2 - \frac{C_{B2}}{6}\delta_B^3) \\
&\quad + \frac{\mu_{BT}}{ik_y}(C_{B2} - 3k^2(-C_{B1}\delta_B + \frac{C_{B2}}{2}\delta_B^2)) \\
&\quad + \frac{2k^2}{ik_y}(-\frac{k_x(\tau_T-\tau_B)}{k_xU_{int}-\omega}(\frac{C_{B1}}{2}\delta_B^2 - \frac{C_{B2}}{6}\delta_B^3) + (-C_{B1}\delta_B + \frac{C_{B2}}{2}\delta_B^2))))
\end{aligned}
$$

and

$$
\lambda = \frac{\frac{\mu_{BT}}{k^2+k_y^2}\left(k-3k^2\delta_B\right) + \frac{k\delta_B^2}{2}\left(1+\frac{(\mu_{BT}-2)k^2}{k^2+k_y^2}\right) - \left(\frac{2k^2}{k^2+k_y^2}+1\right)\left(\frac{-k_x(\tau_T-\tau_B)}{k_xU_{int}-\omega}\frac{\delta_B^2}{2} - \delta_B\right)}{\frac{\mu_{BT}}{k^2+k_y^2}\left(-k\delta_B + 3k^2\frac{\delta_B^2}{2} - 1\right) - \frac{k\delta_B^3}{6}\left(1+\frac{(\mu_{BT}-2)k^2}{k^2+k_y^2}\right) - \left(\frac{2k^2}{k^2+k_y^2}+1\right)\left(\frac{k_x(\tau_T-\tau_B)}{k_xU_{int}-\omega}\frac{\delta_B^3}{6} - \frac{\delta_B^2}{2}\right)}
$$

and U_{int} is the velocity at the interface.

Appendix B

The long wavelength limit of the interface mode

The normal vorticity eigenfunction at leading order is,

$$\begin{aligned} \chi^P_{0T} &= C'_{01} e^{-k_z(y-y_f)} \\ \chi^P_{0B} &= C'_{05}(e^{k_z y} - e^{-k_z y}), \end{aligned}$$

where,

$$\begin{aligned} C'_{01} &= if_0 \frac{-\mu_{BT} k_z (d_y U_T - d_y U_B)(e^{k_z y_f} + e^{-k_z y_f}) + (d_y^2 U_T - \mu_{BT} d_y^2 U_B)(e^{k_z y_f} - e^{-k_z y_f})}{e^{k_z y_f} - e^{-k_z y_f} + \mu_{BT}(e^{k_z y_f} + e^{-k_z y_f})}. \\ C'_{05} &= if_0 \frac{(d_y^2 U_T - \mu_{BT} d_y^2 U_B) + k_z (d_y U_T - d_y U_B)}{e^{k_z y_f} - e^{-k_z y_f} + \mu_{BT}(e^{k_z y_f} + e^{-k_z y_f})}. \end{aligned}$$

The normal velocity eigenfunction at the first order is,

$$\begin{aligned} \phi_{1T} &= (C_{11} + C_{13} y) e^{-k_z y}, \\ \phi_{1B} &= (C_{15} + C_{17} y) e^{-k_z y} + (C_{16} + C_{18} y) e^{-k_z y}. \end{aligned} \tag{B.1}$$

where,

$$\begin{bmatrix} C_{11} \\ C_{13} \end{bmatrix} = \frac{1}{A_{11}A_{22} - A_{12}A_{21}} \begin{bmatrix} A_{22} & -A_{12} \\ -A_{21} & A_{11} \end{bmatrix} \begin{bmatrix} B_1 \\ B_2 \end{bmatrix} \frac{if_0}{\delta_{99}} e^{-k_z y_f}$$

$$
\begin{aligned}
C_{18} &= \frac{2k_z}{\alpha}(C_{11}+C_{13}y_f)e^{-k_z y_f} \\
C_{17} &= \lambda C_{18} \\
C_{16} &= \frac{-1}{2k_z}(C_{17}+C_{18}) \\
C_{11} &= -C_{16}.
\end{aligned}
$$

The associated constants are,

$$
\begin{aligned}
A_{11} &= k_z\Big(-1+\frac{2}{\alpha}((1+\lambda)cosh(k_z y_f)+\lambda(k_z y_f-1)e^{-k_z y_f}-(1+k_z y_f)e^{k_z y_f})\Big) \\
A_{12} &= 1-k_z y_f+\frac{2k_z y_f}{\alpha}((1+\lambda)cosh(k_z y_f)+\lambda(k_z y_f-1)e^{-k_z y_f}-(1+k_z y_f)e^{k_z y_f}) \\
A_{21} &= k_z\Big(1-\frac{2\mu_{BT}}{\alpha}(-(1+\lambda)sinh(k_z y_f)+\lambda(k_z y_f-1)e^{-k_z y_f}+(1+k_z y_f)e^{k_z y_f})\Big) \\
A_{22} &= k_z y_f-1-\frac{2\mu_{BT}k_z y_f}{\alpha}(-(1+\lambda)sinh(k_z y_f)+\lambda(k_z y_f-1)e^{-k_z y_f}+(1+k_z y_f)e^{k_z y_f}) \\
B_1 &= [d_y U] \\
B_2 &= \frac{d_y^2 U_T-\mu_{BT}d_y^2 U_B}{2k_z} \\
\lambda &= \frac{(\mu_{BT}-1)e^{-k_z y_f}-(\mu_{BT}+1)(-1+2k_z y_f)e^{k_z y_f}}{(1-\mu_{BT})(1+2k_z y_f)e^{-k_z y_f}-(\mu_{BT}+1)e^{k_z y_f}} \\
\alpha &= \lambda((1+2k_z y_f)e^{k_z y_f}-e^{k_z y_f})+(e^{-k_z y_f}+(-1+2k_z y_f)e^{k_z y_f}).
\end{aligned}
\tag{B.2}
$$

The solution to the normal vorticity equation at the first order is,

$$
\begin{aligned}
\chi_{1T}^P &= \frac{e^{k_z y}}{-2k_z}\int_y^\infty \mathscr{H}_{1T}e^{-k_z s}ds+\Big(C'_{12}+\frac{1}{-2k_z}\int_{y_f}^y \mathscr{H}_{1T}e^{k_z s}ds\Big)e^{-k_z y}, \\
\chi_{1B}^P &= 2C'_{13}sinh(k_z y)+\frac{e^{k_z y}}{2k_z}\int_0^y \mathscr{H}_{1B}e^{-k_z s}ds-\frac{e^{-k_z y}}{2k_z}\int_0^y \mathscr{H}_{1B}e^{k_z s}ds,
\end{aligned}
$$

where the constants of integration, C'_{12}, C'_{13} are,

$$
\begin{aligned}
C'_{13} &= \frac{1}{sinh(k_z y_f)+\mu_{BT}cosh(k_z y_f)}\Big(-\frac{e^{k_z y_f}}{2k_z}\int_{y_f}^\infty \mathscr{H}_{1T}e^{-k_z s}ds \\
&\quad -\frac{1+\mu_{BT}}{2}\frac{e^{k_z y_f}}{2k_z}\int_0^{y_f} \mathscr{H}_{1B}e^{-k_z s}ds+\frac{1-\mu_{BT}}{2}\frac{e^{-k_z y_f}}{2k_z}\int_0^{y_f} \mathscr{H}_{1B}e^{k_z s}ds\Big), \\
C'_{12} &= e^{k_z y_f}\Big(2C'_{13}sinh(k_z y_f)+\frac{e^{k_z y_f}}{2k_z}\int_0^{y_f} \mathscr{H}_{1B}e^{-k_z s}ds \\
&\quad -\frac{e^{-k_z y_f}}{2k_z}\int_0^{y_f} \mathscr{H}_{1B}e^{k_z s}ds+\frac{e^{k_z y_f}}{2k_z}\int_{y_f}^\infty \mathscr{H}_{1T}e^{-k_z s}ds\Big),
\end{aligned}
$$

and

$$\mathscr{H}_{1j} \equiv -ik_z d_y U_j \phi_{1j} + i\left(\omega_1 - \frac{U_j}{\delta_{99}}\right)\chi^P_{0j}.$$

Appendix C

Kinetic energy density

The kinetic energy density inside the boundary layer can be defined as,

$$\begin{aligned} E_{bl} &\equiv \frac{1}{2\lambda_x\lambda_z\delta_{99}}\Bigg[\rho_B\int_0^{\lambda_z}\int_0^{\lambda_x}\int_0^{y_f}(u_B^2+v_B^2+w_B^2)dy\ dx\ dz \\ &\quad +\rho_T\int_0^{\lambda_z}\int_0^{\lambda_x}\int_{y_f}^{\delta_{99}}(u_T^2+v_T^2+w_T^2)dy\ dx\ dz\Bigg]. \end{aligned} \tag{C.1}$$

Substituting into equation C.1, the following

$$\begin{aligned} u &= \frac{u_{\vec{k}}e^{i(k_xx+k_zz)}+u_{\vec{k}}^*e^{-i(k_xx+k_zz)}}{2}, \\ w &= \frac{w_{\vec{k}}e^{i(k_xx+k_zz)}+w_{\vec{k}}^*e^{-i(k_xx+k_zz)}}{2}, \end{aligned}$$

where $*$ denotes the complex conjugate, and integrating along x and z axes leads to

$$\begin{aligned} E_{bl} &= \frac{1}{4\delta_{99}}\Bigg[\rho_B\int_0^{y_f}(u_{\vec{k},B}u_{\vec{k},B}^*+v_{\vec{k},B}v_{\vec{k},B}^*+w_{\vec{k},B}w_{\vec{k},B}^*)dy \\ &\quad +\rho_T\int_{y_f}^{\delta_{99}}(u_{\vec{k},T}u_{\vec{k},T}^*+v_{\vec{k},T}v_{\vec{k},T}^*+w_{\vec{k},T}w_{\vec{k},T}^*)dy\Bigg]. \end{aligned}$$

Substituting the following identities into the above expression,

$$\begin{aligned} u_{\vec{k}} &= \frac{i}{k^2}(k_x\partial_y v_{\vec{k}}-k_z\eta_{\vec{k}}), \\ w_{\vec{k}} &= \frac{i}{k^2}(k_z\partial_y v_{\vec{k}}+k_x\eta_{\vec{k}}), \end{aligned}$$

and simplifying it further gives,

$$E_{bl} = \frac{1}{4k^2\delta_{99}}\Bigg[\rho_B \int_0^{y_f} (|\partial_y v_{\vec{k}}|^2 + k^2|v_{\vec{k}}|^2 + |\eta_{\vec{k}}|^2)dy + \rho_T \int_{y_f}^{\delta_{99}} (|\partial_y v_{\vec{k}}|^2 + k^2|v_{\vec{k}}|^2 + |\eta_{\vec{k}}|^2)dy\Bigg]. \tag{C.2}$$

Appendix D

Adjoint Orr-Sommerfeld operator

The adjoint Orr-Sommerfeld equation is derived based on the following definition of the inner product,

$$\left\langle \begin{bmatrix} \phi^\dagger \\ f^\dagger \delta(y-y_f) \end{bmatrix}, \begin{bmatrix} \rho\mathscr{L}_{os} & 0 \\ -\mathscr{C}_v & \mathscr{L}_{int} \end{bmatrix} \begin{bmatrix} \phi \\ f \end{bmatrix} \right\rangle = \left\langle \begin{bmatrix} \rho\mathscr{L}_{os}^\dagger & 0 \\ \mathscr{C}_f^\dagger & \mathscr{L}_{int}^\dagger \end{bmatrix} \begin{bmatrix} \phi^\dagger \\ f^\dagger \delta(y-y_f) \end{bmatrix}, \begin{bmatrix} \phi \\ f \end{bmatrix} \right\rangle = 0$$

where, $\langle X, Y \rangle \equiv \int_0^\infty X^* Y dy$ and $\dagger, *$ denote the adjoint variable and the conjugate transpose respectively. The operators $\mathscr{L}_{os,j}$ and $\mathscr{L}_{int}$ are defined in the following way,

$$\mathscr{L}_{os,j} \equiv -\mathscr{L}_j - i\omega(d_y^2 - k^2),$$

$$\mathscr{L}_{int} \equiv -\mathscr{I} - i\omega.$$

The definition of the adjoint can be further expanded into,

$$\begin{aligned} \Rightarrow \rho_B \int_0^{y_f} \phi_B^{\dagger *} \mathscr{L}_{os,B} \phi_B \, dy \qquad & \rho_B \int_0^{y_f} (\mathscr{L}_{os,B}^\dagger \phi_{os,B}^\dagger)^* \phi_B \, dy \\ + \rho_T \int_{y_f}^\infty \phi_T^{\dagger *} \mathscr{L}_{os,T} \phi_T \, dy \quad = \quad & + \rho_T \int_{y_f}^\infty (\mathscr{L}_{os,T}^\dagger \phi_T^\dagger)^* \phi_T \, dy \\ f^{\dagger *} \Big(\mathscr{C}_v \phi + \mathscr{L}_{int} f \Big) \qquad & f \Big(\mathscr{C}_f^\dagger \phi^\dagger + \mathscr{L}_{int}^\dagger f^\dagger \Big)^*. \end{aligned} \tag{D.1}$$

where the last term on either side of the equation is evaluated at the interface $y = y_f$. Expanding the first term on the L.H.S of equation D.1,

$$\begin{aligned}\rho_B \int_0^{y_f} \phi_B^{\dagger *} \mathscr{L}_{os,B} \phi_B \, dy &= \rho_B \int_0^{y_f} \phi_B^{\dagger *} \Big(\underbrace{-i\omega(d_y^2 - k^2)}_{T1} + \underbrace{ik_x U(d_y^2 - k^2)}_{T2} \\ &\quad \underbrace{- ik_x d_y^2 U}_{T3} - \underbrace{\nu_B (d_y^2 - k^2)^2}_{T4} \Big) \phi_B \, dy. \end{aligned} \tag{D.2}$$

Performing integration by parts on $T1$ leads to,

$$\begin{aligned}-i\rho_B\omega \int_0^{y_f} \phi_B^{\dagger *}(d_y^2 - k^2)\phi_B \, dy &= -i\rho_B\omega \int_0^{y_f} \phi_B (d_y^2 - k^2)\phi_B^{\dagger *} \, dy \\ &\quad -i\rho_B\omega \Big[\phi_B^{\dagger *} d_y \phi_B - d_y \phi_B^{\dagger *} \phi_B \Big]_0^{y_f}. \end{aligned} \tag{D.3}$$

Similarly for $T2$,

$$\begin{aligned}i\rho_B k_x \int_0^{y_f} \phi_B^{\dagger *} U (d_y^2 - k^2)\phi_B \, dy &= i\rho_B k_x \int_0^{y_f} \phi_B U (d_y^2 - k^2)\phi_B^{\dagger *} \, dy \\ &\quad + i\rho_B k_x \int_0^{y_f} \phi_B (2 d_y U d_y \phi_B^{\dagger *} + d_y^2 U \phi_B^{\dagger *}) \, dy \\ &\quad + i\rho_B k_x \Big[\phi_B^{\dagger *} U d_y \phi_B - (d_y \phi_B^{\dagger *} U + \phi_B^{\dagger *} d_y U)\phi_B \Big]_0^{y_f} \end{aligned} \tag{D.4}$$

and $T4$,

$$\begin{aligned}-\rho_B\nu_B \int_0^{y_f} \phi_B^{\dagger *}(d_y^2 - k^2)^2 \phi_B \, dy &= -\rho_B\nu_B \int_0^{y_f} \phi_B (d_y^2 - k^2)^2 \phi_B^{\dagger *} \, dy \\ &\quad -\rho_B\nu_B \Big[\phi_B^{\dagger *} d_y^3 \phi_B - d_y \phi_B^{\dagger *} d_y^2 \phi_B + d_y^2 \phi_B^{\dagger *} d_y \phi_B \\ &\quad + d_y^3 \phi_B^{\dagger *} \phi_B - 2k^2 (\phi_B^{\dagger *} d_y \phi_B - d_y \phi_B^{\dagger *} \phi_B) \Big]_0^{y_f}. \end{aligned} \tag{D.5}$$

Equation D.2 can be rewritten using equations D.3, D.4 and D.5 in the following manner,

$$\rho_B \int_0^{y_f} \phi_B^{\dagger *} \mathscr{L}_{os,B} \phi_B \, dy = \rho_B \int_0^{y_f} \mathscr{L}_{os,B}^{\dagger *} \phi_B^{\dagger *} \phi_B \, dy + \Big[\mathscr{B}_B \Big]_0^{y_f} \tag{D.6}$$

where,

$$\begin{aligned}
\mathscr{L}^{\dagger}_{os,B} &\equiv i(\omega^{\dagger} - k_x U_B)(d_y^2 - k^2) - ik_x 2 d_y U_B d_y - \nu_B (d_y^2 - k^2)^2 \\
\mathscr{B}_B &\equiv \rho_B \Big[- i\omega(\phi_B^{\dagger *} d_y \phi_B - d_y \phi_B^{\dagger *} \phi_B) + ik_x(\phi_B^{\dagger *} U d_y \phi_B - (d_y \phi_B^{\dagger *} U + \phi_B^{\dagger *} d_y U)\phi_B) \\
&\quad -\nu_B \Big(\phi_B^{\dagger *} d_y^3 \phi_B - d_y \phi_B^{\dagger *} d_y^2 \phi_B + d_y^2 \phi_B^{\dagger *} d_y \phi_B + d_y^3 \phi_B^{\dagger *} \phi_B \\
&\quad -2k^2(\phi_B^{\dagger *} d_y \phi_B - d_y \phi_B^{\dagger *} \phi_B) \Big) \Big].
\end{aligned}$$

Similarly, the adjoint operator can be obtained for the top fluid following the same procedure,

$$\rho_T \int_{y_f}^{\infty} \phi_T^{\dagger *} \mathscr{L}_{os,T} \phi_T \, dy = \rho_T \int_{y_f}^{\infty} \mathscr{L}^{\dagger *}_{os,T} \phi_T^{\dagger *} \phi_T \, dy + \Big[\mathscr{B}_T \Big]_{y_f}^{\infty} \tag{D.7}$$

where,

$$\begin{aligned}
\mathscr{L}^{\dagger}_{os,T} &\equiv i(\omega^{\dagger} - k_x U_T)(d_y^2 - k^2) - ik_x 2 d_y U_T d_y - \nu_T (d_y^2 - k^2)^2 \\
\mathscr{B}_T &\equiv \rho_T \Big[- i\omega(\phi_T^{\dagger *} d_y \phi_T - d_y \phi_T^{\dagger *} \phi_T) + ik_x(\phi_T^{\dagger *} U d_y \phi_T - (d_y \phi_T^{\dagger *} U + \phi_T^{\dagger *} d_y U)\phi_T) \\
&\quad -\nu_T \Big(\phi_T^{\dagger *} d_y^3 \phi_T - d_y \phi_T^{\dagger *} d_y^2 \phi_T + d_y^2 \phi_T^{\dagger *} d_y \phi_T + d_y^3 \phi_T^{\dagger *} \phi_T \\
&\quad -2k^2(\phi_T^{\dagger *} d_y \phi_T - d_y \phi_T^{\dagger *} \phi_T) \Big) \Big].
\end{aligned}$$

The term $\Big[\mathscr{B}_B\Big]_0^{y_f} + \Big[\mathscr{B}_T\Big]_{y_f}^{\infty}$ can be simplified further using the boundary conditions on ϕ. Homogeneous boundary conditions are imposed on the adjoint variable, $\phi^{\dagger}$, at the wall and in the free-stream,

$$\begin{aligned}
\phi_B^{\dagger}(0) = 0 \quad ; \quad d_y \phi_B^{\dagger}(0) = 0 \\
\phi_T^{\dagger}(y \to \infty) = 0 \quad ; \quad d_y \phi_T^{\dagger}(y \to \infty) = 0
\end{aligned}$$

and the following boundary conditions at the interface (at $y = y_f$),

$$\begin{aligned}
\phi_B^\dagger - \phi_T^\dagger &= 0 \\
d_y\phi_B^\dagger - d_y\phi_T^\dagger &= 0 \\
\mu_B(d_y^2+k^2)\phi_B^\dagger - \mu_T(d_y^2+k^2)\phi_T^\dagger &= 0 \\
-\rho_B\Big[(i\omega^\dagger - ik_xU_B)d_y - \nu_B(d_y^3 - 3k^2d_y)\Big]\phi_B^\dagger & \\
\rho_T\Big[(i\omega^\dagger - ik_xU_T)d_y - \nu_T(d_y^3 - 3k^2d_y)\Big]\phi_T^\dagger &= f^\dagger. \qquad \text{(D.8)}
\end{aligned}$$

For the adjoint continuous modes the free-stream condition, is relaxed to,

$$|\phi_T^\dagger| < \infty \quad ; \quad |d_y\phi_T^\dagger| < \infty \qquad\qquad y \to \infty$$

Upon imposing the adjoint boundary conditions D.8, the L.H.S. of D.1 reduces to,

$$\left\langle \begin{bmatrix} \phi^\dagger \\ f^\dagger\delta(y-y_f) \end{bmatrix}, \begin{bmatrix} \rho\mathscr{L}_{os} & 0 \\ -\mathscr{C}_v & \mathscr{L}_{int} \end{bmatrix} \begin{bmatrix} \phi \\ f \end{bmatrix} \right\rangle = \left\langle \begin{bmatrix} \rho\mathscr{L}_{os}^\dagger & 0 \\ \mathscr{C}_f^\dagger & \mathscr{L}_{int}^\dagger \end{bmatrix} \begin{bmatrix} \phi^\dagger \\ f^\dagger\delta(y-y_f) \end{bmatrix}, \begin{bmatrix} \phi \\ f \end{bmatrix} \right\rangle$$

which is the R.H.S of D.1. The operators, $\mathscr{L}_{int}^\dagger$ and $\mathscr{C}_f^\dagger$ are therefore defined as,

$$\begin{aligned}
\mathscr{L}_{int}^\dagger &\equiv \mathscr{L}_{int}^* \\
\mathscr{C}_f^\dagger\phi^\dagger &\equiv \Big(-k^4\sigma + ik_x(\mu_T d_y^2U_T - \mu_B d_y^2U_B)d_y - ik_x\mu_B(d_yU_T - d_yU_B)(d_y^2+k^2)\Big)\phi_B^\dagger\Big|_{y_f}.
\end{aligned}$$

We define the system of adjoint Orr-Sommerfeld and interface equations as,

$$\begin{bmatrix} \mathscr{L}_{os}^\dagger & 0 \\ \mathscr{C}_f^\dagger & \mathscr{L}_{int}^\dagger \end{bmatrix} \begin{bmatrix} \phi^\dagger \\ f^\dagger \end{bmatrix} = 0.$$

D.1 Bi-orthogonality condition

Following the definition of the adjoint in equation D.1 we can write,

$$\begin{aligned}
\left\langle \begin{bmatrix} \phi_m^\dagger \\ f_m^\dagger\delta(y-y_f) \end{bmatrix}, \begin{bmatrix} \rho\mathscr{L}_{os} & 0 \\ \mathscr{C}_v & \mathscr{L}_{int} \end{bmatrix} \begin{bmatrix} \phi_n \\ f_n \end{bmatrix} \right\rangle &= \left\langle \begin{bmatrix} \rho\mathscr{L}_{os}^\dagger & 0 \\ \mathscr{C}_f^\dagger & \mathscr{L}_{int}^\dagger \end{bmatrix} \begin{bmatrix} \phi_m^\dagger \\ f_m^\dagger\delta(y-y_f) \end{bmatrix}, \begin{bmatrix} \phi_n \\ f_n \end{bmatrix} \right\rangle \\
&= 0 \qquad \text{(D.9)}
\end{aligned}$$

for any two eigenfunctions denoted m and n of adjoint and original systems respectively. Substituting $\mathscr{L}_{os} = -\mathscr{L} - i\omega(d_y^2 - k^2)$ and $\mathscr{L}_{int} = -\mathscr{I} - i\omega$ into the first term in equation D.9 and rearranging we obtain,

$$-i\omega_n \left\langle \begin{bmatrix} \phi_m^\dagger \\ f_m^\dagger \delta(y-y_f) \end{bmatrix}, \begin{bmatrix} \rho(d_y^2-k^2) & 0 \\ 0 & 1 \end{bmatrix} \begin{bmatrix} \phi_n \\ f_n \end{bmatrix} \right\rangle = \left\langle \begin{bmatrix} \phi_m^\dagger \\ f_m^\dagger \delta(y-y_f) \end{bmatrix}, \begin{bmatrix} \rho\mathscr{L} & 0 \\ \mathscr{C}_v & \mathscr{I} \end{bmatrix} \begin{bmatrix} \phi_n \\ f_n \end{bmatrix} \right\rangle. \tag{D.10}$$

Repeating the same operation for the second term in equation D.9 yields

$$-i\omega_m \left\langle \begin{bmatrix} \rho(d_y^2-k^2) & 0 \\ 0 & 1 \end{bmatrix} \begin{bmatrix} \phi_m^\dagger \\ f_m^\dagger \delta(y-y_f) \end{bmatrix}, \begin{bmatrix} \phi_n \\ f_n \end{bmatrix} \right\rangle = \left\langle \begin{bmatrix} \rho\mathscr{L}^\dagger & 0 \\ -\mathscr{C}_f^\dagger & \mathscr{I}^\dagger \end{bmatrix} \begin{bmatrix} \phi_m^\dagger \\ f_m^\dagger \delta(y-y_f) \end{bmatrix}, \begin{bmatrix} \phi_n \\ f_n \end{bmatrix} \right\rangle \tag{D.11}$$

where $\mathscr{I}^\dagger \equiv \mathscr{I}^*$ and $\mathscr{L}^\dagger \equiv ik_x 2d_y U_T d_y + \nu_T(d_y^2 - k^2)^2$. Using integration by parts, The equation D.11 can re-written as,

$$-i\omega_m \left\langle \begin{bmatrix} \phi_m^\dagger \\ f_m^\dagger \delta(y-y_f) \end{bmatrix}, \begin{bmatrix} \rho(d_y^2-k^2) & 0 \\ 0 & 1 \end{bmatrix} \begin{bmatrix} \phi_n \\ f_n \end{bmatrix} \right\rangle = \left\langle \begin{bmatrix} \phi_m^\dagger \\ f_m^\dagger \delta(y-y_f) \end{bmatrix}, \begin{bmatrix} \rho\mathscr{L} & 0 \\ \mathscr{C}_v & \mathscr{I} \end{bmatrix} \begin{bmatrix} \phi_n \\ f_n \end{bmatrix} \right\rangle + \mathscr{B}\mathscr{T}.$$

where the term $\mathscr{B}\mathscr{T}$ is defined as,

$$\begin{aligned} \mathscr{B}\mathscr{T} \equiv\ & [\rho(-i\omega_m + ik_x U)d_y\phi_n - ik_x d_y U\phi_n - \mu(d_y^3\phi_n - 3k^2 d_y\phi_n)]\phi_m^{\dagger *} \\ & -[\mu(d_y^2+k^2)\phi_n]d_y\phi_m^{\dagger *} + [d_y\phi_n]\mu(d_y^2+k^2)\phi_m^{\dagger *} + C_f^{\dagger *}\phi_m^{\dagger *} f \end{aligned} \tag{D.12}$$

and evaluated at the interface, $y = y_f$. Using the adjoint boundary conditions, the term $\mathscr{B}\mathscr{T}$ can easily be shown as zero. Therefore,

$$-i\omega_m \left\langle \begin{bmatrix} \phi_m^\dagger \\ f_m^\dagger \delta(y-y_f) \end{bmatrix}, \begin{bmatrix} \rho(d_y^2-k^2) & 0 \\ 0 & 1 \end{bmatrix} \begin{bmatrix} \phi_n \\ f_n \end{bmatrix} \right\rangle = \left\langle \begin{bmatrix} \phi_m^\dagger \\ f_m^\dagger \delta(y-y_f) \end{bmatrix}, \begin{bmatrix} \rho\mathscr{L} & 0 \\ \mathscr{C}_v & \mathscr{I} \end{bmatrix} \begin{bmatrix} \phi_n \\ f_n \end{bmatrix} \right\rangle. \tag{D.13}$$

The R.H.S of equation D.13 and equation D.10 are identical. Therefore the L.H.S. of equations D.10 and D.13 must be equal thereby leading to the condition,

$$(\omega_m - \omega_n)\left\langle \begin{bmatrix} \phi_m^\dagger \\ f_m^\dagger \delta(y - y_f) \end{bmatrix}, \begin{bmatrix} \rho(d_y^2 - k^2) & 0 \\ 0 & 1 \end{bmatrix} \begin{bmatrix} \phi_n \\ f_n \end{bmatrix} \right\rangle = 0.$$

Therefore,

$$\left\langle \begin{bmatrix} \phi_m^\dagger \\ f_m^\dagger \delta(y - y_f) \end{bmatrix}, \begin{bmatrix} \rho(d_y^2 - k^2) & 0 \\ 0 & 1 \end{bmatrix} \begin{bmatrix} \phi_n \\ f_n \end{bmatrix} \right\rangle = \delta_{mn}. \tag{D.14}$$

Appendix E

Adjoint Squire operator

The adjoint Squire operator $\mathscr{S}^{\dagger}$ is defined as follows:

$$\langle \chi^{H\dagger}, \rho\mathscr{S}_{sq}\chi^{H}\rangle = \langle \rho\mathscr{S}^{\dagger}_{sq}\chi^{H\dagger}, \chi^{H}\rangle = 0 \tag{E.1}$$

where, $\mathscr{S}_{sq} \equiv -\mathscr{S} - i\omega$. Expanding the definition of the adjoint

$$\begin{aligned} \rho_B \int_0^{y_f} \chi_B^{H\dagger *}\mathscr{S}_{sq,B}\chi_B^H \, dy &= \rho_B \int_0^{y_f} (\mathscr{S}^{\dagger}_{sq,B}\chi_B^{H\dagger})^*\chi_B^H \, dy \\ +\rho_T \int_{y_f}^{\infty} \chi_T^{H\dagger *}\mathscr{S}_{sq,T}\chi_T^H \, dy &\quad +\rho_T \int_{y_f}^{\infty} (\mathscr{S}^{\dagger}_{sq,T}\chi_T^{H\dagger})^*\chi_T^H \, dy. \end{aligned} \tag{E.2}$$

Expanding the first term of the L.H.S. of equation E.2,

$$\rho_B \int_0^{y_f} \chi_B^{H\dagger *}\mathscr{S}_{sq,B}\chi_B^H \, dy = \rho_B \int_0^{y_f} \chi_B^{H\dagger *}\Big(-i\omega + ik_x U - \underbrace{\nu_B(d_y^2 - k^2)}_{T1}\Big)\chi_B^H \, dy. \tag{E.3}$$

Performing integration by parts on $T1$ leads to,

$$\begin{aligned} -\rho_B\nu_B \int_0^{y_f} \chi_B^{H\dagger *}(d_y^2 - k^2)\chi_B^H \, dy &= -\rho_B\nu_B \int_0^{y_f} \chi_B^H(d_y^2 - k^2)\chi_B^{H\dagger *} \, dy \\ &\quad -\rho_B\nu_B\Big[\chi_B^{H\dagger *}d_y\chi_B^H - d_y\chi_B^{H\dagger *}\chi_B^H\Big]_0^{y_f}. \end{aligned} \tag{E.4}$$

Equation D.2 can be rewritten using equation E.4 in the following manner,

$$\begin{aligned} \rho_B \int_0^{y_f} \chi_B^{H\dagger *}\mathscr{S}_{sq,B}\chi_B^H \, dy &= \rho_B \int_0^{y_f} \chi_B^H\mathscr{S}^{\dagger *}_{sq,B}\chi_B^{H\dagger *} \, dy \\ &\quad +\mu_B\Big[\chi_B^{H\dagger *}d_y\chi_B^H - d_y\chi_B^{H\dagger *}\chi_B^H\Big]_0^{y_f} \end{aligned} \tag{E.5}$$

where,

$$\mathscr{S}^{\dagger}_{sq,B} \equiv i(\omega^{\dagger} - k_x U_B) - \nu_B(d_y^2 - k^2).$$

Similarly the adjoint operator can be derived for the top fluid,

$$\begin{aligned}\rho_T \int_0^{y_f} \chi_T^{H\dagger *} \mathscr{S}_{sq,T} \chi_T^H \, dy &= \rho_T \int_0^{y_f} \chi_T^H \mathscr{S}^{\dagger *}_{sq,T} \chi_T^{H\dagger *} \, dy \\ &\quad + \mu_T \left[\chi_T^{H\dagger *} d_y \chi_T^H - d_y \chi_T^{H\dagger *} \chi_T^H \right]_0^{y_f} \end{aligned} \tag{E.6}$$

where,

$$\mathscr{S}^{\dagger}_{sq,T} \equiv i(\omega^{\dagger} - k_x U_T) - \nu_T(d_y^2 - k^2).$$

Using equations E.2, E.5 and E.6 we conclude that the definition of the adjoint in equation E.1 can be satisfied by ensuring,

$$\mu_B \left[\chi_B^{H\dagger *} d_y \chi_B^H - d_y \chi_B^{H\dagger *} \chi_B^H \right]_0^{y_f} + \mu_T \left[\chi_T^{H\dagger *} d_y \chi_T^H - d_y \chi_T^{H\dagger *} \chi_T^H \right]_{y_f}^{\infty} = 0. \tag{E.7}$$

Since for any general χ^H, $\langle \rho \mathscr{S}^{\dagger}_{sq} \chi^{H\dagger}, \chi^H \rangle = 0$, it implies,

$$\mathscr{S}^{\dagger}_{sq,j} \chi_j^{H\dagger} = 0 \tag{E.8}$$

Equation E.8 is the adjoint Squire equation. The adjoint Squire boundary conditions are derived by setting the boundary terms E.7 to zero. The interfacial boundary conditions require,

$$[\chi^H] = 0; \quad [\mu d_y \chi^H] = 0.$$

Hence by setting,

$$[\chi^{H\dagger}] = 0 \quad ; \qquad [\mu d_y \chi^{H\dagger}] = 0$$

the boundary terms E.7 at the interface can be ensured to be zero. Homogeneous boundary conditions are imposed on the adjoint variable in the free stream and at the wall in

order to fulfil the same requirement,

$$\chi_B^{H\dagger}(0) = 0 \quad ; \qquad \chi_T^{H\dagger}(y \to \infty) = 0.$$

E.1 Bi-orthogonality condition

From the definition of the adjoint E.2 it follows,

$$\begin{aligned} \langle \chi_m^{H\dagger}, \rho \mathscr{S}_{sq} \chi_n^H \rangle &= \langle \rho \mathscr{S}_{sq}^\dagger \chi_m^{H\dagger}, \chi_n^H \rangle \\ &= 0 \end{aligned} \tag{E.9}$$

for any two eigenfunctions of χ_n^H and $\chi_m^{H\dagger}$ of the Squire equation and and its adjoint respectively. Replacing $\mathscr{S}_{sq}$ by $-\mathscr{S} - i\omega$ in equation E.9,

$$-i\omega_n \langle \chi_m^{H\dagger}, \rho \chi_n^H \rangle = \langle \chi_m^{H\dagger}, \rho \mathscr{S} \chi_n^H \rangle. \tag{E.10}$$

Similarly the adjoint can be expanded as,

$$-i\omega_m \langle \rho \chi_m^{H\dagger}, \chi_n^H \rangle = \langle \rho \mathscr{S}^\dagger \chi_m^{H\dagger}, \chi_n^H \rangle. \tag{E.11}$$

Integrating by parts equation E.11 and using adjoint Squire boundary conditions leads to:

$$-i\omega_m \langle \chi_m^{H\dagger}, \rho \chi_n^H \rangle = \langle \chi_m^{H\dagger}, \rho \mathscr{S} \chi_n^H \rangle. \tag{E.12}$$

Since the $R.H.S$ of equations E.10 and E.12 are identical, therefore their $L.H.S$ should also be equal,

$$\begin{aligned} -i\omega_m \langle \chi_m^{H\dagger}, \rho \chi_n^H \rangle &= -i\omega_n \langle \chi_m^{H\dagger}, \rho \chi_n^H \rangle, \\ \Rightarrow (\omega_m - \omega_n) \langle \chi_m^{H\dagger}, \rho \chi_n^H \rangle &= 0. \end{aligned} \tag{E.13}$$

Equation E.13 implies that unless $\omega_m = \omega_n$, the inner product, $\langle \chi_m^{H\dagger}, \rho\chi_n^H \rangle$, must vanish. In mathematical notation this can be re-written as

$$\langle \chi_m^{H\dagger}, \rho\chi_n^H \rangle \quad = \quad \delta_{mn}. \tag{E.14}$$

Appendix F

M-norm and its convergence

The amplification in the energy associated with a single-fluid system has been studied for a variety of flows for instance: Poiseuille, Couette and Blasius boundary layer flows (Butler & Farrell, 1992; Reddy & Henningson, 1993). In these studies, the kinetic energy norm defined as,

$$\|q\|_E \equiv \frac{1}{4\ell}\int_0^\infty (|u_{\vec{k}}|^2 + |v_{\vec{k}}|^2 + |w_{\vec{k}}|^2)dy. \tag{F.1}$$

is optimized over all possible initial conditions. The perturbation is expanded using the Orr-Sommerfeld and Squire eigenfunctions, as shown in equation 4.25. Progressive inclusion of higher modes of the basis leads to a convergent series in terms of the maximum transient growth, G_{max}, that is

$$\lim_{N\to\infty} |G_{max}| < \infty.$$

A criterion, $\Delta G_{max}(N)/G_{max}(N)$ with $\Delta G_{max}(N) \equiv G_{max}(N+10) - G_{max}(N)$ is chosen to study the convergence and is referred to as the residual. Figure F.1 shows the convergence of the kinetic energy norm for the single-fluid boundary layer.

In the case of two-fluid boundary layer, the kinetic energy norm does not converge with the inclusion of larger number of eigenfunctions, as shown in figure F.2(a). Although the residual drops below 1% when 150 modes are included, it does not show a monotonic decrease.

A variety of norms have been proposed to improve the convergence of G_{max} in different flow configurations (Noorden *et al.*, 1998; South & Hooper, 1999; Yecko & Zaleski, 2005;

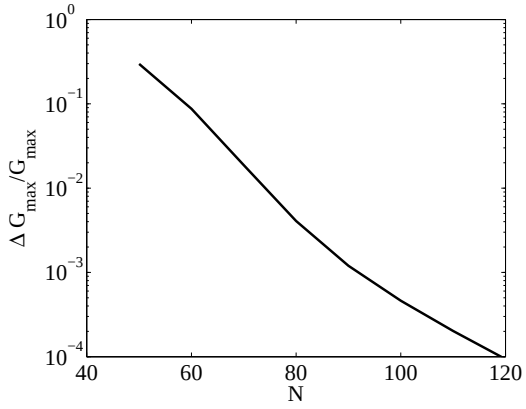


Figure F.1: Convergence of the kinetic energy norm for a single fluid boundary layer. $k_x = 0.001, k_z = 2, Re = 800$.

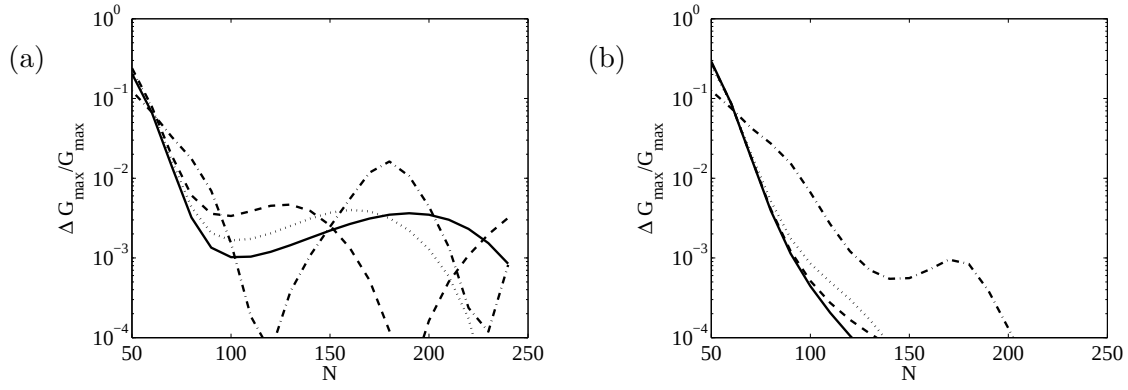


Figure F.2: (a) Convergence of the kinetic energy norm for a two-fluid boundary layer. (b) Convergence of the M-norm for the two-fluid boundary layer $k_x = 0.001, k_z = 2, Re = 800$. ——, $\mu_{BT} = 0.8$; $\cdots$, $\mu_{BT} = 0.6$; - - -, $\mu_{BT} = 0.4$; — $\cdot$ —, $\mu_{BT} = 0.2$

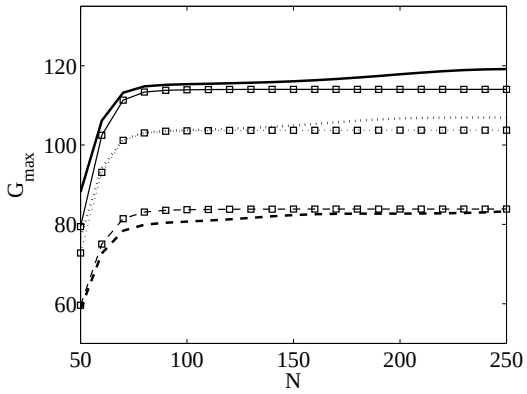


Figure F.3: Comparison of the M-norm and the kinetic energy norm. $k_x = 0.001, k_z = 2, Re = 800$. ——, $\mu_{BT} = 0.8$; · · · ·, $\mu_{BT} = 0.6$; - - -, $\mu_{BT} = 0.4$; □ markers indicate G_{max} computed using M-norm and no markers indicate G_{max} evaluated with the kinetic energy norm.

Malik & Hooper, 2007). However, the M-norm suggested by Malik & Hooper (2007) was adopted in the present study since it was found to converge for all the viscosity ratios tested. Figure F.2(b) shows the convergence trend of the M-norm for a variety of viscosity ratios. The residual drops below 10^{-4} for all cases within 200 modes and shows a steep decrease with increasing N. Finally a comparison is made of G_{max} computed using the kinetic energy norm and the M-norm in figure F.3. As the number of modes increases, G_{max} computed using the kinetic energy norm increases slowly. However the use of the M-norm leads to convergence and G_{max} attains a unique value. The prediction using the M-norm does not deviate appreciably from that of the kinetic energy norm and was therefore used to to study the effect of viscosity stratification.

Bibliography

Abu-Ghannam, B. & Shaw, R. 1980 Natural transition of boundary layers-the effects of turbulence, pressure gradient, and flow history. *Journal of Mechanical and Engineering Science* **22**, 213–228.

Andersson, P., Berggren, M. & Henningson, D. S. 1999 Optimal disturbances and bypass transition in boundary layers. *Physics of Fluids* **11** (1), 134–150.

Belcher, S. E. & Hunt, J. C. R. 1998 Turbulent flow over hills and waves. *Annual Review of Fluid Mechanics* **30**, 507–538.

Benney, D. J. & Gustavsson, L. H. 1981 A new mechanism for linear and nonlinear hydrodynamic instability. *Studies in Applied Mathematics* **64** (3), 185–209.

Berger, S. A. & Aroesty, J. 1977 'e^9': Stability theory and boundary layer transition. *Tech. Rep.*. Rand Corporation.

Berlin, S. & Henningson, D. S. 1999 A nonlinear mechanism for receptivity of free-stream disturbances. *Physics of Fluids* **11**, 3749–3760.

Boomkamp, P. A. M., Boersma, B. J., Miesen, R. H. M. & Beijnon, G. V. 1997 A Chebyshev collocation method for solving two-phase flow stability problems. *Journal of Computational Physics* **132** (2), 191 – 200.

Boomkamp, P. A. M. & Miesen, R. M. 1996 Classification of instabilities in parallel two-phase flow. *International Journal of Multiphase Flow* **22**, 67–88.

Brandt, L., Schlatter, P. & Henningson, D. 2004 Transition in boundary layers subject to free-stream turbulence. *Journal of Fluid Mechanics* **517**, 167–198.

Butler, K. M. & Farrell, B. F. 1992 Three-dimensional optimal perturbation in viscous shear flow. *Physics of Fluids* **A 4**, 1637–1650.

Case, K. M. 1960 Stability of inviscid plane couette flow. *Physics of Fluids* **3** (2), 143–148.

Case, K. M. 1961 Hydrodynamic stability and the inviscid limit. *Journal of Fluid Mechanics* **10**, 420–429.

Charru, F. & Hinch, E. J. 2000 'Phase diagram' of interfacial instabilities in a two-layer Couette flow and mechanism of the long-wave instability. *Journal of Fluid Mechanics* **414**, 195–223.

Chernyshenko, S. I. & Baig, M. F. 2005 The mechanism of streak formation in near-wall turbulence. *Journal of Fluid Mechanics* **544**, 99–131.

Cossu, C., Pujals, G. & Depardon, S. 2009 Optimal transient growth and very large–scale structures in turbulent boundary layers. *Journal of Fluid Mechanics* **619**, 79–94.

Craik, A. 1991 The continuous spectrum of the Orr-Sommerfeld equation: note on a paper of Grosch and Salwen. *Journal of Fluid Mechanics* **226**, 565–571.

Craik, A. D. D. 1966 Wind-generated waves in thin liquid films. *Journal of Fluid Mechanics* **26** (02), 369–392.

Danabasoglu, G. & Biringen, S. 1990 A Chebyshev matrix method for the spatial modes of the Orr-Sommerfeld equation. *International Journal for Numerical Methods in Fluids* **11**, 1033 – 1037.

Drazin, P. G. & Reid, W. H. 1981 *Hydrodynamic Stability*. Cambridge University Press.

Ellingsen, T. & Palm, E. 1975 Stability of linear flow. *Physics of Fluids* **18** (4), 487–488.

Gaster, M. 1975 A theoretical model of a wave packet in the boundary layer on a flat plate. *Proceedings of the Royal Society of London. Series A, Mathematical and Physical Sciences* **347** (1649), 271–289.

Grosch, C. E. & Salwen, H. 1978 The continuous spectrum of the Orr-Sommerfeld equation. Part 1. The spectrum and the eigenfunctions. *Journal of Fluid Mechanics* **87**, 33–54.

Gustavsson, L. H. 1979 Initial-value problem for boundary layer flows. *Physics of Fluids* **22(9)**, 1602–1605.

Gustavsson, L. H. 1981 Resonant growth of three-dimensional disturbances in plane Poiseuille flow. *Journal of Fluid Mechanics* **112**, 253–264.

Gustavsson, L. H. 1991 Energy growth of three-dimensional disturbances in plane Poiseuille flow. *Journal of Fluid Mechanics* **224**, 241–260.

Gustavsson, L. H. & Hultgren, L. S. 1980 A resonance mechanism in plane Couette flow. *Journal of Fluid Mechanics* **98**, 149–159.

Haj-Hariri, H. 1988 Transformations reducing the order of the parameter in differential eigenvalue problems. *Journal of Computational Physics* **77**, 472–484.

Gad-el Hak, M. 2000 *Flow control: passive, active, and reactive flow management*. Cambridge Univ. Press, London.

Hendrickson, G. S. & Hill, E. G. 1987 Effects of de-/anti-icing fluids on airfoil characteristics. Technical report. Boeing.

Herbert, T. 1997 Parabolised stability equations. *Annual Review of Fluid Mechanics* **29**, 245–83.

Hernon, D., Walsh, E. J. & McEligot, D. M. 2007 Experimental investigation into the routes to bypass transition and the shear-sheltering phenomenon. *Journal of Fluid Mechanics* **591**, 461–479.

Hinch, E. J. 1984 A note on the mechanism of the instability at the interface between two shearing fluids. *Journal of Fluid Mechanics* **144**, 463–465.

Hodson, H. P. & Howell, R. J. 2005 Bladerow interactions, transition, and high-lift aerofoils in low-pressure turbines. *Annual Review of Fluid Mechanics* **37**, 71–98.

Hooper, A. P. & Boyd, W. G. C. 1983 Shear-flow instability at the interface between viscous fluids. *Journal of Fluid Mechanics* **128**, 507–528.

Hooper, A. P. & Boyd, W. G. C. 1987 Shear-flow instability due to a wall and a viscosity discontinuity at the interface. *Journal of Fluid Mechanics* **179**, 201–225.

Hultgren, L. S. & Gustavsson, L. H. 1981 Algebraic growth of disturbances in a laminar boundary layer. *Physics of Fluids* **24** (6), 1000–1004.

Hunt, J. C. R. 1977 A review of rapidly distorted turbulent flows and its applications. *Fluid Dynamics Research* **9** (01), 121–152.

Hunt, J. C. R. & Durbin, P. A. 1999 Perturbed vortical layers and shear sheltering. *Fluid Dynamics Research* **24** (06), 375–404.

Jacobs, R. G. & Durbin, P. A. 1998 Shear sheltering and the continuous spectrum of the Orr-Sommerfeld equation. *Physics of fluids* **10(8)**, 2006–2011.

Jacobs, R. G. & Durbin, P. A. 2001 Simulations of bypass transition. *Journal of Fluid Mechanics* **428**, 185–212.

Jordinson, R. 1971 Spectrum of eigenvalues of the Orr-Sommerfeld equation for Blasius flow. *Physics of fluids* **14(11)**, 2535–2537.

Joslin, R. 1998 Aircraft laminar flow control 1. *Annual Review of Fluid Mechanics* **30** (1), 1–29.

Kao, T. W. & Park, C. 1972 Experimental investigations of the stability of channel flows. part 2. two-layered co-current flow in a rectangular channel. *Journal of Fluid Mechanics Digital Archive* **52** (03), 401–423.

Kendall, J. M. 1991 Studies on laminar boundary layer receptivity to free-stream turbulence near a leading edge. *ASME FED* **114**, 43.

Kim, J. & Bewley, T. R. 2007 A linear systems approach to flow control. *Annual Review of Fluid Mechanics* **39**, 383417.

Klebanoff, P. 1971 Effect of freestream turbulence on the laminar boundary layer. *Bull. Am. Phys. Soc* **10** (11), 1323.

Landahl, M. T. 1980 A note on an algebraic instability of inviscid parallel shear flows. *Journal of Fluid Mechanics* **98**, 243–251.

Lasheras, J., Cho, J. & Maxworthy, T. 1986 On the origin and evolution of streamwise vortical structures in a plane, free shear layer. *Journal of Fluid Mechanics* **172**, 231–258.

Lasheras, J. & Choi, H. 1988 Three-dimensional instability of a plane free shear layer: an experimental study of the formation and evolution of streamwise vortices. *Journal of Fluid Mechanics* **189**, 53–86.

Lasheras, J. & Hopfinger, E. 2000 Liquid jet instability and atomization in a coaxial gas stream. *Annual Review of Fluid Mechanics* **32**, 275–308.

Lasseigne, D. G., Joslin, R. D., Jackson, T. L. & Criminale, W. O. 1999 The transient period for boundary layer disturbances. *Journal of Fluid Mechanics* **381**, 89.

Lauchle, G. & Gurney, G. 1984 Laminar boundary-layer transition on a heated underwater body. *Journal of Fluid Mechanics* **144**, 79–101.

Liepmann, H. & Fila, G. 1947 Investigations of effects of surface temperature and single roughness elements on boundary-layer transition. Technical Report 1196. NACA.

Lin, C. C. 1961 Some mathematical problems in the theory of the stability of parallel flows. *Journal of Fluid Mechanics* **10**, 430–438.

Lindzen, R. S. 1988 Instability of plane parallel shear flow (toward a mechanistic picture of how it works). *Pure and Applied Geophysics* **126**, 103–121, 10.1007/BF00876917.

Liu, Y., Zaki, T. A. & Durbin, P. A. 2008 Boundary-layer transition by interaction of discrete and continuous modes. *Journal of Fluid Mechanics* **604**, 199–233.

Luchini, P. 2000 Reynolds-number-independent instability of the boundary layer over a flat surface: optimal perturbations. *Journal of Fluid Mechanics* **404**, 289–309.

Ludwieg, H. & Hornung, H. 1989 The instability of a liquid film on a wall exposed to an air flow. *Journal of Fluid Mechanics* **200**, 217–233.

Mack, L. M. 1976 A numerical study of the temporal eigenvalue spectrum of the Blasius boundary layer. *Journal of Fluid Mechanics* **73**, 497–520.

Malik, S. V. & Hooper, A. P. 2005 Linear stability and energy growth of viscosity stratified flows. *Physics of Fluids* **17**, 024101.

Malik, S. V. & Hooper, A. P. 2007 Three-dimensional disturbances in channel flows. *Physics of Fluids* **19**, 052102.

Marmottant, P. & Villermaux, E. 2004 On spray formation. *Journal of Fluid Mechanics* **498**, 73–111.

Maslowe, S. A. & Spiteri, R. J. 2001 The continuous spectrum for a boundary layer in a streamwise pressure gradient. *Physics of fluids* **13**, 1294–1299.

Matsubara, M. & Alfredsson, P. H. 2001 Disturbance growth in boundary layers subjected to free-stream turbulence. *Journal of Fluid Mechanics* **430**, 149–168.

Miesen, R. & Boersma, B. J. 1995 Hydrodynamic stability of a sheared liquid film. *Journal of Fluid Mechanics* **301**, 175–202.

Miles, J. W. 1959 On the stability of heterogeneous shear flows. Part 2. *Journal of Fluid Mechanics* **16** (02), 209–227.

Morkovin, M., Reshotko, E. & Herbert, T. 1994 Transition in open flow systems - a reassessment. *Bull. Am. Phys. Soc* **39**, 1882.

Morkovin, M. V. 1969 *Viscous Drag Reduction*, chap. On the many faces of transition. Plenum.

Nakamura, L., Kershaw, R. & Grait, N. 1996 Prediction of near-surface gusts generated by deep convection. *Meteorological Applications* **3**, 157–167.

Nelson, J. J., Alving, A. E. & Joseph, D. D. 1995 Boundary layer flow of air over water on a flat plate. *Journal of Fluid Mechanics* **284**, 159–169.

Noorden, T. L. V., Boomkamp, P. A. M., Knaap, M. C. & Verheggen, T. M. M. 1998 Transient growth in parallel two-phase flow: Analogies and differences with single-phase flow. *Physics of Fluids* **10** (8), 2099–2101.

Olsson, P. J. & Henningson, D. S. 1995 Optimal disturbance growth in watertable flow. *Stud. Appl. Maths* **94**, 183–210.

Orr, W. M. F. 1907 The stability or instability of the steady motions of a perfect liquid and of a viscous liquid. part i: A perfect liquid. part ii: A viscous liquid. *Proc. R. Irish Acad.* **A 27**, 9–138.

Orszag, S. A. 1971 Accurate solution of the Orr-Sommerfeld stability equation. *Journal of Fluid Mechanics* **50** (4), 689–703.

Ozgen, S., Carbonaro, M. & Sarma, G. S. R. 2002 Experimental study of wave characteristics on a thin layer of de/anti-icing fluid. *Physics of Fluids* **14** (10), 3391–3402.

Ozgen, S., Degrez, G. & Sarma, G. S. R. 1998 Two-fluid boundary layer instability. *Physics of Fluids* **10**, 2746 – 2757.

Panton, R. L. 1996 *Incompressible flow*. John Wiley & Sons, Inc.

Phillips, O. M. 1969 Shear-flow turbulence. *Annual Review of Fluid Mechanics* **1**, 245–264.

Reddy, S. C. & Henningson, D. S. 1993 Energy growth in viscous channel flows. *Journal of Fluid Mechanics* **252**, 209 – 238.

Reed, H. L., Saric, W. S. & Arnal, D. 1996 Linear stability theory applied to boundary layers. *Annual Review of Fluid Mechanics* **28**, 389–428.

Renardy, Y. 1987 The thin-layer effect and interfacial stability in a two-layer Couette flow with similar liquids. *Physics of Fluids* **30** (6), 1627–1637.

Reshotko, E. A. 1976 Boundary layer stability and transition. *Annual Review of Fluid Mechanics* **8**, 311–349.

Reshotko, E. A. 2001 Transient growth: A factor in bypass transition. *Physics of Fluids* **13**, 1067–1075.

Roach, P. & Brierley, D. H. 1992 The influence of a turbulent free-stream on zero pressure gradient transitional boundary layer development part 1: Test cases T3A and T3B. In *Numerical simulation of unsteady flows and transition to turbulence*, pp. 319–347. ERCOFTAC.

Salwen, H. & Grosch, C. E. 1981 The continuous spectrum of the Orr-Sommerfeld equation. Part 2. Eigenfunction expansions. *Journal of Fluid Mechanics* **104**, 445–465.

Saric, W. S., Reed, H. L. & Kerschen, E. J. 2002 Boundary layer receptivity to free-stream disturbances. *Annual Review of Fluid Mechanics* **34**, 291–319.

Schlichting, H. 1933 Berechnung der Anfachung kleiner Störungen bei der Plattenströmung. *ZAMM* **13**, 171–174.

Schlichting, H. 1987 *Boundary-Layer Theory*, 7th edn. McGraw-Hill.

Schmid, P. J. 2007 Non-modal stability theory. *Annual Review of Fluid Mechanics* **39**, 129–162.

Schmid, P. J. & Henningson, D. S. 2001 *Stability and Transition in Shear Flows*. Springer-Verlag.

Schrader, L.-U., Brandt, L. & Henningson, D. S. 2009 Receptivity mechanisms in three-dimensional boundary-layer flows. *Journal of Fluid Mechanics* **618**, 209–241.

Schubauer, G. & Skramstad, H. 1947 Laminar boundary-layer oscillations and transition on a flat plate. *Journal Res. Nat. Bur. Standards* **38**, 251–292.

Schubauer, G. & Skramstad, H. 1948 Laminar boundary-layer oscillations and transition on a flat plate. *N.A.C.A Rep* **909**.

South, M. J. & Hooper, A. P. 1999 Linear growth in two-fluid plane Poiseuille flow. *Journal of Fluid Mechanics* **381**, 121–139.

Strazisar, A. J., Reshotko, E. & Prahl, J. M. 1977 Experimental study of the stability of heated laminar boundary layers in water. *Journal of Fluid Mechanics* **83** (02), 225–247.

Tennekes, H. & Lumley, J. L. 1972 *A First Course in Turbulence*. The MIT Press.

Timoshin, S. N. 1997 Instabilities in a high-Reynolds-number boundary layer on a film-coated surface. *Journal of Fluid Mechanics* **353**, 163–195.

Tollmien, W. 1929 Über die Entstehung der Turbulenz. *Nachr. Ges. Wiss. Göttingen* **1**, 21–44.

Trefethen, L. N., Trefethen, A. E., Reddy, S. C. & Driscoll, T. A. 1993 Hydrodynamic stability without eigenvalues. *Science* **261** (5121), 578–584.

Tumin, A. 2003 Multimode decomposition of spatially growing perturbations in a two-dimensional boundary layer. *Physics of Fluids* **15** (9), 2525–2540.

Voke, P. R. & Yang, Z. 1995 Numerical study of bypass transition. *Physics of Fluids* **7**, 2256–2264.

Westin, K. J. A., Boiko, A. V., Klingmann, B. G. B., Kozlov, V. V. & Alfredsson, P. H. 1994 Studies on laminar boundary layer receptivity to free-stream turbulence near a leading edge. *Journal of Fluid Mechanics* **281**, 193–218.

Yecko, P. 2008 Disturbance growth in two-fluid channel flow: The role of capillarity. *International Journal of Multiphase Flow* **34**, 272–282.

Yecko, P. & Zaleski, S. 2005 Transient growth in two-phase mixing layers. *Journal of Fluid Mechanics* **528**, 43–52.

Yecko, P., Zaleski, S. & Fullana, J. M. 2002 Viscous modes in two-phase mixing layers. *Physics of Fluids* **14** (12), 4115–4122.

Yih, C. 1990 Wave formation on a liquid layer for de-icing airplane wings. *Journal of Fluid Mechanics* **212**, 41–53.

Yih, C. S. 1967 Instability due to viscosity stratification. *Journal of Fluid Mechanics* **27**, 337–352.

Zaki, T. A. & Durbin, P. A. 2005 Mode interaction and the bypass route to transition. *Journal of Fluid Mechanics* **531**, 85–111.

Zaki, T. A. & Durbin, P. A. 2006 Continuous mode transition and the effects of pressure gradient. *Journal of Fluid Mechanics* **563**, 357–388.

Zaki, T. A. & Saha, S. 2009 On shear sheltering and the structure of vortical modes in single and two-fluid boundary layers. *Journal of Fluid Mechanics* **626**, 113–148.

Zhang, X. F., Vera, M., Hodson, H. & Harvey, N. 2006 Separation and transition control on an aft-loaded ultra-high-lift LP turbine blade at low Reynolds numbers: Low-speed investigation. *Journal of Turbomachinery* **128** (3), 517–527.